ulm university universität ulm

Annual Report 2010

Institute of Optoelectronics

Cover photo:
Free-standing GaN wafer with a thickness of about 1.5 mm grown by hydride vapor phase epitaxy (see articles on pages 55 and 63). The wafer was self-separated from the original sapphire substrate by the strain induced during cool-down owing to the different thermal expansion coefficients of GaN and sapphire, enforced by a hexagonally shaped mask interlayer.

Contents

Articles

Lists of Publications

1: Mohamed Fikry
2: Rudolf Rösch
3: Ahmed Al-Samaneh
4: Peter Unger
5: Dietmar Wahl
6: Alexander Hein
7: Rainer Michalzik
8: Rainer Blood
9: Benedikt Westenfelder
10: Robert Leute
11: Martin Klein
12: Ilona Argut
13: Stephan Schwaiger
14: Gerlinde Meixner
15: Anna Bergmann
16: Ferdinand Scholz
17: Frank Demaria
18: Wolfgang Schwarz
19: Alexander Kern
20: Alyona Lainburg
21: Junjun Wang

Missing in the picture:

Christine Bunk, Karl Joachim Ebeling, Kamran Forghani, Sükran Kilic, Frank Lipski, Hildegard Mack, Jürgen Mähnß, Susanne Menzel, Eva Schmid

Ulm University
Institute of Optoelectronics

Albert-Einstein-Allee 45, 89081 Ulm, Germany
URL: http://www.uni-ulm.de/opto
Fax: +49–731/50–26049
Phone: +49–731/50–

Head of Institute

Prof. Dr.	Peter Unger	–26054	peter.unger@uni-ulm.de

Deputy Head

Prof. Dr.	Ferdinand Scholz	–26052	ferdinand.scholz@uni-ulm.de

President of Ulm University

Prof. Dr.	Karl Joachim Ebeling	–22000	karl.ebeling@uni-ulm.de

Senior Research Assistant

PD Dr.-Ing.	Rainer Michalzik	–26048	rainer.michalzik@uni-ulm.de

Cleanroom Management

Dr.-Ing.	Jürgen Mähnß	–26053	juergen.maehnss@uni-ulm.de

Secretaries

	Christine Bunk	–26051	christine.bunk@uni-ulm.de
	Sükran Kilic	–26059	suekran.kilic@uni-ulm.de
	Hildegard Mack	–26060	hildegard.mack@uni-ulm.de
	Eva Schmid	–26050	eva.schmid@uni-ulm.de

Research Staff

M.Sc.	Ahmed Al-Samaneh	–26037	ahmed.al-samaneh@uni-ulm.de
Dipl.-Ing.	Anna Bergmann	–26038	anna.bergmann@uni-ulm.de
Dr.-Ing.	Frank Demaria	–26046	frank.demaria@uni-ulm.de
M.Sc.	Mohamed Fikry	–26195	mohamed.fikry@uni-ulm.de
M.Sc.	Kamran Forghani	–26039	kamran.forghani@uni-ulm.de
Dr.-Ing.	Abdel-Sattar Gadallah*	–26036	abdel-sattar.gadallah@uni-ulm.de
Dipl.-Ing.	Alexander Hein	–26046	alexander.hein@uni-ulm.de
Dipl.-Ing.	Ihab Kardosh*	–26035	ihab.kardosh@uni-ulm.de
Dipl.-Ing.	Alexander Kern	–26037	alexander.kern@uni-ulm.de
Dipl.-Ing.	Martin Klein	–26043	martin.klein@uni-ulm.de
Dipl.-Math.	Alyona Lainburg*	–26057	alyona.lainburg@uni-ulm.de
Dipl.-Phys.	Robert Leute	–26056	robert.leute@uni-ulm.de
Dipl.-Phys.	Frank Lipski	–26039	frank.lipski@uni-ulm.de
Dr.-Ing.	Fernando Rinaldi*	–26046	fernando.rinaldi@uni-ulm.de
Dipl.-Phys.	Stephan Schwaiger*	–26056	stephan.schwaiger@uni-ulm.de
Dipl.-Ing.	Wolfgang Schwarz	–26038	wolfgang.schwarz@uni-ulm.de
Dipl.-Phys.	Dietmar Wahl	–26037	dietmar.wahl@uni-ulm.de
M.Sc.	Junjun Wang	–26195	junjun.wang@uni-ulm.de
Dipl.-Phys.	Benedikt Westenfelder	–26454	benedikt.westenfelder@uni-ulm.de
Dr.-Ing.	Thomas Wunderer*	–26454	thomas.wunderer@uni-ulm.de

Technical Staff

Ilona Argut	–2 60 56	ilona.argut@uni-ulm.de
Rainer Blood	–2 60 44	rainer.blood@uni-ulm.de
Gerlinde Meixner	–2 60 41	gerlinde.meixner@uni-ulm.de
Susanne Menzel	–2 60 41	susanne.menzel@uni-ulm.de
Rudolf Rösch	–2 60 57	rudolf.roesch@uni-ulm.de
Josef Theisz*	–2 60 30	josef.theisz@uni-ulm.de

* Member has left the institute meanwhile

Preface

The year 2010 was again very fruitful for the Institute of Optoelectronics. Research in the VCSELs and Optical Interconnects Group dealt with vertical-cavity lasers with polarization-stable single-mode light output for integration with atomic clocks, bidirectional optical interconnects over standard multimode fibers, densely packed VCSEL arrays, VECSEL-type devices for particle sensing in microfluidics, as well as ultracompact optical traps.

The GaN group continued their studies of non- and semipolar structures in the frame of the transregional research group "PolarCoN". In October, we could host again more than 50 scientists at a summer school in Schloss Reisensburg near Günzburg. The research group could additionally find special attention on the occasion of a symposium at the Annual Meeting of the Deutsche Physikalische Gesellschaft in Regensburg. Besides many excellent quantum well and device structures grown by MOVPE, our HVPE-grown thick GaN layers improved further, as documented on the title page of this report. Our fairly new engagement in graphene research within the project SALVE has been stabilized by another 3-years funding period approved by the DFG.

In the High-Power Semiconductor Laser Group, the temperature management of optically pumped semiconductor disk lasers has been further investigated. Novel double-band Bragg reflector mirror designs have been evaluated showing optimized thermal resistance.

Four members of the Institute, namely Abdel-Sattar Gadallah, Andrea Kroner, Sarad Bahadur Thapa, and Thomas Wunderer received their Ph.D. degrees. Furthermore, six Diploma Theses, five Master Theses, four Bachelor Theses, and two Semester Projects have been carried out in 2010.

In April 2010, Ahmed Al-Samaneh received the Best Student Paper Award at the Conf. on *Semiconductor Lasers and Laser Dynamics IV*, as part of *SPIE Photonics Europe* in Brussels, Belgium for his work on VCSELs for atomic clocks.

In May 2010, Rainer Michalzik was offered to become the Director of the Institute of Optoelectronics at the University of Duisburg-Essen in Duisburg, Germany.

Rainer Michalzik
Ferdinand Scholz
Peter Unger Ulm, March 2011

Time-Resolved In-Situ Temperature Measurements Using Band-Edge Absorption Spectroscopy During MBE Growth

Dietmar Wahl and Michael Mertens

It is a well-known problem in molecular beam epitaxy (MBE) that the real sample temperature is in most cases unknown during the growth process. We have used a commercial band-edge absorption spectroscopy system to determine the sample temperature during bake-out and growth of different types of samples. Time-resolved in-situ measurements show how the sample temperature is influenced by different external effects and also demonstrate some limitations of precise temperature determination. This helps to understand the temperature behavior of GaAs-based samples during a growth run.

1. Introduction

One of the most crucial parameters in semiconductor epitaxy processes is the substrate temperature. In strongly chemistry-based techniques, e.g., metal-organic vapor-phase epitaxy, it has a major influence on the chemical reactions between incoming atoms or molecules and thus the efficiency of these processes. In molecular beam epitaxy, the more important effect is the change of surface mobility of the adsorbed adatoms[2] with temperature. It influences the crystal quality and defect density. Also the ratio of adsorption and desorption of particles of different species (which determines the material composition) can be temperature-dependent. Nearly all properties of the grown material like luminescence spectrum and efficiency, surface roughness or carrier mobilities are strongly influenced by the substrate temperature during the epitaxial process ([1], pp. 183 ff.).

In MBE growth chambers, the sample temperature can be determined in different ways, namely thermocouple (TC), pyrometry or RHEED[3]-assisted methods, as well as band-edge absorption spectroscopy (BAS). Each method offers different degrees of precision, reproducibility, and range of use:

- **Thermocouple**
  The thermocouple is usually located behind the sample holder near the sample heater and has no physical contact with the rotating sample. The entire temperature range of interest is covered and the measurement is reproducible. Therefore it is predestined for temperature control.

[2] In crystal growth, atoms which are adsorbed at a substrate surface are called *adatoms*. Their behavior is influenced by chemical bonding to the surface material.

[3] Reflection high-energy electron diffraction (RHEED) is a technique to investigate the surface condition of a crystalline sample by the diffraction pattern caused by a focused electron beam.

- **Pyrometer**
  Pyrometers detect black-body radiation emitted from the sample itself. To obtain a suitable black-body spectrum, the sample must have a temperature of 400 °C or more. The emission factor (0.7 for GaAs [2]) may have to be corrected for changes in the emission characteristics of the sample holder or of the transmissivity of the chamber viewport over time. Heat radiation reflections from the effusion cells can have strong influences on the registered spectrum and the calculated temperature.

- **RHEED**
  During bake-out of GaAs wafers, desorption of the oxide layer on top of the sample takes place. This transition from amorphous to ordered surface condition can be recognized in an abrupt change of the RHEED pattern from diffuse scattering to a diffraction pattern according to a structured surface. This transition happens at a substrate temperature of 582 ±1 °C [3]. A second but very inaccurate use of RHEED is to distinguish between different patterns caused by different surface conditions, which depend on the temperature but also on the arsenic flux. This method has very limited use since the patterns change only slowly over a temperature range of several tens of Kelvin.

- **Band-edge absorption spectroscopy**
  BAS is based on intrinsic absorption of light passing through semiconductor material. Detected with a spectrometer, the wavelength of the absorption edge in the measured spectrum can be related to a certain temperature. Observing the shift to longer wavelengths with increasing temperature allows to determine the substrate temperature over a wide range.

2. Principles of Band-Edge Absorption Spectroscopy

Semiconductors experience a reduction of their bandgap energy E_g with increasing temperature. This shift can be described by the empirical Varshni formula [4]

$$E_\mathrm{g}(T) = E_\mathrm{g}(0\,\mathrm{K}) - \frac{\alpha T^2}{\beta + T} \quad .$$

The material-dependent parameters α and β for intrinsic GaAs are noted in Table 1. More sophisticated models of the temperature dependence of semiconductor bandgaps have been established by Viña et al. [6] and Pässler et al. [7].

Table 1: Varshni parameters of intrinsic GaAs according to Thurmond [5].

Parameter	Value
$E_\mathrm{G}(0\,\mathrm{K})$	$1.519\,\mathrm{eV}$
α	$5.405 \cdot 10^{-4}\,\mathrm{eV/K}$
β	$204\,\mathrm{K}$

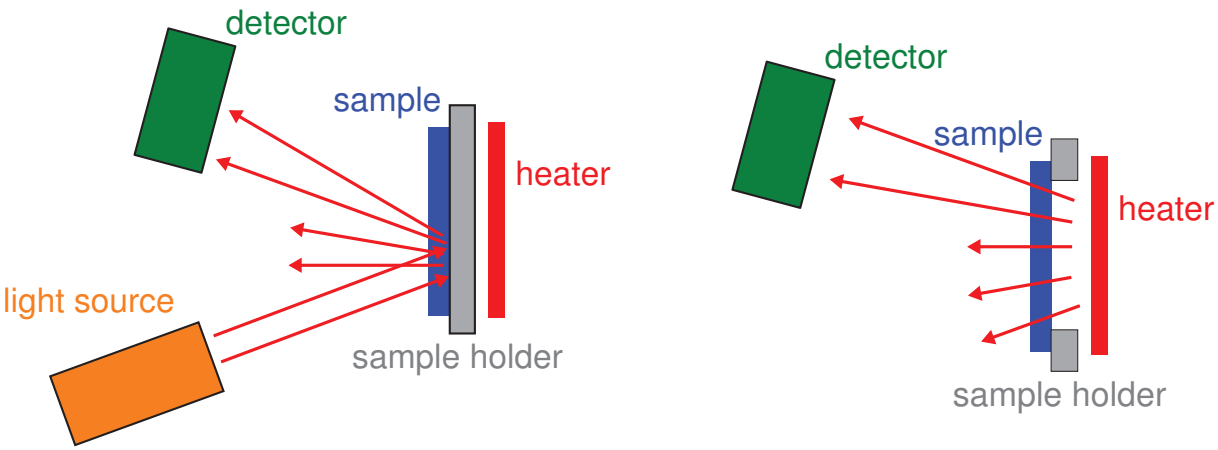

Fig. 1: Schematic drawing of the reflection mode (left) and the transmission mode (right) of band-edge absorption spectroscopy. The reflection mode requires an external light source and one additional viewport in the growth chamber.

In BAS, light has to pass at least once through a semiconductor substrate. For high-bandgap material (e.g., sapphire) the visible range is favored, for lower-bandgap semiconductors like GaAs, the near-infrared spectral range from 800 to 1400 nm is appropriate for detection of the absorption edge. The measurement can be done in reflection mode as shown in the left part of Fig. 1, which means that the sample is illuminated by an external light source with a continuous spectrum. The light enters the substrate and is scattered at the unpolished back side of the wafer. This mode can be used for both, indium-mounted and indium-free-mounted wafers. For this configuration an additional viewport of the vacuum system is needed. With indium-free-mounted wafers on substrate holders with an opening, one can use the black-body-like radiation from the substrate heater. In this transmission mode (right part of Fig. 1), the light is scattered at the unpolished back side of the wafer before passing through the material. In both modes, scattering is important to make the setup more insensitive to the location of the detector. Light with higher energy than the bandgap energy is strongly absorbed when passing the semiconductor, while lower-energy photons are transmitted nearly without losses. This leads to an optical spectrum as shown in Fig. 2. Spectral shifts indicate changes in the temperature of the semiconductor due to the temperature-dependent bandgap.

2.1 Experimental setup

The MBE system used for these investigations is a solid-source Riber 32 growth chamber, equipped with two gallium cells, three aluminum cells, one indium cell and a valved arsenic cracker. Doping can be introduced by a solid-source silicon cell for n-type material and a CBr_4 gas line for p-doping. The system reaches a base pressure of $2 \cdot 10^{-11}$ Torr by means of the attached cryo pump and an ion getter pump.

For temperature determination by BAS, we have used the commercially available BandiT system (NIR Model). The system consists of the controller with integrated spectrometer and computer interface, the detector head for fiber coupling, and a halogen lamp for

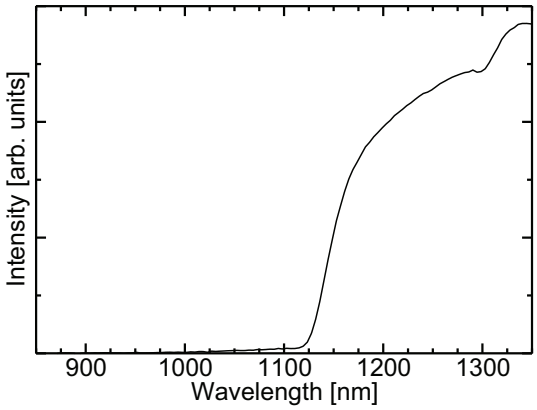

Fig. 2: Transmission spectrum of light passing through an undoped GaAs substrate at a temperature of 582 °C (verified by RHEED transition).

reflection mode measurements[4] (see Fig. 3). The detector head with the fiber coupler was connected to the pyrometer viewport of the chamber which is directed onto the sample if the manipulator with the substrate holder is in growth position. The halogen lamp, which is necessary for reflection mode measurements, could not be installed because of the lack of an adequate second viewport. So only transmission mode measurements were performed. This limits the lowest measurable temperature to approximately 400 °C. Below this temperature, the black-body-like substrate heater emission spectrum is too weak for a reliable detection of the absorption edge.

The BandiT system does not refer to a theoretical band-edge but relies on comparison with reference data supplied by the manufacturer. These references are specified by the material, thickness, doping type, doping level and manufacturer of the substrate. Our substrate material was not included in the supplied substrate database. As a best suited reference we chose a substrate with same doping and doping level and similar thickness than our actual wafer type. This might be the reason why the determined temperature varies from the real one by approximately 5 K. This deviation was determined by observing the deoxidation behavior with the RHEED system. Nevertheless the data are much more precise than those obtained with thermocouple measurements or pyrometry at lower temperatures.

The software subtracts from the measured spectrum a black-body part which is not correlated to absorption features. The remaining, corrected and normalized spectrum is used to create a linear fit to the lower part of the absorption edge. The intersection of this straight line and the abscissa results in a wavelength which is compared with the above-mentioned reference data to determine the substrate temperature.

Problems occur when the black-body part dominates the received spectrum. This can be the case when, due to misalignment, the detector head collects light not from the sample but from other hot parts in the chamber like for example the substrate holder. In some geometrical circumstances, strong black-body radiation from the glowing cells can directly be reflected into the detector by the polished wafer surface. Under such conditions, the fit algorithm cannot properly determine the actual temperature.

[4]More information about the BandiT system and its specifications can be found at the manufacturer's website: *http://www.k-space.com/Products/BandiT.html*

Fig. 3: Hardware of the BandiT band-edge absorption spectroscopy system, consisting of a controller with spectrometer, a fiber-coupled detector head and a halogen lamp.

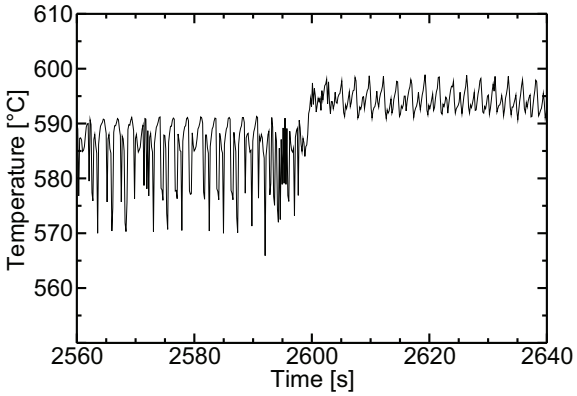

Fig. 4: Spurious temperature oscillations caused by the rotation of the substrate. At 2600 s, the Ga shutter was opened, which results in a rise of the sample temperature.

2.2 Time-resolved measurements

The BandiT system enables real-time measurements and data recording. The algorithm calculates the temperature from each spectrum every 1 to 2 seconds and saves it in a data file. The measured spectra are only shown on the computer screen but are not saved, since the amount of data would be far too large. Thus after measurement it is not possible to check the fit results and the original spectra.

The sample holder is rotating during preparation and growth to ensure good homogeneity or at least radially symmetric growth conditions. During rotation, the wafer can tilt by approximately some tenths of a degree, which influences the obtained spectrum. This results in a spurious variation of the calculated substrate temperature. As can be seen in Fig. 4, these oscillations can exceed 10 K. The time period of the oscillations in the recorded temperature can clearly be correlated to the rotation period of the sample holder.

From time to time the system produces some measurement errors. These can be identified by drastic one-point outliers in the saved temperature function. Especially during cool-down or at lower substrate temperatures the errors occur because of the low intensity of the heater's black-body radiation. These artefacts have been deleted in the diagrams shown here.

Time-resolved measurements of the temperature were performed during the entire growth of the samples presented in what follows.

3. Time-Resolved Investigations During MBE Growth

Two samples, namely an edge-emitting laser structure containing a quantum dot active region and a vertical-cavity surface-emitting laser (VCSEL), have been investigated during their complete growth process. The long growth times and thick layers are the sources of several effects which should be taken into account in future applications of band-edge absorption spectroscopy.

3.1 Sample A: quantum dot edge-emitting laser

The sample is an edge-emitting laser structure with five $In_{0.7}Ga_{0.3}As/GaAs$ quantum dot (QD) layers in the active region for an emission wavelength of about 1250 nm. The active region is surrounded by two 1.3 µm thick AlGaAs layers containing up to 50 % aluminum. The lower one is n-doped (Si), the upper one is p-doped (C), both up to a level of $2 \cdot 10^{18}\,\mathrm{cm}^{-3}$.

Growth conditions

The layer stack was grown on a 500 µm thick n-doped GaAs wafer with (001)-oriented surface. The wafer was thermally deoxidized under arsenic flux at a thermocouple temperature of 540 °C. The BAS temperature for deoxidation was 589 °C. This temperature was also used for the growth of the AlGaAs layers. In MBE growth, lower substrate temperatures are chosen for the growth of indium-containing layers to decrease indium desorption. For the quantum dot layers, the growth temperature was decreased to 420 °C (TC) or 470 °C (BAS). Previous experiments had shown that this growth temperature leads to optimized optical properties and good crystal quality of the quantum dots.

Experimental results

The complete temperature profile determined by the BandiT system is shown in Fig. 5. At the beginning, the temperature is quite stable during the growth of the first AlGaAs cladding layer. Because the absorption edge is caused by the lowest bandgap, the higher bandgap of the cladding layers should not be problematic. For the second cladding layer one can see a slightly oscillating temperature. Because the thermocouple showed stable behavior, these oscillations seem not to be caused by the heater but originate from the BandiT device. As a possible reason, Fabry–Pérot resonances of light passing the growing AlGaAs layer may influence the obtained spectra in such a way that the fitting algorithm determines a slightly changing temperature.

Figure 6 depicts a more detailed graph of the temperature profile during growth of the quantum dot layers. The recurring temperature drops indicate ten-second-long growth interruptions between quantum dot layer and barrier material. The Ga cell (Ga1) used for the barrier was kept at 886 °C. The cell growth of the QDs involved a second Ga cell (Ga2) at 718 °C and an In cell at 658 °C. During all this time, the thermocouple temperature and the temperature controller output were quite constant, which means that heat generation by the substrate heater was also constant. Rising substrate temperatures can clearly be correlated to the openings of different shutters. If the hot Ga1 cell is opened, the substrate temperature is 2 K higher than with the combination of the Ga2 and In cells. This shows that the hot cells act as additional head sources from the front side, which increase the sample temperature but do not influence the thermocouple measurement behind the sample. This effect is expected to be larger for higher growth rates that require higher cell temperatures.

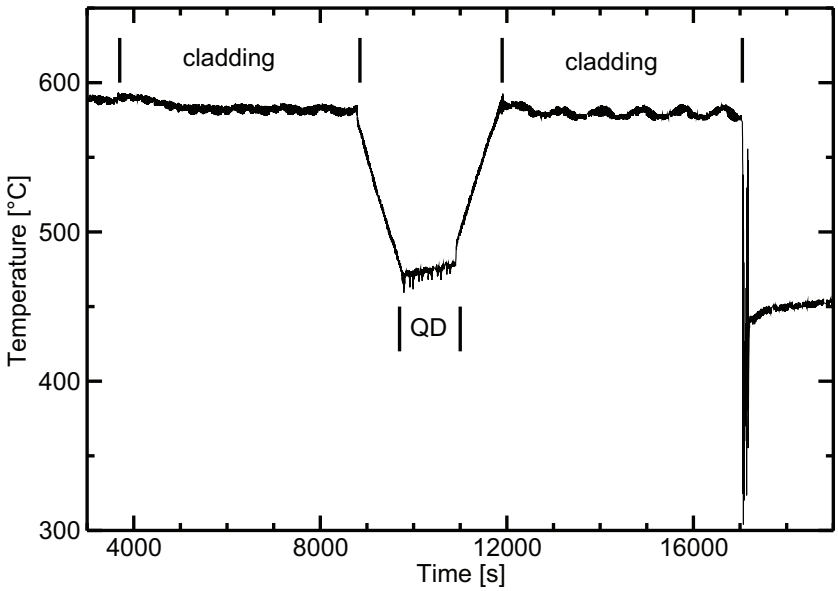

Fig. 5: Temperature profile determined with band-edge absorption spectroscopy of sample A. The oscillations during growth of the second cladding layer are no real fluctuations of the sample temperature but are caused by the measurement method.

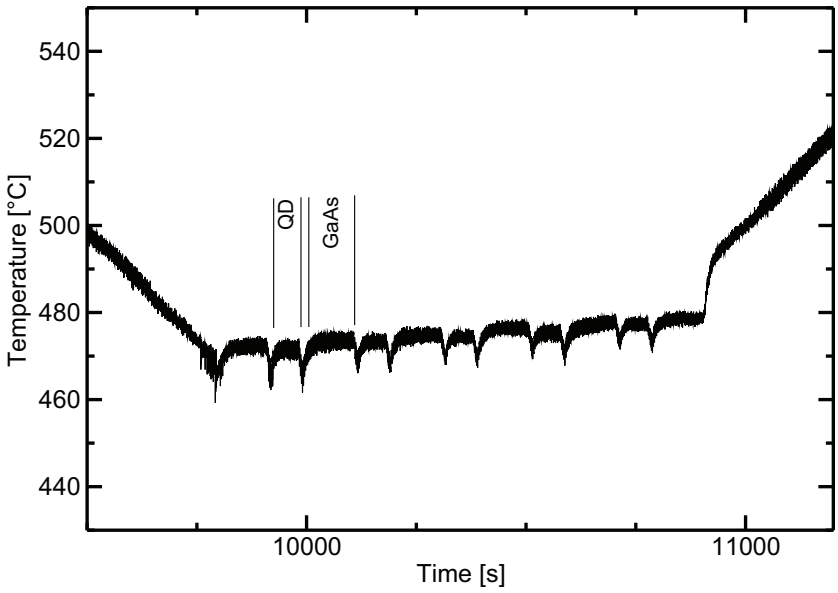

Fig. 6: Detailed time-dependent temperature during growth of the quantum dot active region of sample A. The temperature dips indicate closure of all shutters for 10 seconds, separating quantum dot and barrier material growth.

3.2 Sample B: vertical-cavity surface-emitting laser

The second investigated sample is a VCSEL structure. The main difference to sample A are the Bragg mirrors which are necessary for constituting the vertical cavity. The Bragg mirrors consist of periodically repeated AlGaAs layers with varying aluminum content from 20 % to 90 %, which results in a periodic variation of the refractive index. The period length of these layers is designed to be one half of the wavelength in the material. In this special VCSEL, the first grown mirror contains ten repetitions, the second one 38 mirror periods. The active region is composed of three $In_{0.06}Ga_{0.94}As/Al_{0.27}Ga_{0.73}As$ quantum wells with 8 nm thickness.

Growth conditions

The sample was grown on a (001)-oriented n-doped GaAs substrate with a thickness of 350 µm. The removal of the oxide layer could be observed by RHEED at a thermocouple temperature of 530 °C, while BAS determined the sample temperature to be 580 °C. For the growth of the quantum well region, the temperature was reduced to prevent huge indium desorption and to obtain good optical properties.

Experimental results

The calculated BAS temperature is varying in a range of up to 70 K around the initial temperature, which can be seen in Fig. 7. These strong oscillations are caused by the growing Bragg mirror. However, in contrast to simple expectations, the oscillation period cannot be correlated to the growth of the periodic Bragg mirror layers. A closer look at the recorded data in Fig. 8 shows a temperature drop of a few Kelvin when shutters get closed. During the growth of each mirror period, three sheets of delta doping are incorporated by closing all cells except the doping sources. As described earlier, this can be identified by a small temperature drop. Figure 8 reveals that one mirror period is grown within 760 s. The huge temperature oscillations have a time period of 1050 s. Periodic structures lead to a massive distortion of the detected spectrum and thus to a deviation of the calculated temperature. These results clearly show the limits of BAS. For complicated layer structures it can be applied only to monitor the preprocessing and start of the growth.

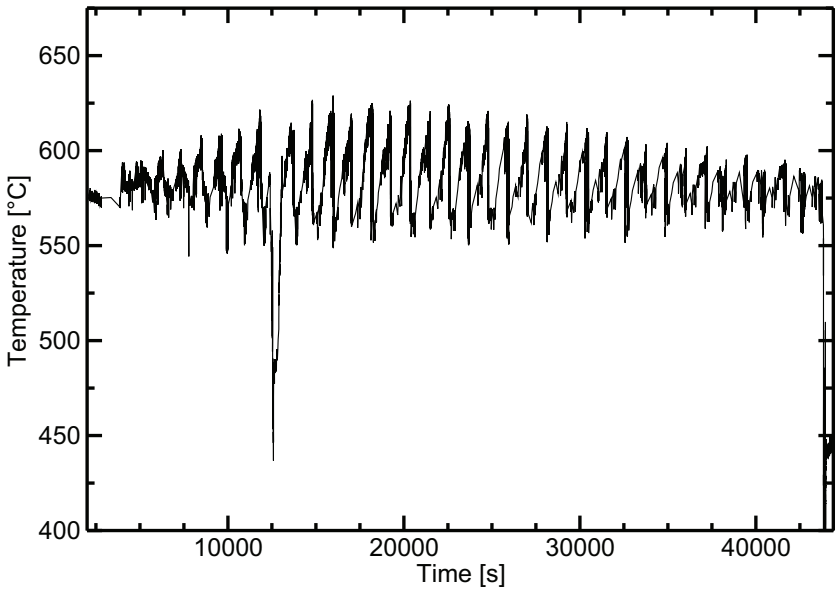

Fig. 7: Temperature profile determined with band-edge absorption spectroscopy of sample B. The spectral influence of the Bragg mirror layers on the detected signal lead to strong spurious temperature fluctuations.

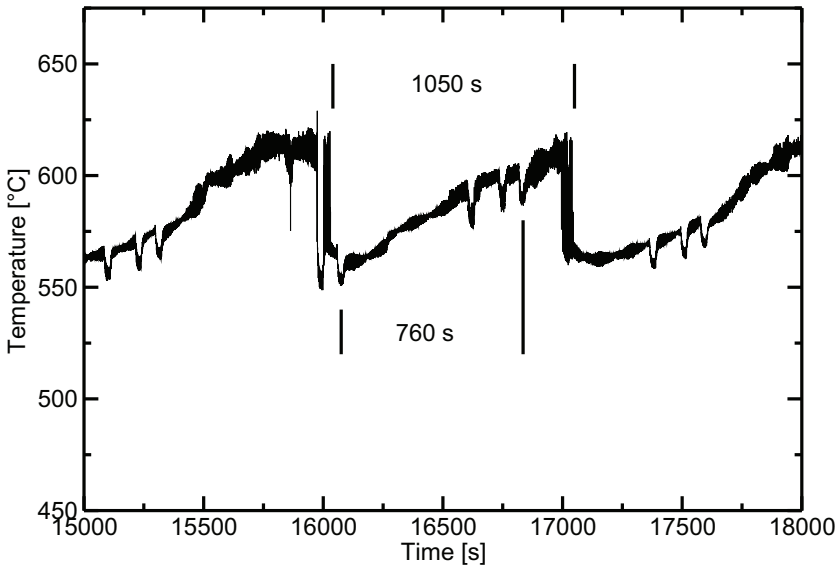

Fig. 8: Detailed temperature plot during growth of sample B. The oscillation period of $\approx 1050\,\mathrm{s}$ is not equal to the growth time of one Bragg mirror period (760 s).

4. Conclusion

Band-edge absorption spectroscopy, which is based on the physical properties of the sample material, is an additional method for substrate temperature measurement in MBE systems. The resulting temperature is much more realistic than values obtained from thermocouple or pyrometer which are strongly influenced by the geometry of the growth chamber. As long as non-periodic layer structures are grown, BAS can be used for ongoing monitoring and recording of the sample temperature. Periodic layer stacks lead to strong oscillations of the calculated temperature, caused by major changes of the detected spectrum.

References

[1] R.F.C. Farrow (Ed.), *Molecular Beam Epitaxy*. Park Ridge: Noyes Publications, 1995.

[2] Pyrometer Device Manual: MODLINE PLUS Infrared Thermometer, Edition 3, IRCON Inc., March 1989.

[3] A.J. SpringThorpe, S.J. Ingrey, B. Emmerstorfer, and P. Mandeville, "Measurement of GaAs surface oxide desorption temperatures", *Appl. Phys. Lett.*, vol. 50, pp. 77–79, 1987.

[4] Y.P. Varshni, "Temperature dependence of the energy gap in semiconductors", *Physica*, vol. 43, pp. 149–154, 1967.

[5] C.D. Thurmond, "The standard thermodynamic functions for the formation of electrons and holes in Ge, Si, GaAs, and GaP", *J. Electrochem. Soc.*, vol. 122, pp. 1133–1141, 1975.

[6] L. Viña, S. Logothetidis, and M. Cordona, "Temperature dependence of the dielectric function of germanium", *Phys. Rev. B*, vol. 30, pp. 1979–1991, 1984.

[7] R. Pässler and G. Oelgart, "Appropriate analytical description of the temperature dependence of exciton peak positions in $GaAs/Al_xGa_{1-x}As$ multiple quantum wells and the Γ_{8v}–Γ_{6c} gap of GaAs", *J. Appl. Phys.*, vol. 82, pp. 2611–2616, 1997.

Towards Integrated VCSEL Arrays for Optofluidic Sorting Applications

Anna Bergmann

We present the concept of an ultra-small, potentially low-cost microfluidic sorting unit based on vertical-cavity surface-emitting lasers. The densely packed lasers are integrated with the microfluidic channel and form an optical lattice. We show first results in an experimental setup, followed by tests of the first generation of integrated setups. A promising novel integration approach and future prospects are introduced.

1. Introduction

In 1970, Arthur Ashkin for the first time reported particle movement by laser beams [1]. He found that forces arising from light momentum transfer attract a particle to the center of a focused laser beam. Since then, scientists from different fields of research have spent much effort to render the principle of optical trapping useful for many areas. One of these areas affects the field of biophotonics, e.g., the manipulation of DNA [2] or red blood cells [3]. Micrometer-sized fluidic channels are a popular medium to handle extremely small volumes with a rather high throughput. By merging them with lasers for optical manipulation, analyzing and sorting of particles can be combined in a so-called lab-on-a-chip. In the competition towards increased miniaturization, vertical-cavity surface-emitting lasers (VCSELs) offer particular advantages. Besides the inexpensive fabrication and the circular beam profile they offer the possibility of two-dimensional array formation with almost arbitrary geometries and high device density. Their output powers in the milliwatt range are sufficient for the manipulation of particles. Owing to the low power consumption, integration into handheld, battery-driven devices seems feasible.

2. Optofluidic Sorting Principle

One possibility of performing automated sorting is to combine a sensing unit with a unit for continuous deflection. Figure 1 shows an overview of the optofluidic sorting approach we are going to realize. The sorting takes place in a microfluidic channel with a width of several tens of micrometers. Flow direction of the particle solution is from left to right, where the channel splits into a Y-junction. The sensing unit consists of a VCSEL with extended cavity (VECSEL) and will not be detailed here. Particles passing the cavity will be classified, for example by size or refractive index, and a suitable control signal is induced for the optical lattice responsible for deflection. An optical lattice is a one- or two-dimensional arrangement of optical traps, a promising technique to achieve deflection

in microfluidics. It can be generated by interferometric light patterns [4], holographic tweezers [5], or, in our case, arrays of densely packed VCSELs. At each trap of the lattice the particles are attracted and deflected stepwise, provided that the trapping force is in the same range as the fluidic drag force. In the presented sorting approach, the VCSELs are arranged in two linear arrays tilted by a certain angle, which allows particle deflection in two directions.

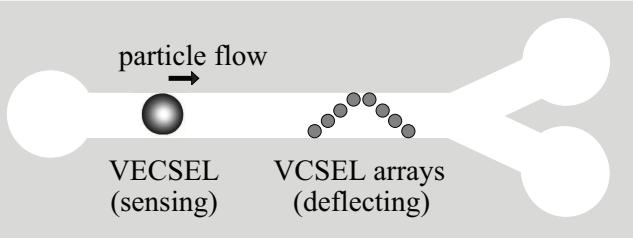

Fig. 1: Schematic of the optofluidic sorting approach. The VECSEL for particle detection is followed by linear VCSEL arrays for particle deflection. The microfluidic channel splits into two channel outlets.

The working principle of the sorting device is depicted in Fig. 2. With a signal "large particle" received from the analysis unit, the lasers of the left array are switched on, resulting in a redirection of the particle into the upper branch, whereas for the analysis signal "small particle", the right laser array is switched on in order to direct the particle into the lower outlet of the microfluidic channel.

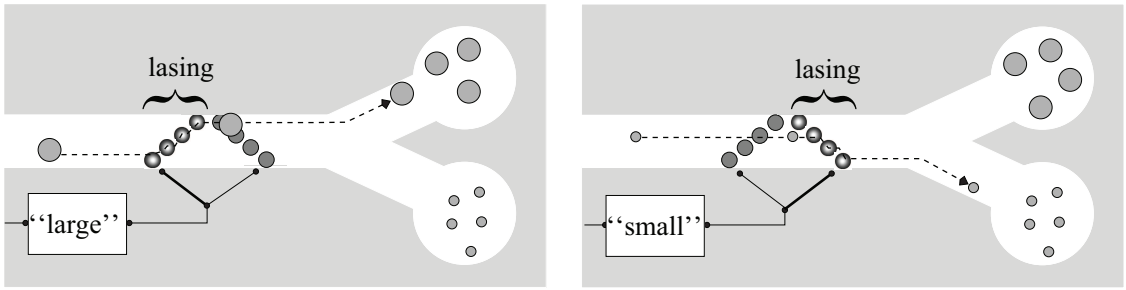

Fig. 2: Working principle of the optofluidic sorting approach. According to the signal received from the analysis unit, larger particles are directed into the upper outlet (left), whereas smaller ones are directed into the lower outlet of the microfluidic channel (right).

3. Continuous Deflection of Particles in Microfluidic Channels

Continuous deflection of particles using external optics for beam steering has already been reported [6]. The left part of Fig. 3 shows snapshots of such a deflection experiment with a 10 µm particle. The particle approaches the tilted linear laser array (1, 2) and is stepwise deflected into the upper branch of a Y-junction (3–5). The experimental setup for this deflection experiment is depicted in the right part of Fig. 3. The VCSEL array with a pitch of about 25 µm and 30° tilt relative to the particle flow direction is electrically contacted on a copper laser mount. The first objective lens collimates the beam, and the second one with high numerical aperture (NA) provides beam focusing inside the microfluidic channel. The 50 µm wide channel was fabricated from polydimethylsiloxane (PDMS) by soft lithography. For observation, the setup is illuminated by a white light

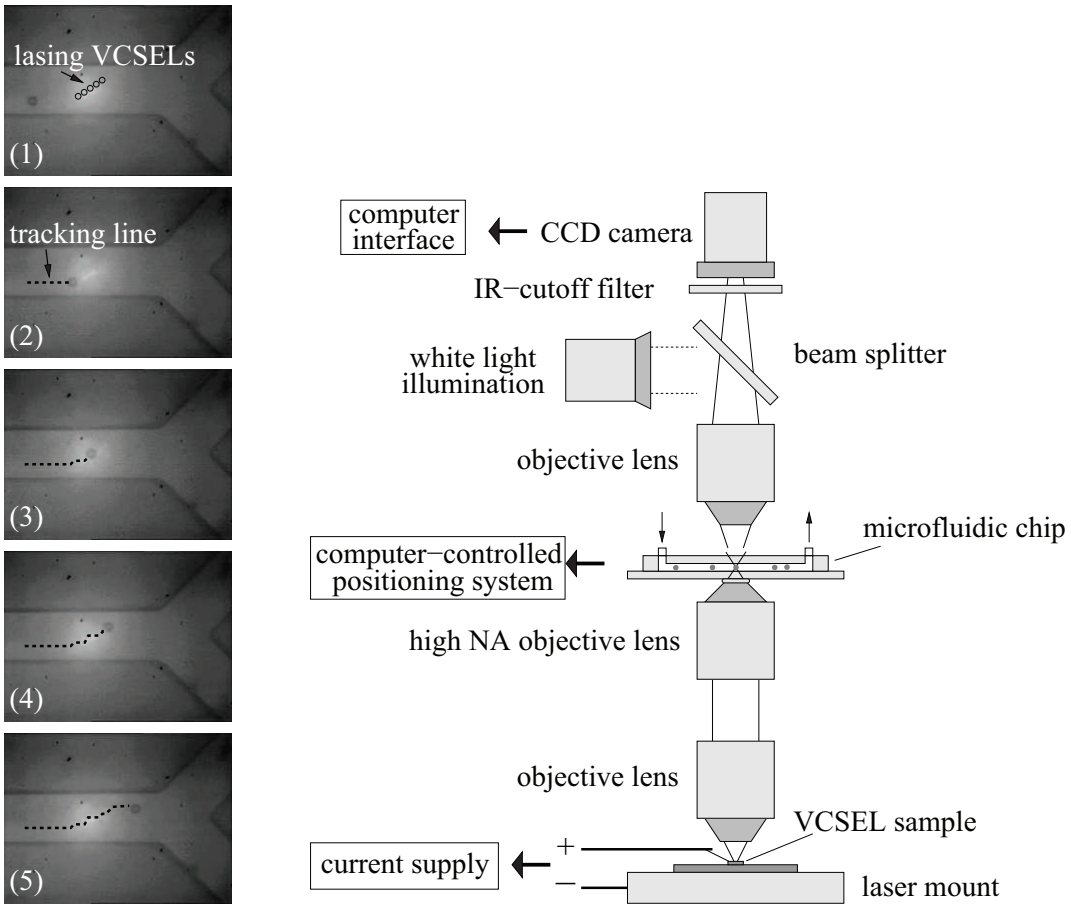

Fig. 3: Left: Snapshots of a deflection experiment in a microfluidic channel with 50 µm width. An arriving 10 µm diameter polystyrene particle approaches the tilted laser array and is stepwise redirected to the upper branch of the Y-junction at the traps of the optical lattice. Right: Optical trapping setup used for the deflection experiment. Beam focusing in the microfluidic channel is achieved by two objective lenses. The observation system basically consists of a light source, a CCD camera, and a computer interface.

source. By means of an objective lens and a CCD camera connected with a computer, the experiment is easily observable.

Extending this setup by an array pointing downwards, it will be possible to direct particles into the outlet of choice, depending on the signal received from the preceding analysis unit. However, it is evident that the used setup is rather bulky, which calls for drastic miniaturization.

4. Integration of Laser Arrays and Microfluidic Channel

Integration is crucial for miniaturized, low-cost optofluidic sorting devices. In an earlier approach we have accomplished the integration of lasers and microfluidics by soldering the laser chip to the lower surface of the microfluidic chip [7]. Figure 4 shows a schematic of this integration concept. Metal fanout tracks are structured on the lower surface of the

glass slide sealing the microfluidic channel. The laser chip is attached to the microfluidic chip, and both electrical and mechanical connection are achieved by indium solder bumps. However, it is reasonable to expect a poor heat dissipation in this concept.

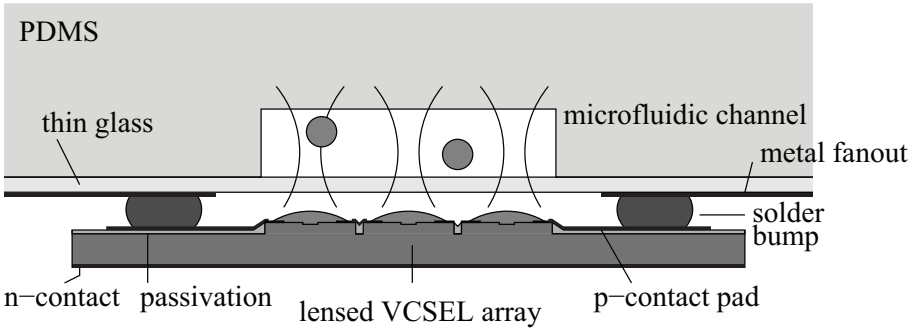

Fig. 4: Earlier approach of the VCSEL chip integrated with the microfluidic channel. Indium solder bumps provide both electrical and mechanical connection.

Figure 5 shows snapshots of a 15 µm particle continuously deflected by such an integrated laser array with a tilt angle of 20°. The PDMS microfluidic channel has a width of 100 µm and is highlighted by horizontal lines for better visualization. An incoming particle approaches the tilted laser array (1, 2). It is stepwise redirected at the traps of the optical lattice and deviated from its initial path (3–5). Unfortunately, the particle movement is rather slow and the deflection is incomplete, due to low laser performance mainly caused by the insufficient heat dissipation. This thermal limitation is supposed to be removed with the new integration approach.

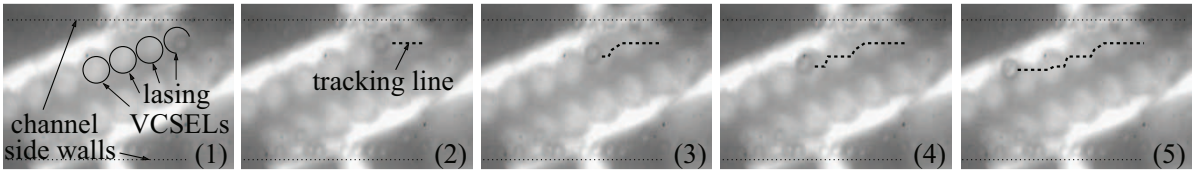

Fig. 5: Snapshots of a deflection experiment with the integrated setup from Fig. 4. The width of the microfluidic channel (highlighted by horizontal lines) is 100 µm. A 15 µm particle approaches the integrated laser array (flow direction from right to left) and is attracted at each trap of the optical lattice and thus stepwise redirected to the lower part of the channel.

The intended way of integration utilizes bottom emission. In this approach, a laser chip with both p- and n-contacts on the upper side is soldered upside down (flip-chipped) onto a structured heat sink. Both the electrical and mechanical connection are achieved via indium solder bumps, structured lithographically on the fanout tracks of the heat sink. After soldering, the substrate is removed from the back side of the laser chip to enable laser emission.

The microfluidic chip consists of a polymer structured by hot embossing and a 30 µm thin glass slide sealing off the channel. For beam shaping, photoresist microlenses are provided on the lower surface of the glass slide. The lenses are fabricated by means of

photolithography combined with thermal reflow. After successful fabrication of the two components, laser and microfluidic chip are merged by an adhesive. Figure 6 shows a sketch of the complete device.

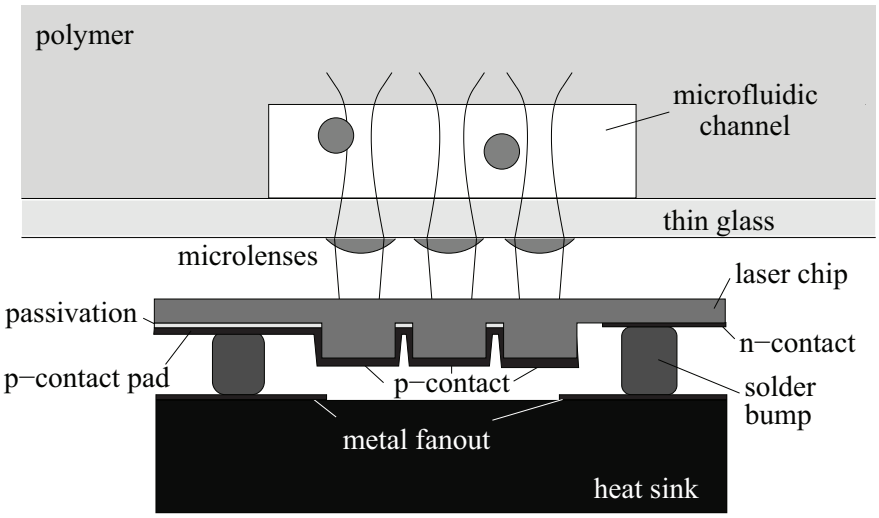

Fig. 6: Schematic of the intended integration concept. The linear laser arrays are soldered upside down onto a heat sink. Indium solder bumps connect both p- and n-contact with the metal fanout on the heat sink. The laser chip is positioned at a very small distance to the microfluidic chip, which has microlenses on the lower surface.

5. Conclusion

We have presented a novel concept of a fully integrated, VCSEL-based optofluidic sorting device, with a main focus on the sorting unit which is controlled by a sensing unit. Laser arrays and microfluidic channels were fabricated and characterized in an experimental setup to verify the sorting principle and the suitability of the lasers. Furthermore, particle deflection has been shown in the first generation of an integrated setup. The next generation will incorporate the VCSEL arrays for deflection into both output channels. The integrated sorting performance is supposed to be enhanced by overcoming the thermal limitations with a flip-chip soldering approach with incorporated heat sink. An additional path of improvement is to further reduce the laser pitch from presently 26 µm to 18 µm.

Acknowledgment

This project is financed by the Baden-Württemberg Stiftung gGmbH.

References

[1] A. Ashkin, "Acceleration and trapping of particles by radiation pressure", *Phys. Rev. Lett.*, vol. 24, no. 4, pp. 156–159, 1970.

[2] M.D. Wang, H. Yin, R. Landick, J. Gelles, and S.M. Block, "Stretching DNA with optical tweezers", *Biophysical Journal*, vol. 72, pp. 1335–1346, 1997.

[3] C. Xie, M.A. Dinno, and Y.-Q. Li "Near-infrared Raman spectroscopy of single optically trapped biological cells", *Opt. Lett.*, vol. 27, no. 4, pp. 249–251, 2002.

[4] M.P. MacDonald, G.C. Spalding, and K. Dholakia, "Microfluidic sorting in an optical lattice", *Nature*, vol. 426, pp. 421–424, 2003.

[5] J.E. Curtis, B.A. Koss, and D.G. Grier, "Dynamic holographic optical tweezers", *Optics Communications*, vol. 207, pp. 169–175, 2002.

[6] A. Kroner, C. Schneck, F. Rinaldi, R. Rösch, and R. Michalzik, "Application of vertical-cavity laser-based optical tweezers for particle manipulation in microfluidic channels", in *Nanophotonics II*, D.L. Andrews, J.-M. Nunzi, A. Ostendorf (Eds.), Proc. SPIE 6988, pp. 69881R-1–12, 2008.

[7] R. Michalzik, A. Kroner, A. Bergmann, and F. Rinaldi, "VCSEL-based optical trapping for microparticle manipulation", in *Vertical-Cavity Surface-Emitting Lasers XIII*, K.D. Choquette, C. Lei (Eds.), Proc. SPIE 7229, pp. 7229-1–13, 2009.

VCSEL–PIN Transceiver Chips for Bidirectional Gbit/s Data Communication Over Multimode Fiber

Alexander Kern

We present the fabrication and characterization of monolithically integrated transceiver chips with vertical-cavity surface-emitting lasers (VCSELs) and PIN photodetectors for bidirectional optical data communication at 850 nm wavelength over a single butt-coupled standard multimode fiber. With such a low-cost transmission configuration, data rates of 9 Gbit/s in back-to-back mode and 7 Gbit/s over a 500 m long 50 µm core diameter fiber are well possible.

1. Introduction

True bidirectional multimode fiber (MMF) transmission using monolithically integrated transceiver (TRx) chips is one possible way to satisfy the demand for increasingly compact and low-priced high-speed optical interconnection in local-area networks, the industrial or automotive sector. A worthwhile attempt to use a VCSEL as an efficient laser source and a resonant-cavity-enhanced photodetector is introduced in [1]. Such a dual-purpose device is switched between two operation modes. Half-duplex operation at 1.25 Gbit/s data rate over a 50 µm core diameter MMF with 500 m length was demonstrated. Full-duplex data transmission is only possible with spatially separated devices. Unfortunately this solution is not well suited for low-cost links owing to resonant detection, giving very little room for detuning and thus requiring temperature control at both fiber ends. Non-resonant detection is achieved with separate epitaxial layers for photodiode (PD) and VCSEL [2, 3].

In previous work [4] we have studied the transmission performance of TRx chips containing VCSELs and metal–semiconductor–metal (MSM) detectors matched to 200 µm diameter polymer-clad silica (PCS) step-index fibers. Later, the VCSEL–MSM chips were miniaturized for 100 µm core diameter graded-index (GI) MMFs in order to increase the fiber length through a higher bandwidth–distance product. Up to 2.5 Gbit/s full-duplex operation over 50 m fiber were thus demonstrated [5].

Here, for the first time, PIN-type PDs are used in miniaturized VCSEL-based 850 nm-range transceivers for bidirectional optical interconnects via a single, two-side butt-coupled standard MMF, as shown in Fig. 1. The monolithic integration of both components as well as a design avoiding the use of external optics saves space, weight and module cost. To our knowledge, the data rates demonstrated in this paper are the highest reported so far. In addition, our chips do not require temperature control and are suited for full-duplex operation.

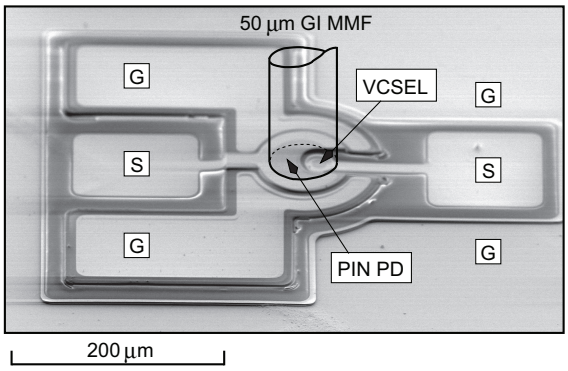

Fig. 1: Scanning electron micrograph of a monolithically integrated VCSEL and PIN PD device. A GI MMF butt-coupled to the transceiver chip is schematically indicated.

2. Transceiver Chip Design and Fabrication

In the full-monolithic chip, the layers for the PIN PD are grown on top of the VCSEL layers in the same epitaxial run using molecular beam epitaxy on GaAs substrates. An up to 3 µm thick undoped GaAs absorption layer is sandwiched between p- and n-doped $Al_{0.3}Ga_{0.7}As$. The higher bandgap energy of these two contact layers provides a spectral window for the wavelengths of interest at around 850 nm. In order to minimize the energy band discontinuities between the absorption and contact layers, linearly graded n- and p-$Al_xGa_{1-x}As$ ($x = 0 \rightarrow 0.3$) is employed, ensuring an easier escape of the light-induced carriers from the undoped GaAs.

A 150 nm thick intrinsic $Al_{0.9}Ga_{0.1}As$ etch stop layer separates the detector layers from the VCSEL and partially acts as an insulator by reducing capacitive coupling between the two devices. The resonator of the VCSEL is built by an n-type doped bottom Bragg mirror grown on an n-doped GaAs substrate and equivalent p-type top mirror pairs. The inner cavity has an optical thickness of one wavelength and contains three 8 nm thick GaAs quantum wells. A 32 nm thick p-doped AlAs layer in the first top mirror pair above the active region is designated for current confinement after an oxidation step. The VCSEL growth is terminated with a 30 nm highly p-doped GaAs layer, which provides a low resistance p-contact and at the same time prevents oxidation of the subjacent aluminum-containing layers.

Eight lithographic steps are necessary for processing the transceiver chip shown in Fig. 2. In the first step, the detector layers on top of the VCSEL are removed by a combination of two reactive-ion etching (RIE) and two wet-etching processes. The uppermost VCSEL layer is not affected by the etching, since it is protected by an etch stop layer with a high aluminum content, as mentioned above. Dry-etching with $SF_6/SiCl_4$ for high etching selectivity between GaAs and $Al_xGa_{1-x}As$ [6] terminates on the 200 nm thick p-doped $Al_{0.3}Ga_{0.7}As$ layer. Wet-etching with a citric acid/H_2O_2 solution ensures sufficient selectivity between $Al_xGa_{1-x}As$ layers with 30 % and 90 % aluminum content [7]. Followed by a selective wet-etching of $Al_{0.9}Ga_{0.1}As$ with hydrofluoric acid, the highly p-doped GaAs cap layer of the VCSEL can now be exposed.

PIN PDs have vertically displaced contacts and thus require an additional etch step to

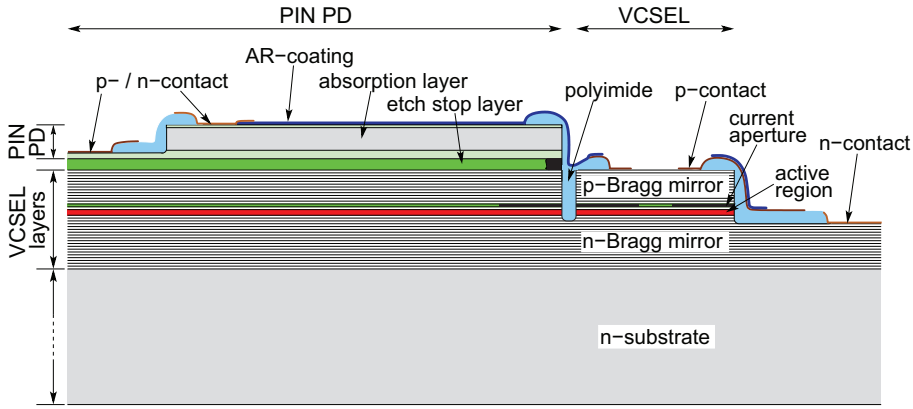

Fig. 2: Schematic cross-sectional view of the fully processed transceiver chip.

expose the p-doped $Al_{0.3}Ga_{0.7}As$ contact layer, as can be seen in the left part of Fig. 2. This step can be accomplished in analogy to the previous dry-etching processes. By means of the described selective etching techniques, a uniform layer topography all over the wafer can be guaranteed in spite of a layer thickness inhomogeneity from epitaxial growth. The third etching process spatially separates the VCSEL and the photodetector by a 2 to 4 µm narrow trench and gives access to the current confinement layer, as seen in the right part of Fig. 2. It is performed just with $SiCl_4$ without selectivity. Also this process step requires reactive-ion etching, since steep mesa side walls are crucial for the miniaturization and dense integration of VCSEL and PIN PD. Selective oxidation in a hot water vapor atmosphere forms the current aperture in the AlAs layer. The fourth and fifth lithography steps provide planarization and passivation with polyimide. Afterwards, both, p- and n-contacts of the PD and VCSEL are evaporated and annealed in order to form low-resistance contacts. In the last lithography step, an Al_2O_3 quarter-wave antireflection (AR) layer is sputtered on the area of the transceiver chip which is exposed to incident light. The reflectivity of the semiconductor surface is thus reduced from approximately 30 % to 1.3 % over a spectral width of nearly 50 nm [5].

3. Device Characteristics

The VCSEL structure underneath the PIN PD leads to back-reflection of the incident non-absorbed light and thus to double-pass absorption. The responsivity of a transceiver PD with 3 µm thick GaAs absorption layer reaches 0.61 A/W at 850 nm, which corresponds to a quantum efficiency of nearly 88 %. For high-speed measurements, both, VCSEL and PIN PD can be contacted directly on wafer by two coplanar microwave probes with a ground–signal–ground (GSG) configuration, as indicated in Fig. 1. The small-signal modulation responses of the PIN PDs are determined by means of a reference laser diode with 7 GHz cut-off frequency which is driven by a constant current superimposed with a low-power RF modulating signal generated by a sweep oscillator. The laser beam is focused via free-space optics on the transceiver PIN PD. The PD under test is biased with a constant voltage, where a bias-tee separates the RF and DC current signals. According to the frequency response in Fig. 3 (left), the bandwidth of a 3 µm thick, 60 µm diameter PIN

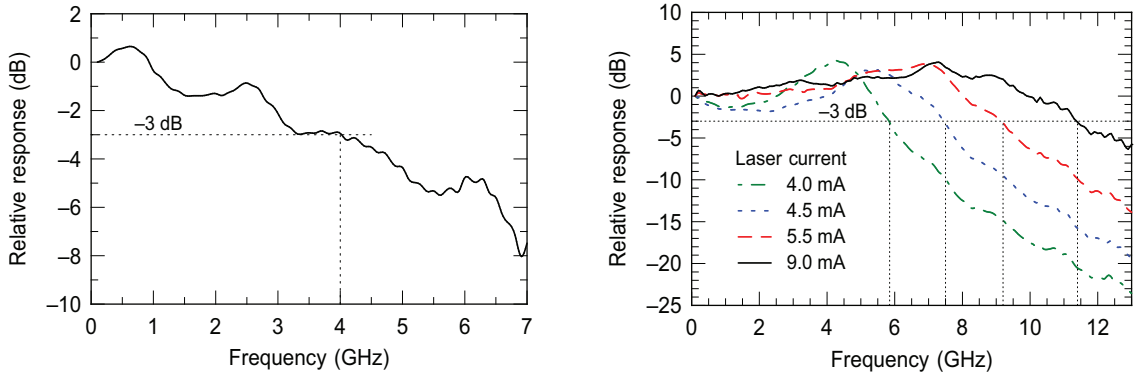

Fig. 3: Small-signal frequency responses of an integrated 3 µm thick transceiver PIN photodiode with a 3 dB-bandwidth of 4 GHz (left) and a typical transceiver VCSEL with a maximum 3 dB-bandwidth of approximately 11.5 GHz (right).

PD is limited to 4 GHz. The resistor–capacitor (RC) low-pass and drift time bandwidths are expected to be about 14 GHz (for $R = 50\,\Omega$) and 15 GHz, respectively. We attribute the much smaller experimental value to parasitic coupling with the highly doped VCSEL layers. Both, the responsivity and the 3 dB-bandwidth of the PD is almost independent of the bias voltage.

The experimental setup for VCSEL small-signal characterization is very similar to the one of the PIN PD. Here, a fiber-coupled reference PD with 25 GHz cut-off frequency is used, where the VCSEL under test is contacted on chip via a GSG microprobe. An RF attenuator between bias-tee and sweep oscillator is used to attenuate the backward microwave reflections due to impedance mismatch between the VCSEL and the 50 Ω measurement system. A typical frequency response of an integrated VCSEL with about 8 µm oxide aperture diameter is shown in Fig. 3 (right). A maximum 3 dB-bandwidth of 11.5 GHz is observed for an operating current of 9 mA. With a threshold current of 3.5 mA, a maximum output power of 3.5 mW, and optical emission at around 810 nm, there is much room for further optimization.

4. Digital Data Transmission

The small-signal bandwidths of the PIN PDs are nearly three times lower compared to those of the VCSELs and thus limit the maximum data rates of the transceivers. First, data transmission experiments were performed in back-to-back (BTB) mode in order to avoid dispersion effects of the glass fiber. As can be seen in Fig. 4, quasi error-free data transmission in half-duplex mode is well possible up to 8 Gbit/s for both word lengths, where about 2 dB more power is needed for the operation with a $2^{15} - 1$ long bit sequence. All optical eye diagrams are well open and show little difference between shorter and longer words. A rather limiting case is the free-space operation at 9 Gbit/s for the word length of $2^{15} - 1$ bits. Nevertheless, 8 Gbit/s is still the highest data rate ever obtained with bidirectional transceiver chips.

Further investigations into digital data transmission were made using a 500 m long 50 µm core diameter GI MMF with a bandwidth–distance product ($B \times L$) of $\sim 2\,\mathrm{GHz} \times \mathrm{km}$

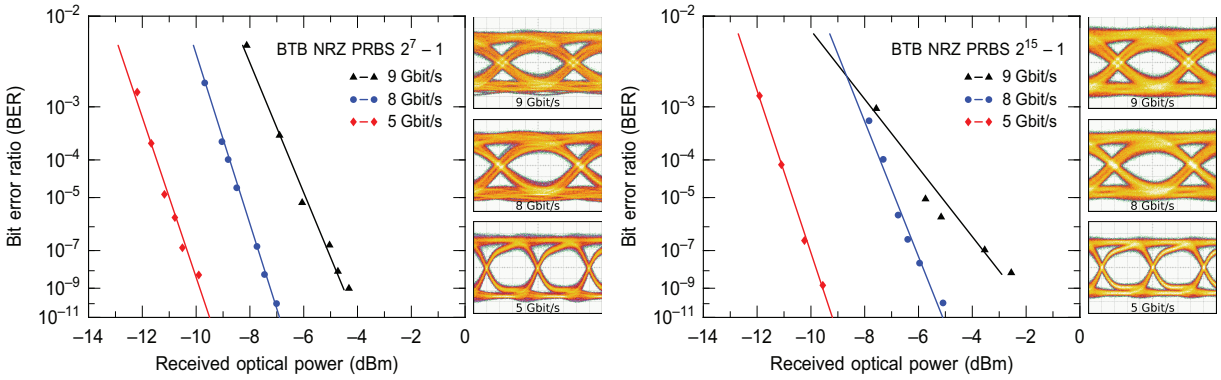

Fig. 4: BER characteristics for BTB half-duplex $2^7 - 1$ (left) and $2^{15} - 1$ (right) word length non-return-to-zero (NRZ) pseudorandom bit sequence (PRBS) data transmission and optical eye diagrams for 9, 8, and 5 Gbit/s.

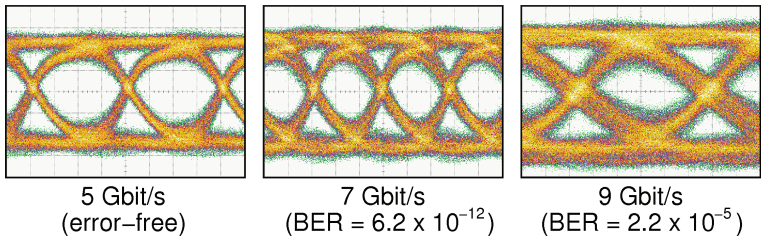

Fig. 5: Optical eye diagrams for half-duplex 2^7-1 word length non-return-to-zero pseudorandom data transmission at 5 Gbit/s (left), 7 Gbit/s (center), and 9 Gbit/s (right), all over 500 m GI MMF.

that was butt-coupled (about 40 µm distance) to each chip. The optical eye diagrams in Fig. 5 indicate quasi error-free data transmission up to 7 Gbit/s. Whereas BTB operation in Fig. 4 (left) was still well possible up to 9 Gbit/s, in this configuration it was limited by the $B \times L$ of the MMF, as can be seen from the higher BER in Fig. 5 (right).

5. Conclusion

In this article, a new kind of monolithically integrated 850 nm wavelength transceiver chip has been presented for bidirectional optical data transmission over standard multimode fibers. The chips consist of PIN photodiodes and oxide-confined, top-emitting VCSELs, integrated to match 50 µm core diameter GI MMFs. The main fabrication steps including the sophisticated selective dry- and wet-etching techniques were introduced.

PIN PDs with a maximum bandwidth of 4 GHz and VCSELs with 11.5 GHz can handle data rates of 9 Gbit/s in back-to-back half-duplex mode. Quasi error-free data transmission over 500 m butt-coupled standard MMF could be demonstrated up to 7 Gbit/s. Full-duplex data transmission experiments and detailed studies of the alignment tolerances will be made in the near future.

References

[1] J.D. Ingham, R.V. Penty, and I.H. White, "Bidirectional multimode-fiber communication links using dual-purpose vertical-cavity devices", *J. Lightwave Technol.*, vol. 24, no. 3, pp. 1283–1294, 2006.

[2] A.M. Kasten, A.V. Giannopoulos, C. Long, C. Chen, and K.D. Choquette, "Fabrication and characterization of individually addressable vertical-cavity surface-emitting laser arrays and integrated VCSEL/PIN detector arrays", in *Vertical Cavity Surface Emitting Lasers XI*, K.D. Choquette, J.K. Guenter (Eds.), Proc. SPIE 6484, pp. 64840C-1–6, 2007.

[3] P. Kazlas, J. Wasserbauer, J. Scott, D. Paananen, S. Swirhun, and D. Lewis, "Monolithic vertical-cavity laser/p-i-n photodiode transceiver array for optical interconnects", *IEEE Photon. Technol. Lett.*, vol. 10, no. 11, pp. 1530–1532, 1998.

[4] M. Stach, F. Rinaldi, M. Chandran, S. Lorch, and R. Michalzik, "Bidirectional optical interconnection at Gb/s data rates with monolithically integrated VCSEL-MSM transceiver chips", *IEEE Photon. Technol. Lett.*, vol. 18, no. 22, pp. 2386–2388, 2006.

[5] R. Michalzik, A. Kern, M. Stach, F. Rinaldi, and D. Wahl, "True bidirectional optical interconnects over multimode fiber", in *Optoelectronic Interconnects and Component Integration IX*, A.L. Glebov, R.T. Chen (Eds.), Proc. SPIE 7607, pp. 76070B-1–17, 2010.

[6] S. Salimian and C.B. Cooper, III, "Selective dry etching of GaAs over AlGaAs in $SF_6/SiCl_4$ mixtures", *J. Vac. Sci. Technol. B*, vol. 6, no. 6, pp. 1641–1644, 1988.

[7] J.-H. Kim, D.H. Lim, and G.M. Yang, "Selective etching of AlGaAs/GaAs structures using the solutions of citric acid/H_2O_2 and de-ionized H_2O/buffered oxide etch", *J. Vac. Sci. Technol. B*, vol. 16, no. 2, pp. 558–560, 1998.

Short-Cavity Integrated VECSELs: A Fabrication Approach

Wolfgang Schwarz

We outline the fabrication of an electrically pumped surface-emitting laser with a short vertical extended cavity (VECSEL) for sensing applications. The emission wavelength is detuned by introducing microparticles into the cavity via a microfluidic channel. Multiple longitudinal modes can fit inside the resonator. A reproducible detuning of the extended cavity demands a longitudinal mode spacing of at least a few nanometers. The related resonator length of 80 µm therefore requires a tailored fabrication and mounting procedure.

1. Introduction

For gas sensing, locking a laser to an atomic transition line, or detecting biological samples, a single-pass scheme is most commonly used [1–3]. Here the optical field is absorbed or scattered during a single encounter with the sample under test.

The cross-section can be enhanced if the sample is part of an optical resonator, as demonstrated for THz spectroscopy [4] and for optically pumped VECSELs [5]. When the sample is introduced into the standing-wave pattern inside the extended cavity, it affects the laser mode and changes of the beam shape as well as of the emission wavelength are induced. The detection of the beam shape can be realized with an image sensor. Image processing has to be done to extract the modal pattern. Signal processing algorithms like multidimensional fast Fourier transform (FFT) have a $O(N\log N)$ complexity [6], with N being the number of image points. In a typical image, N can exceed 10^5. Unlike the beam shape, the spectrum can be optically analyzed by a grating in a parallel fashion. The resulting signal can be captured by a single line of a charge-coupled device (CCD) with $N \approx 10^3$. Evaluation is thus much faster, which is a favorable advantage in high-throughput applications with frame rates in excess of 1 kHz.

2. Fabrication Steps

The presented device consists of three functional elements, as shown in Fig. 1: (i) the vertical-cavity surface-emitting laser (VCSEL), interfaced electrically and thermally by a structured heat sink, (ii) the curved surface of the external mirror which is coated with a highly reflective coating, and (iii) a microfluidic channel carrying a suspension of the samples to be analyzed. This section describes the fabrication of the elements in detail. The requirement of a 80 µm short extended resonator including a microfluidic channel puts tight constraints onto the fabrication procedure: Bond wires are too thick to interface the device electrically. Thus flip-chip mounting is the only approach which allows to shrink the cavity to the necessary length.

2.1 VCSEL and heat sink

The VCSEL was grown on silicon-doped GaAs by molecular beam epitaxy. The structure consists (in growth direction) of an AlAs etch stop layer, a distributed Bragg reflector (DBR) for the output coupler, an undoped barrier region of GaAs for the inner cavity embedding three quantum wells with a thickness of 8 nm each, and a highly reflecting DBR with a phase matching layer. Modulation doping with silicon and carbon is employed to achieve low optical and electrical losses in the n-doped output coupler and the p-doped reflector. The Al content in the AlGaAs DBRs is varied between 0.2 and 0.9 for sufficient index contrast. The p-mirror includes a thin AlAs layer for oxide confinement. After substrate removal, any Al containing surfaces are prone to corrosion. Therefore the phase matching layer is terminated by a GaAs layer which is sufficiently chemically stable. However, this layer absorbs light with wavelengths shorter than 870 nm by a fraction of approximately $10^{-3}\,\mathrm{nm}^{-1}$, which is too much for being part of an optical resonator with an enhanced field at this layer. For this reason, the layer structure was tuned for laser emission at 895 nm, which requires $In_{0.06}Ga_{0.94}As$ quantum wells. After wet etching of the p-mesas, the underetched microresist present on top of the mesas was not stripped, but used as a lift-off mask for the subsequent evaporation of the Ge/Au/Ni/Au n-contact. The AlAs layer in the p-doped DBR exposed by mesa etching was selectively oxidized to diameters ranging from 6 µm to 20 µm in water vapor at 646 K. The p-contact metals Ti/Pt/Au were evaporated in a lift-off process. Gold electroplating was done on the n-contact to grow vias with the same height as the mesas, and the surface between the mesas and vias was passivated with Durimide®. The complete wafer surface was metalized with a diffusion barrier of Ta/Au to suppress penetration of the solder metal into the vias and mesas. About 500 nm thick Au was plated onto the mesas and vias and the exposed diffusion barrier was dry etched with argon and tetrafluoromethane. The wafer substrate was thinned to 170 µm thickness and diced into $1.5\times1.5\,\mathrm{mm}^2$ pieces. The heat sinks were structured on floating zone (FZ) high-purity silicon with a specific resistivity $> 10^4\,\Omega\cdot\mathrm{cm}$. A thin layer of Al_2O_3 was sputtered on the wafers, acting both as passivation and as etch stop layer in the following dry etching steps. A thin Ta/Au layer was sputtered

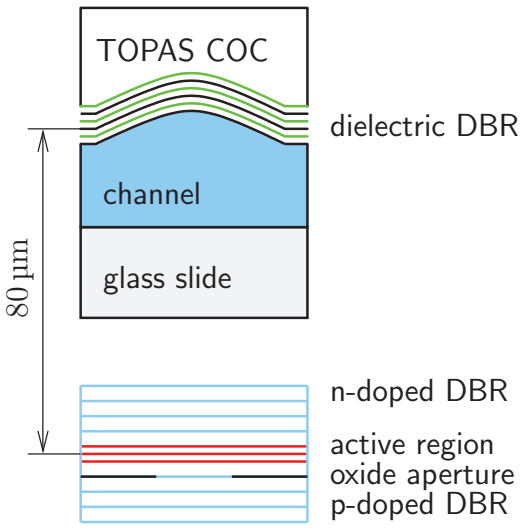

Fig. 1: Schematic drawing of the resonator structure. It comprises the VCSEL at the bottom, the microfluidic channel, and the hot-embossed concave-shaped Topas® COC channel wall, which is coated with a dielectric Bragg reflector to form the resonator mirror. Electrical contacts and the heat sink are omitted.

on the wafer surface as a seed layer for plating. Tracks of 2 µm thick Au were plated, which act as etch mask for dry etching of the exposed seed layer. The wafer surface was planarized with Durimide®, leaving apertures for the solder bumps and the bondpads. A diffusion barrier of Ta/Au was sputtered on the wafer surface and 500 nm of Au were plated on the apertures for the bumps. Again the second diffusion barrier was dry etched. The micromachining was finished by evaporation of 4 µm In in a lift-off process for the solder bumps and dicing of $1.8 \times 12.3\,\mathrm{mm}^2$ pieces. The VCSEL chips and the heat sinks were flip-chip soldered in a formic acid atmosphere at 473 K. The solder gap between VCSEL chip and the heat sink was filled with Crystalbond™ to stabilize the chip during substrate removal. The substrate was spray etched in a $NH_4OH : H_2O_2$ solution down to the etch stop layer. The etch stop layer and the Crystalbond™ were removed with diluted hydrofluoric acid and an organic solvent, respectively. The remaining epitaxial layers of the laser are fragile and were mechanically fixed with an underfill (Loctite™ 3593).

2.2 External mirror and microfluidic channel

The external mirror was hot-embossed into cyclo-olefin-copolymer Topas® COC 5013 at temperatures close to the glass transition temperature of 400 K. Topas® COC material was chosen for its low birefringence and high transparency. Contrary to polymethyl methacrylate (PMMA), its low water absorption prevents swelling in water, and it supports the deposition of stable dielectric mirrors with thicknesses up to a few micrometers, which is crucial for the present application. By reactive ion beam sputter deposition of oxides of aluminum and tantal, mirror reflectivities in excess of 98 % have been realized on BK7 glass, as shown in Fig. 2. The radius of curvature of the embossed external mirror ranges from about 160 to 290 µm and allows stable resonator modes for beam waists of

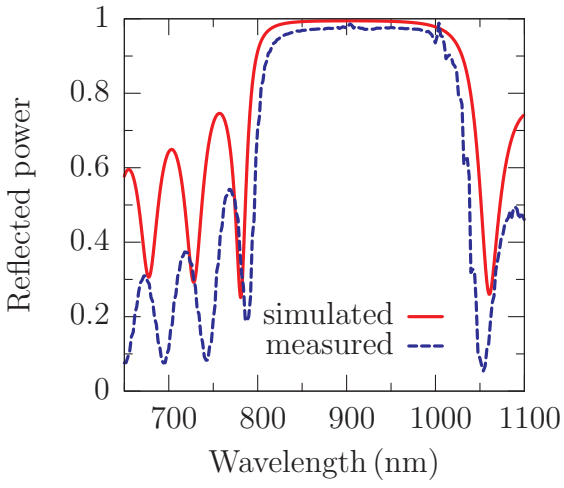

Fig. 2: Measured and simulated power reflectivity spectrum of a 9.5 pairs DBR coating on BK7 glass.

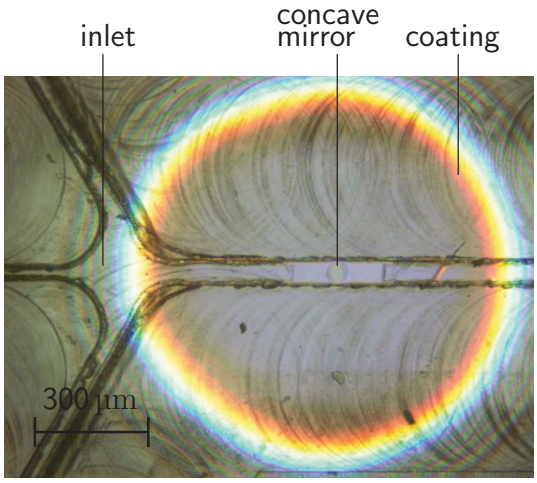

Fig. 3: Optical confocal microscope image of an embossed fluidic channel with an inlet for hydrodynamic focusing and a concave resonator mirror which is coated with a dielectric DBR.

8 and 10 µm. Figure 3 depicts the embossed channels. There is an inlet with one center channel for injection of the particles and two outer channels for a sheath fluid. If the flow rate of the sheath fluid is higher than in the center, the particles are confined to the center of the channel (hydrodynamic focusing [7]). The channel is wide enough to limit the clipping losses of the resonator. In the region of the resonator mirrors, the channel walls are coated with a dielectric DBR via a shadow mask. A 30 µm thin glass slide is fixed to the channel by compression bonding which closes the channel vertically. As a last step, the VCSEL is forward biased, actively aligned to the concave-shaped mirror for laser operation and fixed with a photocurable adhesive.

3. Conclusion

The fabrication of an integrated optical sensor based on an extended vertical resonator is demonstrated and details of the fabrication process are presented. Extensive characterization will follow in the near future.

We thank the Karlsruhe Institut für Technologie (KIT), Institut für Mikrostrukturtechnik for providing the microfluidic chips. This project is financed by the Baden-Württemberg Stiftung gGmbH.

References

[1] A. Hangauer, A. Spitznas, J. Chen, R. Strzoda, H. Link, and M. Fleischer, "Laser spectroscopic oxygen sensor for real time combustion optimization", *Procieda Chemistry*, vol. 1, no. 1, pp. 955–958, 2009.

[2] S. Knappe, "MEMS Atomic Clocks", Chap. 3.18 in *Comprehensive Microsystems*, Y. Gianchandani, O. Tabata, and H. Zappe (Eds.), pp. 571–612. Amsterdam: Elsevier, 2008.

[3] P.K. Horan and L.L. Wheeless, Jr., "Quantitative single cell analysis and sorting", *Science*, vol. 198, no. 4313, pp. 149–157, 1977.

[4] R. Mendis, V. Astley, J. Liu, and D.M. Mittleman, "Terahertz microfluidic sensor based on a parallel-plate waveguide resonant cavity", *Appl. Phys. Lett.*, vol. 95, no. 17, pp. 171113-1–3, 2009.

[5] P.L. Gourley, "Biocavity laser for high-speed cell and tumour biology", *J. Phys. D: Appl. Phys.*, vol. 36, no. 14, pp. 228–239, 2003.

[6] M. Frigo and S.G. Johnson, "Design and implementation of FFTW3", *Proc. IEEE*, vol. 93, no. 2, pp. 216–231, 2005.

[7] M.L. Shuler, R. Aris, and H.M. Tsuchiya, "Hydrodynamic focusing and electronic cell-sizing techniques", *Appl. Microbiol.*, vol. 24, no. 3, pp. 384–388, 1972.

Dynamic Characteristics of VCSELs for Cs-Based MEMS Atomic Clocks

Ahmed Al-Samaneh and Dietmar Wahl

We have fabricated flip-chip-bondable vertical-cavity surface-emitting lasers (VCSELs) emitting at 894.6 nm wavelength for Cs-based atomic clock applications. For polarization control, we have integrated shallow semiconducting surface gratings in the top Bragg mirror. A modulation bandwidth of more than 5 GHz is reached at only 0.5 mA bias. Modulation current efficiency factors larger than 12 GHz/$\sqrt{mA}$ are achieved. The intrinsic modulation characteristics of the VCSELs are investigated by precisely fitting measured small-signal modulation response curves and relative intensity noise spectra. A K-factor of less than 0.40 ns and a maximum 3 dB bandwidth exceeding 22 GHz are obtained.

1. Introduction

There is much recent interest in atomic clocks with low power consumption, ultra-small volume, and long-term instabilities below, e.g., 10^{-11} over one day. Mobile satellite navigation and the synchronization of communication networks are most prominent applications. For example, miniaturized atomic clocks would be important elements for the precision time protocol (PTP), which is an approach to distribute synchronization over next-generation IP-based packet networks.

VCSELs are compelling light sources for such clocks, since they simultaneously meet the requirements of high-temperature operation while emitting a low-noise, narrow-linewidth, single-mode, single-polarization beam. Employing the coherent population trapping (CPT) effect [1] of the Cs D1 line, the laser is harmonically modulated at about 4.6 GHz with a center wavelength of about 894.6 nm. Sub-mA threshold currents of VCSELs contribute to low dissipated power, and the vertical emission is advantageous for hybrid integration with the clock microsystem. In addition to employing CPT, the realization of ultra-miniaturized atomic clocks requires fabrication techniques known from micro-electro-mechanical systems (MEMS). In 2008, the European Commission (EC) launched the collaborative research project *MEMS atomic clocks for timing, frequency control & communications* (MAC-TFC, www.mac-tfc.eu) within its seventh framework programme, aiming to realize the first European miniature-size atomic clock.

2. VCSEL Design and Fabrication

The VCSEL wafers are grown by solid-source molecular beam epitaxy on n-doped (100)-oriented GaAs substrates. The VCSEL layer structure is as described in [2]. For polarization control, we have integrated shallow semiconducting surface gratings in a quarter-wave

thick GaAs antiphase layer added to the top Bragg mirror [3]. Such an inverted grating has quarter-wave etch depth, 0.6 or 0.7 µm period, and 50 % duty cycle. As expected from the design, the polarization is orthogonal to the grating lines.

For the purpose of integration with the atomic clock microsystem, flip-chip-bondable VCSEL chips have been realized. As seen in Fig. 1 (left), the chip has a size of 300 × 300 µm^2 and can be RF- (radio frequency) tested on-wafer using microwave probes with a signal–ground configuration. However, the design involves increased processing complexity compared to regular VCSELs with a substrate-side n-contact. This originates from the necessity of etching mesas down to the highly n-doped contact layer, applying several polyimide planarizaion layers containing dicing trenches as well as circular holes for n-vias, and electroplating of Au n-vias. As the last step, bondpads are evaporated. Figure 1 (right) depicts a cross-sectional view of a flip-chip-bondable VCSEL chip.

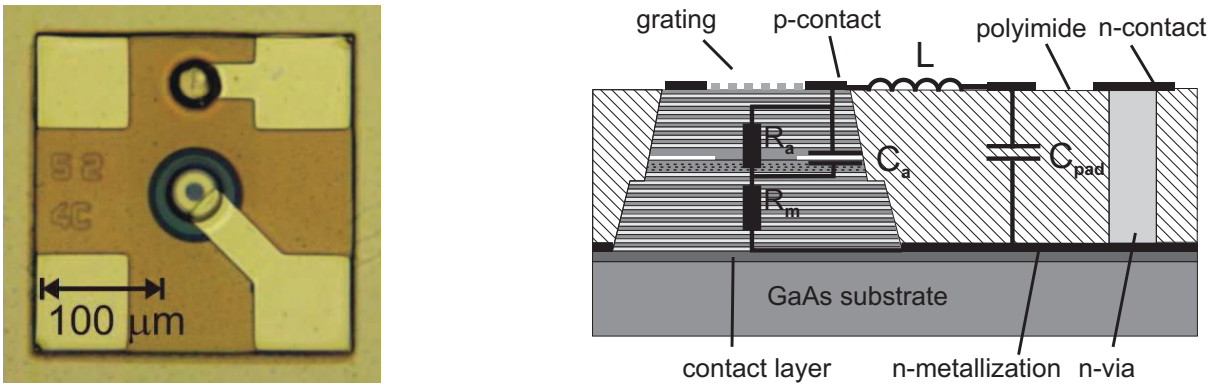

Fig. 1: Optical micrograph of a fully processed flip-chip-bondable VCSEL chip to be incorporated into atomic clock microsystems (left) and a schematic cross-sectional drawing with an associated equivalent-circuit model (right).

3. Dynamic Characterization

Cs-based MEMS atomic clocks require VCSELs with modulation bandwidths exceeding 5 GHz at low driving currents of, e.g., 2 mA. In this section, the dynamic characteristics of flip-chip-bondable VCSEL chips are presented; mainly the small-signal modulation response. The microwave reflection spectra of the VCSEL chips are also measured, as well as the relative intensity noise (RIN) spectra as a means to determine the intrinsic modulation behavior of the lasers.

3.1 Small-signal modulation characteristics

Small-signal modulation response curves of flip-chip-bondable VCSELs have been measured. In what follows, all modulation response functions relate the square of the fluctuations of the optical output power to those of the modulating electrical power. In other words, they relate the RF electrical power at the photodetector output to the RF electrical power which modulates the VCSEL. Therefore, it should be emphasized that the

associated 3 dB corner frequency $f_{3\,\mathrm{dB}}$ corresponds to an only 1.5 dB decay of the modulated optical signal. As a figure of merit, the modulation current efficiency factor (MCEF) specifies the increase of the 3 dB corner frequency with bias current I as [4]

$$\mathrm{MCEF} = \frac{f_{3\,\mathrm{dB}}}{\sqrt{I - I_{\mathrm{th}}}} \,, \tag{1}$$

where I_{th} is the threshold current.

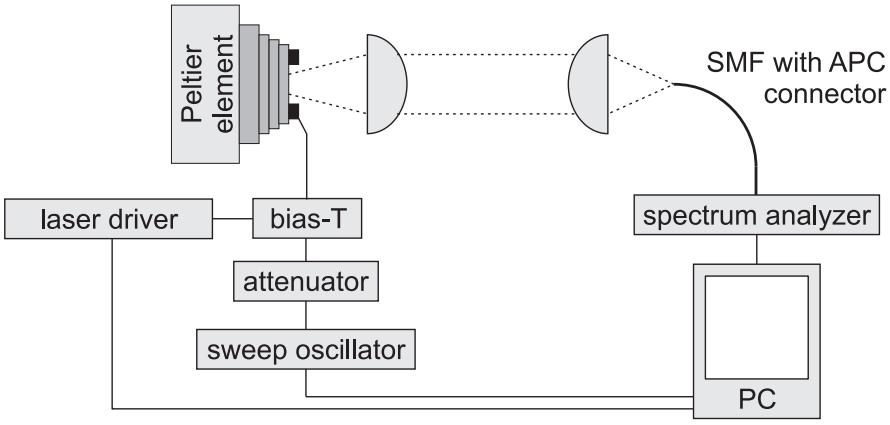

Fig. 2: Schematic drawing of the experimental setup for measurements of the small-signal modulation response.

Figure 2 illustrates the experimental setup employed to measure the small-signal modulation response. The VCSEL is driven by a constant current generated by a laser driver (ILX Lightwave, model LDC-3724B) and a low-power RF modulating signal generated by a sweep oscillator (Hewlett Packard, model HP83620A). The VCSEL chip is contacted via a coplanar microprobe (Cascade Microtech Inc., model ACP40-SG-200) with a signal–ground configuration. A bias-tee (Anritsu, model A3N1026) is used to combine the RF and DC current signals. An RF attenuator (Hewlett Packard, model HP8493C) attenuates the backward microwave reflections due to impedance mismatch between the VCSEL and the 50 Ω measurement system. The light is coupled into a single-mode fiber (SMF) and measured by a spectrum analyzer (Hewlett Packard, HP70000 system) through its internal RF photodetector[2]. To avoid unwanted optical feedback, both sides of the single-mode fiber are angle-polished[3]. Moreover anti-reflection-coated lenses are employed. Using a Peltier element, the temperature of the wafer holder can be increased up to 120 °C. All measurement instruments are controlled by a personal computer (PC) using the general purpose interface bus (GPIB). The small-signal modulation response curves of a VCSEL with 3 µm active diameter at different bias currents are depicted in Fig. 3 (left) for room-temperature operation. The frequency characteristics of all cables, bias-tees, attenuators, and the RF photodetector are numerically subtracted to obtain only the modulation response of the VCSEL.

[2]Lightwave section, HP70810B.

[3]Angled physical contact (APC) connector: The normal to the front surface of the optical fiber is tilted by 8 degrees with respect to the fiber axis.

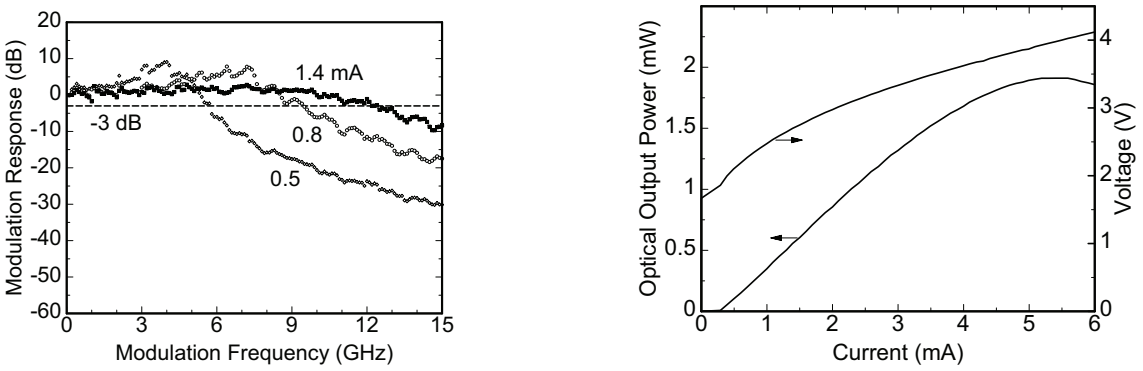

Fig. 3: Small-signal modulation response curves of a flip-chip-bondable VCSEL chip with 3 µm active diameter at different bias currents (left), and LIV characteristics of the same device (right). Both measurements were done at 20 °C ambient temperature.

A 3 dB bandwidth of 5.7 GHz is obtained at only 0.5 mA bias current. This bias is just 0.25 mA above threshold, see Fig. 3 (right). The maximum bandwidth is about 12 GHz, which well exceeds the 5 GHz specification for MAC-TFC. The modulation behavior at different bias currents was also measured at an elevated substrate temperature of 65 °C for the same VCSEL. Figure 4 depicts the extracted 3 dB corner frequencies versus $\sqrt{I - I_{\mathrm{th}}}$ at 20 and 65 °C ambient temperatures, where the MCEF values are as high as 12.3 and 10.6 GHz/$\sqrt{\mathrm{mA}}$, respectively.

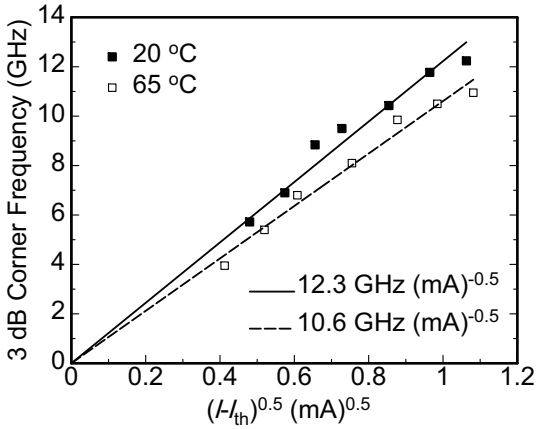

Fig. 4: 3 dB corner frequency in dependence of $\sqrt{I - I_{\mathrm{th}}}$ for the VCSEL from Fig. 3 at 20 and 65 °C ambient temperatures. The two lines are linear fits. Their slopes are given and represent the MCEFs.

3.2 Intrinsic modulation behavior

The modulation response curves introduced so far represent the superposition of the intrinsic frequency modulation response of the VCSEL and the modulation response of the electrical parasitics attributed to the structure of the VCSEL chip. The extrinsic

bandwidth limitation associated with the electrical parasitics can be represented by an electrical equivalent-circuit model. In order to obtain the intrinsic modulation characteristics of the VCSEL, two additional RF measurement techniques are applied in this work. The first method consists of measuring the microwave reflection curves, namely the S-parameter S_{11} from which the electrical parasitic elements of the equivalent-circuit model can be extracted and its bandwidth limitation be calculated [5]. The second technique is the measurement of the relative intensity noise (RIN) spectra [6]. It should be emphasized that each method allows to extract the intrinsic modulation behavior of the VCSEL. We have employed both techniques in order to improve the consistency of our results. In what follows we are presenting these two techniques in more details.

3.3 Microwave reflection spectrum

From a small-signal analysis of the laser rate equations, the modulation response introduced in the previous section can be approximated by the three-pole transfer function [4]

$$|M(f)|^2 = \frac{A f_\mathrm{r}^4}{(f_\mathrm{r}^2 - f^2)^2 + (\gamma f/(2\pi))^2} \cdot \frac{1}{1 + (f/f_\mathrm{p})^2} \,. \tag{2}$$

The first term represents the intrinsic carrier–photon interaction, which results in the ideal damping-limited modulation behavior of the semiconductor laser, where A is a device-dependent constant, f_r is the resonance frequency, and γ is the damping coefficient. The second term accounts for the parasitic elements found in the laser equivalent-circuit model, where f_p is its 3 dB corner frequency. A simple first-order low-pass is assumed. The approximation (2) does not account for the laser bandwidth limitation due to carrier transport, which seems not to be a speed-limiting effect for the frequency range up to 20 GHz. Figure 1 (right) depicts the physical origin of an equivalent-circuit model for the VCSEL impedance behavior, quite similar to the one proposed in [6]. The model takes into account the bondpad capacitance C_pad, the series resistance of the mirror R_m, the track inductance L, and the oxide aperture resistance R_a. C_a represents a combination of the capacitance of the active region and of the oxide layer. Above laser threshold, the active region is modeled as a short-circuit for small-signal conditions due to Fermi level pinning. At low frequencies, the VCSEL impedance is real and is given by the sum of R_m and R_a. As the frequency increases, C_a dominates over R_a, and the real part of the impedance reduces to R_m. From the input impedance

$$Z(f) = \left(\mathrm{i}2\pi f C_\mathrm{pad} + \left(\frac{R_\mathrm{a}}{1 + \mathrm{i}2\pi f C_\mathrm{a} R_\mathrm{a}} + R_\mathrm{m} + \mathrm{i}2\pi f L \right)^{-1} \right)^{-1} \tag{3}$$

of the equivalent circuit, one can obtain the reflection coefficient or scattering parameter

$$S_{11} = \frac{Z - Z_0}{Z + Z_0} \,, \tag{4}$$

where i is the imaginary unit and Z_0 is the impedance of the measurement system, which is usually 50 Ω. The microwave reflection spectra $S_{11}(f)$ of VCSEL chips are measured at

different bias currents using a 50 Ω network analyzer[4] in order to obtain the associated input impedance spectra $Z(f)$. By allowing the equivalent-circuit parameters to vary, the measured input impedance can be fit. For all curve fits in what follows, the Levenberg–Marquardt algorithm is applied.

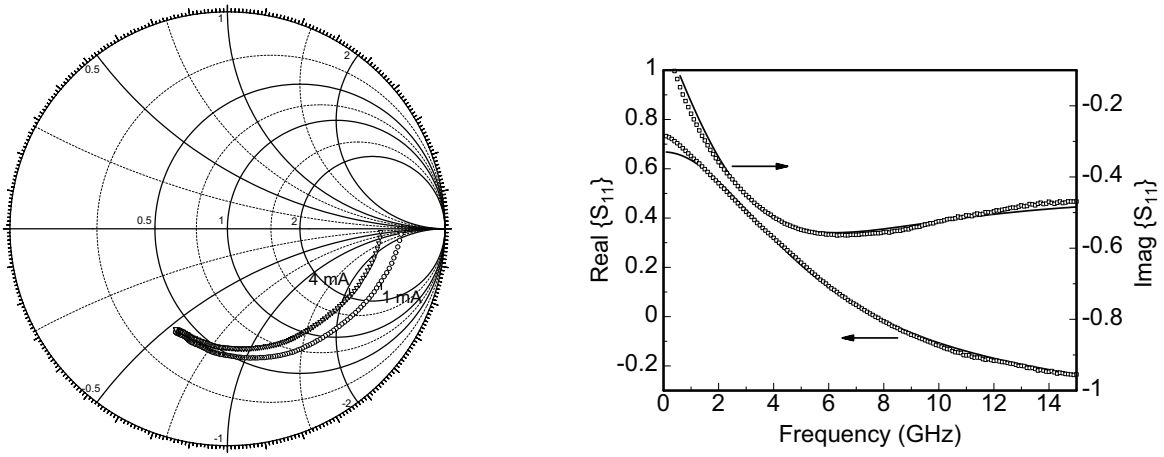

Fig. 5: Measured S_{11} spectra in a Smith chart of a VCSEL chip with 3.6 µm active diameter at 1 and 4 mA bias currents at room temperature (left). Real and imaginary parts of S_{11} of the same VCSEL at 3 mA drive current at room temperature (right). The solid lines (right) represent the modeled S_{11} using the equivalent-circuit model displayed in Fig. 1 (right) fit to the measurement data.

Figure 5 (left) depicts measured S_{11} data in a Smith chart over a frequency range from 0.1 to 15 GHz in 100 MHz steps at 1 and 4 mA bias currents. Figure 5 (right) illustrates the real and imaginary parts of the measured S_{11} spectrum for the same VCSEL chip at 3 mA bias current along with curve fits from the equivalent-circuit model. The resulting R_m, C_pad, and L are 47 Ω, 180 fF, and 70 pH, respectively. The extracted R_a and C_a values change with bias current and are listed in Table 1. In particular, R_a decreases

Table 1: Extracted values of the equivalent-circuit elements at different bias currents for the VCSEL chip from Fig. 5.

Bias current (mA)	1	2	3	4
R_a (Ω)	271	230	205	191
C_a (fF)	376	392	403	414

with increasing bias current, which is consistent with the decrease of the VCSEL differential resistance in the current–voltage curve at higher bias. We also observe that C_a increases with bias current. This bias-dependent behavior might be attributed to the diffusion capacitance C_d representing the transport of charge carriers through the active

[4]Spectrum analyzer HP8510C, S-parameter test-set HP8517A, and synthesized sweeper HP83651A.

region. C_d increases with increasing bias current [7]. Based on the extracted values of the equivalent-circuit elements, the electrical bandwidth can be determined from the 3 dB corner frequency f_p of the parasitic transfer function

$$M_\mathrm{p}(f) = \frac{V_{R_\mathrm{a}}}{V_\mathrm{s}} = \frac{\frac{A_3}{Z_0} \cdot \frac{A_2}{A_1+A_2+A_3}}{\left(1+\frac{A_2}{A_1}\right) \cdot \left(1+\frac{A_3}{Z_0} \cdot \frac{A_2}{A_1+A_2+A_3}\right) - 1} \tag{5}$$

with

$$A_1 = \frac{R_\mathrm{a}}{1 + \mathrm{i}2\pi f C_\mathrm{a} R_\mathrm{a}} \ , \tag{6}$$

$$A_2 = \mathrm{i}2\pi f L + R_\mathrm{m} \ , \tag{7}$$

and

$$A_3 = \frac{1}{\mathrm{i}2\pi f C_\mathrm{pad}} \ , \tag{8}$$

where V_s and V_{R_a} are the small-signal modulating voltages generated by the source and reaching the active region, respectively. Inserting the fit parameters, the 3 dB bandwidth of $|M_\mathrm{p}(f)|^2$ is approximately 5.2 GHz, showing a weak dependence on the bias current. Using (2) and the extracted f_p, precise fits of the measured modulation response curves can be performed, as evident from Fig. 6. Doing this, we have implicitly approximated $|M_\mathrm{p}(f)|^2$ from (5) by the first-order low-pass term in (2). The deviation is less than 0.15 dB up to a frequency of 15 GHz. Finally, the resonance frequency f_r and the damping coefficient γ can be extracted. The so-called K-factor is then obtained from the slope of the damping coefficient plotted against the square of the resonance frequency, as shown in Fig. 7. The theoretical damping-limited 3 dB bandwidth is then given as [4]

$$f_\mathrm{max} = \frac{\sqrt{8}\pi}{K} \ . \tag{9}$$

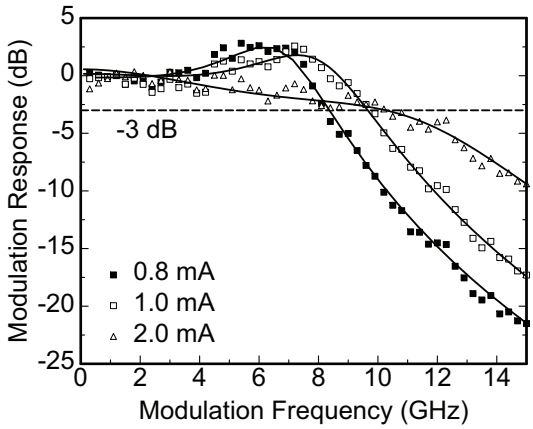

Fig. 6: Small-signal modulation response curves of a flip-chip-bondable VCSEL with 3.6 µm active diameter at different bias currents and room temperature. The solid lines are curve fits according to (2).

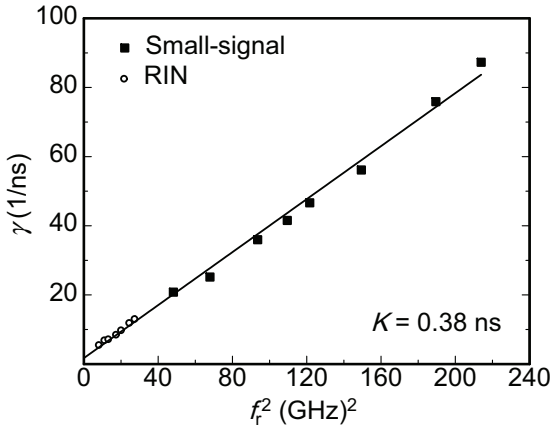

Fig. 7: Damping coefficient γ versus resonance frequency f_r squared of a VCSEL with 3.6 µm active diameter. Square symbols are the values obtained by curve fitting of measured small-signal modulation characteristics shown in Fig. 6, while circles are the values obtained by fitting the measured RIN spectra shown in Fig. 8 (right).

3.4 Relative intensity noise

Even with a noise-free VCSEL current driver, fluctuations will be present in a VCSEL's steady-state output power because of spontaneous emission. This noise characteristic is conveniently described by the RIN. More specifically, RIN relates the noise of the optical power $\delta P(t)$ to the mean power $\langle P \rangle$ as [8]

$$\mathrm{RIN} = \frac{\langle \delta P^2 \rangle}{\langle P \rangle^2} \ , \tag{10}$$

where the angular brackets denote an average over the observation time. Since the RIN is parasitics-free (note that the laser is driven by a CW signal), it can be employed not only to determine the noise characteristics of a laser, but also to examine its intrinsic modulation behavior. The RIN spectrum can be fit to extract f_r and γ using [4]

$$\mathrm{RIN}(f) = \frac{C f^2 + D}{(f_\mathrm{r}^2 - f^2)^2 + (\gamma f/(2\pi))^2} \ , \tag{11}$$

where C and D are device-dependent constants. Figure 8 (left) shows the experimental setup employed to measure the RIN spectra. It is similar to the one used for small-signal modulation response measurements. A wide-band (10 GHz) low-noise amplifier (LNA, Miteq, model AMF-3D-001100-25-13P) is added after an external optical receiver (Picometrix, model AD-50xr). The optical receiver consists of an RF photodetector and a transimpedance amplifier with 20 dB gain. The noise spectrum is recorded using a microwave spectrum analyzer (Hewlett Packard, HP70000 system)[5]. The frequency characteristics of all cables, the bias-tee, the optical receiver, and the amplifier as well as the noise floor of the microwave spectrum analyzer and the shot noise of the RF photodiode

[5]The RF section HP70908A is employed.

are numerically subtracted to obtain the RIN of the VCSEL. The RIN spectra for different currents and fit curves using (11) are depicted in Fig. 8 (right) for a VCSEL that is nominally identical to the one from Fig. 6.

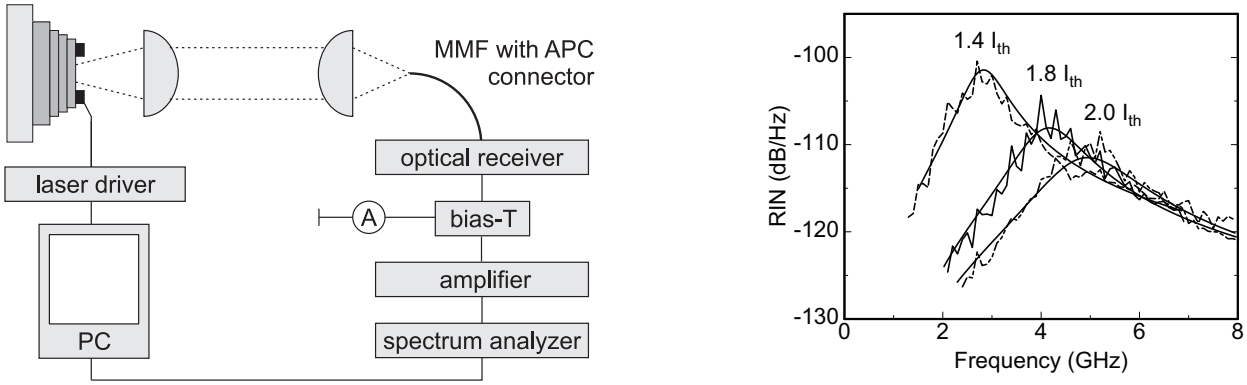

Fig. 8: Experimental setup used to measure RIN (left). RIN spectra of a VCSEL chip with 3.6 µm active diameter at different drive currents and room temperature (right). The solid lines are curve fits according to (11).

The resonance frequencies f_r and damping coefficients γ have been extracted and added to Fig. 7. The resultant K-factor is 0.38 ns and the maximum 3 dB bandwidth f_max is 23.4 GHz according to (9), with a high level of consistency between data points from the small-signal response and the RIN approach. The bandwidth of the VCSEL chips is thus limited by the electrical parasitics which have a 3 dB electrical bandwidth of only 5.2 GHz. The extraction procedure was more difficult from the RIN curves compared to the modulation response curves, especially for the damping coefficients which depend somewhat on the initial estimates. Moreover, the dynamic range of the RIN measurements is low due to the high noise floor originating mainly from the thermal noise of the optical receiver and to smaller extent from the thermal noise of the LNA. Shot noise plays a subordinate role. Therefore, increasing the dynamic range demands reducing the thermal noise and consequently smaller electrical bandwidths of the employed optical receiver and the LNA. The (f_r^2,γ) data points from RIN measurements in Fig. 7 are only in the low-frequency range due to the limited bandwidths of the employed LNA and the optical receiver (less than 10 GHz). For a reliable extraction of the data points, the resonance frequency should be about 3 to 4 GHz smaller than the system bandwidth, which limits the maximum extractable f_r to about 5 to 6 GHz.

4. Conclusion

We have reported the dynamic characterization of 894.6 nm VCSELs to be incorporated in Cs-based MEMS atomic clocks. The required modulation bandwidth of about 5 GHz is reached close above threshold. Maximum bandwidths above 10 GHz have been measured even at elevated temperatures up to 65 °C. For the investigation of the intrinsic modulation characteristics of the VCSELs, precise curve fitting procedures of measured RIN and

small-signal modulation spectra have been employed. A K-factor of less than 0.4 ns and a maximum 3 dB bandwidth exceeding 22 GHz are obtained.

5. Acknowledgments

The authors thank Y. Men for performing the electron beam lithography for grating fabrication. They wish to thank S. Renz, W. Schwarz, G. Liu, and T. Purtova, for their help in the processing and characterization. A very special thanks goes to Pierluigi Debernardi for the invention of the surface grating technique employed in this work and numerous simulations done in the past. Funding by the EC within its seventh framework programme (FP7) under grant agreement number 224132, project MAC-TFC is acknowledged.

References

[1] N. Cyr, M. Têtu, and M. Breton, "All-optical microwave frequency standard: a proposal", *IEEE Transactions on Instrumentation and Measurement*, vol. 42, no. 2, pp. 640–649, 1993.

[2] A. Al-Samaneh and D. Wahl, "Continuous-wave characteristics of MEMS atomic clock VCSELs", *Annual Report 2009, Institute of Optoelectronics, Ulm University*, pp. 41–46, 2009.

[3] R. Michalzik, J.M. Ostermann, and P. Debernardi, "Polarization-stable monolithic VCSELs", in *Vertical-Cavity Surface-Emitting Lasers XII*, C. Lei, J.K. Guenter (Eds.), Proc. SPIE 6908, pp. 69080A-1–16, 2008.

[4] R. Michalzik and K.J. Ebeling, "Operating Principles of VCSELs", Chap. 3 in *Vertical-Cavity Surface-Emitting Laser Devices*, H. Li and K. Iga (Eds.), pp. 53–98. Berlin, Germany: Springer-Verlag, 2003.

[5] R. Olshansky, P. Hill, V. Lanzisera, and W. Powazinik, "Frequency response of 1.3 μm InGaAsP high speed semiconductor lasers", *IEEE J. Quantum Electron.*, vol. QE-42, no. 9, pp. 1410–1418, 1987.

[6] D. Wiedenmann, R. King, C. Jung, R. Jäger, R. Michalzik, P. Schnitzer, M. Kicherer, and K.J. Ebeling, "Design and analysis of single-mode oxidized VCSEL's for high-speed optical interconnects", *IEEE J. Select. Topics Quantum Electron.*, vol. 5, no. 3, pp. 503–511, 1999.

[7] S.M. Sze, *Physics of Semiconductor Devices*, 2nd edition. New York, USA: John Wiley and Sons, 1981.

[8] K. Petermann, *Laser Diode Modulation and Noise*. Dordrecht, The Netherlands: Kluwer Academic Publishers, 1991.

Luminescence Properties of Epitaxially Grown GaN and InGaN Layers Around ZnO Nanopillars

Mohamed Fikry

GaN and InGaN layers grown around ZnO nanopillars by metalorganic vapor phase epitaxy (MOVPE) are investigated by means of photoluminescence (PL) and locally resolved cathodoluminescence (CL). A multi layer growth process involving deposition at different growth conditions in a step-wise manner has been employed for the coaxially grown GaN. Then InGaN/GaN quantum wells and barriers have been deposited as the final growth stage. A sharp peak at 3.46 eV in low temperature PL with FWHM of 23 meV confirmed the high quality of the deposited GaN layers. The existence of InGaN layers has been confirmed by another PL peak at 3.16 eV that has been shifted to 3.11 eV as the InGaN deposition temperature was reduced by 15° C and the trimethylindium (TMIn) flow was increased by 40 sccm. For more efficient investigations of single pillars, position control has been achieved through the growth of single ZnO nanopillars on top of GaN pyramids. Locally resolved CL mapping along single rods has revealed a relatively homogeneous indium distribution along the nonpolar side facets of the overgrown nano-pillars.

1. Introduction

The controlled synthesis of nano-structures based on GaN and related group III-N alloys has been receiving significant attention in recent years as possible candidates for the development of nanophotonic devices. Moreover, due to their high surface to volume ratio, tuneable direct band gap and high chemical stability, GaN based nanostructures promise a high potential as sensing elements for biomedical applications. As a first step towards the afore-mentioned goals, a process for producing high quality group III-N nanostructures with controlled positions is required. Well ordered and vertically aligned GaN nanorods have been recently achieved [1,2]. However, according to our experience, it is more difficult to obtain upright and well-ordered GaN nanorods directly by MOVPE in comparison to ZnO nanopillars grown by vapour-transport methods [3,4]. Moreover, the lattice constant of ZnO is close to that of GaN. Therefore, we have chosen such nanopillar structures as templates for the subsequent epitaxial sheathing by GaN-InGaN layers.

The ZnO nanopillars used as templates in these studies had typical diameters of 100-300 nm and heights of 1-2 μm. They have been grown by the vapour-transport method on a-plane sapphire substrates covered by a uniform ZnO nano-crystalline seed layer which was deposited in a preceding growth step via simple chemical vapour deposition [3]. The thin nano seed layer was formed rapidly on the substrate by sublimation and thermal

decomposition of zinc acetate dihydrate at moderate temperatures and pressures. Subsequently, growth of ZnO nano-wires was performed by a carbo-thermal vapour-transport method yielding nano-wires with c-axis up-right orientation [3].

The ZnO pillars have then been transferred to our AIXTRON AIX 200 RF low pressure MOVPE system. Trimethylgallium (TMGa) and ammonia (NH_3) were used for the deposition of GaN layers whereas trimethylindium (TMIn) and triethylgallium (TEGa) have been used for the deposition of the quantum wells and the barriers.

2. GaN Layers Around ZnO Nanopillars

A major issue for the hetero-epitaxial growth of GaN on ZnO using MOVPE is the high sensitivity of ZnO in the GaN growth environment: At elevated temperatures, ZnO decomposes by reacting with hydrogen and ammonia. Therefore, we have established a multi-layer growth process based on our experience in the growth of GaN layers on ZnO templates by MOVPE [5]. In order to protect the ZnO from being etched at the onset of the growth process, the nanorods were first covered by GaN at 550 °C using N_2 as a carrier gas. Then, we raised the growth temperature in order to improve the GaN quality. As the temperature was increased to 1050 °C using H_2 as carrier gas, hollow GaN tubes were achieved. The corresponding SEM pictures are shown in our previous works [5] and [6]. Figure 1 shows a low temperature (25 K) photoluminescence spectrum of such a nanorod ensemble where the spot size of the exciting laser was around 100 µm. As the spectrum was taken from a large ensemble of nanorods, we believe that the sharp peak at 3.46 eV with a FWHM of 23 meV confirms relatively high material quality of the deposited GaN layers. However, a blue luminescence centered at around 2.9 eV is still observed which is either defect related or resulting from Zinc doping of GaN. Our assumption for defect related blue luminescence is based on the fact that the low temperature casting layers in our multi growth process are of very low material quality. Moreover, the other two peaks centered at 3.195 eV and 3.28 eV are believed to originate from stacking faults in GaN. TEM investigations are planned for confirmation.

3. InGaN Layer Overgrowth

After the deposition of GaN as the final layer of the multi-layer growth process at 1050 °C, the temperature was reduced for the deposition of three coaxial thin InGaN/GaN layers and barriers, respectively. We have demonstrated in our previous work [6] the successful growth of a single coaxial quantum well with about 4 nm thickness as confirmed by transmission electron microscopy (TEM). For these layers, we used growth conditions optimized for c-plane GaN resulting in well/barrier thicknesses of 3 - 4 nm and 7 - 8 nm, respectively. We would then expect an In incorporation of about 9 % in the QWs. In low temperature PL, the expected InGaN peak was found at 3.16 eV with a FWHM of 190 meV (solid line in Fig. 2). Now considering that the 4 nm quantum well is formed only along the non-polar side facets of the rods, this corresponds to an In content of 9.7 %. Moreover, in comparison to the result in Fig. 1, another higher intensity peak at 3.35 eV was observed indicating the possible existence of ZnO remains. As a further check for the

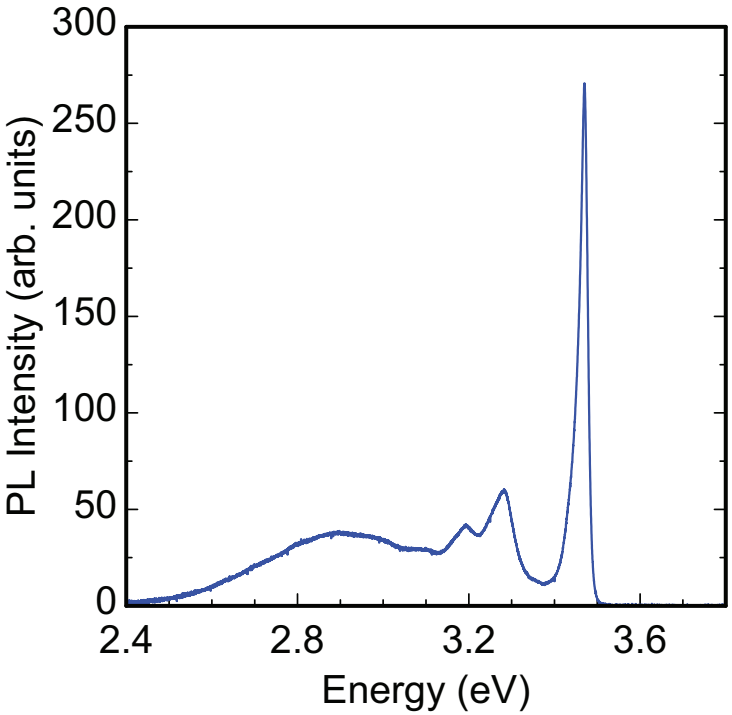

Fig. 1: Low temperature (25 K) PL spectrum for an ensemble of ZnO nanopillars overgrown with GaN layers.

In incorporation into the InGaN layers, the InGaN deposition temperature was reduced by 15 °C and the TMIn flow was raised by 40 sccm. In low temperature PL, a shift in the InGaN peak from 3.16 eV to 3.11 eV was observed, whereas no shift was observed for the assumed ZnO peak at 3.35 eV (dashed line in Fig. 2). This confirmed the expected increase of In incorporation into the quantum wells and it was calculated to be 1.5 %.

4. Position Control of ZnO Nanopillars

As mentioned in the introductory section, the ZnO nanopillar templates were prepared using the seed layer (SL) approach. This process is quite random and did not involve position control measures. However, for the purpose of simple addressing and efficient characterization of single rods, an effective position control approach needed to be implemented. An efficient approach that avoids the expense of e-beam lithography has been investigated. Growth of single ZnO nanorods on top of GaN micro-pyramids has been achieved (Fig. 3 (a)) where we made use of growth selectivity on the different surface planes of GaN pyramids [7]. The GaN micro-pyramids were prepared using the epitaxial lateral overgrowth (ELOG) technique employing a SiO_2 mask and photolithography. The degree of control of the subsequently grown ZnO rod diameters is relatively low since they range between 200 nm to 700 nm. However, this process is still investigated to reveal a narrower deviation window. Figure 4 shows the result of overgrowing such pillar-pyramid complex with GaN where the degree of ZnO desorption proved to be higher compared to the more densely packed nano-pillars prepared by the seed layer approach due to the

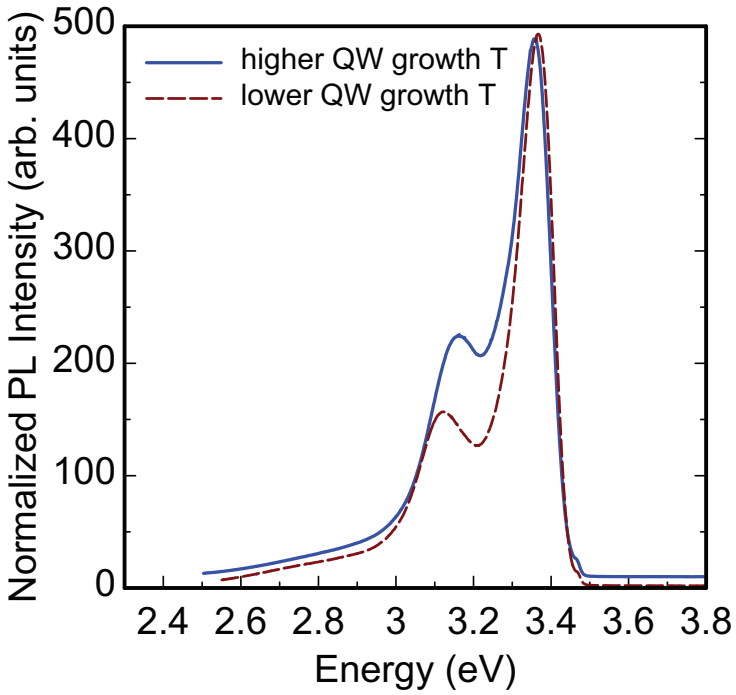

Fig. 2: Low temperature PL spectrum of coaxially overgrown ZnO nanopillars with GaN and 3 InGaN quantum wells. Solid line: quantum well grown at 855 °C. Dashed line: quantum well grown at 840 °C and TMIN flow increased by 40 sccm.

higher local V/III ratio.

5. Spatially Resolved Cathodoluminescence Mapping Along Single Pillars

The In distribution and defect distribution profile along these novel structures were still open questions. Overgrown single ZnO rods grown on top of GaN pyramids have been chosen as the best candidate structure for efficient cathodoluminescence studies. The rod-pyramid complexes were overgrown using the afore-mentioned step-wise multi growth procedure for GaN described in section 2, in addition to three InGaN/GaN wells and barriers (Fig. 3 (b)). Due to the much lower density for these samples, the increase of pillar diameter is relatively larger than for our other templates prepared without position control measures. An average diameter increase of around 500 nm was observed in comparison to around 200 nm for our previous templates. Moreover, the top of the rods was covered by a pyramid-like cap with semi-polar facets closing the top part of the hollow tubes, and we could clearly see the hexagonal symmetry formed by the non-polar side facets. Figure 5 shows a low temperature CL line scan from top to bottom of a single overgrown rod, where an electron acceleration voltage of 5 kV and a spectral resolution of 3.2 nm have been used. Each spectral scan in Fig. 5 is shifted in intensity for comparison of each position along the rod. Line-scans 1 and 2 were measured at the pyramid-like cap structure on top of the pillar, while line-scan 10 was measured at the interface between the

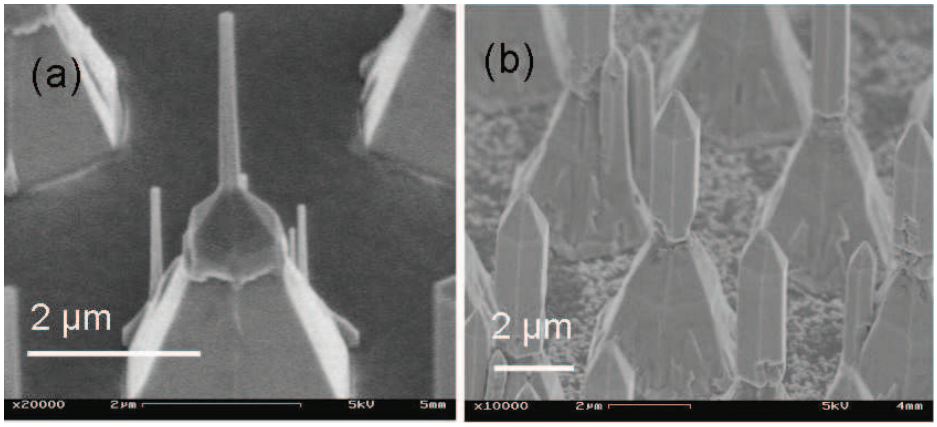

Fig. 3: SEM pictures of (a) a single ZnO nanorod grown on top of GaN pyramids and (b) these ZnO nanorods overgrown with GaN and InGaN quantum wells.

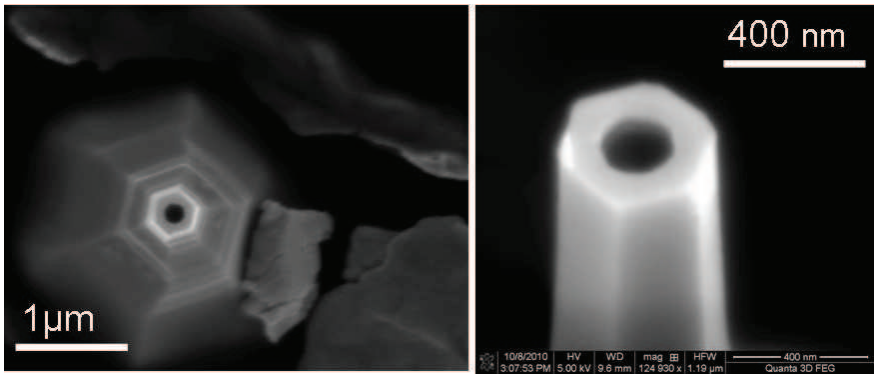

Fig. 4: SEM pictures of hollow GaN nanotubes grown on top of GaN micro-pyramids after desorption of ZnO. Left: top view and right: angular view.

GaN micro-pyramid's top and the pillar's bottom. The high luminescence contribution at 388 nm emerges mainly from the middle part of the rod with the non-polar side facets (line-scans 3 to 8), whereas it dies out at the afore-mentioned top and bottom areas of the pillar. The emission's full width at half maximum for line scans taken from the middle of the rod were measured to have an average of 170 meV, which is slightly narrower than those measured by photoluminescence from an ensemble of nanorods in section 2. For the interface between the pillar and the pyramid, this is assumed to be related to unintentional impurity incorporation during the nucleation of the ZnO nano-pillar. This could be excessive zinc or oxygen doping into GaN or excessive gallium doping into ZnO. For the pyramid-like cap structure on top of the pillar, the nature of defects is still not clear but further TEM investigations are planned for clarification.

The luminescence distribution of the peak at 388 nm along the middle part of the rod with the non-polar side facets (Fig. 6 (b)) shows a relatively homogeneous profile without signs of localized luminescent centers. Tracing the luminescence along the lateral direction perpendicular to the rod's axis, we do not expect to see perfect homogeneity since there exist the edges between the different m-plane side facets that could cause disturbances in

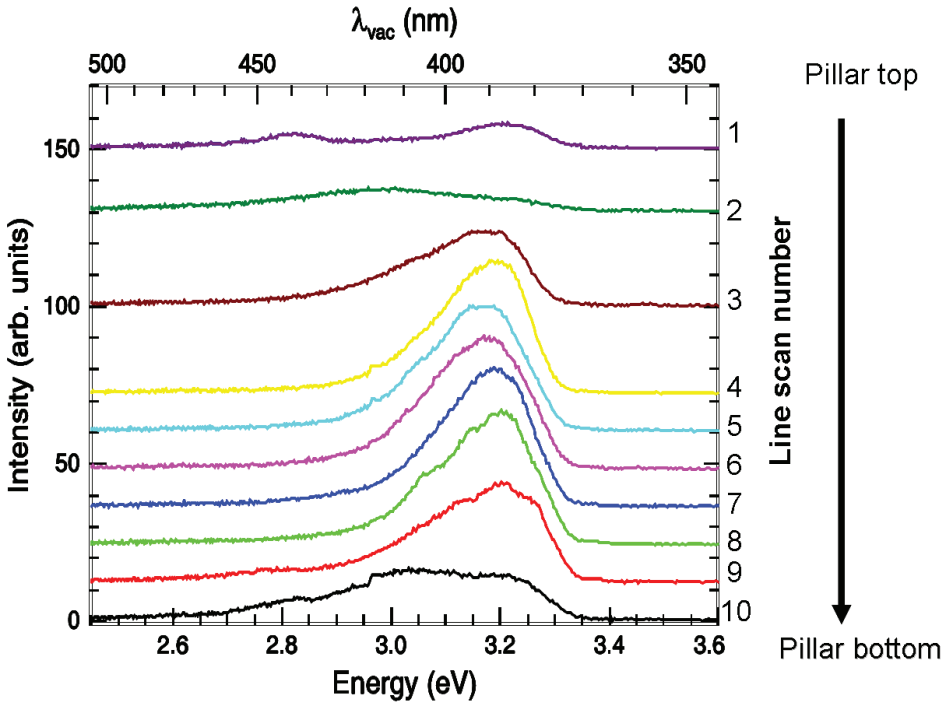

Fig. 5: Low temperature CL linescan from top to bottom along a ZnO nanopillar overgrown with GaN and InGaN layers.

strain and In incorporation. For the same growth experiments on the more densely packed seed layer samples, cathodoluminescence studies revealed randomly distributed localized luminescent centers along single m-planes (not shown here). Moreover, blue shifting of the center peak positions are observed near the pillar's top and bottom (comparing line-scans 3 to 9 in Fig. 5). These small shifts in peak position are assumed to be predominantly caused by different degree of strain at the top and the bottom parts of the pillar compared to the middle part. However, slightly different In incorporation can not be excluded.

The luminescence contribution from the pyramid was weaker than from the rod and was observed at a wavelength of 420 nm (not shown here). Such luminescence peak shift between the nonpolar and semipolar facets of the rod and the pyramid, respectively, is believed to result from possible different In incorporation, different quantum well thicknesses as well as the effect of presence and absence of the piezoelectric field.

6. Conclusion

We have studied the luminescence properties of coaxially deposited GaN and InGaN layers around ZnO nanopillars by MOVPE and we were able to conclude their fairly high material quality. Moreover, successful position control of these novel structures was achieved by growth of single rods on top of GaN pyramids. This has facilitated efficient locally resolved cathodoluminescence mapping along single rods. A high contribution with

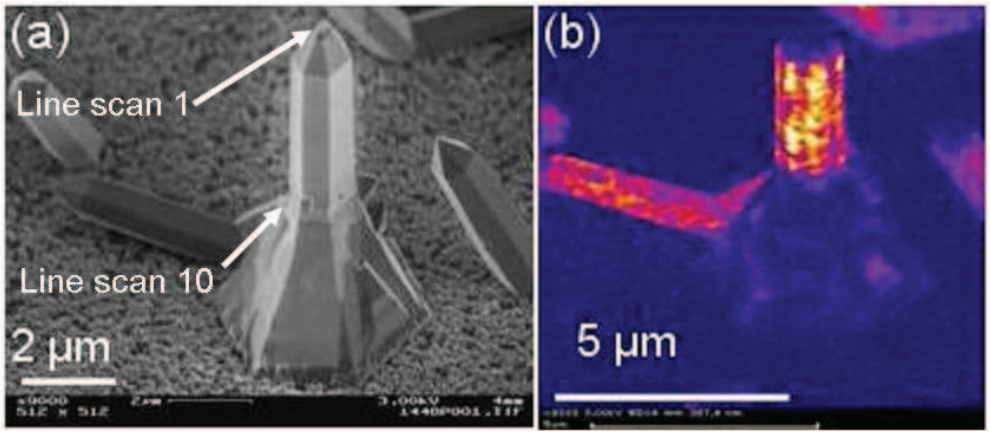

Fig. 6: (a) SEM picture of a single ZnO rod overgrown with GaN and InGaN on top of a GaN pyramid. (b) Spatial distribution of the CL emission at 3.195 eV for the rod-pyramid complex shown in (a).

a relatively uniform luminescence distribution at 388 nm emerges from single non-polar side facets of the rod indicating the existence of InGaN quantum wells.

7. Acknowledgement

We would like to cordially thank Manfred Madel for growing the ZnO nanopillars used in these studies, Ingo Tischer for undertaking the cathodoluminescence measurements, S.B. Thapa and E. Angelopoulos for their previous work on the epitaxial growth of GaN on ZnO as well as I. Argut, Y. Men and T. Wunderer for their help with sample processing. This work has been partly financially supported by the Helmholtz Association within the project "PINCH Photonics".

References

[1] S.D. Hersee, X. Sun, and X. Wang, "The controlled growth of GaN nanowires", *Nano Lett.*, vol. 6, pp. 1808–1811, 2006.

[2] K. Kishino, H. Sekiguchi, and A. Kikuchi, "Improved Ti-mask selective-area growth (SAG) by RF-plasma-assisted molecular beam epitaxy demonstrating extremely uniform GaN nanocolumn arrays", *J. Cryst. Growth*, vol. 311, pp. 2063–2068, 2009.

[3] A. Reiser, V. Raeesi, G.M. Prinz, M. Schirra, M. Feneberg, U. Roeder, R. Sauer and, K. Thonke, "Growth of high-quality, uniform c-axis-oriented zinc oxide nano-wires on a-plane sapphire substrate with zinc oxide templates", *Microelectron. J.*, vol. 40, pp. 306–308, 2009.

[4] J.Y. Park, Y.S. Yun, Y.S. Hong, H. Oh, J. Kim, and S.S. Kim, "Synthesis, electrical and photoresponse properties of vertically well-aligned and epitaxial ZnO nanorods

on GaN-buffered sapphire substrates", *Appl. Phys. Lett.*, vol. 87, pp. 123108-1–3, 2005.

[5] S.B. Thapa, J. Hertkorn, T. Wunderer, F. Lipski, F. Scholz, A. Reiser, Y. Xie, M. Feneberg, K. Thonke, R. Sauer, M. Duerrschnabel, L.D. Yao, D. Gerthsen, H. Hochmuth, M. Lorenz, and M. Grundmann, "MOVPE growth of GaN around ZnO nanopillars", *J. Cryst. Growth*, vol. 310, pp. 5139–5142, 2008.

[6] F. Scholz, S.B. Thapa, M. Fikry, J. Hertkorn, T. Wunderer, F. Lipski, A. Reiser, Y. Xie, M. Feneberg, K. Thonke, R. Sauer, M. Duerrschnabel, L.D. Yao, and D. Gerthsen, "Epitaxial growth of coaxial GaInN-GaN hetero-nanotubes", *IOP Conference Series: Materials Science and Engineering*, vol. 6, pp. 012002-1–4, 2009.

[7] Y.J. Hong, S.J. An, H.S. Jung, C.H. Lee, and G.C. Yi "Position-controlled selective growth of ZnO nanorods on Si substrates using facet-controlled GaN micropatterns", *Adv. Mater.*, vol. 19, pp. 4416–4419, 2007.

Studies on Si-doped AlGaN Epilayers

Kamran Forghani

Growth optimization of Si doped AlGaN epilayers—with 20 %, 30 % and 45 %Al content—grown on AlGaN-sapphire by MOVPE was investigated. We could realize n-type carrier concentrations from about $2 \times 10^{18}\,cm^{-3}$ *to* $1 \times 10^{19}\,cm^{-3}$. *The layers with high levels of dopants suffer from crack formation. Therefore, we used a short period super lattice to manage the strain between the doped layer and the undoped buffer layer. The XRD investigations were performed to reveal the strain evolution in our layers with respect to the dopant concentration. Using variable temperature Hall measurements on such films, the activation energy of the Si-donors was evaluated. We found a fairly small activation energy confirming that the doping concentrations are in the range of the Mott transition.*

1. Introduction

AlGaN as a wide-bandgap semiconductor material has found increasing scientific and practical interest in the last few years. This is, in large part, due to its use in UV light emitting diodes (LEDs) [1] as well as laser diodes (LDs) [2]. Although LEDs and LDs have been commercially developed in the near-UV (above 400 nm) and visible region, the construction of such devices becomes much more challenging as the wavelength shortens. One essential part of UV-LEDs and UV-LDs is the growth of n-doped AlGaN epilayers. It is expected that the realization of a reasonable n-type conductivity in AlGaN is more challenging than in GaN due to the formation of defects with increase of the Al- or Si-content. Additionally, an increase of the donor activation energy with increasing Al-content is expected because of a gradual increase in the effective electron mass and a decrease in the dielectric constant. Therefore, we study the doping of AlGaN with Si as a common donor. The grown Si-doped films must be suitable templates for the growth of LEDs and LDs. Therefore, they must be crack-free. However, the critical thicknesses of the doped films is much less than in the undoped films. We have attempted to find out the possible reasons as this phenomenon is not yet well understood.

Nowadays, there are many reports about the activation energy of Si in n-doped AlGaN (from GaN:Si to AlN:Si). However, these values vary over a wide range as different buffer layers (in terms of crystal quality) and different dopant concentrations were investigated. In order to understand the effect of dopant concentration on activation energy, the films with different doping concentration, but with similar buffer layers are compared in this work.

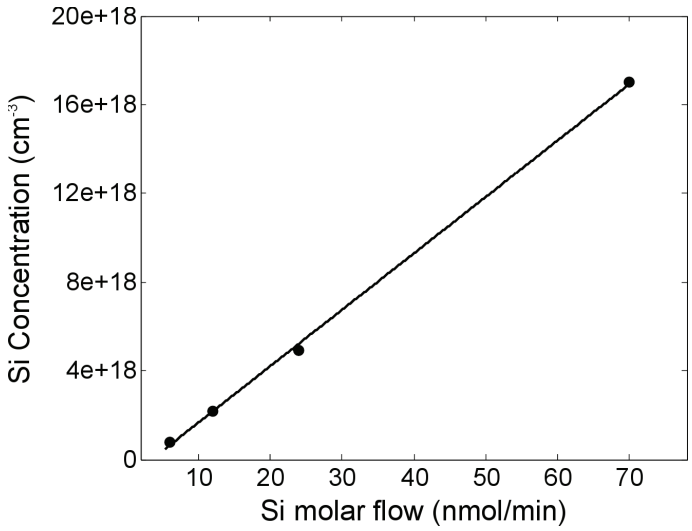

Fig. 1: Linear relation between Si concentration measured by SIMS and Si molar flow in samples A, B ,C and D.

2. Experimental Details

All samples investigated in this study were grown on (0001) sapphire substrates in a low-pressure horizontal reactor (Aixtron AIX-200/4 RF-S). Trimethylgallium (TMGa) and trimethylaluminum (TMAl) were used as group-III precursors and ammonia as group-V precursor. The aluminum incorporation in the undoped buffer layers was set to about 20 %, 30 % and 45 % as confirmed by photoluminescence (PL). The standard growth temperature was set to 1120 °C. Similar to our high quality GaN layers [3], we used a nucleation layer (NL) of oxygen doped AlN with a thickness of about 25 nm. Silane was used as the Si source.

Some of the samples which were used for the following investigations were grown on our previously developed AlGaN epilayers with an in-situ deposited SiN nano-mask [4]. The nano-masking improves the crystal quality [5] of the epilayers leading to higher performance of LEDs grown on such templates [6].

Variable temperature Hall-effect measurements were applied to determine the activation energy of the donors in the AlGaN films.

3. Results and Discussions

3.1 Effect of Si doping on strain

In order to investigate the effect of Si concentration on the evolution of strain in AlGaN films, four samples A, B, C, D—all with 20 % Al—were grown with identical strucures; 500 nm Si-doped AlGaN on 500 nm undoped AlGaN. The doping levels in those samples were $8.0 \times 10^{17}\,\mathrm{cm}^{-3}$, $2.2 \times 10^{18}\,\mathrm{cm}^{-3}$, $4.9 \times 10^{18}\,\mathrm{cm}^{-3}$ and $1.7 \times 10^{19}\,\mathrm{cm}^{-3}$, respectively for samples A–D. There were no intentional measures taken in order to increase the crystal quality of the epilayers. The Si incorporation into the solid phase (AlGaN) shows a linear behavior with the Si effective molar flow in this range (Fig. 1).

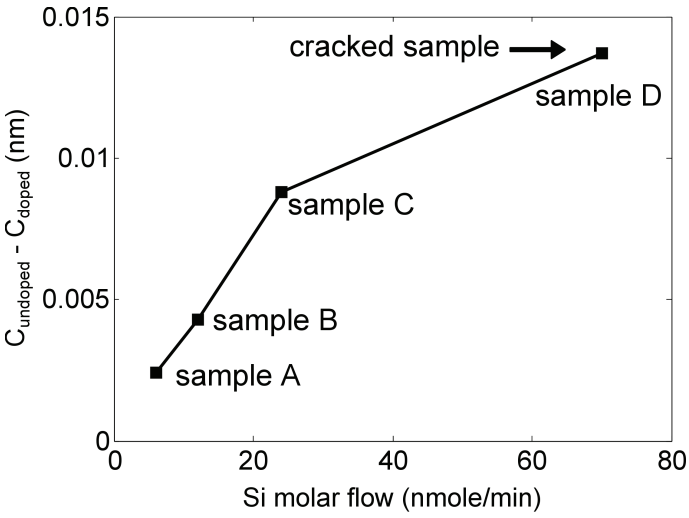

Fig. 2: The mismatch between c-lattice constant of the buffer layer and the doped layer increases as Si concentration increases.

The samples were crack free, except the last sample (sample D) which had a very high doping level. In other words, we observed that, the higher the Si concentration is, AlGaN epilayers exhibit less critical thicknesses. XRD Ω-2Θ scans—(004) reflections—of the samples A–D reveal that the c-lattice constant shrinks as the Si concentration increases (Fig. 2).

Reciprocal space mapping (RSM) of asymmetric (105)-reflections was carried out (Fig. 3) in order to determine the strain of these layers.

As the Si concentration increases from sample A to slightly higher concentrations in sample B, a broadening of the XRD peak is visible. Emergence of a side peak with lower q_z and higher q_x in reciprocal space is visible as the Si concentration increases from sample B to samples C and D.

Clearly, the a-lattice constant of the top doped epilayer increases with increasing Si concentration while the c-lattice constant decreases, implicating a biaxial tensile strain induced in the crystal structure by Si doping. This Si induced-tensile strain was observed also by others, e.g. by Romano et al. [7] in GaN. They have concluded that this might be due to a coalescence phenomenon during growth, as a slight roughening of the film surface is often observed in Si doped GaN epilayers. However, our AlGaN:Si films showed even smoother surfaces with Si doping. According to M. Moram et al. [8] Si is able to 'pin' the dislocations, hindering them from climbing. Preventing the dislocations from climb during film growth leads to less absorbtion of tensile stress that develops during growth.

However, similar investigation on AlGaN films seems to be necessary in order to understand whether this argument still holds in the case of Si-doped AlGaN films.

3.2 Electrical properties of n-doped AlGaN epilayers

We have grown several samples with Al contents of 20 %, 30 % and 45 % in order to evaluate the possible donors' activation energy of the AlGaN over the composition range of 20 % to 45 %. A summary of the structure of the samples is listed in Table 1, and the details can be found in Ref. [9]. Samples B and C as described in section 3.1 consist of

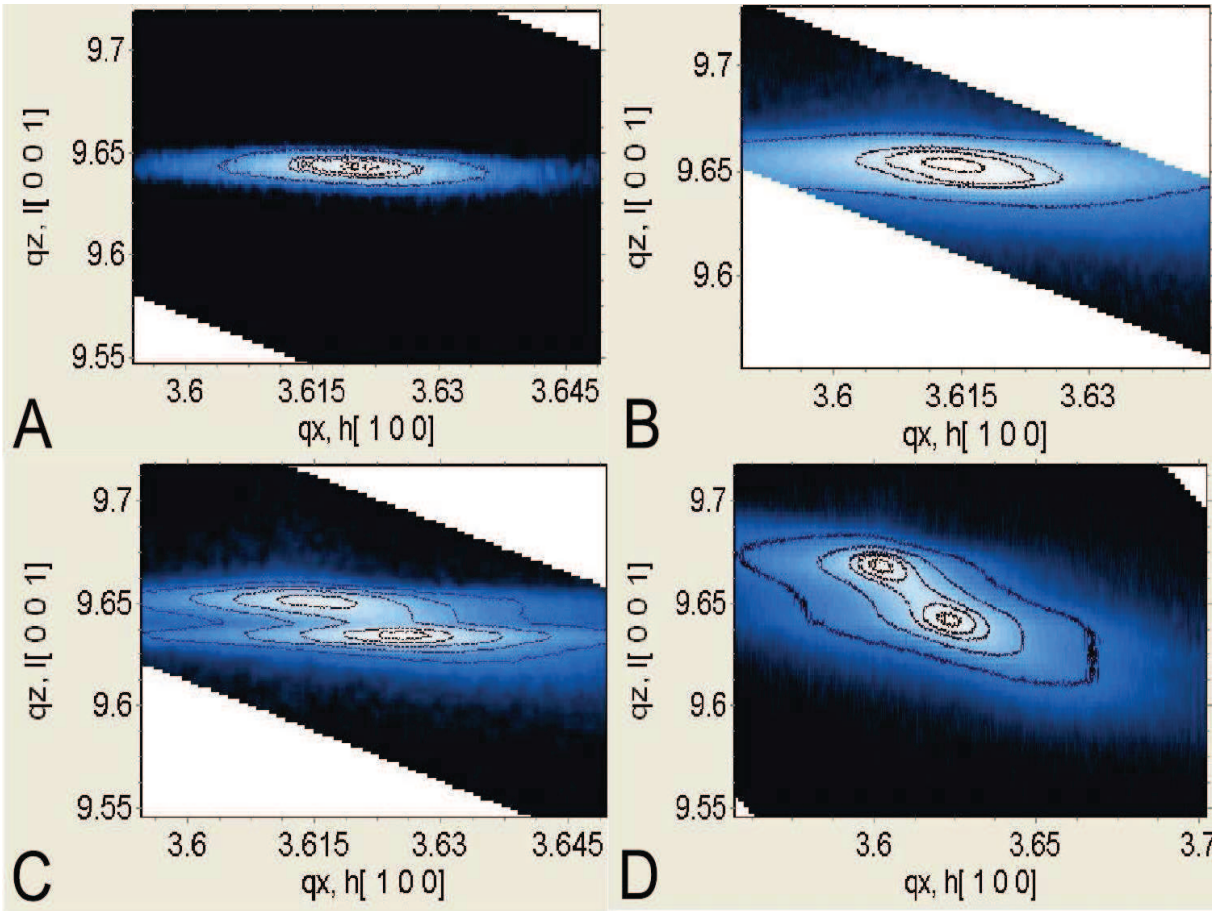

Fig. 3: Reciprocal space mappings of samples A, B, C and D: An increase of the a-lattice constant ($\propto\frac{1}{q_x}$) in comparison to the undoped AlGaN buffer layer is visible. The opposite scenario is valid for the c-lattice constants ($\propto\frac{1}{q_z}$), confirming the symmetric measurements.

Table 1: Structure and doping doses of the samples shown in Fig. 4.

Sample	Al content	Si-molar flow (nmole/min)	SiN nanomasking	SPSL
B	20 %	12	—	—
C	20 %	24	—	—
E	20 %	12	150 nm above NL	—
F	30 %	12	On NL	—
G	30 %	24	On NL	Yes
I	45 %	12	—	Yes

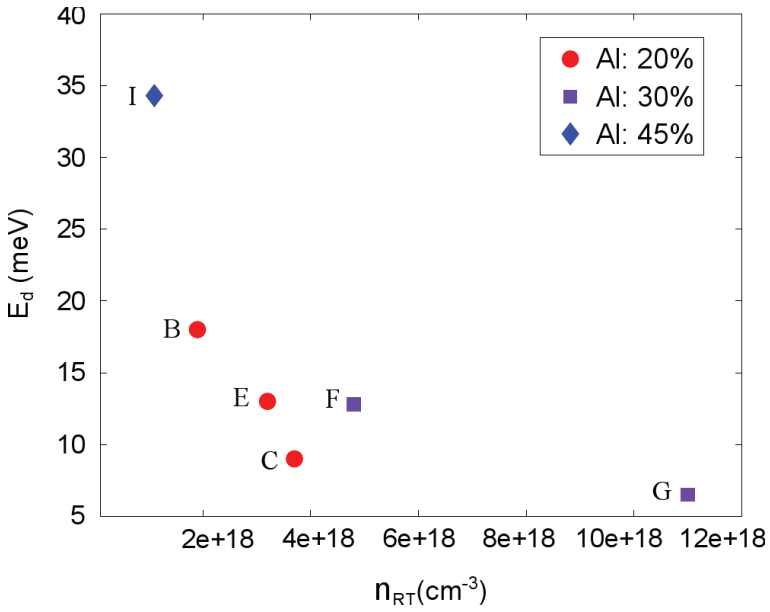

Fig. 4: Activation energy of the Si-donors (ΔE_d) evaluated for several AlGaN epilayers with different Si contents or Al contents; samples' details in Table 1.

500 nm $Al_{0.2}Ga_{0.8}N$:Si grown on an undoped $Al_{0.2}Ga_{0.8}N$ buffer layer with the thickness of 500 nm. Therefore, we can compare the change in the activation energy due to the change of the dopant concentration in $Al_{0.2}Ga_{0.8}N$. Sample E was grown on our high quality $Al_{0.2}Ga_{0.8}N$ templates with a 3400 nm thick undoped part and a 500 nm doped part on top. A SiN nanomask was deposited *in-situ* 150 nm above the NL to significantly reduce the dislocation density in this sample. The silane effective molar flow was set identically to that of sample B. Thus, we could study the influence of the SiN nanomask in our templates on the donors' activation energy. In order to have a similar comparison, we have grown samples F and G with higher Al content (30 %). These samples are $Al_{0.3}Ga_{0.7}N$:Si with different Si doping levels grown on buffer layers with a SiN nanomask deposited on the NL. Because the SiN interlayer is less effective at higher Al contents, we did not use that interlayer for the growth of sample I ($Al_{0.45}Ga_{0.55}N$). It consists of a 500 nm thick un-doped $Al_{0.45}Ga_{0.55}N$ buffer layer with 500 nm thick $Al_{0.45}Ga_{0.55}N$:Si on top. The silane molar flow for the growth of the doped part is identical to that of samples B, E and F (Table 1).

As the Al content—or the silane molar flow— increased in the films, severe crack formation was evident. As investigated in section 3.1, this is due to the generation of a tensile strain with increasing Si content in the AlGaN films. In order to suppress the formation of cracks, we have tried to compensate the rising tensile strain by inducing more compressive strain from the buffer layer. Therefore, a series of short period super lattices (SPSLs) were grown below the Si-doped part to reduce the average a-lattice constant of the buffer layer. In the current work, the SPSL consists of 120 pairs of AlN(2 nm)—$Al_xGa_{1-x}N$ (3.5 nm) sequences for an $Al_xGa_{1-x}N$ film. The growth of such SPSLs resulted in the growth of completely crack free wafers and very smooth surfaces. The samples that required the growth of SPSLs are indicated in Table 1 (samples G and I).

The activation energy of the donors (ΔE_d) was evaluated for these layers using variable temperature Hall measurements. The details of these evaluations are explained in Ref. [9].

The donor activation energy is depicted in Fig. 4 for the samples shown in Table. 1 with different Si- and Al-contents.

Looking to samples B and C (similarly samples F and G), it is clear that as the doping concentration is increased ΔE_d approaches very low values (below 10 meV). This dependency of ΔE_d to carrier concentration can be explained by the Mott transition also known as metal-nonmetal transition [10]. For the samples with higher concentrations of Si compared to the Mott critical concentration, one can expect to observe a more metallic behavior of conductivity. A continuous increase of the Si concentration leads to the formation of a donor band. As such an impurity band widens further with an increase of the impurity content, it can even overlap with the conduction band [11]. This delocalization of the carriers leads to a very low activation energy.

The critical Mott density N_c is given by [10, 12]:

$$N_c \approx (\frac{0.25}{a_b})^3, \tag{1}$$

where, a_b is the effective Bohr radius. Our calculations show that N_c is equal to $1.1 \times 10^{18}\, cm^{-3}$ for GaN, $2.0 \times 10^{18}\,\mathrm{cm}^{-3}$ for $Al_{0.20}Ga_{0.80}N$, $2.6 \times 10^{18}\,\mathrm{cm}^{-3}$ for $Al_{0.30}Ga_{0.70}N$ and $3.7 \times 10^{18}\,\mathrm{cm}^{-3}$ for $Al_{0.45}Ga_{0.55}N$. The calculated value for N_c of GaN in Ref. [12], based on Mott's model, confirms the correctness of our calculations.

All samples depicted in Fig. 4 except sample I ($Al_{0.45}Ga_{0.55}N$) have donor concentrations fairly higher than N_c. Looking to sample E in Fig. 4, it is clear that this sample has higher carrier concentration than sample B while both have been grown with the same silane molar flow. A similar situation exists for samples F and G which have been doped with silane molar flows, identical to samples B and C respectively. A possible explanation might be the deposition of a SiN interlayer during growth of such films which increases the total Si content of the films. SiN deposition may increase the Si impurity during the growth or enhance the Si diffusion to the upper layers.

Comparing samples C (20 %) and F (30 %) which show similar carrier concentrations, one can conclude that the sample with higher Al content has higher activation energy (Fig. 4). A similar comparison can be made between sample B (with 20 % Al content) and sample I (with 45 % Al-content).

4. Conclusion

Growth of n-doped AlGaN with 20 %, 30 %, 45 % Al-content was realized. As the Al-content in the epilayers or the dopant concentration increases, cracks were observed on the surfaces. XRD investigations showed that the crack formation is due to the increase of the tensile strain in the doped part of the films due to the Si doping. However, the mechanisms conributing to the rising tensile strain is not yet clear. A series of SPSLs was grown in order to compensate the tensile strain by inducing more compressive strain.

We have calculated critical donors concentration (Mott density) for our AlGaN:Si films. Having evaluated all the samples with variable temperature Hall-effect measurements, we

confirmed for the samples with Si concentrations higher than N_c, the donors activation energies are very low. In such samples, donor activation energy decreases with increasing Si content. It was found that samples with higher Al-content exhibit also higher donor activation energies. The samples with a SiN nanomask show much higher carrier concentrations than the samples without any SiN nanomask. This might be due to Si diffusion during growth originated from deposition of the SiN interlayers.

5. Acknowledgments

The assistance of M. Gharavipour in characterization of the samples and respective evaluations is gratefully acknowledged. The author would like to thank R. Rösch and I. Argut for preparing samples for Hall measurements and K. Thonke and F. Lipski for fruitful discussions, B. Neuschl for providing PL evaluations in addition to the Fraunhofer Institute for Applied Solid State Physics for providing SIMS evaluations. The author acknowledges the support from Dr. W. Limmer for Hall-effect measurements. This work was financially supported by the German Federal Ministry of Education and Research (BMBF) within the framework of the "Deep UV-LED" project.

References

[1] A. Khan, K. Balakrishnan, and T. Katona, "Ultraviolet light-emitting diodes based on group three nitrides", *Nat. Photonics*, vol. 2, pp. 77–84, 2008.

[2] H. Yoshida, Y. Yamashita, M. Kuwabara, and H. Kan, "A 342-nm ultraviolet AlGaN multiple-quantum-well laser diode", *Nat. Photonics*, vol. 2, pp. 551–554, 2008.

[3] J. Hertkorn, P. Brückner, S.B. Thapa, T. Wunderer, F. Scholz, M. Feneberg, K. Thonke, R. Sauer, M. Beer, and J. Zweck, "Optimization of nucleation and buffer layer growth for improved GaN quality", *J. Cryst. Growth*, vol. 308, pp. 30–36, 2007.

[4] J. Hertkorn, F. Lipski, P. Brückner, T. Wunderer, S.B. Thapa, F. Scholz, A. Chuvilin, U. Kaiser, M. Beer, and J. Zweck, "Process optimization for the effective reduction of threading dislocations in MOVPE grown GaN using in situ deposited SiN_x masks", *J. Cryst. Growth*, vol. 310, pp. 4867–4870, 2008.

[5] K. Forghani, M. Klein, F. Lipski, S. Schwaiger, J. Hertkorn, R.A.R. Leute, F. Scholz, M. Feneberg, B. Neuschl, K. Thonke, O. Klein, U. Kaiser, R. Gutt, and T. Passow, "High quality AlGaN epilayers grown on sapphire using SiN interlayers", *J. Cryst. Growth*, vol. 315, pp. 216–219, 2011.

[6] M. Kunzer, R. Gutt, L. Kirste, T. Passow, K. Forghani, F. Scholz, K. Köhler, and J. Wagner, "Improved quantum efficiency of 350 nm LEDs grown on low dislocation density AlGaN buffer layers", *Phys. Stat. Sol.* (accepted, to be published in 2011).

[7] L.T. Romano, C.G. Van de Walle, J.W. Ager, W. Götz, and R.S. Kern, "Effect of Si doping on strain, cracking, and microstructure in GaN thin films grown by metalorganic chemical vapor deposition", *J. Appl. Phys.*, vol. 87, pp. 7745–7783, 2000.

[8] M.A. Moram, M.J. Kappers, F. Massabuau, R.A. Oliver, and C.J. Humphreys, "The effects of Si doping on dislocation movement and tensile stress in GaN", (to be published in *J. Appl. Phys.*)

[9] M. Gharavipour, *Doping studies of AlGaN with high Al content*, Master Thesis, Ulm University, Ulm, Germany, Jan. 2011.

[10] N.F. Mott, "Metal-insulator transition", *Rev. Mod. Phys.*, vol. 40, pp. 677–683, 1968.

[11] H. Morkoç, *Handbook of Nitride Semiconductors and Devices, Electronic and Optical Processes in Nitrides* (1st ed.), pp. 589–590, Berlin: Wiley-VCH, 2008.

[12] A. Ferreira da Silva and C. Persson, "Critical concentration for the doping-induced metal-nonmetal transition in cubic and hexagonal GaN", *J. Appl. Phys.*, vol. 92, pp. 2550–2555, 2002.

Optimizing Structured SiN-masks for Self Separation of Full 2"-GaN Wafers by Hydride Vapor Phase Epitaxy

Martin Klein

Using a previously shown method, we prepared 2"-GaN wafers as templates for a self separation process. Self separation is happening during cooldown after growing thick layers of GaN in our hydride vapor phase epitaxy (HVPE) reactor. Our templates consist of GaN grown by metalorganic vapor phase epitaxy (MOVPE) directly on sapphire. These GaN layers are masked with 200 *nm of SiN that are structured by means of optical lithography. They are subsequently overgrown with a thin GaN layer by metalorganic vapor phase epitaxy (MOVPE). Previous experiments found that the ideal interlayer for self separation during cooldown in HVPE is created when using a hexagonally shaped pattern as mask. We now tried several possible variations of this pattern to find the optimal geometrical proportions supporting the desired self separation.*

1. Introduction

Becoming a more and more common material, galliumnitride (GaN) still suffers from the lack of suitable substrates. This leads to the need for heteroepitaxy in mid and low price applications. Although homoepitaxy is used for producing blue lasers, available GaN substrates are much too costly for growing LEDs and transistors. To achieve affordable homoepitaxial substrates, great efforts have been made in the field of ammonothermal growth [1, 2]. Yet thick layers grown by HVPE are still a good candidate to provide GaN wafers for future industrial processes and this technique is under constant research. Nevertheless this is still not a trivial task. Differences in the thermal expansion coefficients of GaN and sapphire result in big layer curvatures and the large mismatch in lattice constants leads to strain and defects in the GaN layer. In order to cope with these problems, several methods have been developed to remove the GaN layer from the substrate such as laser-lift-off (LLO) [3], mechanical polishing [4] or growth on etchable substrates like GaAs [5] and ZnO [6]. Another approach is the usage of interlayers to weaken the material bond at a defined position. This technique can be used to generate a predetermined breaking point at which the layer separates from the template. During process cooldown the difference in thermal expansion coefficients of the sapphire substrate and the GaN layer leads to a large strain at the interface. The forces inherited in this procedure result in the separation of the GaN layer from the substrate at the predetermined position. Our institute has been working on developing this technique for quite some time. This lead to a standardized procedure for creating working breaking point layers [7].

A substantial part of developing such a layer is finding a good compromise between top layer quality and easy separation of the GaN layer from the substrate. SiN masks have proven to be a good starting point to meet these requirements. First, SiN is deposited by means of plasma enhanced chemical vapor deposition (PECVD) and subsequently structured by optical lithography and reactive ion dry etching (RIE) technique. These masks are overgrown by MOVPE to create a starting layer for HVPE growth, where subsequently thick GaN layers are grown on top of these templates. During this last growth-step, the thin SiN layer dissolves. This is a result from the harsh process conditions in HVPE growth. The dissolved mask material etches the underlying GaN which has been deposited in MOVPE. This leaves a porous interlayer that promotes separation at this exact position. Self separation finally occurs during cooldown of this HVPE process. Up to date self separation can be achieved with high repeatability. Nevertheless the goal to create full 2" freestanding wafers has only been reached by chance, most wafers are cracking into pieces during separation. This is the motivation to find new mask designs which specifically address this problem.

2. Experimental

In our latest investigations we created various new hexagonal mask designs in order to find the influence of the masked area and the trench width on material growth and separation. The findings of our previous studies were used as starting values.

Table 1: Geometries of separation masks.

Mask name	Pattern type	Trench width	Period
HexFL_v2	hexagon	1.5 µm	30 µm
HexFL_v4	hexagon	2.5 µm	30 µm
HexFL_v1	hexagon	3.0 µm	30 µm
HexFL_v5	hexagon	4.5 µm	30 µm
HexFL_v3	hexagon	1.5 µm	40 µm
HexFL_v6	separated hexagon	3.0µm	39µm

Table 1 shows the geometrical details of the used masks. For most of the masks there was no change in the principal structure of the hexagonal pattern compared to earlier studies [7]. This approach is shown on the left side of Fig. 1. In contrary to this approach, the structure shown on the right side of this figure shows a completely new idea. With this pattern, consisting of separated hexagons, we intended to investigate the influence of the connections between the hexagons in our conventional mask.

For overgrowing these templates we used our commercial Aixtron single-wafer HVPE-system with a horizontal quartz-tube. The system is heated by a five zone furnace which enables to set a temperature of 850 °C in our source zone and 1050 °C in the growth zone. In the source zone, GaCl is formed by streaming HCl over a bath of liquid gallium.

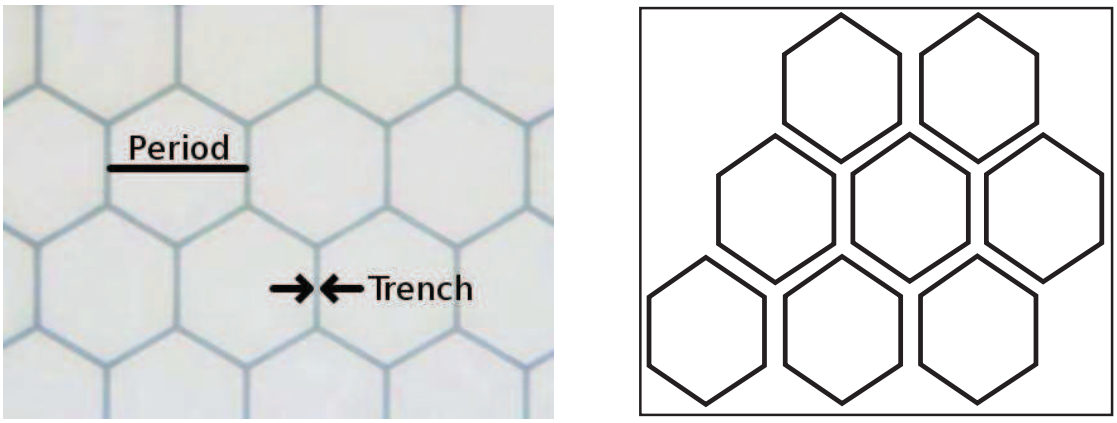

Fig. 1: Structures of connected and separated hexagons.

Ammonia is used as nitrogen precursor. These two gas streams are carefully adjusted to meet optimal growth conditions on the supplied template residing in the growth zone. As carrier gases we use a 1:1 mixture of H_2 and N_2. The V/III-ratio is in the range of $80 - 90$. The reactor pressure is set to 900 hPa.

At first the templates were overgrown by about 70 µm of GaN with a fairly low growth rate of 35 µm/h. In this first step we optimized growth conditions for lateral growth, thereby promoting a fast coalescence of the GaN surface. After this first step we investigated the resulting layers to find differences in material quality, depending on the mask. Next we grew another 12 hours with a growth rate of about 85 µm/h. The goal was to get a freestanding GaN layer of about 1 mm.

These freestanding samples have been investigated by means of x-ray diffraction (XRD) and photoluminescence (PL) to compare the mask designs and to confirm the suspected good quality. Additionally we conducted an etch pit density (EPD) experiment to verify our data gathered by these studies.

In a second experiment, we varied the thickness of the structured SiN layer to see if we can create a weaker bond between the template and the layer. This weaker bond could result in a more homogenous separation of the top layer.

3. Results and Discussion

3.1 Mask overgrowth

As described in the previous section, we stopped growth after a layer thickness of about 75 µm to investigate the overgrowth of our masked templates. Figure 2 shows microscopic pictures of the surfaces of the resulting layers in Nomarski mode with a magnification of 500. All samples show a flat surface with no significant differences.

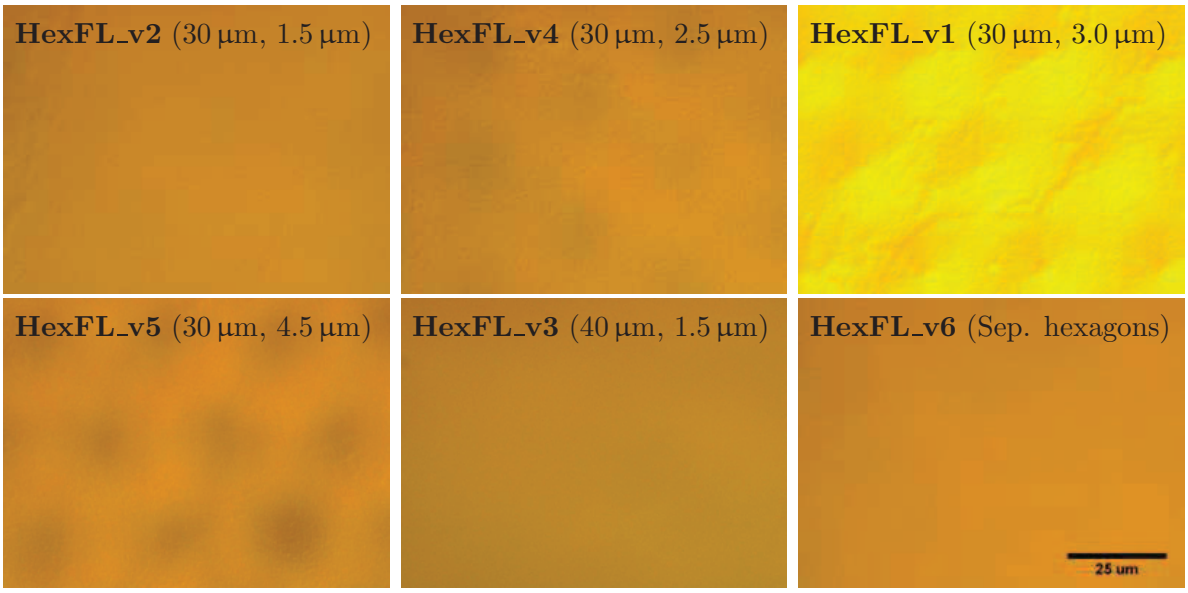

Fig. 2: Layer surface after growing 75 µm of GaN. Pictures from optical Nomarski microscope with a magnification of 500.

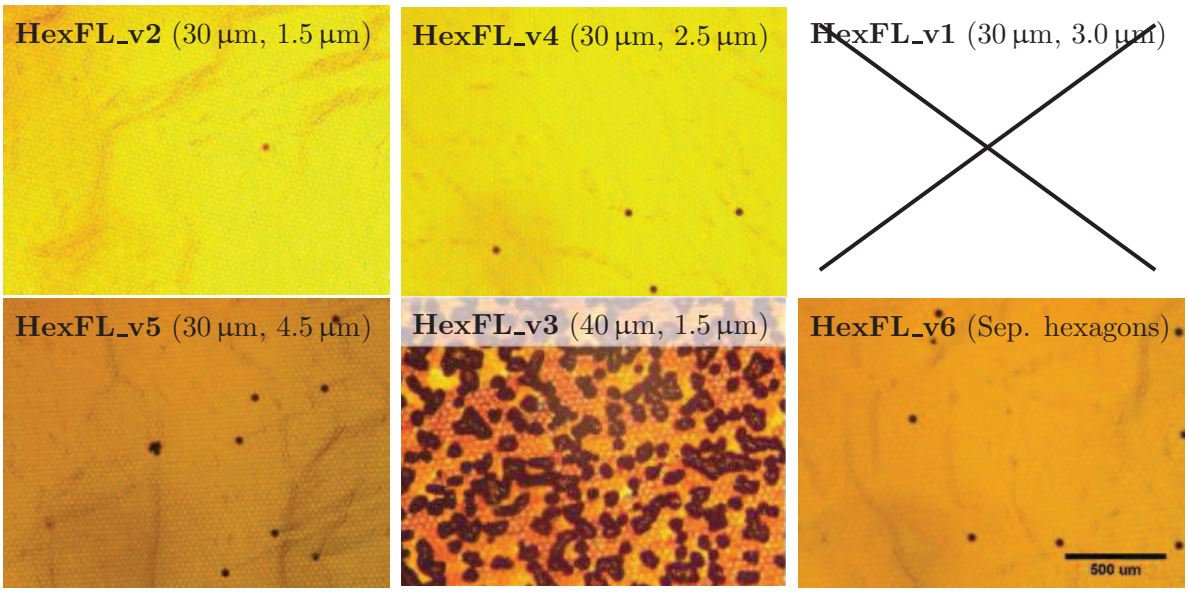

Fig. 3: Layer surface with pits after growing 75 µm of GaN. Pictures from optical Nomarski microscope with a magnification of 25. No such image has been made from mask HexFL_v1.

At a lower magnification of 25 some pits are visible on every sample as seen in Fig. 3. These result from defects in the mask or in lithographic structuring. For structure HexFL_v3 we experience a bad coalescence. Obviously, the mask coverage was too large. On the other hand, the sizes of the mask trenches seem not to affect the mask overgrowth. We noticed that the density of such defects increases with the distance from the wafer center, regardless of the mask pattern.

3.2 Self separation

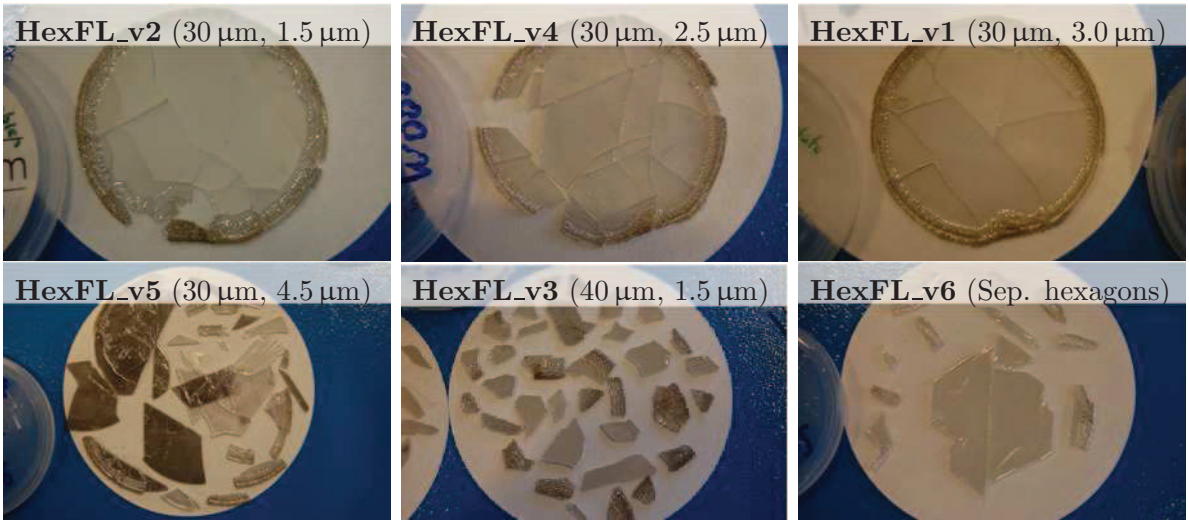

Fig. 4: Photographs of the final, separated layers. Freestanding GaN with about 1 mm thickness.

After these midgrowth investigations, we did a second HVPE overgrowth of these templates to achieve a total layer thickness of 1 mm. Photographs of the resulting layers are shown in Fig. 4. No separation took place at the intended position for mask design HexFL_v6. With the separation layer not working, forces are still too strong for the toplayer to be stable during cooldown. This results in separation of pieces by cracks in the toplayer. The same behaviour holds true for the HexFL_v5 mask with 4.5 µm trenches. In case of the separated hexagons, the assumption is that when separation starts at one place of the weak layer it stops before reaching the next weak spot. With the 4.5 µm trenches the bond between template and layer generally seems to be too strong for separation at this position.

The other extreme can be found in pattern HexFL_v3. With trenches of only 1.5 µm and a large period of 40 µm, the connection between template and layer is too weak. So separation begins at different places at the same time leading to big strain inhomogenieties in the layer. As a result, the freestanding top layer bursts into tiny pieces during separation. By using a mask coverage lying between those values the separation process seems to be fairly stable. This results in the separation of big chunks, which can include the whole wafer diameter and consist of up to one third of the total top layer surface.

3.3 SiN thickness variation

In addition to investigating different mask patterns we tried to vary the thickness of our structured SiN layer. Whereas our standard process is based on a SiN thickness of 200 nm, we fabricated samples with a SiN thickness of 400 nm and 800 nm for this study. Figure 5 shows microscopic pictures of the surface of the fully processed templates. The structure with 400 nm SiN layer has a perfectly developed MOVPE GaN layer with almost no

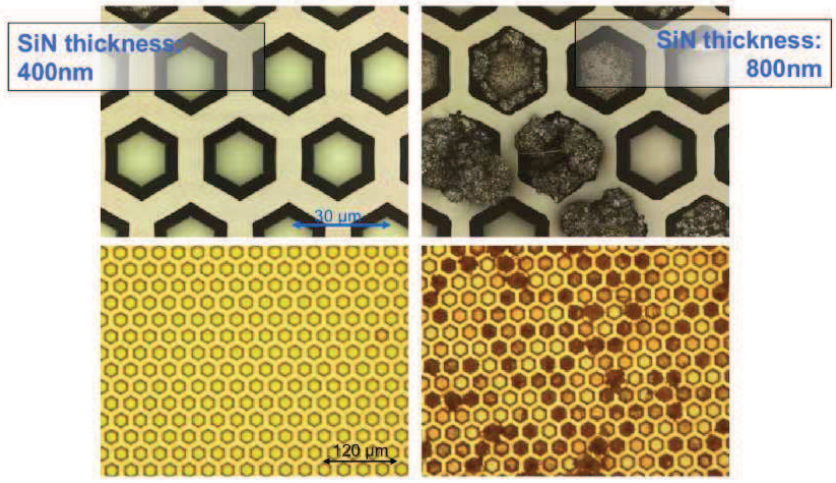

Fig. 5: Microscopic images of structured and overgrown SiN with 400 nm and 800 nm SiN layer thickness.

mask defects. In contrast some GaSi alloy developed on the 800 nm mask during MOVPE growth. With these alloys residing on the mask this template is not suitable for HVPE growth.

When overgrowing the 400 nm mask, we also faced severe problems. The resulting layer showed many pits and although the mask pattern works well with a 200 nm SiN layer this new sample didn't show proper separation. The reason for this behaviour hasn't been found yet.

3.4 Layer quality

For determining the quality of our layers we conducted several measurements on the resulting freestanding samples. In Fig. 6 the results of a full sample x-ray diffraction (XRD) map of the (002)-reflection is shown. The diagonal of the shown piece is spanning the whole wafer diameter. Thus the resulting values for the (002) full width at half maximum (FWHM) seem to be extremely low and homogenous over the whole wafer. We also achieved comparatively low bow values in the range of 160 km^{-1}. These values seem to depend on the size of the investigated piece, so further studies on this subject have to be done in the future. Comparing the various mask patterns no significant differences could be found in XRD measurements. All samples show extremely good layer quality.

PL investigations also indicate an excellent material quality as seen in Fig. 7. Many sharp peaks can be distinguished. Among these the Si and O donor bound exciton transition could be identified with very extremely narrow linewidths in the range of 500 µeV. Samples grown on different masks show comparable spectra.

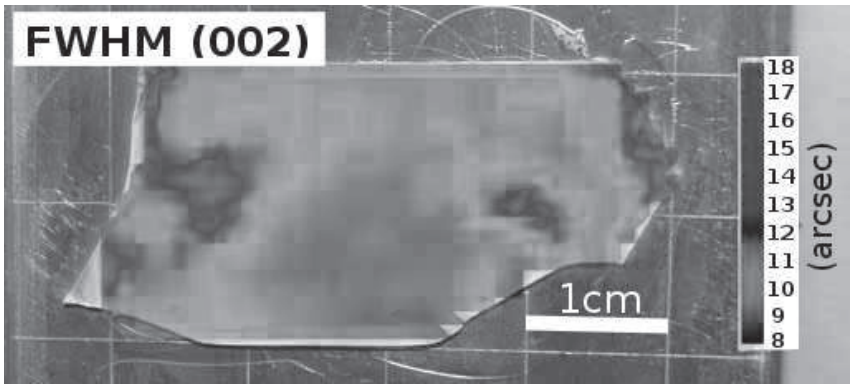

Fig. 6: XRD quality map of a big freestanding sample.

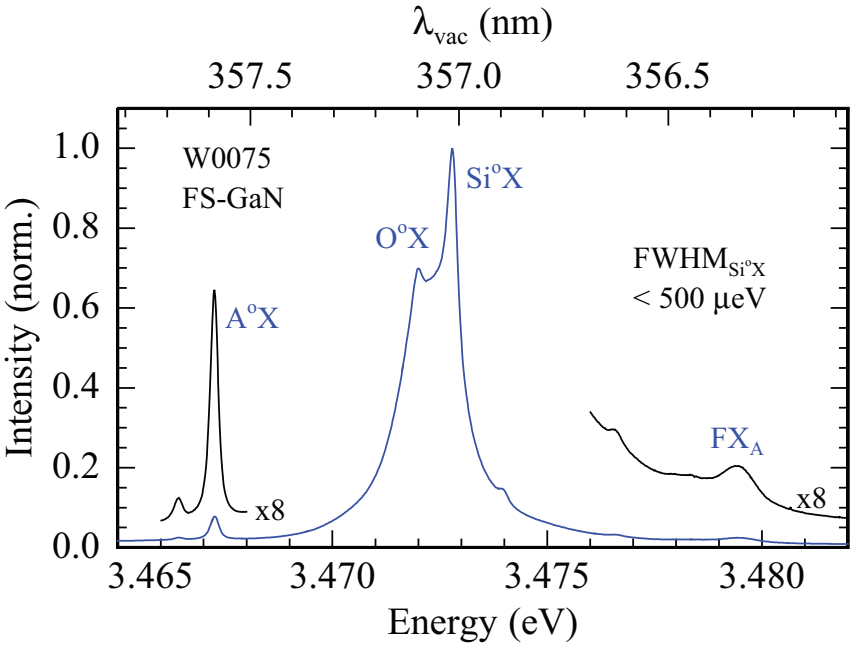

Fig. 7: Low temperature bandedge PL of a freestanding sample.

An etch pit density (EPD) investigation carried out on a sample piece, previously etched by molten KOH, shows a value of $5.5 \cdot 10^5\,\mathrm{cm}^{-2}$ which confirms the outstanding layer quality.

4. Conclusion

Several new mask patterns for self separation processes during cooldown in HVPE have been tested and the geometrical limits of these patterns for a successful self separation have been found. Within fairly large boundaries, the different masks did not lead to significantly different results. It could also be shown that a thicker dielectric layer is ineffective for the self separation process. Finally the homogenous and excellent quality of thick HVPE GaN layers has been proven.

5. Acknowledgements

The good cooperation with F. Lipski in all aspects of this work is gratefully acknowledged. We would also like to thank I. Argut for the technical support in preparing our templates and B. Neuschl from the Institute of Quantum Matter for carrying out PL investigations. This work was financially supported by Freiberger Compound Materials GmbH, Freiberg.

References

[1] T. Hashimoto, E. Letts, M. Ikari, and Y. Nojima, "Improvement of crystal quality in ammonothermal growth of bulk GaN", *J. Cryst. Growth*, vol. 312, pp. 2503–2506, 2009.

[2] R. Dwilinski, R. Doradzinski, J. Garczynski, L. Sierzputowski, R. Kucharski, M. Zajac, M. Rudzinski, R. Kudrawiec, J. Serafinczuk, and W. Strupinski, "Recent achievements in AMMONO-bulk method", *J. Cryst. Growth*, vol. 312, pp. 2499–2502, 2009.

[3] C. R. Miskys, M. K. Kelly, O. Ambacher, and M. Stutzmann, "Freestanding GaN substrates and devices", *phys. stat. sol. (c)*, vol. 0, pp. 1627–1650, 2003.

[4] S. Nakamura, M. Senoh, S. Nagahama, N. Iwasa, T. Yamada, T. Matsushita, H. Kiyoku, Y. Sugimoto, T. Kozaki, H. Umemoto, M. Sano, and K. Chocho, "InGaN/GaN/AlGaN-based laser diodes with cleaved facets grown on GaN substrates", *Appl. Phys. Lett.*, vol. 73, pp. 832–834, 1998.

[5] K. Motoki, T. Okahisa, N. Matsumoto, M. Matsushima, H. Kimura, H. Kasai, K. Takemoto, K. Uematsu, T. Hirano, M. Nakayama, S. Nakahata, M. Ueno, D. Hara, Y. Kumagai, A. Koukitu, and H. Seki, "Preparation of large freestanding GaN substrates by hydride vapor phase epitaxy using GaAs as a starting substrate", *Jpn. J. Appl. Phys.*, vol. 40, pp. L140–L143, 2001.

[6] F. Lipski, S. B. Thapa, J. Hertkorn, T. Wunderer, S. Schwaiger, F. Scholz, M. Feneberg, M. Wiedenmann, K. Thonke, H. Hochmuth, M. Lorenz, and M. Grundmann, "Studies towards freestanding GaN in hydride vapor phase epitaxy by in-situ etching of a sacrificial ZnO buffer layer", *phys. stat. sol. (c)*, vol. 6, pp. 352–355, 2009.

[7] F. Lipski, T. Wunderer, S. Schwaiger, and F. Scholz "Fabrication of freestanding 2"-GaN wafers by hydride vapour phase epitaxy and self-separation during cooldown", *phys. stat. sol. (a)*, vol. 207, pp. 1287–1291, 2010.

Semi-insulating GaN by Fe-Doping in Hydride Vapor Phase Epitaxy Using a Solid Iron Source

Frank Lipski

Using a solid iron source, Fe-doping during GaN growth by hydride vapor phase epitaxy (HVPE) on sapphire was realized. The doping concentration could be controlled by varying the gas flow over the iron source and was verified by secondary ion mass spectrometry (SIMS). After removal of the sapphire substrate, semi-insulating freestanding (FS) GaN of high quality was achieved, with a resistivity of up to $4 \cdot 10^8\,\Omega cm$ *at room temperature. For Fe-doped samples on sapphire, a partial release of the high, compressive strain at room temperature has been observed. The measurement of the full-width-half-maximum (FWHM) of high resolution X-ray (HRXRD) rocking curves was hampered by the serious wafer bow for both GaN on sapphire and freestanding GaN. Nevertheless, we observed values for FS-GaN as low as* $40\,arcsec$ *and* $80\,arcsec$ *for the (002) and (102)-reflection, respectively.*

1. Introduction

In the past few years, tremendous progress in the fabrication of freestanding GaN substrates of 2" diameter has been achieved [1]. The mass production of GaN substrates is starting up. Laser diodes (LD) are nowadays commonly grown on freestanding GaN, showing far better performance compared to LDs on foreign substrates [2]. Commercially available GaN substrates are produced by hydride vapor phase epitaxy (HVPE) on foreign substrates like sapphire and separated therof after growth. Currently, HVPE offers the best compromise of crystal quality, growth speed, investment, running costs and flexibility. Other favorite growth techniques for GaN substrates like high pressure growth [3], ammonothermal growth [4] and the Na-flux [5] method mainly suffer from far slower growth rates resulting in a time consuming development process and require high investment for upscaling to mass production.

However, nominally undoped high quality material obtained by HVPE generally shows a fairly high n-type conductivity due to background impurities, such as Si and O, which are unavoidable with the standard HVPE process [6]. While this is acceptable and even preferable for optoelectronic applications like LDs and LEDs with backside contacts, it is not suitable for GaN based electronics, where a degradation of the device performance due to parasitic capacitance or current leakage is noticeable. However, due to its potential use for high-power, high-frequency and high-temperature applications, there is a strong increase in the research on GaN based electronics, such as AlGaN/GaN high electron mobility transistors. These activites are accompanied by an emerging demand for semi-insulating (SI) GaN wafers.

Although there is no way to completely prevent Si and O impurities in HVPE, semi-insulating GaN can still be achieved by additional doping of electron trapping centers. It has been shown that transition metals like Cr and Fe act as a deep acceptor in GaN and can be used to compensate the background donors [7, 8].

For metal organic vapor phase epitaxy (MOVPE) ferrocene is used as Fe source typically. This metal organic precursor is not suited for use in HVPE, because ferrocene decomposes too early in hot wall reactors typically used in HVPE systems. For the investigations of this work, we have chosen solid iron as source which can be used similarly to the Ga source, creating the $FeCl_2$ precursor inside the reactor chamber by an HCl-stream over elemental iron. We investigated the efficiency and controllability of such a kind of source as well as the crystal quality and electrical properties of the resulting Fe-doped GaN.

2. Experimental

The HVPE growth was performed in a commercial Aixtron single-wafer HVPE system with a horizontal quartz-tube, heated in a furnance with five zones. A 1:1 mixture of nitrogen and hydrogen was used as carrier gas, as it showed to minimize cracking [10]. Ammonia was applied as nitrogen precursor, while GaCl was used as precursor for the group-III element. It was formed inside the reactor by streaming HCl gas over a liquid Ga source heated to 850° C and injected directly above the substrate. In our system, two identical channels of this type are available and the second one was filled with a solid iron wire with a purity of 99.99% and a diameter of 1 mm. The HCl-flow in these two channels can be adjusted independently. With an additional dilution setup, the HCl-flow in the Fe channel could be diluted down to $1 \cdot 10^{-3}$ sccm. In all experiments, the substrate temperature during growth was kept constant at 1050° C and the pressure of the reactor at 900 hPa.

The doping concentration was measured by secondary ion mass spectrometry (SIMS). Resistivity- and Hall-measurements were performed at room temperature with Van-der-Pauw geometry. The crystal quality and strain situation was analyzed by high resolution X-ray diffraction (HRXRD) and low temperature photoluminescence (PL) at 10 K.

For the HVPE growth, we used GaN templates on (0001) sapphire substrates with a slight misorientation towards the a-plane. These templates were grown with an Aixtron 200/4 RF-S system. First an oxygen doped AlN nucleation layer was deposited at a temperature of 900° C and afterwards covered with a GaN-layer of about 2.5 µm. For defect reduction and strain relaxation a very thin SiN-interlayer was deposited during the MOVPE process [9]. This interlayer was deposited after a GaN layer of 300 nm and overgrown with another 2.2 µm GaN. The SiN itself is less than one monolayer and leads to templates with strong compressive strain allowing crack-free growth of comparably thick HVPE layers on sapphire.

For the fabrication of freestanding GaN layers, the templates have been processed further prior to the HVPE growth. We were using a self-separation process, which takes place during cool-down from the growth temperature due to strong thermal forces, caused by the different thermal expansion coefficients of GaN and sapphire. To facilitate the separation, a predetermined breaking point is defined. We found that a dielectric mask of

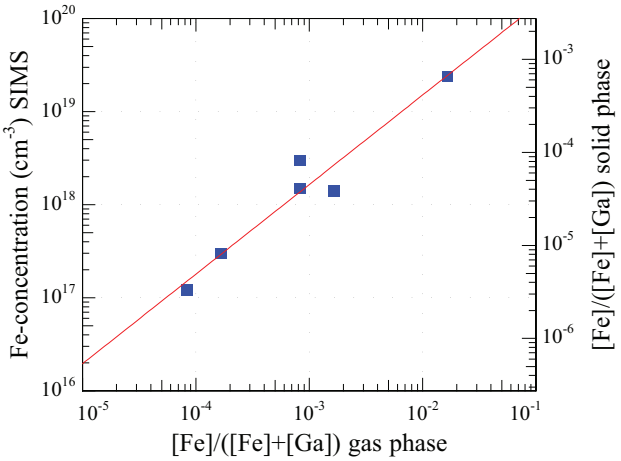

Fig. 1: Doping concentration measured by SIMS dependent on the concentration of Fe in the gas phase.

SiN dissolves during the HVPE process, leading to cavities in the GaN buffer below and finally to a defined separation. The SiN mask with a thickness of 200 nm was deposited by plasma enhanced vapor deposition (PECVD) on top of the templates described above. Afterwards, the mask was structured with a hexagonally shaped pattern by optical lithography and dry etching. Finally, a second MOVPE growth step was carried out before the templates were transfered to HVPE. Details of the separation process and its mask design can be found elsewhere [12].

3. Results and Discussion

The formation of $FeCl_2$ by a HCl gas flow over solid iron is very efficient. In a first experiment we changed the amount of solid iron inside the reactor and measured the Fe-concentration in the grown samples by SIMS. Starting with some mm length, the measured Fe-concentration in the GaN samples increased with increasing wire length, but saturated when we reached several cm length. A further increase of the wire did not lead to a higher doping level. Consequently, we assume a total conversion of all HCl-molecules to $FeCl_2$ for some cm length of the iron wire. For the GaCl-formation we assume a total conversion of all HCl-molecules of the 30 sccm-flow too, which allows to calculate the ratio of GaCl and $FeCl_2$ in the gas phase. Based on this calculation, we found, that the incorporation of Fe-atoms into the crystal is not as efficient as it is for Ga-atoms. In Fig. 1 the compositions in gas phase and in solid phase are given. Nevertheless, in first experiments, the Fe concentration exceeded the values needed for compensation of background donors by several magnitudes. To realize the desired low Fe-concentrations, a dilution setup for the used HCl was required, enabling an improved control of the doping level. Moreover a reactor contamination by too much $FeCl_2$ is avoided which could otherwise lead to background doping with Fe in later growth runs [13].

3.1 Strain situation

When growing Fe-doped samples with HVPE, we noticed an increased cracking tendency for comparably thin layers of 30 µm. A similar situation has been observed during our

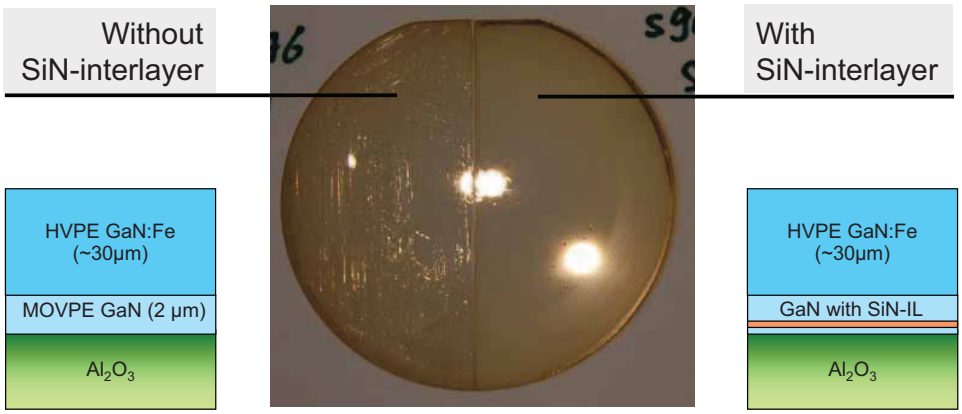

Fig. 2: 30 µm thick Fe-doped GaN by HVPE. Two different templates of half a 2" wafer have been overgrown in the same HVPE run: the left one without SiN-interlayer, the right one with included SiN-layer.

studies on Si-doping by HVPE [14]. In that case, the introduction of a SiN monolayer during the template growth, typically applied for defect reduction, improved the situation dramatically and successfully helped to avoid cracking. The SiN interlayer leads to a higher compressive strain for GaN on sapphire at room temperature and consequently to a less tensile strain at growth temperature. Applying this technique in the case of Fe-doping the same effect was visible. A photograph of the results after an HVPE growth run of a 30 µm thick GaN layer with a doping concentration of approx. $1 \cdot 10^{19}\,\mathrm{cm}^{-3}$ is shown in Fig. 2. In this experiment, we used two different half wafers as a template, one with and one without the SiN interlayer described above. The sample with the SiN-interlayer shows a nice crack-free surface morphology, whereas the other shows many cracks already visible with bare eye.

A strain investigation by HRXRD for these samples is complicated due to the serious curvature, leading to big error bars for the lattice constants. Nevertheless, a tendency to a reduced compressive strain with increased Fe concentration is visible (Fig. 3). Further-

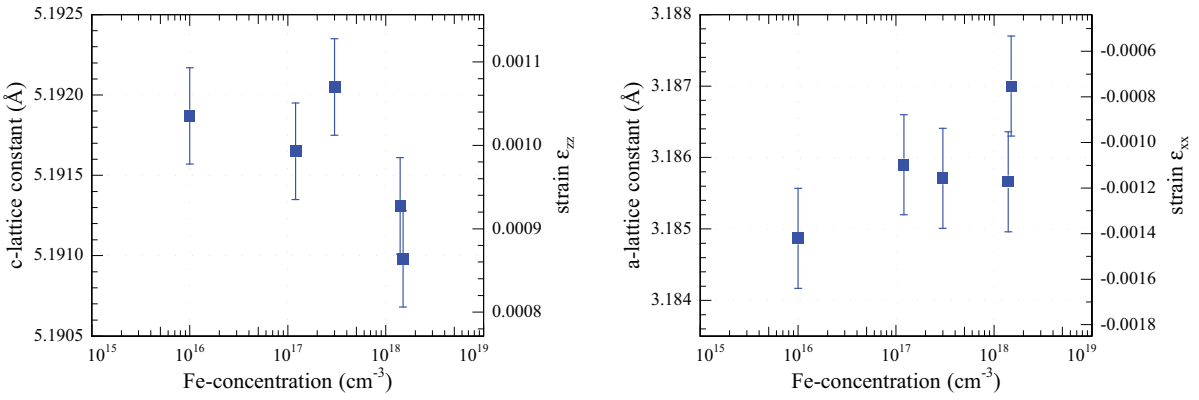

Fig. 3: Lattice constants determined by HRXRD-measuerments according to [16]. The strong bow leads to big error bars, nevertheless a reduced compressive strain for higher Fe-concentrations is noticable.

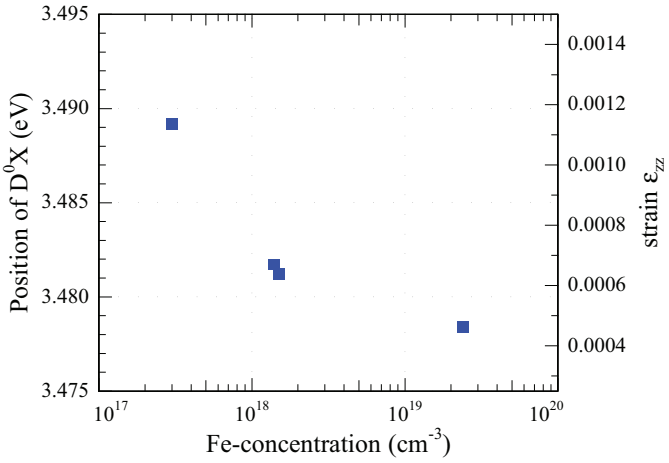

Fig. 4: PL measurements at 10 K of the donor-bound-exciton D^0X provide accurate strain data.

more, we determined the strain more accurately by PL measurements of the position of the donor-bound-exciton D^0X line (fig. 4). Unfortunately, the intensity of the D^0X peak decreases with higher Fe-concentration and can even vanish totally, making the analysis difficult in this case. The strain values in the diagram have been calculated by solving the Hamilton operator according to [15]. The same tendency is clearly observable.

3.2 Crystal quality

At low doping concentrations, the surface morphology did not significantly change compared to undoped samples. Further increase of the Fe concentration lead to a degradation of the surface morphology starting from about $1 \cdot 10^{19}\,\mathrm{cm}^{-3}$ (Fig. 5). Buried and overgrown cracks are visible at a doping concentration of $1 \cdot 10^{20}\,\mathrm{cm}^{-3}$.

An analysis of the crystal quality by HRXRD rocking curve measurements is hampered by the strong bow of the samples. The curvature of samples can lead to a broadening of measured FWHM similar to crystal imperfections like dislocations [17,18]. To distinguish between the different contributions to the broadening, a reduced beam size is required. Unfortunately, the X-ray system used for the measurements did not allow this reduction sufficiently.

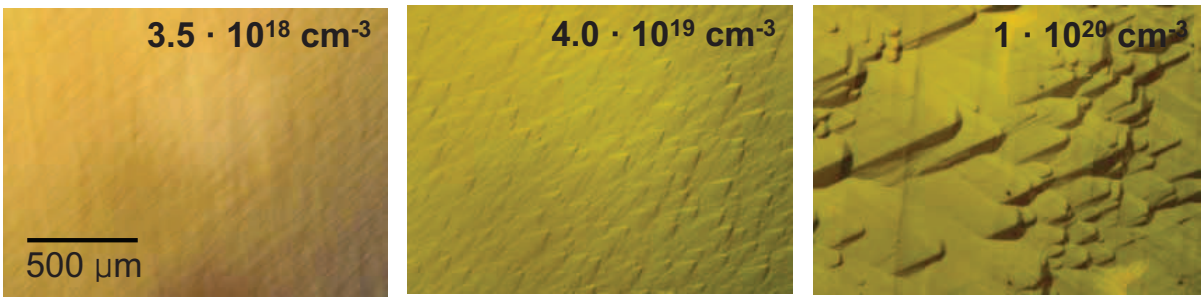

Fig. 5: Surfaces of differently doped samples from optical microscope in Nomarski contrast. For very high Fe concentrations, a degradation of the surface morphology is visible. On the sample with a Fe-concentration of more than $1 \cdot 10^{20}\,\mathrm{cm}^{-3}$, even some overgrown cracks are visible.

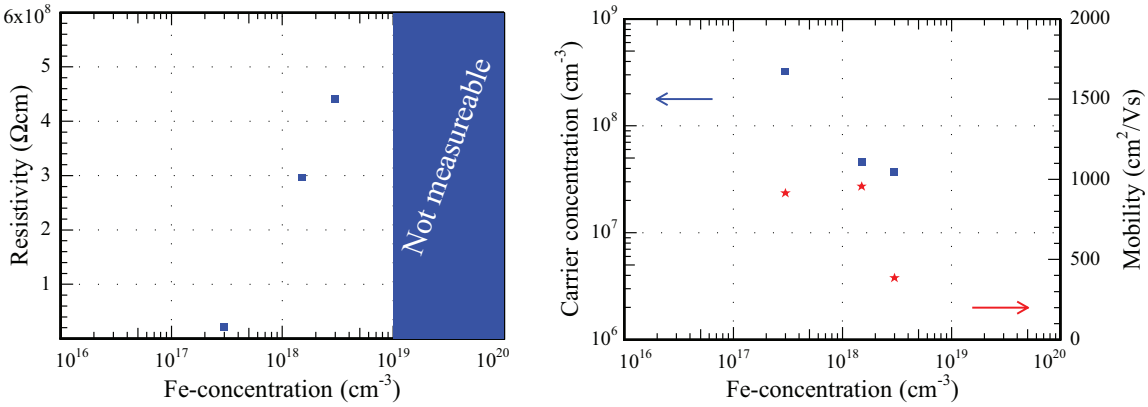

Fig. 6: Resistivity, carrier concentration and mobility of freestanding GaN dependent on the Fe-concentration, determined by RT-Hall measurements.

3.3 Electrical characterization

Resistivity measurements of the GaN samples on sapphire showed very low values due to a conductive layer at the interface to the sapphire by the O-doped AlN-nucleation as well as due to the included SiN-interlayer, acting as a kind of delta-doping. For accurate determination of the electrical properties of the HVPE GaN, the conductive layers must be removed. Therefore we have grown thick freestanding samples with a thickness of about 600 µm. A controlled self-separation during cool-down can be achieved by including an additional SiN-interlayer [12]. In order to remove leftovers from the separation layer, the backsides of the freestanding samples have been mechanicaly polished. We could achieve resistivity values above $4 \cdot 10^8\,\Omega$cm with a Fe concentration of about $3 \cdot 10^{18}\,\mathrm{cm}^{-3}$ after the removal of about 100 µm [19]. Samples with even higher Fe concentration could not be measured with the used setup. In Fig. 6, resistivity values as well as resulting carrier concentrations and mobility values dependent on the doping concentration are shown.

4. Conclusion

Solid iron as source for Fe-doping in HVPE has been investigated. It is a simple and well controllable method for realizing SI-GaN by HVPE. To achieve the required doping concentrations, a dilution setup for the HCl stream is necessary. A degradation of the crystal quality due to the Fe doping was not observed for Fe-concentrations in the range of $10^{18}\,\mathrm{cm}^{-3}$, which is approximately necessary for the compensation of background donors. Freestanding highly resistive GaN substrates with values up to $4 \cdot 10^8\,\Omega$cm and above could be fabricated.

Acknowledgement

I like to thank E. Richter of the Ferdinand-Braun-Institut für Höchstfrequenztechnik in Berlin for Hall-measurements and L. Kirste of the Fraunhofer-Institut für Angewandte Festkörperphysik in Freiburg for SIMS-measurements. Furthermore I want to thank H. Wu and W. Pang for their master theses on this topic.

References

[1] T. Paskova, D.A. Hanser, and K.R. Evans, "GaN substrates for III-nitride devices", *Proc. IEEE*, vol. 98, pp. 1324–1338, 2010.

[2] M. Furitsch, A. Avramescu, C. Eichler, K. Engl, A. Leber, A. Miler, C. Rumbolz, G. Brüderl, U. Strauß, A. Lell, and V. Härle, "Comparison of degradation mechanisms of blue-violet laser diodes grown on SiC and GaN substrates", *phys. stat. sol. (a)*, vol. 203, pp. 1797–1801, 2006.

[3] I. Grzegory, B. Lucznik, M. Bockowski, and S. Porowski, "Crystallization of low dislocation density GaN by high-pressure solution and HVPE methods", *J. Cryst. Growth*, vol. 300, pp. 17–25, 2007.

[4] R. Dwilinski, R. Doradzinski, J. Garczynski, L. Sierzputowski, R. Kucharski, M. Zajac, M. Rudzinski, R. Kudrawiec, J. Serafinczuk, and W. Strupinski, "Recent achievements in AMMONO-bulk method", *J. Cryst. Growth*, vol. 312, pp. 2499–2502, 2010.

[5] H. Yamane, M. Shimada, S.J. Clarke, and F.J. DiSalvo, "Preparation of GaN single crystals using a Na flux", *Chemistry of Materials*, vol. 9, pp. 413–416, 1997.

[6] Ch. Hennig, S. Hagedorn, T. Wernicke, G. Tränkle, M. Weyers, and E. Richter, "GaN substrates by HVPE", *Proc. SPIE*, vol. 6910, pp. 69100I-1–10, 2008.

[7] B. Monemar and O. Lagerstedt, "Properties of VPE-grown GaN doped with Al and some iron-group metals", *J. Appl. Phys.*, vol. 50, pp. 6480–6491, 1979.

[8] S. Heikman, S. Keller, S.P. DenBaars, and U.K. Mishra, "Growth of Fe doped semi-insulating GaN by metalorganic chemical vapor deposition", *Appl. Phys. Lett.*, vol. 81, pp. 439–441, 2002.

[9] J. Hertkorn, F. Lipski, P. Brückner, T. Wunderer, S.B. Thapa, F. Scholz, A. Chuvilin, U. Kaiser, M. Beer, and J. Zweck, "Process optimization for the effective reduction of threading dislocations in MOVPE grown GaN using in situ deposited SiN_x masks", *J. Cryst. Growth*, vol. 310, pp. 4867–4870, 2008.

[10] E. Richter, Ch. Hennig, M. Weyers, F. Habel, J.D. Tsay, W.Y. Liu, P. Brückner, F. Scholz, Yu. Makarov, A. Segal, and J. Kaeppeler, "Reactor and growth process optimization for growth of thick GaN layers on sapphire substrates by HVPE", *J. Cryst. Growth*, vol. 277, pp. 6–12, 2005.

[11] F. Scholz, P. Brückner, F. Habel, M. Peter, and K. Köhler, "Improved GaN layer morphology by hydride vapor phase epitaxy on misoriented Al_2O_3 wafers", *Appl. Phys. Lett.*, vol. 87, pp. 181902-1–3, 2005.

[12] F. Lipski, T. Wunderer, S. Schwaiger, and F. Scholz, "Fabrication of freestanding 2"-GaN wafers by hydride vapour phase epitaxy and self-separation during cooldown", *phys. stat. sol. (a)*, vol. 207, pp. 1287–1291, 2010.

[13] W. Pang, "Investigations on Fe doping of GaN in hydride vapor phase epitaxy", *Master Thesis, Ulm University*, 2009.

[14] F. Lipski, "Si-doped GaN by hydride-vapour-phase-epitaxy using a Ga:Si-solution as doping source", *Annual Report, Institute of Optoelectronics, Ulm University*, pp. 53–58, 2007.

[15] D. Fu, R. Zhang, B. Wang, Z. Zhang, B. Liu, Z. Xie, X. Xiu, H- Lu, Y. Zheng, and G. Edwards, "Modification of the valence band structures of polar and nonpolar plane wurtzite-GaN by anisotropic strain", *J. Appl. Phys.*, vol. 106, pp. 023714-1–8, 2009.

[16] M.A. Moram, and M.E. Vickers "X-ray diffraction of III-nitrides", *Reports on Progress in Physics*, vol. 72, pp. 036502-1–40, 2009.

[17] M.A. Moram and M.E. Vickers and M.J. Kappers and C.J. Humphreys, "The effect of wafer curvature on x-ray rocking curves from gallium nitride films", *J. Appl. Phys.*, vol. 103, pp. 093528-1–6, 2008.

[18] J.E. Ayers, "The measurement of threading dislocation densities in semiconductor crystals by X-ray diffraction", *J. Cryst. Growth*, vol. 135, pp. 71–77, 1994.

[19] H. Wu, "Fabrication of Intentionally Doped Freestanding GaN layers by Hydride Vapor Phase Epitaxy", *Master Thesis, Ulm University*, 2010.

Heteroepitaxial Growth of Planar Semipolar ($10\bar{1}1$) GaN by Metalorganic Vapor Phase Epitaxy

Stephan Schwaiger

We report on the growth of planar semipolar ($10\bar{1}1$) *GaN on* ($11\bar{2}3$) *pre-patterned sapphire. This method allows the growth of semipolar oriented* ($10\bar{1}1$) *GaN on large scale. By x-ray diffaction, only the peaks of the desired* ($10\bar{1}1$) *plane could be observed. The in-plane orientations could be determined as* $[0001]_{GaN} \parallel [0001]_{sapphire}$ *and* $[11\bar{2}0]_{GaN} \parallel [10\bar{1}0]_{sapphire}$. *Scanning electron microscopy, transmission electron microscopy and atomic force microscopy measurements show coalesced surfaces with root mean square roughness values below 2 nm (10 µm×10 µm). Further investigations using photoluminescence spectroscopy show spectra that are dominated by the near band edge emission. The high crystal quality is confirmed by small full width at half maximum values of x-ray rocking curve measurements of less than 400 arcsec.*

1. Introduction

Devices like light emitting diodes (LEDs) based on GaN are usually grown in c-direction. Due to induced biaxial strain and the lattice geometry of group-III nitrides, huge piezoelectric fields are present within heterostructures along this particular direction. The resulting band bending causes some undesirable effects on the quantum wells (QWs) grown in that direction [1], like spatial separation of the wave functions of electrons and holes. Consequently, the recombination probability (recombination rate) of electrons and holes is reduced, the emission wavelength is redshifted and dependent on the drive current due to screening [2]. This is known as quantum confined Stark effect (QCSE).

One possibility to reduce these negative effects is to grow in semipolar or nonpolar direction. Due to the lack of real bulk GaN substrates, nowadays these structures have to be grown on foreign substrates and therefore the research is still focussed on the growth on different templates. Nonpolar GaN can be grown on several different foreign substrates but still suffers from a huge amount of stacking faults [3–5]. Various semipolar orientations of GaN have been also investigated on different substrates, like ($10\bar{1}1$) GaN on silicon [6], $MgAl_2O_4$ [7], or as facets grown on c-plane sapphire [8]. ($11\bar{2}2$) GaN has been grown on m-plane sapphire [9] or on facets of c-plane oriented GaN stripes [10]. Just recently Okada et al. presented a method to grow ($11\bar{2}2$) GaN on r-plane sapphire [11]. Another possible approach is to use sliced pieces from hydride vapor phase epitaxial (HVPE) grown material [12, 13], but these templates are quite expensive and very limited in size. Up to now the perfect substrate is still missing and therefore there is a lot of research in this field at the moment.

From this background, in this study, we propose the planar growth of semipolar $(10\bar{1}1)$ oriented GaN directly on pre-patterned sapphire (Fig. 1) in a similar approach as Hikosaka et al. or Okada et al. [6, 11]. For this purpose the use of $(11\bar{2}3)$ sapphire seems to be

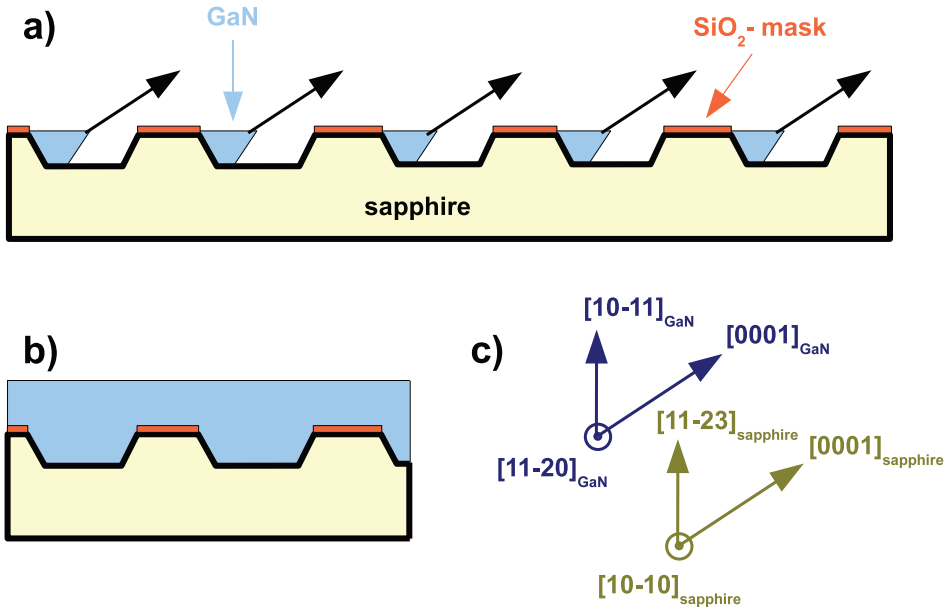

Fig. 1: Schematic figure of the basic idea. a) Grooves are etched into $(11\bar{2}3)$ sapphire, the growth starts at the sidewalls in c-direction. b) The GaN islands coalesce, resulting in a planar semipolar $(10\bar{1}1)$ GaN layer. c) The crystal orientations of the sapphire and the semipolar GaN.

appropriate as the inclination angle between $(0001)_{Al_2O_3}$ and $(11\bar{2}3)_{Al_2O_3}$ is nearly the same like the angle between $(0001)_{GaN}$ and $(10\bar{1}1)_{GaN}$. Calculations show that the piezoelectric fields within QWs grown in that direction will be drastically reduced when compared to c-plane growth [14]. Additionally, this surface is regarded as naturally stable facet since it exhibits an automatically formed and very smooth surface [15]. A higher indium incorporation efficiency is also observed, which can be advantageous for longer wavelength light emitters [16].

2. Experimental

As starting substrate n-oriented sapphire was used. The $(11\bar{2}3)$-surface was lithographically structured with grooves along the in-plane m-direction. Therefore we deposited a 200 nm silicon dioxide (SiO_2) mask via plasma-enhanced chemical vapor deposition which also acts as a mask for the selective area growth (SAG). A 550 nm thick mask of nickel and gold, structured with a (3 µm opening) x (3 µm mask) stripe pattern was used for dry etching of the sapphire via reactive ion etching (RIE). After removal of the remaining mask material, the sapphire exhibits approximately 1.2 µm deep grooves, each with one smooth c-plane-like side facet. The subsequent growth was carried out in a commercial horizontal flow Aixtron-200/4 RF-S HT reactor with the standard precursors trimethylgallium (TMGa), trimethylaluminum (TMAl) and high purity ammonia (NH_3). Pd diffused

hydrogen was used as carrier gas. The process temperature was controlled by a pyrometer at the backside of the rotation tray. To start growth we used an oxygen doped low temperature AlN nucleation layer [17,18], followed by approximately 1 µm GaN with a V/III ratio of 650 at a temperature of 1130°C and a pressure of 150 hPa, resulting in stripes of semipolar GaN. Simply elongating the growth time leads to coalesced layers. The growth rate was roughly 2.2 µm/h (on closed layers).

To characterize the samples and their crystal quality we used x-ray diffraction (XRD) rocking curve measurements (XRC) and ω-2θ scans as well as low temperature (14 K) photoluminescence (PL) measurements. Particularly, the latter enables to judge about typical defects in semi- and nonpolar GaN layers, like basal plane stacking faults (BSFs) [19]. The Surface quality could be accessed via scanning electron microscopy (SEM), transmission electron microscopy (TEM), optical phase contrast microscopy (OM) and atomic force microscopy (AFM).

3. Results and Discussion

Figure 1 shows the growth principle. The GaN growth starts from the groove facets of the sapphire wafer in the usual c-direction, which has a certain inclination to the surface (Fig. 1 a) resulting in a flat and planar semipolar layer (Fig. 1 b). The crystal orientation was measured via a symmetrical XRD ω-2θ-scan (Fig. 2). The sapphire substrate peaks

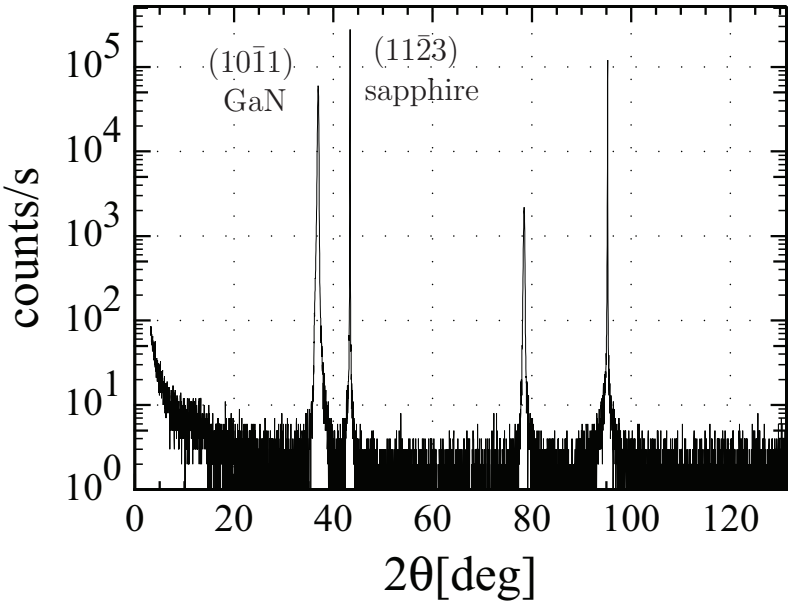

Fig. 2: XRD ω-2θ scan showing the peaks of ($11\bar{2}3$) sapphire and ($10\bar{1}1$) GaN (plus second order peaks). No other peak owing to another orientation of GaN is visible.

and the ($10\bar{1}1$)-reflection of GaN are clearly visible; no other crystal orientation could be observed. Additionally, the skew geometric (0002) peak of GaN and the (0006) reflection of sapphire appear at the same φ-angle (rotation around the surface normal) and at the

expected χ-angle (rotation around the cut of the surface with the scattering plane)[not shown]. Therefore we conclude an orientation of the GaN film as sketched in Fig. 1 with a semipolar $(10\bar{1}1)$ surface. The in-plane orientations were investigated by selected area electron diffraction of cross-section samples and were found to be $[0001]_{\mathrm{GaN}} \parallel [0001]_{\mathrm{sapphire}}$ and $[11\bar{2}0]_{\mathrm{GaN}} \parallel [10\bar{1}0]_{\mathrm{sapphire}}$.

The SEM micrograph (Fig. 3) reveals the morphology of the samples. The GaN starts to

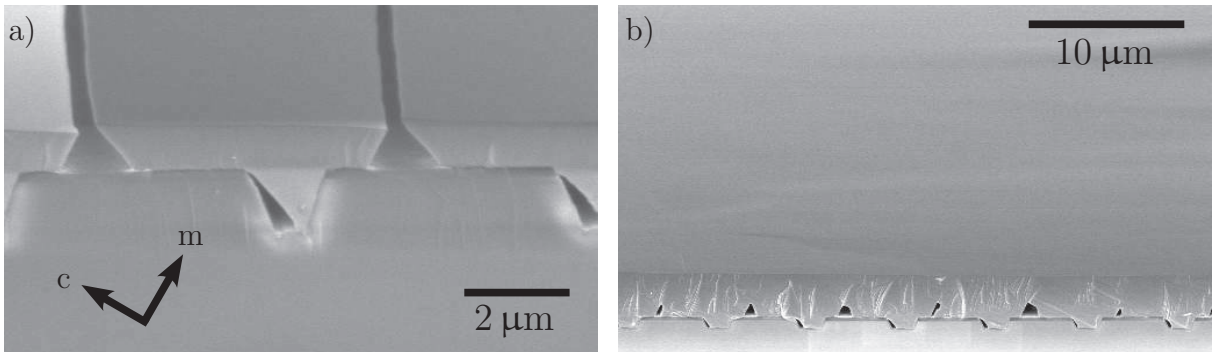

Fig. 3: a) SEM micrograph of the cross-section of an uncoalesced sample. The crystal orientations are the same as sketched in fig 1c). b) Coalesced layer with flat surface.

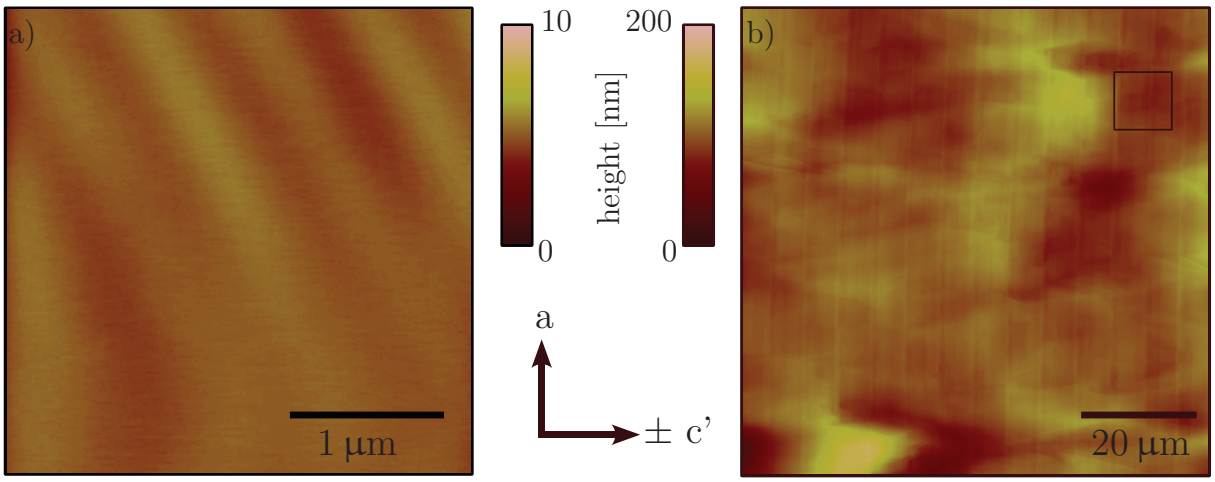

Fig. 4: Surface morphology of $(10\bar{1}1)$-oriented stripes (a) and of an coalesced layer (b). The root mean square roughness (rms) values have measured to approx. 0,2 nm (a, 3 µm × 3 µm measurement) and to approx. 15 nm (b, 80 µm × 80 µm measurement). A 10 µm × 10 µm area from b) results in 1 nm.

grow within the grooves of the prepared sapphire substrate. As proposed, this happens only on the c-plane like side-facet of the trench, resulting in growth directed exclusively in c-directon. Although a complete nucleation layer was deposited, no growth took place on the SiO_2 covered ridges. This area could be overgrown comparable to the well known epitaxial lateral overgrowth (ELOG) principle when the GaN reaches the height of the

trenches and is able to grow more in lateral direction. The wings in the two different directions show different behavior. The so called "+c"-wing growing directly in "+c"-direction exhibits a semipolar (10$\bar{1}$1) facet, whereas the slower grown "-c"-wing is terminated by a "-c"-facet. The wing tilt of the overgrown area is about 0.2° ("+c"-wing), as visible in XRD measurements.

By elongating the growth time coalescence of the stripes could be achieved. We assume that this takes place similar as for other orientations [20]: The fast developing "+c"-wing buries the "-c"-wing and leads to planar and flat surfaces. The excellent surface quality was confirmed by AFM and TEM measurements (Fig. 4). The root mean square roughness determined by AFM was as small as 0.1 nm for a 1 µm×1 µm-scan and below 0.3 nm for a 3 µm×3 µm-scan, respectively. An atomically flat surface was found by HR-TEM investigations [21].

The high crystal quality was verified by narrow XRC peaks. The full width at half maximum (FWHM) of both, the symmetrical (10$\bar{1}$1) reflection and the asymmetrical (0002) and (10$\bar{1}$2) reflections were smaller than 400 arcsec, respectively. Furthermore, the low-temperature PL-spectra (Fig. 5) revealed a comparably strong and dominating near band edge emission (NBE) at 3.464 eV (slightly strained) for the stripes and at 3.471 eV (nearly unstrained) for the coalesced sample. Typically, in semi- and nonpolar GaN

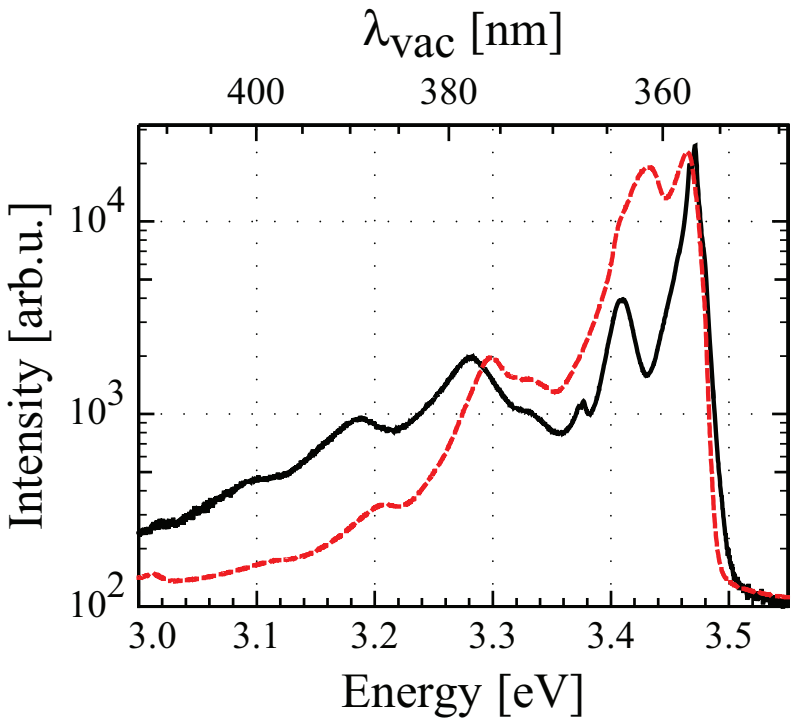

Fig. 5: Photoluminescence spectra recorded at low temperature (15 K) for uncoalesced (dashed) and coalesced (solid line) samples. Visible are the NBE as dominant peak (3.464 eV for stripes, 3.471 eV for the coalesced sample) and some defect related emission lines (e.g. 3.430 eV or 3.300 eV).

grown on unpatterned sapphire this luminescence is quite weak and the defect correlated

luminescence is dominating. Nevertheless some of the typical defect related peaks are also visible in our samples. The transition around 3.41 eV, which can be attributed to basal plane stacking faults [22], could not be suppressed completely. Also, the lower energy peaks (around 3.30 eV), usually assigned to (pyramidal) stacking faults (and partial dislocations) [23] are still visible. The local distribution of stacking faults was investigated by transmission electron microscopy (Fig. 6). The highest density of stacking faults can

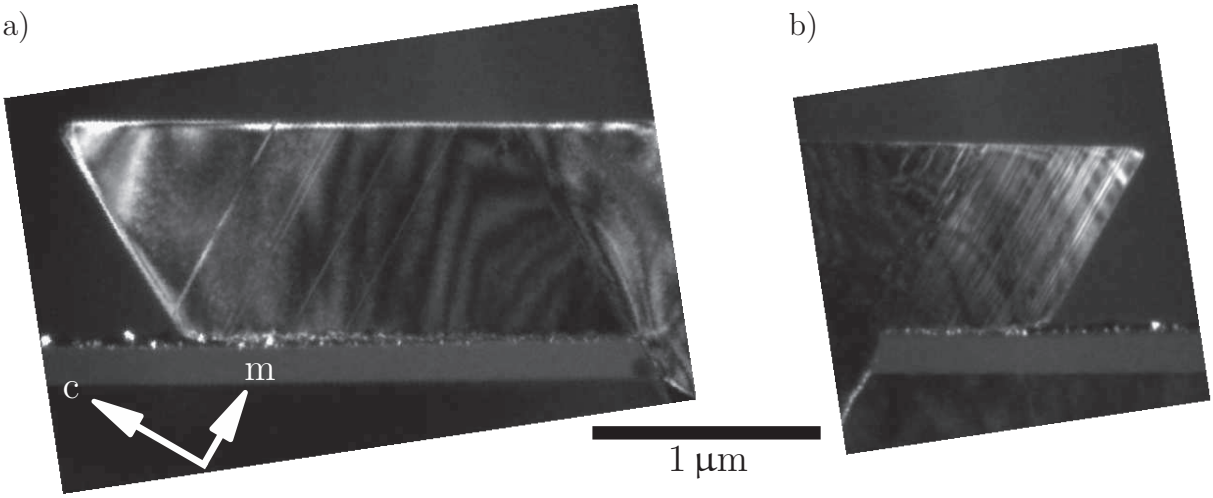

Fig. 6: TEM micrograph of "+c"-wing (a) and "-c"-wing (b) of an uncoalesced sample. (Basal plane) stacking faults are visible as white lines running perpendicular to the c-direction.

be found in the "-c"-wing, the "+c"-wing of the laterally overgrown area provides the lowest density.

4. Conclusion

In summary, planar semipolar $(10\bar{1}1)$ GaN on $(11\bar{2}3)$ pre-patterned sapphire was successfully grown. This method allows large area growth of semipolar oriented $(10\bar{1}1)$ GaN on sapphire. Compared to other growth techniques and the resulting quality of nonpolar GaN on sapphire this approach is quite promising, in particular if further optimization steps are included.

5. Acknowledgement

The author likes to thank Jürgen Däubler for the measurements and results during his diploma thesis and Johannes Biskupek (Central Facility of Electron Microscopy, University of Ulm) for transmission electron microscopy measurements. Additionally the support of Rudolf Rösch, Ilona Argut and Rainer Blood ist acknowledged. This work was financially supported by the Deutsche Forschungsgemeinschaft within the project "Polarization Field Control in Nitride Light Emitters (PolarCoN)" under contract no. Scho 393/22–1.

References

[1] F. Bernardini, V. Fiorentini, and D. Vanderbilt, "Spontaneous polarization and piezoelectric constants of III-V nitrides", *Phys. Rev. B*, vol. 56, pp. R10024–R10027, 1997.

[2] T. Takeuchi, C. Wetzel, S. Yamaguchi, H. Sakai, H. Amano, and I. Akasaki, "Determination of piezoelectric fields in strained GaInN quantum wells using the quantum-confined stark effect", *Appl. Phys. Lett.*, vol. 73, pp. 1691–1693, 1998.

[3] M.D. Craven, S.H. Lim, F. Wu, J.S. Speck, and S.P. DenBaars, "Structural characterization of nonpolar ($11\bar{2}0$) a-plane GaN thin films grown on ($1\bar{1}02$) r-plane sapphire", *Appl. Phys. Lett.*, vol. 81, pp. 469–471, 2002.

[4] B. Imer, F. Wu, M.D. Craven, J.S. Speck, and S.P. DenBaars, "Stability of ($1\bar{1}00$) m-plane GaN films grown by metalorganic chemical vapor deposition", *Jpn. J. Appl. Phys.*, vol. 45, pp. 8644–8647, 2006.

[5] A-T. Cheng, Y-K. Su, W-C. Lai, and Y-Z. Chen, "Metalorganic vapor phase epitaxy growth of m-plane GaN using $LiAlO_2$ substrates", *Jpn. J. Appl. Phys.*, vol. 47, pp. 3074–3076, 2008.

[6] T. Hikosaka, T. Narita, Y. Honda, M. Yamaguchi, and N. Sawaki, "Optical and electrical properties of (1-101) GaN grown on a 7° off-axis (001) Si substrate", *Appl. Phys. Lett.*, vol. 84, pp. 4717–4719, 2004.

[7] T.J. Baker, B.A. Haskell, F. Wu, P.T. Fini, J.S. Speck, and S. Nakamura, "Characterization of planar semipolar gallium nitride films on spinel substrates", *Jpn. J. Appl. Phys.*, vol. 44, pp. L920–L922, 2005.

[8] T. Wunderer, P. Brückner, B. Neubert, F. Scholz, M. Feneberg, F. Lipski, M. Schirra, and K. Thonke, "Bright semipolar GaInN/GaN blue light emitting diode on side facets of selectively grown GaN stripes", *Appl. Phys. Lett.*, vol. 89, pp. 041121-1–3, 2006.

[9] T.J. Baker, B.A. Haskell, F. Wu, J.S. Speck, and S. Nakamura, "Characterization of planar semipolar gallium nitride films on sapphire substrates", *Jpn. J. Appl. Phys.*, vol. 45, pp. L154–L157, 2006.

[10] K. Nishizuka, M. Funato, Y. Kawakami, S. Fujita, Y. Narukawa and T. Mukai, "Efficient radiative recombination from ($11\bar{2}2$)-oriented $In_xGa_{1-x}N$ multiple quantum wells fabricated by the regrowth technique", *Appl. Phys. Lett.*, vol. 85, 3122–3124, 2004.

[11] N. Okada, A. Kurisu, K. Murakami, and K. Tadatomo, "Growth of semipolar ($11\bar{2}2$) GaN layer by controlling anisotropic growth rates in *r*-plane patterned sapphire substrate", *Appl. Phys. Exp.*, vol. 2, pp. 091001-1–3, 2009.

[12] M. Ueda, K. Kojima, M. Funato, Y. Kawakami, Y. Narukawa, and T. Mukai, "Epitaxial growth and optical properties of semipolar (11$\bar{2}$2) GaN and InGaN/GaN quantum wells on GaN bulk substrates", *Appl. Phys. Lett.*, vol. 89, pp. 211907-1–3, 2006.

[13] T. Paskova, R. Kroeger, S. Figge, D. Hommel, V. Darakchieva, B. Monemar, E. Preble, A. Hanser, N.M. Williams, and M. Tutor, "High-quality bulk a-plane GaN sliced from boules in comparison to heteroepitaxially grown thick films on r-plane sapphire", *Appl. Phys. Lett.*, vol. 89, pp. 051914-1–3, 2006.

[14] M. Feneberg, F. Lipski, R. Sauer, K. Thonke, T. Wunderer, B. Neubert, P. Brückner, and F. Scholz, "Piezoelectric fields in GaInN/GaN quantum wells on different crystal facets", *Appl. Phys. Lett.*, vol. 89, pp. 242112-1–3, 2006.

[15] T. Wunderer, F. Lipski, J. Hertkorn, P.Brückner, F. Scholz, M. Feneberg, M. Schirra, K. Thonke, A. Chuvilin, and U. Kaiser, "Bluish-green semipolar GaInN/GaN light emitting diodes on 1$\bar{1}$01 GaN side facets", *phys. stat. sol. (c)*, vol. 5, pp. 2059–2062, 2008.

[16] F. Scholz, T. Wunderer, B. Neubert, M. Feneberg, and K. Thonke, "GaN-based light-emitting diodes on selectively grown semipolar facets", *MRS Bull.*, vol. 34, pp. 328–333, 2009.

[17] B. Kuhn, and F. Scholz, "An oxygen doped nucleation layer for the growth of high optical quality GaN on sapphire", *phys. stat. sol. (a)*, vol. 188, pp. 629–633, 2001.

[18] J. Hertkorn, P. Brückner, S.B. Thapa, T. Wunderer, F. Scholz, M. Feneberg, K. Thonke, R. Sauer, M. Beer, and J. Zweck, "Optimization of nucleation and buffer layer growth for improved GaN quality", *J. Crystal Growth*, vol. 308, pp. 30–36, 2007.

[19] R. Liu, A. Bell, F.A. Ponce, C.Q. Chen, J.W. Wang, and M.A. Khan, "Luminescence from stacking faults in gallium nitride", *Appl. Phys. Lett.*, vol. 86, pp. 021908-1–3, 2005.

[20] S. Schwaiger, S. Metzner, T. Wunderer, I. Argut, J. Thalmair, F. Lipski, M. Wieneke, J. Bläsing, F. Bertram, J. Zweck, A. Krost, J. Christen, and F. Scholz, "Growth and coalescence behavior of semipolar (11$\bar{2}$2) GaN on pre-structured r-plane sapphire substrates", *phys. stat. sol. (b)*, DOI:10.1002/pssb.201046336 (6 pages).

[21] S. Schwaiger, I. Argut, T. Wunderer, R. Rösch, F. Lipski, J. Biskupek, U. Kaiser, and F. Scholz, "Planar semipolar (10$\bar{1}$1) GaN on (11$\bar{2}$3) sapphire", *Appl. Phys. Lett.*, vol. 96, pp. 231905-1–3, 2010.

[22] T. Paskova (Ed.), *Nitrides with Nonpolar Surfaces. Growth, Properties and Devices*, Weinheim: Wiley-VCH Verlag, 2008.

[23] P.P. Paskov, R. Schifano, B. Monemar, T. Paskova, S. Figge, and D. Hommel, "Emission properties of a-plane GaN grown by metalorganic chemical-vapor deposition", *J. Appl. Phys.*, vol. 98, pp. 093519-1–7, 2005.

Properties of Semipolar InGaN QWs Grown on 3D Inverse GaN Pyramids

Thomas Wunderer

The properties of thin InGaN films deposited via MOVPE on non-planar GaN surfaces are investigated in detail. Using a comprehensive combination of different investigation methods including transmission electron microscopy, spatially and time-resolved cathodoluminescence experiments and modeling of the radiative recombination kinetics a precise description of the semipolar QW properties can be presented.

1. Introduction

Today's commercially available GaN based light emitting devices are limited in their efficiency. High piezoelectric fields hamper the radiative recombination of carriers within the QWs. The fields result from the biaxially strained InGaN films and the polar character of the hexagonal wurtzite crystal structure. Together, they cause a local separation of electron and hole wave functions and consequently less efficient device structures [1, 2]. This fact is most prominent for high In-compositions which are needed for longer wavelength emitters. Less polar crystal orientations, wherefore a higher recombination probability is expected [3, 4], could be one way to overcome the so-called 'green gap'.

That is why many groups are currently dealing with the properties of non- and semipolar group III-nitrides [5, 6]. Today, the most convincing way to fabricate high performance non- and semipolar GaN devices is to use GaN substrates with high material quality. They can be obtained from quasi-GaN-boules with a thickness of a view millimeters which are typically grown in the conventional c-direction and then prepared for the desired crystal orientation [7]. The substrates typically feature a very low defect density which seems to be the key factor for the remarkable device performance on such substrates [6]. However, the high prize and the small sample size are limiting factors for commercial applications [8]. An interesting alternative approach for semipolar device structures is the usage of three-dimensional (3D) GaN and naturally formed semipolar side facets. We could demonstrate that high material quality can be achieved using inverse GaN pyramids at low fabrication costs on large substrate sizes [9].

In this work the properties of thin InGaN films which have been deposited onto the 3D surfaces are investigated. The specific geometry of the underlying structure influences the growth behavior during the deposition process via metal-organic vapor phase epitaxy (MOVPE).

2. Fabrication Procedure

The epitaxial growth was performed by low pressure MOVPE in an Aixtron single wafer reactor. First, high quality GaN templates with a thickness of about 2 µm were grown on c-plane sapphire wafers. The optimized fabrication procedure includes the deposition of a SiN interlayer for efficient defect reduction [10]. Then, a 200 nm thick SiO_2 layer was deposited via plasma enhanced chemical vapor deposition (PECVD). Optical lithography and dry etching techniques were subsequently applied for structuring the SiO_2 mask into hexagonal patterns. Afterwards, the samples have been taken back into the MOVPE reactor to grow the 3D structures. Thereon, we have grown the InGaN QWs. In order to get an appropriate In incorporation, the QWs as well as the GaN barriers in between were grown at a reduced temperature of about 800 °C, whereas all other layers have been typically grown in the temperature range of $T = 950$–1050°C

3. InGaN Properties

The structural properties of an InGaN/GaN MQW stack deposited on 3D GaN are strongly influenced by the specific geometry of the underlying structure [11]. Different to planar growth, the structured surface may affect the thicknesses as well as the composition of the ternary InGaN films which directly influence the optical properties of the structure. A particularly strong variation of the QW emission wavelength was found on a relatively large inverse GaN pyramids with 13 µm long $\{11\bar{2}2\}$ side facets. Spatially resolved cathodoluminescence investigations showed an enormous shift of the wavelength from about 530 nm at the top of the structure towards 380 nm at the inner tip of the inverse pyramid (Fig. 1).

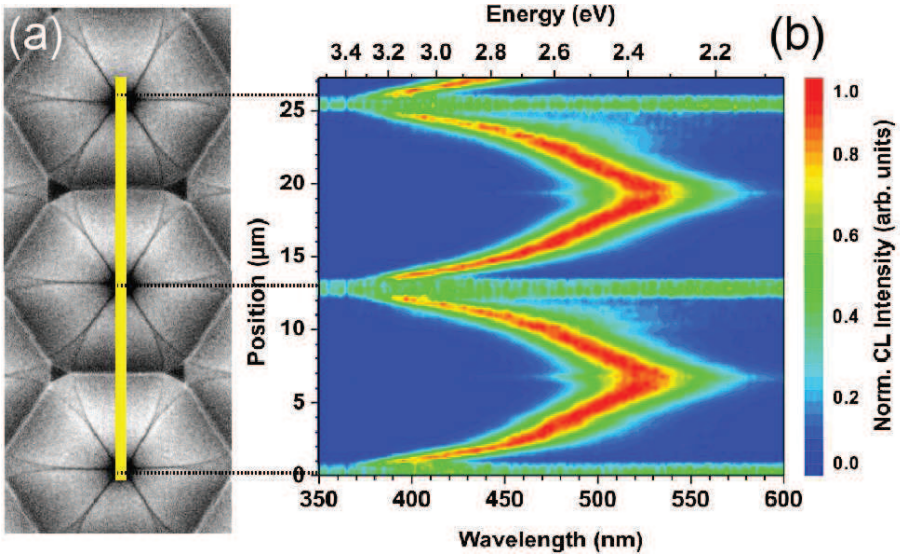

Fig. 1: SEM top view of inverse pyramid structure with $\{11\bar{2}2\}$ facets and a period length of 13 µm (a) and respective CL wavelength linescan (b). The data was acquired by S. Metzner, Otto-von-Guericke-Universität Magdeburg.

The emission wavelength of an InGaN QW is dependent on various parameters. The most prominent factors are the indium composition, the QW thickness and the piezoelectric field which changes the transition energy within the QW due to the quantum confined Stark effect (QCSE). All parameters are strongly correlated and, therefore, can not be treated isolated. We have been able to build a comprehensive picture of the QW properties by combining the structural and optical properties with theoretical model calculations.

First, the QW thickness was determined along the complete facet length using transmission electron microscopy (TEM). A small lamella was prepared using focused ion beam (FIB) techniques to cut the desired specimen perpendicular to the facet surface. The determined QW thickness from the TEM images along the facet is shown in Fig. 2.

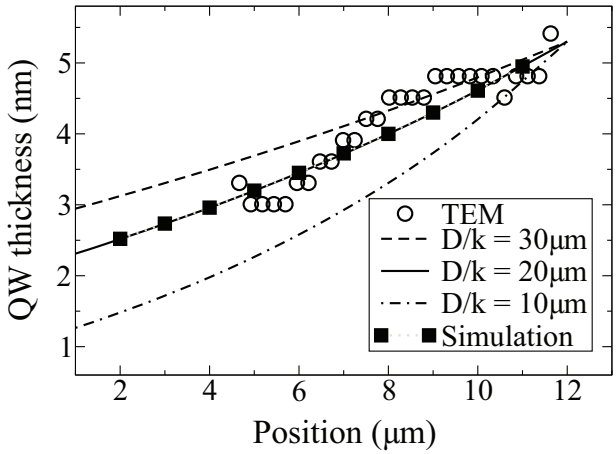

Fig. 2: QW thickness along inverse pyramid facet. Position 0 corresponds to the inner tip.

It was found that gas phase diffusion processes in selective area growth (SAG) can precisely describe the growth behavior using MOVPE [12]. We confirmed that the QW thicknesses on 3D GaN with only one facet type can also be well modeled by gas phase diffusion (not shown). That is the reason why we applied the gas phase diffusion model to our problem taking into account the specific geometry of the 3D structure. For simplicity, we first used a constant InGaN composition to determine the QW thickness which should be sufficiently accurate due to the low indium concentration. As shown in Fig. 2, the best matching was found for $D/k = 20\,\mu\text{m}$ for the film, where D is the diffusion coefficient and k is the rate constant for the first-order heterogeneous surface adsorption and can be understood as a value for the actual incorporation of the respective species [13, 14].

To fully describe the QW properties, two other parameters, the indium composition and the strength of the piezoelectric field, have to be quantized for any position along the facet. The values can be gained by including two additional independent measures - the transition energy and the radiative life time. Cathodoluminescence experiments can provide access to both of them. The spectral properties as well as the time-dependence of the radiation can be gained with the necessarily spatial accuracy. Figs. 3 and 4 show the transition energy and radiative life time of the QW emission for any position along the facet.

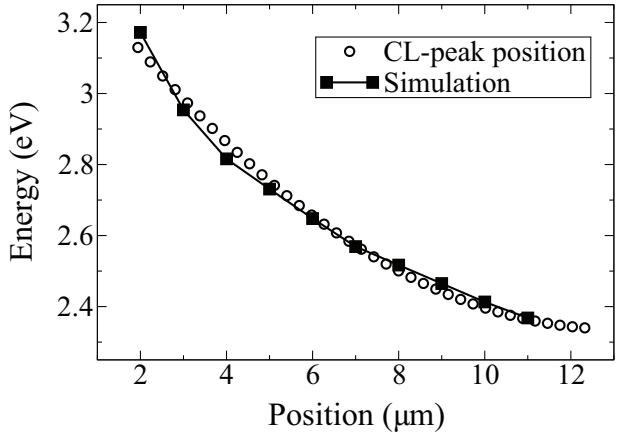

Fig. 3: QW transition energy along inverse pyramid facet. Position 0 corresponds to the inner tip.

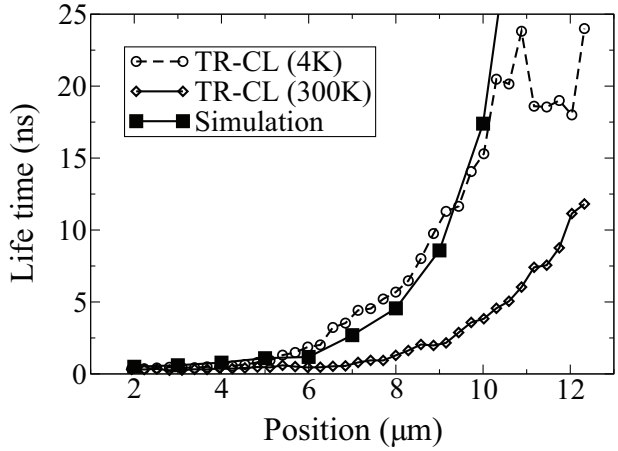

Fig. 4: Carrier life time along inverse pyramid facet. Position 0 corresponds to the inner tip.

As can be seen, the model calculations perfectly match the experimental data. The simulation is based on a fairly comprehensive model of the QW properties solving self-consistently the Schrödinger and Poisson equation for each individual point along the facet.

As a result, we now know the indium composition and the strength of the piezoelectric field for all data points along the facet (Fig. 5). A fairly constant indium composition of about 20 % is found on the upper half of the inverse pyramid and is then strongly decreasing towards the inner tip. This finding can be understood when looking closer to the growth conditions used to deposit the InGaN films. Typically, InGaN is grown under a high overdose of TMIn. Despite a smaller D/k for indium (here: $D/k = 5\,\mu\text{m}$), the oversupply of TMIn is still present for the upper half of the pyramid and, therefore, the composition within the solid is mainly determined by the growth rate of the film and not by the gas composition. This is different in the lower half of the pyramid. Here, actually the gas composition determines the composition in the solid as the oversupply of indium is not valid any more (not shown).

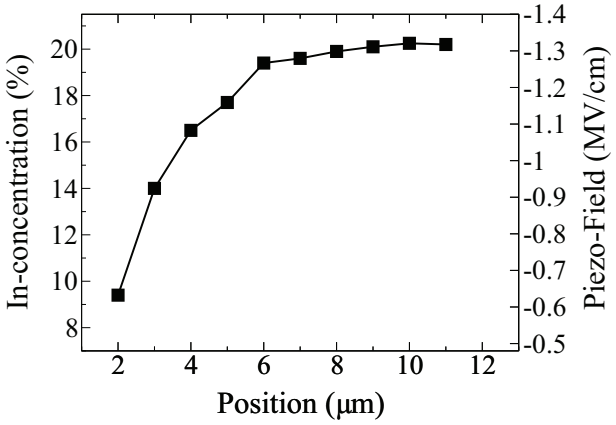

Fig. 5: In-composition along inverse pyramid facet. Position 0 corresponds to the inner tip.

For the piezoelectric tensor elements, we have found the best matching to the experimental data using the values from the most recent publications [15, 16]. This leads to a piezoelectric field of about -1.3 MV/cm^2 for an In-composition of 20 % on the semipolar $\{11\bar{2}2\}$ plane. This is about 1/3 of the value found for QWs grown on c-plane GaN.

Interestingly, the structure is well suited to determine the piezoelectric field without knowledge of the piezoelectric constants or exact indium composition. Bulashevich et al. developed an analytical approach to determine the piezoelectric polarization by varying the QW thickness [17]. Due to the QCSE the change in QW thickness directly converts into a shift of the emission wavelength. Using our inverse pyramid structure, we have access to an accurate variation of the QW thickness originating from gas phase diffusion. Furthermore, we have shown that a nearly constant In-content can be assumed in the upper half of the facet. This structure therefore is ideally suited for the determination of the piezoelectric field using Bulashevich's model:

$$E_{e,h} - E^0_{e,h} = -\frac{512 m_{e,h} e^2 F^2 d^4}{243 \pi^6 \hbar^2 \chi^2} \tag{1}$$

with $E^0_{e,h}$ as the ground state for electrons and holes without electrical field F:

$$E^0_{e,h} = \frac{\pi^2 \hbar^2}{2 m_{e,h} d^2} \tag{2}$$

Hereby, e and h represents electrons and holes, χ is the screening of the field by carriers. Due to the low excitation we can set $\chi = 1$ in our case. The thickness of the QWs is given by d. Fig. 6 shows the measured emission energy via CL and the respective model calculations for different values of the piezoelectric field. The best matching has been achieved for a piezoelectric field of about 1-1.3 MV/cm. This value can be gained without the knowledge of the exact In-composition and piezoelectric constants. However, assuming about 20 % indium in the QWs (see above) the value fits very well to the findings from Shen et al. [18].

Finally, the determined data set is used to estimate the internal quantum efficiency (IQE) at different positions of the structure. Assuming that at low temperature (4 K) the carrier

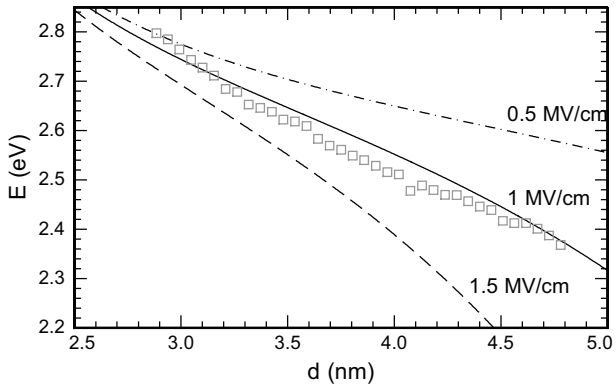

Fig. 6: CL emission energy along upper half of inverse pyramid in correlation with determined QW thickness (squares) (section 4). Shift of emission energy for different field strengths using the analytic model of Bulashevich et al. [17]. Curves are normalized.

recombination is mainly driven by radiative recombination processes, an upper value for the IQE can be given:

$$\eta_{IQE}(300\,\mathrm{K}) = \frac{\tau(300\,\mathrm{K})}{\tau_\mathrm{r}(300\,\mathrm{K})} \leq \frac{\tau(300\,\mathrm{K})}{\tau_\mathrm{r}(4\,\mathrm{K})} \leq \frac{\tau(300\,\mathrm{K})}{\tau(4\,\mathrm{K})} \tag{3}$$

The life times along the facet (Fig. 4) were combined with the emission wavelength at the specific position (Fig. 3). The following diagram for the IQE vs. wavelength can than be created (Fig. 7). The diagram shows the typical drop of the IQE towards longer wavelength emission which is known as the green gap. Although the piezoelectric polarization could be reduced by about 2/3 in comparison to c-plane devices, the fields are still quite strong for high indium compositions. Additionally, it is assumed that point defects at the interfaces of the QWs play a significant role as non-radiative recombination channels which are generated during the low temperature growth of the QWs. Together, they limit the overall efficiency, especially in the green wavelength regime.

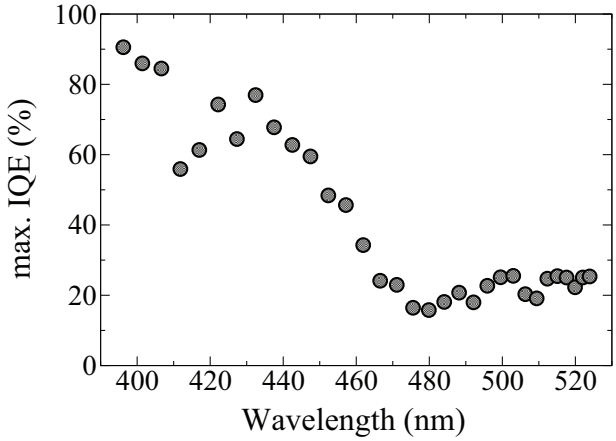

Fig. 7: Max. IQE vs wavelength determined using Equ. 3 and the carrier life times from Fig. 4.

4. Conclusion

A detailed study of InGaN QWs deposited on semipolar $\{11\bar{2}2\}$ side facets of inverse pyramids is presented. A comprehensive combination of different investigation methods including TEM, spatially and time-resolved CL experiments and modeling of the radiative recombination process allow the exact determination of QW thickness, indium composition and piezoelectric polarization. Furthermore the data set is used to estimate an IQE for different wavelength. Despite a significant reduction of the piezoelectric field, the 'green gap' is still present.

Acknowledgement

We gratefully acknowledge the fruitful cooperation with M. Feneberg and S. Metzner (Otto-von-Guericke-Universität Magdeburg) for the model calculations and CL investigations, respectively. L. Lechner and J. Biskupek (Ulm University) performed great work for the TEM investigations.

References

[1] J.S. Im, H. Kollmer, J. Off, A. Sohmer, F. Scholz, and A. Hangleiter, "Reduction of oscillator strength due to piezoelectric fields in GaN/$Al_xGa_{1-x}N$ quantum wells", *Phys. Rev. B*, vol. 57, pp. R9435–R9438, 1998.

[2] A. Hangleiter, J. Im, H. Kollmer, S. Heppel, J. Off, and F. Scholz, "The role of piezoelectric fields in GaN-based quantum wells", *MRS Internet J. Nitride Semicond. Res.*, vol. 3, p. 15, 1998.

[3] T. Takeuchi, S. Sota, M. Katsuragawa, M. Komori, H. Takeuchi, H. Amano, and I. Akasaki, "Quantum-confined stark effect due to piezoelectric fields in GaInN strained quantum wells", *Jpn. J. Appl. Phys.*, vol. 36, pp. L382–L385, 1997.

[4] T. Takeuchi, H. Amano, and I. Akasaki, "Theoretical study of orientation dependence of piezoelectric effects in wurtzite strained GaInN/GaN heterostructures and quantum wells", *Jpn. J. Appl. Phys.*, vol. 39, pp. 413–416, 2000.

[5] T. Paskova, *Nitrides with Nonpolar Surfaces*. Weinheim: Wiley-VCH, 2008.

[6] J.S. Speck and S.F. Chichibu, Guest Editors, "Nonpolar and semipolar group III nitride-based materials", *MRS Bulletin*, vol. 34, pp. 304–309, 2009, Special issue containing several articles authored by various groups.

[7] K. Fujito, S. Kubo, and I. Fujimura, "Development of bulk GaN crystals and nonpolar/semipolar substrates by HVPE", *MRS Bulletin*, vol. 34, pp. 313–317, 2009.

[8] U. Schwarz and M. Kneissl, "Nitride emitters go nonpolar", *phys. stat. sol. (RRL)*, vol. 1, pp. A44–A46, 2007.

[9] T. Wunderer, J. Wang, F. Lipski, S. Schwaiger, A. Chuvilin, U. Kaiser, S. Metzner, F. Bertram, J. Christen, S.S. Shirokov, A.E. Yunovich, and F. Scholz, "Semipolar GaInN/GaN light-emitting diodes grown on honeycomb patterned substrates", *phys. stat. sol. (c)*, vol. 7, pp. 2140–2143, 2010.

[10] J. Hertkorn, F. Lipski, P. Brückner, T. Wunderer, S. Thapa, F. Scholz, A. Chuvilin, U. Kaiser, M. Beer, and J. Zweck, "Process optimization for the effective reduction of threading dislocations in MOVPE grown GaN using in situ deposited SiN_x masks", *J. Cryst. Growth*, vol. 310, pp. 4867–4870, 2008.

[11] W. Feng, V.V. Kuryatkov, A. Chandolu, D.Y. Song, M. Pandikunta, S.A. Nikishin, and M. Holtz, "Green light emission from InGaN multiple quantum wells grown on GaN pyramidal stripes using selective area epitaxy", *J. Appl. Phys.*, vol. 104, pp. 103530-1–4, 2008.

[12] D. Ottenwälder, "Untersuchungen zur selektiven Epitaxie im Halbleitersystem GaIn(As,P)", Dissertation, Physikalisches Institut der Universität Stuttgart, 1996.

[13] H. Fang, Z.J. Yang, Y. Wang, T. Dai, L.W. Sang, L.B. Zhao, T.J. Yu, and G.Y. Zhang, "Analysis of mass transport mechanism in InGaN epitaxy on ridge shaped selective area growth GaN by metal organic chemical vapor deposition", *J. Appl. Phys.*, vol. 103, pp. 014908-1–4, 2008.

[14] S. Keller, B.P. Keller, D. Kapolnek, A.C. Abare, H. Masui, L.A. Coldren, U.K. Mishra, and S.P.D. Baars, "Growth and characterization of bulk InGaN films and quantum wells", *Appl. Phys. Lett.*, vol. 68, pp. 3147–3149, 1996.

[15] H. Shen, M. Wraback, H. Zhong, A. Tyagi, S.P. DenBaars, S. Nakamura, and J.S. Speck, "Determination of polarization field in a semipolar $(11\overline{2}2)$ InGaN/GaN single quantum well using Franz–Keldysh oscillations in electroreflectance", *Appl. Phys. Lett.*, vol. 94, pp. 241906-1–3, 2009.

[16] M. Feneberg, K. Thonke, T. Wunderer, F. Lipski, and F. Scholz, "Piezoelectric polarization of semipolar and polar GaInN quantum wells grown on strained GaN templates", *J. Appl. Phys.*, vol. 107, pp. 103517-1–6, 2010.

[17] K.A. Bulashevich, S.Y. Karpov, and R.A. Suris, "Analytical model for the quantum-confined Stark effect including electric field screening by non-equilibrium carriers", *phys. stat. sol. (b)*, vol. 243, pp. 1625–1629, 2006.

[18] H. Shen, M. Wraback, H. Zhong, A. Tyagi, S.P. DenBaars, S. Nakamura, and J.S. Speck, "Unambiguous evidence of the existence of polarization field crossover in a semipolar InGaN/GaN single quantum well", *Appl. Phys. Lett.*, vol. 95, pp. 033503-1–3, 2009.

Fabrication of GaN-based Photonic Crystal Structures by Reactive Ion Etching

Junjun Wang

The fabrication of the 2D GaN-based photonic crystal structure at optical scales, a sub-μm scale in our case is very challenging. In our work, a double-etching method proved to be feasible to achieve the periodic GaN/air variation. The pattern was defined in a PMMA resist by electron-beam lithography and transferred to SiO_2 by reactive ion etching (RIE) in a CF_4 plasma and further into GaN by RIE in a chlorine plasma. An interesting phenomenon during RIE was observed: the etching rate at the barrier site is enhanced to about two times of that in the μm scale while the etching rate at the valley site stays the same. If the mask is exhausted during RIE, the etching depth increases before the mask disappearance and decreases after that with further etching. Thus the etching time is a critical parameter to obtain deep enough holes in GaN. Referring to the etching rates of Si_3N_4 and SiO_2 in both kinds of plasma, it might be easier to achieve deep holes when Si_3N_4 substitutes SiO_2.

1. Introduction

Photonic crystals (PC) are structures with periodic variations of the refractive index. In such structures, the light propagation can be controlled or manipulated in a similar way as the electronic energetic bands in crystals by defining photonic bands. Since the first realization of a non-one-dimensional PC in 1987 [1], the PC has attracted much interest worldwide. GaN-based two-dimensional (2D) photonic crystal surface-emitting lasers (PCSEL) are promising to produce single mode lasing over a large area in high power blue-violet emitter applications [2–4]. However, it is challenging to fabricate such a GaN-based PC at an optical wavelength scale. There are very few publications about this topic up to now.

The PC fabrication methods can be considered as either "Bottom Up" or "Top Down" approaches. In the former, periodic GaN pyramids are formed by selective area growth on hexagonally-patterned templates in metal-organic vapor phase deposition system [5]. The refractive index changes gradually at the GaN/air edge in such a pyramidal structure and does not have a high contrast. In this report, a "Top Down" method will be described: the pattern was defined in PMMA by electron beam lithography (EBL) and transferred step by step into GaN by reactive ion etching (RIE). The experimental details will be described in the following.

Our final goal is to integrate the PC into a GaN-based laser diode (LD) emitting at around 410 nm. Based on the calculation of the photonic band diagram, a square lattice

is designed with a hole radius between 60 and 80 nm and the lattice constant between 330 and 380 nm. In order to make the emission interfere better with the PC, the holes should be deep enough to penetrate the waveguide or even the InGaN/GaN quantum wells. So our initial goal is to reach $\sim$ 400 nm deep homogeneous holes in the GaN-based LD.

The main feature of our structure is its sub-μm-scaled size which requires the employment of EBL to define the lattice pattern instead of standard photolithography and determines its special behavior during RIE when the PC pattern is transferred from the EBL resist into the semiconductor structure.

2. Fabrication Processes

The processing steps were investigated using test samples that simply contain 5 pairs InGaN/GaN quantum wells grown on c-plane GaN rather than the LD. The following two kinds of fabrication processes were tried: the single-step and double-step etching methods. The infeasibility of the first one motivate us to investigate the second: to transfer the PC pattern into the sample by CF_4 RIE and chlorine RIE step by step.

2.1 Single-step etching method

Sample A was firstly covered with a layer of the EBL resist of PMMA by spin coating. By EBL we defined the square pattern in the PMMA layer. The whole PC pattern is defined in a square shape with a size of $750\times750\,\mu m^2$. Then, with PMMA acting as mask, the sample was etched by RIE in a chlorine plasma (details shown in Table 1) for 5 min to transfer the PC pattern into the sample. Finally we intended to remove PMMA with 1-methyl-2-pyrrolidone (MP). The PMMA within the circular ring around holes still exists

Table 1: RIE parameters in a chlorine plasma.

Electrode RF power	100 W
Pressure	2 Pa
Cl_2	1.5 sccm
BCl_3	10 sccm
Ar	10 sccm

after we tried to remove it with $\sim$120 °C MP solution. Part of the PMMA rings were removed mechanically by tweezers unintentionally as the gray stripes in Fig. 1. Actually the PMMA was polymerized during the chlorine RIE and became quite resistant. So the single-step etching method proved to be infeasible.

2.2 Double-step etching method

In order to overcome this problem, we developed a double-step etching method employing two masks PMMA and SiO_2 with the later under the former: A layer of 700 nm SiO_2 was

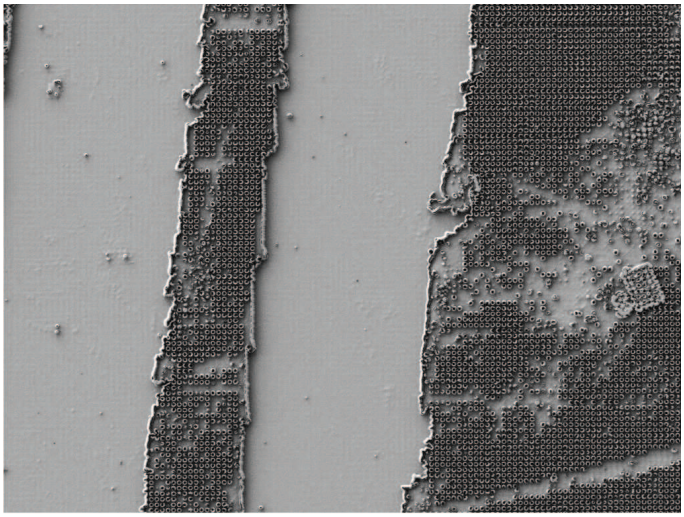

Fig. 1: Top view of sample A.

Table 2: RIE parameters in a CF_4 plasma.

Electrode RF power	60 W
Pressure	5.3 Pa
CF_4	45 sccm

deposited on the samples by plasma-enhanced chemical vapor deposition, followed by a PMMA layer of ∼620 nm. The same PC pattern was defined in PMMA by EBL as that in the single-step etching method. Subsequently, the PC pattern was transferred to the SiO_2 film by RIE in a CF_4 plasma (details shown in Table 2) which did not polymerize the PMMA layer. After removing PMMA with hot MP, the sample was etched by RIE using chlorine plasma with the structured SiO_2 layer as mask. In order to gain a better understanding how both of these etching processes behave, two samples were prepared: sample B before and sample C with the GaN etching in chlorine plasma. The etching times for these two samples are shown in Table 3.

Table 3: The etching periods for sample B and C.

	CF_4 RIE	Chlorine RIE
Sample B	10 min40 sec	—
Sample C	10 min20 sec	10 min

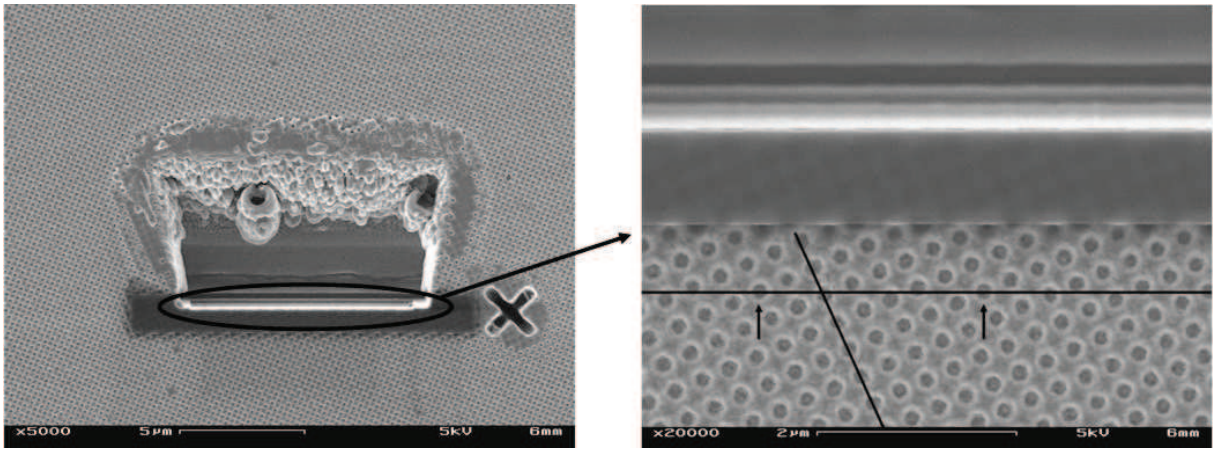

Fig. 2: The groove cut by FIB (left) and the magnified lower side of the groove (right).

3. Focused Ion Beam Characterization

A cross-section image of the PC structure is necessary to evaluate the hole depth and profile. As mentioned, the whole PC pattern is defined in a square shape with a size of $750 \times 750\,\mu m^2$. Therefore, it is very difficult to cleave exactly through such a small area manually or even with a cleaving saw. In such a case, focused ion beam (FIB) turns to be a good choice to characterize the PC cross section. The FIB setup resembles a scanning electron microscope (SEM). While the SEM uses a focused beam of electrons to image the sample, the FIB uses a focused beam of ions instead to image or manipulate the sample. FIB is a destructive method and can be applied to cut a local groove of a few μm^2 (as shown in Fig. 2) into the sample. Then it is possible to characterize the PC cross section from the groove sidewall.

Before the samples were put into the FIB chamber, 80 nm Ni was deposited over the whole sample surface for a better contrast. A layer of C was deposited in the FIB chamber only within several tens μm^2 (the black region in Fig. 2) to avoid the GaN redeposition during milling of the groove.

The images of the PC cross section were taken with such an orientation that the bird's eye views of both the sample surface and groove sidewall are visible in the image (Fig. 3 (left) as an example). Additionally the software integrated in the FIB setup adjusted the lower part of the image for the groove sidewall part to appear in an exact cross section view.

4. Results and Discussion

FIB was utilized to characterize the hole cross section of sample B and C. The depth and the shape of the holes are of our interest. The holes get narrower near the bottom. So it is necessary for FIB to cut exactly through the hole center in order to gain the depth and the diameter of the holes. If the cut is parallel to the photonic crystal direction $\langle 01 \rangle$, it is impossible to handle FIB so accurately that the cut is placed at the hole centers in one

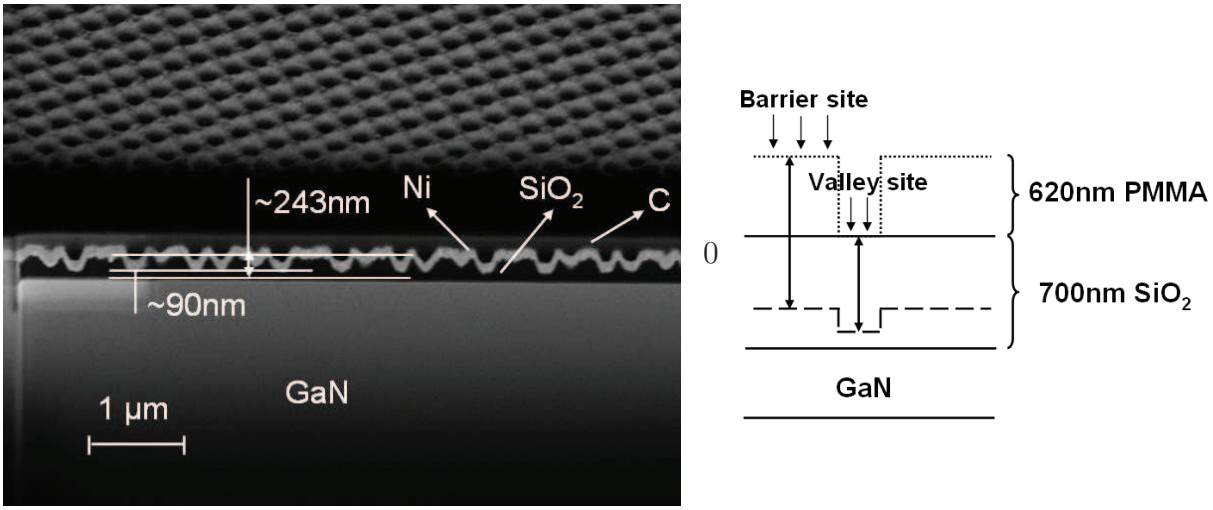

Fig. 3: The FIB image (left) and the schematic diagram about the surface development during the CF_4 RIE (right) of sample B.

line. The trick is to rotate the cut with a certain angle from the ⟨01⟩ direction and the cut crosses holes with many different distances away from the centers. Some of them are close enough to 0 indicated by arrows in Fig. 2 (right) which correspond to the deepest holes in Fig. 3 (left).

The sub-µm-scaled size of the PC structure causes a quite different RIE behavior compared to a micrometer-scaled structure. The specific RIE behavior will be discussed in the following.

For sample B, the PMMA was totally etched away and the SiO_2 was reduced to ∼243 nm with ∼153 nm deep holes in it during the CF_4 RIE. The etching process is schematically shown in Fig. 3 (right): 610 nm SiO_2 at the valley site and 620 nm PMMA + 457 nm SiO_2 at the barrier site were etched away. Then the etching rate at the valley site can be calculated to be 57 nm/min which corresponds very well to the estimation of ∼60 nm/min from the µm-scaled samples. The SiO_2 and PMMA etching rates in our RIE setup were evaluated to be ∼60 nm/min and 40 nm/min on µm-scaled samples. The ratio of 57:40 between the etching rates of SiO_2 and PMMA under the same RIE condition tells us that 884 nm SiO_2 needs the same time to be etched away as 620 nm PMMA. So 620 nm PMMA + 457 nm SiO_2 could be substituted by 1341 nm SiO_2 with respect to the etching rate. Hence, an effective etching rate of 125 nm/min is calculated for SiO_2 at the barrier site. Obviously, the same etching rate at the valley site and a doubled etching rate at the barrier site occur in the sub-µm-scaled structure compared to the µm-scaled one.

For sample C, the image of the cross section is shown in Fig. 4 (left): SiO_2 was totally etched away leaving 92 nm deep holes in GaN. The etching process is schematically shown in Fig. 4 (right). Here, etching rates of SiO_2 and GaN under the chlorine plasma RIE condition (Table 1) in our etching system are evaluated to be 16.6 nm/min and 45 nm/min, respectively. Assuming the etching rate ratio between the barrier and the valley sites to be λ, two equations describing the chlorine plasma etching are like the following:

$$\frac{243}{16.6\lambda} + \frac{x}{45\lambda} = 10 \tag{1}$$

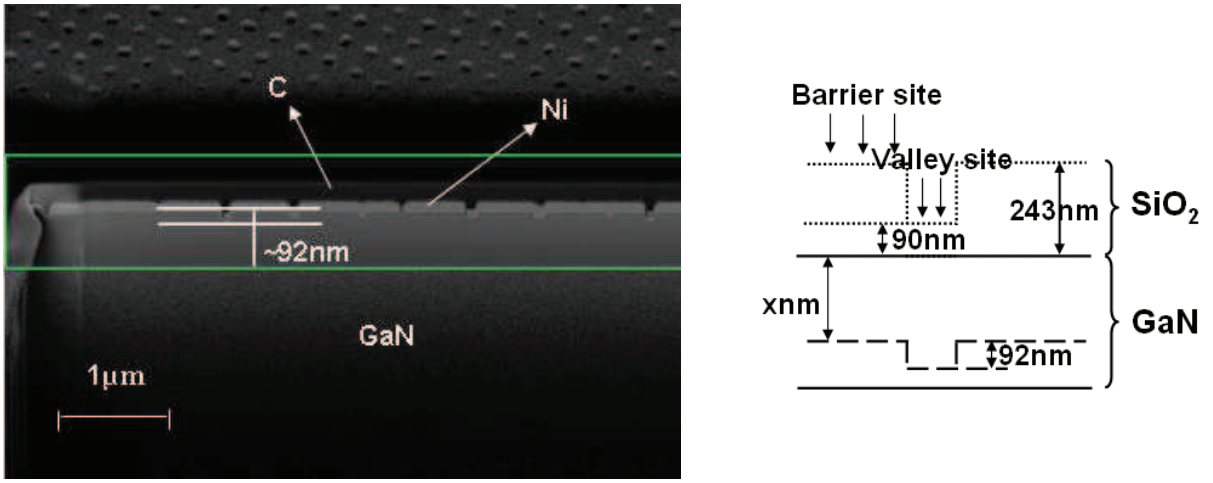

Fig. 4: The FIB image (left) and the schematic diagram about the surface development during the CF_4 RIE (right) of sample C.

$$\frac{90}{16.6} + \frac{x + 92}{45} = 10 \tag{2}$$

λ is calculated to be 2.1 which is close to the value in CF_4 plasma etching.

Not only physical sputtering but also chemical erosion are involved in RIE. The former part is an anisotropic element while the latter is an isotropic one. The chemical erosion attacks the barrier from both the surface and the sidewall, but only has the chance to attack the valley vertically. So the etching rate at the barrier is enhanced compared to the valley site. Additionally, our PC structure (the sub-µm scale) has a high surface-to-volume ratio. This leads to an even larger etching rate enhancement at the barrier site which explains the above mentioned observation.

It is clear that the hole depth decreases when the etching rate at the barrier site is larger than that at the valley site. So after the mask is etched away completely, the hole depth reduces and the PC structure is smeared with further etching. The hole depth reaches its maximum at the point when the mask is etched away.

In order to transfer a deeper pattern from PMMA into the 2nd mask (SiO_2 in the above experiments), either the PMMA thickness or the PMMA/2nd mask selectivity in CF_4 RIE should be increased. However, the PMMA thickness is limited by the EBL resolution. Therefore, a high etching rate of the 2nd mask in CF_4 RIE is required. On the other hand, a low etching rate of the 2nd mask in chlorine RIE enables a longer etching time to transfer a deeper PC pattern into GaN. Referring to Table 4 Si_3N_4 has a pronounced advantage in CF_4 RIE with a relatively small disadvantage in chlorine RIE compared to SiO_2. In this sense, Si_3N_4 is a better candidate than SiO_2 as the 2nd mask.

Taking the above discussion into account, new samples have been designed and prepared. Currenly the FIB characterization is ongoing.

Table 4: The etching rates of SiO_2 and Si_3N_4 under different RIE conditions.

etching rate (nm/min)	CF_4 RIE	chlorine RIE
SiO_2	60	16.6
Si_3N_4	180	22

5. Conclusion and Outlook

A fabrication method for a photonic crystal structure in GaN-based materials was investigated to create a periodic 2D pattern of air holes. A single-etching method was proved to be infeasible. A double-step etching method was implemented resulting in successful etching of periodic air holes in GaN. An interesting phenomenon for reactive ion etching of the sub-μm-scaled PC structure was found: $\sim$ doubled etching rate at the barrier site compared to the valley site. This indicates us the etching time is a critical parameter to obtain deep enough patterns. Si_3N_4 could be a good candidate acting as the 2nd mask. A three-layer resist system PMMA/Ti/AZ1350J is also promising to define the square pattern into GaN in the sub-μm scale [6].

6. Acknowledgments

Much valuable technical support was given by Ilona Argut, Yakiv Mens, Lorenz Lechner and Rudolf Rösch. Many fruitful discussions were done with Robert Leute and Mohamed Fikry.

References

[1] E. Yablonovitch, "Inhibited Spontaneous Emission in Solid-State Physics and Electronics", *Phys. Rev. Lett.*, vol. 58, pp. 2059–2062, 1987.

[2] T.C. Lu, S.W. Chen, L.F. Lin, T.T. Kao, C.C. Kao, P. Yu, H.C. Kuo, S.C. Wang, and S. Fan, "GaN-based two-dimensional surface-emitting photonic crystal lasers with AlN/GaN distributed Bragg reflector", *Appl. Phys. Lett.*, vol. 92, pp. 011129-1–3, 2008.

[3] S.W. Chen, T.C. Lu, Y.J. Hou, T.C. Liu, H.C. Kuo, and S.C. Wang, "Lasing characteristics at different band edges in GaN photonic crystal surface emitting lasers", *Appl. Phys. Lett.*, vol. 96, pp. 071108-1–3, 2010.

[4] T.C. Lu, S.W. Chen, T.T. Kao, and T.W. Liu, "Characteristics of GaN-based photonic crystal surface emitting lasers", *Appl. Phys. Lett.*, vol. 93, pp. 111111-1–3, 2008.

[5] T. Wunderer, J. Wang, F. Lipski, S. Schwaiger, A. Chuvilin, U. Kaiser, S. Metzner, F. Bertram, J. Christen, S.S. Shirokov, A.E. Yunovich, and F. Scholz, "Semipolar

GaInN/GaN light-emitting diodes grown on honeycomb patterned substrates", *phys. stat. sol. (c)*, vol. 7, pp. 2140–2143, 2010.

[6] E. Bassous, L.M. Ephrath, G. Pepper, and D.J. Mikalsen, "A Three-Layer Resist System for Deep U.V. and RIE Microlithography on Nonplanar Surfaces", *J. Electrochem. Soc.*, vol. 130, pp. 478–484, 1983.

Laser Structures with Semipolar Quantum Wells Grown by Selective Area Epitaxy

R.A.R. Leute

Using selective area epitaxy to produce three-dimensional GaN structures, two different concepts for laser diodes (LDs) with semipolar quantum wells (QWs) are developed, each having distinct advantages and disadvantages. The first approach utilizes a stripe with triangular cross-section not only to grow semipolar quantum wells on, but also as waveguide and resonator cavity. Based on simulations of modal characteristics we develope the epitaxial structure and address the difficulties of selective growth of the aluminum containing layers. The second approach integrates the three-dimensional structures with semipolar sidefacets into a conventional LD design with planar cladding layers. Therefore we miniaturize the selectively grown stripes to a submicrometer scale, positioning the active layer with semipolar QWs inside the core of a planar waveguide. For both approaches we present experimental results, regarding structural as well as optical properties including SEM, CL, PL, TEM and gain measurements.

1. Introduction

Selective area growth (SAG) of group III nitrides allows the epitaxy of 3D GaN structures of high crystal quality with semipolar facets based on 2-inch sapphire substrates. The reduced piezoelectric field on these facets promises great advantages of device performance reducing the Quantum Confined Stark Effect (QCSE) and its negative consequences for longer wavelenghts (i.e green) [1]. Additionally, the 3D growth of stripes, pyramids or the like enables us to manipulate the extraction and propagation of light by changing the surface topology. LEDs based on GaN stripes with $\{11\bar{2}2\}$ or $\{10\bar{1}1\}$ facets have been published [2] (see Fig. 1); the selective growth of GaN and the epitaxy of InGaN/GaN QWs is well under control. The fabrication of laser diodes (LDs) based on such three-dimensional structures, however, faces several major challenges due to the more complex device architecture. Particularly, the formation of resonator and waveguide, typically

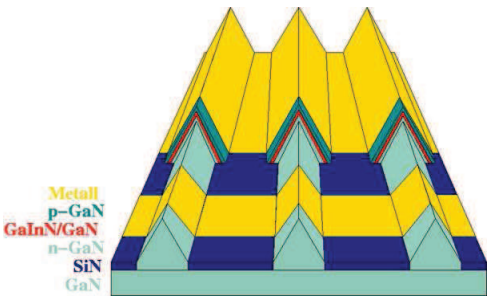

Fig. 1: Realization of a LED with semipolar quantum wells on the sidefacets of GaN stripes with triangular cross-section.

realized by AlGaN/GaN, constitutes the critical task, both regarding expitaxy as well as subsequent processing. We address this issue with two profoundly different approaches.

2. 3D All the Way

Processing a resonator on the side facet of a GaN stripe acting as a quasi substrate is disproportionally complicated. Therefore, we decide to create the resonator epitaxially, aside from mirror facets. The GaN stripe not only provides semipolar facets but acts as waveguide with vertical and lateral optical confinement. However, the growth parameters of AlGaN are challenging for selective epitaxy. The high growth temperature promotes lateral growth, subsequently leading to the emergence of an undesirable c-plane facet whereas the reduced selectivity of the mask material for Al atoms leads to polycrystalline growth on masked areas [3, 4]. Furthermore, Wunderer et al. [5, 6] showed that QWs grown on semipolar side facets suffer from a large gradient of the indium content along the facets, explained by gas phase diffusion. This leads to a broad emission spectrum unfavorable for a laser device. In this report, we focus on the former, even more crucial issue.

2.1 Concept - Simulation - Epitaxy

Regrettably, starting with the established growth of GaN stripes and growing the waveguide layer by layer will not suffice. Solving the vectorial Helmholtz equation, the simulation (Fig. 2) shows the rise of multiple modes. In order to provide lateral confinement, the structure has to be adapted to include a high index core of GaN, enclosed by AlGaN claddings. Two possible structures are shown in figures 3 and 4. For concept SM1 (single mode 1) a GaN core with triangular cross-section is positioned on top of a truncated AlGaN stripe and subsequently overgrown with an upper cladding. This concept allows convenient sizes of several micrometers for the mask patterns but demands a delicate

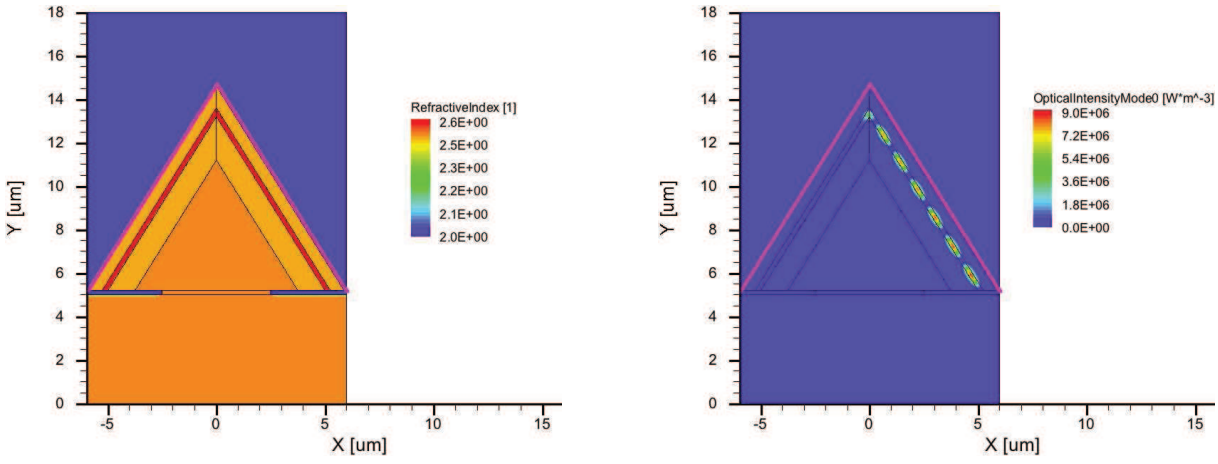

Fig. 2: Concept and simulation of the optical modes for a concept of AlGaN/GaN/AlGaN layers deposited on the side facets of a GaN stripe with triangular cross-section.

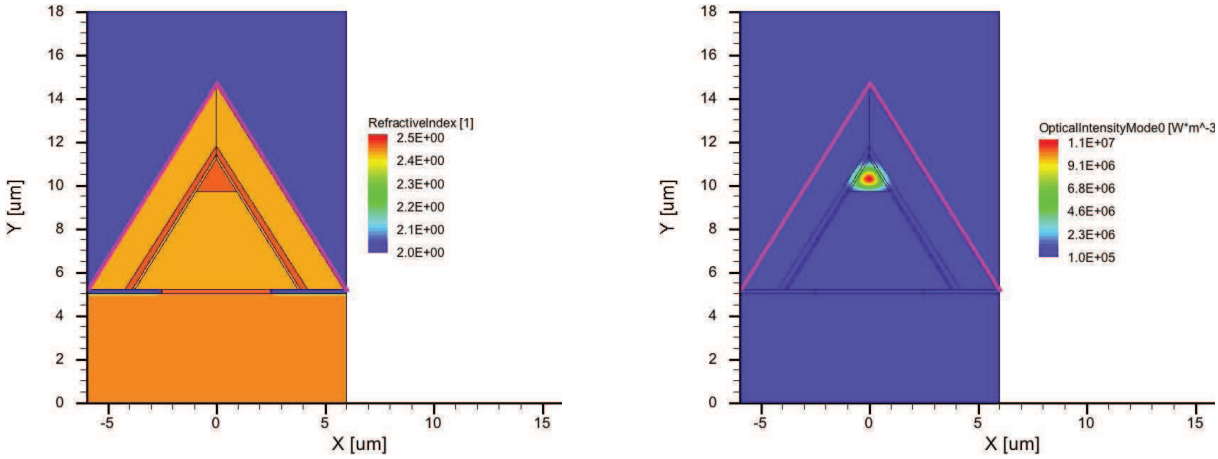

Fig. 3: Concept and simulation of the optical modes for concept SM1. A triangular GaN stripe is grown on top of a truncated AlGaN stripe and consequently enclosed by an upper AlGaN cladding.

control of the epitaxial process in order to obtain a well developed GaN tip before the growth of the second cladding. For concept SM2 the lower AlGaN cladding is realized as a plane layer during the first growth step of the template. After patterning the mask, the GaN core is grown directly at the beginning of the second growth step and subsequently overgrown. The simulation shows good optical confinement for this concept, enhanced by the low refractive index of the dielectric mask ($n = 1.47$ for SiO_2) even for buffer layers with only 5 %, with the advantage of only one 3D growth step of AlGaN needed. Requirements for the mask pattern however are fiercer. In order to get single mode operation the height and base of the GaN core shall not exceed 1.5 µm which is bordering the limits of optical lithography.

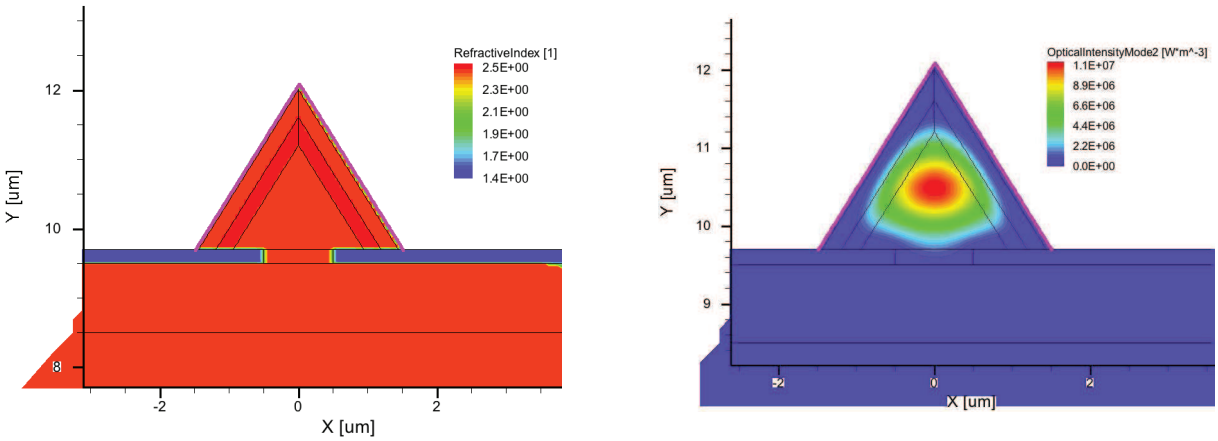

Fig. 4: Concept and Simulation of the optical modes for concept SM2. A planar AlGaN layer is included in the template as the bottom cladding. The waveguide core is directly grown on the template and only one 3D growth step for AlGaN is needed.

2.2 3D growth of AlGaN

For preliminary investigations thin layers, less than 1 µm thick, with low aluminum content (around 5 %) were grown on the side facets of fully developed GaN stripes. On top of an n-doped GaN template, a 200 nm thick SiO_2 mask was deposited by PECVD and patterned by optical lithography and subsequent dry etching. Stripes parallel to $< 10\bar{1}0 >$ or m-direction (resulting in $\{11\bar{2}2\}$ side facets) and stripes parallel to $< 11\bar{2}0 >$ or a-direction (resulting in $\{10\bar{1}1\}$ side facets) with mask opening widths of 4 µm, 6 µm and 8 µm and varying periods were grown. Changing the period and consequently the proportion of masked area results in a local variations of growth conditions. The supply of nitrogen is uniform while the supply of group III elements changes locally with the filling factor leading to local variations of growth rate and V/III ratio, thus giving us a vast parameter set. For this low aluminum content and short growth time, SEM pictures show almost no parasitic nucleation on the mask. With a being the favored growth direction the stripes parallel to a result in stripes with sharp ridges and smooth $\{10\bar{1}1\}$ side facets (not shown) as observed in earlier works [7]. The side is covered with a homogeneous layer of AlGaN, emitting at 351 nm corresponding to approximately 4 % aluminum. The ridge of the stripe exhibits luminescence at higher energy corresponding to approximately 8 % aluminum. This effect seems similar to the indium content gradient in quantum wells on three-dimensional structures. Stripes parallel to m are more prone to lateral growth and exhibit c-plane areas on top as well as rougher sidewalls. Figure 5 shows the cross-section as viewed by SEM as well as spatially resolved low temperature cathodoluminescence (CL). The presence of competing facets aggravates the difference in aluminum content between side facets and tip, nevertheless the $\{11\bar{2}2\}$ facets show a higher aluminum incorporation efficiency than the $\{10\bar{1}1\}$ facets. The CL gives an estimate of approximately 8 % Al content at the top and 5–6 % Al at the sidewalls.

Progressing towards concept SM2, the growth time of the GaN stripe was reduced and the thickness of the covering AlGaN layer was increased. In Fig. 6 the SEM picture of a cross-sections is shown where the material contrast clearly shows the undoped GaN core ensheathed by an AlGaN cladding layer. The exact outlines of the interior cannot be

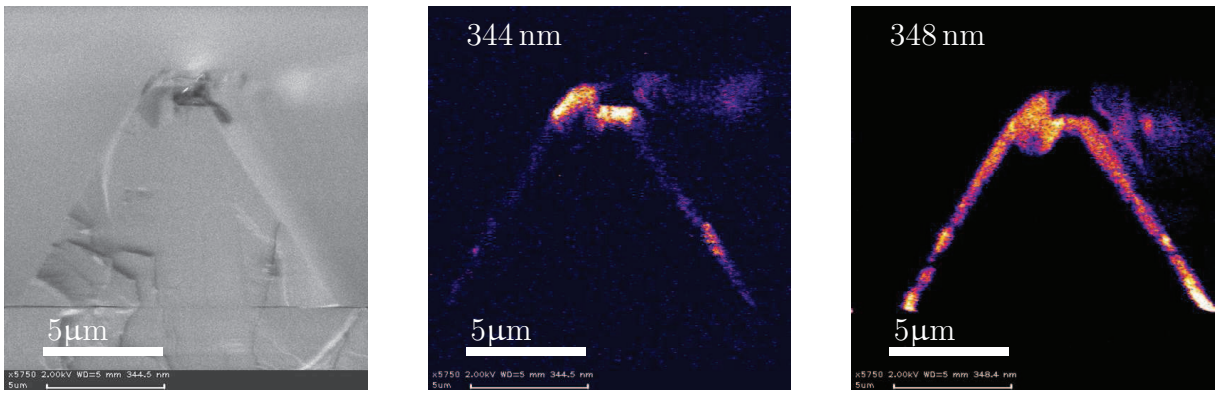

Fig. 5: SEM cross-section and monochromatic CL mappings at 8K of stripe parallel to m with $\{11\bar{2}2\}$ facets. The thin cladding layer of AlGaN is clearly visible. The top of the stripe exhibits luminescence at a higher energy as result of a higher aluminum incorporation.

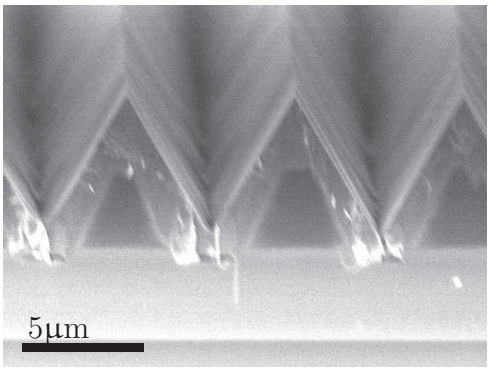

Fig. 6: SEM cross-section of stripes parallel a with $\{10\bar{1}1\}$ facets. The GaN core is overgrown by a thick AlGaN layer.

deduced for certain from this picture, yet the feasibility of the structure SM2 is substantiated. Optimization of the shape, monitored by marker layers and checked by spatially resolved spectroscopy as well as further reduction of the size are necessary. Progressing towards concept SM1, stripes of AlGaN were grown at higher growth temperatures and with more ammonia in order to create a c-plane plateau at the top of the stripe. In the same growth run these plateaus were overgrown with low temperature GaN to create a tip with triangular cross-section, later intended as waveguide core. The upper cladding was not grown. Figure 7 shows a GaN layer on top of the AlGaN plateau, for these dimensions the GaN growth time was not long enough to form a sharp ridge. Clearly visible is the parasitic growth that occurred during the long AlGaN growth and later acts as nucleation site for the low temperature GaN, too. This parasitic growth needs to be suppressed or removed as the mask loses all selectivity once a nucleation has been established. While the growth conditions of AlGaN need to optimized for better mask selectivity to allow the full structure to be realized in one growth run, separating the growth of the SM2 structure into multiple steps can work as a short term workaround. The interruptions will allow removal of parasitic growth by wet etching as well as reestablishing the mask for selective growth.

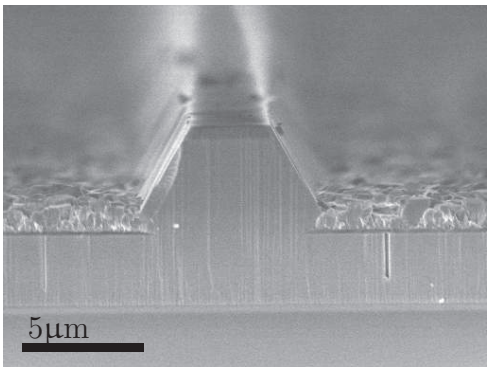

Fig. 7: SEM cross-section of stripes parallel a with $\{10\bar{1}1\}$ side facets. The GaN ridge on top of a truncated AlGaN stripe is clearly visible. Parasitic nucleation on the mask led to polycrystalline growth.

3. Integration by Miniaturization

With an alternate approach we can circumvent almost all difficulties brought about by the three dimensional growth of AlGaN. Decreasing the size of the three-dimensional GaN structures to the point where they fit inside the core of a planar conventional LD

design gives the benefits associated with semipolar GaN/InGaN quantum wells without the drawbacks of developing a new waveguide structure. Figure 8 shows the principle idea of this approach. With the mask constituting a perturbation of the refractive index on the scale of the laser wavelength, the device has the potential to work as a DFB laser, additionally.

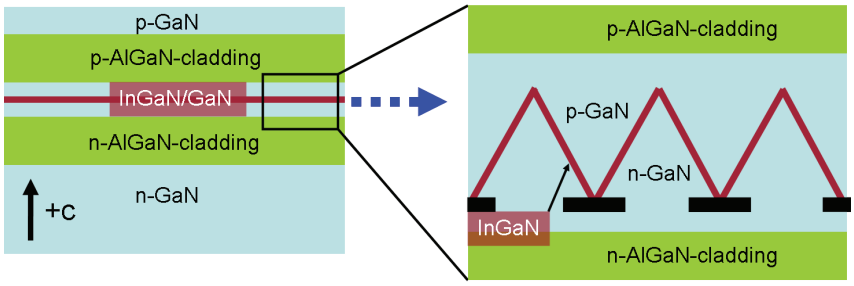

Fig. 8: Shrinking the size of the 3D structures allows the integration of semipolar quantum wells inside a conventional laser diode grown in polar direction.

3.1 Selective growth on a submicrometer scale

In order to reach the submicrometer range of dimensions the dielectric mask needed for selective area growth is reduced to approximately 50 nm thickness and structured via lift-off following e-beam lithography with periodicities of 230 nm to 270 nm corresponding to 3rd order DFB gratings. Our first investigations proved the feasibility of SAG on a submicrometer scale. Figure 9 shows well developed GaN stripes with InGaN/GaN quantum well structures grown on the semipolar side facets. Subsequently these submicrometer structures were planarized with GaN and sandwiched between c-oriented AlGaN waveguide claddings. The planarization and consequently the growth of the upper waveguide cladding depend strongly on the orientation of the stripes. For stripes parallel to *a*-direction (the favored growth direction) we receive an incomplete embedding whereas for stripes parallel to *m*-direction the proposed device structure was succesfully realized, shown in Fig. 10.

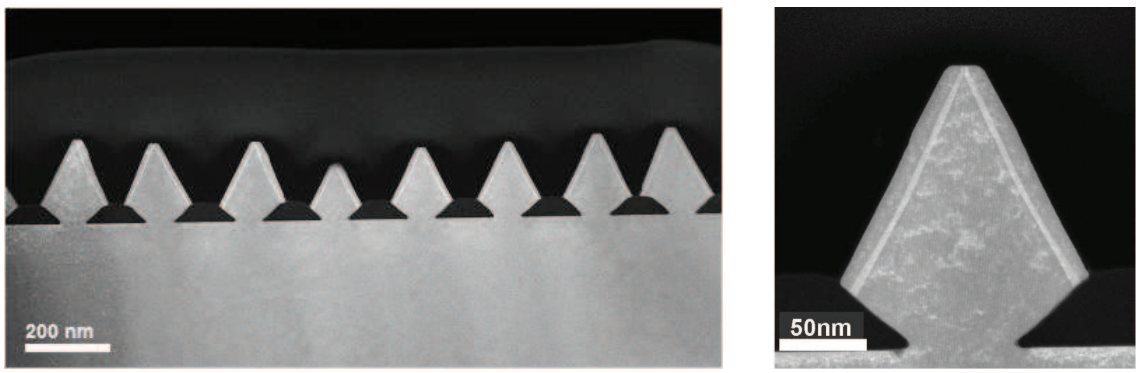

Fig. 9: TEM cross-section images of GaN stripes with semipolar InGaN/GaN quantum wells on the sidefacets.

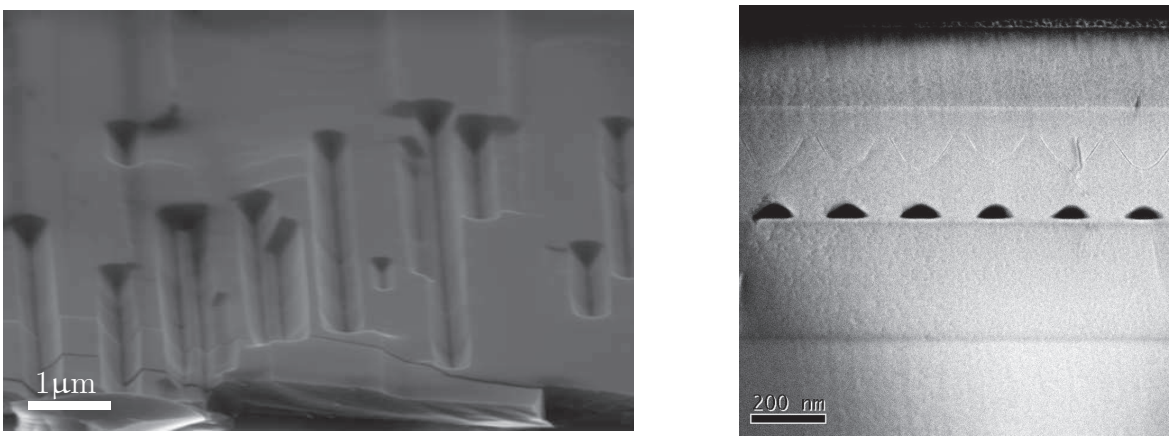

Fig. 10: Comparison of the embedding for different orientations. The SEM picture on the left (topview) shows a sample with stripes oriented along *a*-directin with $\{10\bar{1}1\}$ facets being incompletely planarized whereas the TEM picture on the right (cross-section) shows the immaculate embedding of a structure with $\{11\bar{2}2\}$ side facets.

3.2 Optical investigation - Gain!

In photoluminescence measurements the strong light matter coupling can be observed by a periodic modulation of the spectra. For the PL spetra in Fig. 11 the sample was excited from the top and the light emitted parallel to the surface plane from cleft edges was collected. We observe a huge difference for light emitted parallel and perpendicular to the stripe orientations owing to the periodic change in refractive index experienced by light emitted perpendicular to the stripes. Obviously, the period of the structure and the wavelength of the QW emission need to be balanced carefully. Nevertheless, figure 12 shows optical gain measurements performed on a first not perfectly planarized test structure. Although the losses and pump power are relatively high, net optical gain was achieved showing great promise for future samples with improved waveguiding.

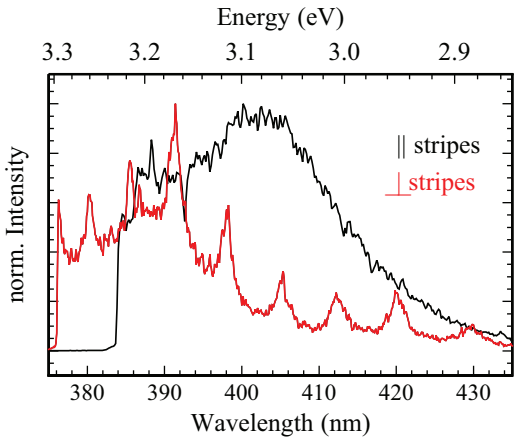

Fig. 11: PL spectra recorded for light emission $\parallel$ and $\perp$ to the stripes.

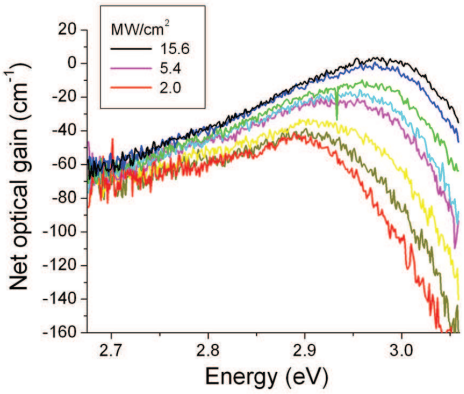

Fig. 12: Optical gain spectra recorded for a not perfectly planarized structure with submicrometer sized 3D GaN structures and semipolar InGaN/GaN QWs.

4. Conclusion

Evolving previously realized designs of light emitting diodes based on selectively grown GaN stripes we have developed two approaches to realize laser diodes with semipolar quantum wells. We have shown the epitaxial feasibility to fabricate an AlGaN/GaN waveguide with triangular cross-section. After establishing a waveguide design, semipolar InGaN/GaN quantum wells are to be included. For the approach of embedding the semipolar quantum wells inside a waveguide grown in polar direction, optical excitation resulted in quantum well emission and optical gain. The focus of further development lies upon improvements of optical confinement and consequent reduction of losses. The simulations were performed at the University of Kassel by B. Witzigmann. Gain measurements were performed by D. Dräger and M. Brendel at the Technical University of Braunschweig. Technical and scientific support by I. Argut, J. Biskupek, R. Blood, A. Chuvilin, F. Demaria, K. Forghani, F. Lipski, Y. Men, S. Schwaiger, W. Schwarz, J. Wang and T. Wunderer is gratefully acknowledged.

References

[1] H. Ohta, S.P. DenBaars, and S. Nakamura, "Future of group-III nitride semiconductor green laser diodes", *J. Opt. Soc. Am. B*, vol. 27, pp. B45–B49, 2010.

[2] B. Neubert, T. Wunderer, P. Brückner, F. Scholz, M. Feneberg, F. Lipski, M. Schirra, K. Thonke, "Semipolar GaN/GaInN LEDs with more than 1 mW optical output power", *J. Cryst. Growth*, vol. 298, pp. 706–709, 2007.

[3] O.-H. Nam, M. D. Bremser, B.L. Ward, R.J. Nemanich and R.F. Davis, "Growth of GaN and $Al_{0.2}Ga_{0.8}N$ on patterened substrates via organometallic vapor phase epitaxy", *Jpn. J. Appl. Phys.*, vol. 36, pp. L532–L535, 1997.

[4] Y. Kato, S. Kitamura, K. Hiramatsu, N. Sawaki, "Selective growth of wurtzite GaN and $Al_xGa_{1-x}N$ on GaN/sapphire substrates by metalorganic vapor phase epitaxy", *J. Cryst. Growth*, vol. 144, pp. 133–140, 1994.

[5] T. Wunderer, F. Lipski, S. Schwaiger, J. Hertkorn, M. Wiedenmann, M. Feneberg, K. Thonke, and F. Scholz, "Properties of blue and green InGaN/GaN quantum well emission on structured semipolar surfaces", *Jpn. J. Appl. Phys.*, vol. 48, pp. 060201-1–060201-3, 2009.

[6] T. Wunderer, M. Feneberg, F. Lipski, J. Wang, R.A.R. Leute, S. Schwaiger, K. Thonke, A. Chuvilin, U. Kaiser, S. Metzner, F. Bertram, J. Christen, G. J. Beirne, M. Jetter, P. Michler, L. Schade, G. Vierheilig, U.T. Schwarz, A.D. Dräger, A. Hangleiter, F. Scholz, "Three-dimensional GaN for semipolar light emitters", *phys. stat. sol. (b)*, DOI: 10.1002/pssb.201046352, 2010.

[7] T. Wunderer, "Optimization of semipolar GaInN/GaN blue/green Light emitting diodes on $\{1\bar{1}01\}$ GaN side facets", *Annual Report 2007*, pp. 67–78. Ulm University, Institute of Optoelectronics.

Heat Induced Dynamics of Gold Nanoparticles on Atomically Clean Graphene

Benedikt Westenfelder

We designed a graphene based TEM sample carrier to enable atomically resolved studies of the heat-induced evolution of deposits on graphene. By in-situ application of electric current to a freestanding sheet of graphene, we obtain local temperatures exceeding 1000 K. We investigated various heat induced phenomena of gold particles on an atomically clean graphene surface. Initially, the gold nanoislands decrease their surface-area-to-volume ratio with increasing temperature by assuming a more spherical shape. At higher temperatures, we observe their migration and a self-organization into parallel straight lines.

1. Introduction

The utilization of the unique properties of graphene as a quasi transparent sample support [1–5] in conjunction with the progressive development of transmission electron microscopy [6] allowed high-contrast imaging of light atoms and molecules and their dynamics for the first time. Furthermore, the remarkable material properties of freely suspended graphene, such as superior electrical conductivity [7], highest mechanical stability [8, 9] as well as enormous thermal stability [10], provide a controlled generation of extreme temperatures by Joule heating [10–13].

In this way one important aspect of in situ sample manipulation can valuably be combined with the aspect of high-contrast imaging. For the in-situ Joule heating of a freely suspended sheet of graphene, we employ a microfabricated, in-situ applicable TEM sample carrier that was developed recently [14]. A graphene flake together with predeposited gold nanoparticles has been positioned directly above the electrode fingers of that carrier (Fig. 1). Its special design allows to obtain reliably temperatures in excess of 1000 K in atomically thin, crystalline and electron transparent single- and few-layer graphene membranes [14]. In this letter, we report on the results from observations of heat-induced dynamics of deposits on an electrically biased graphene membrane. The adsorbates described here are gold nanoislands predeposited by thermal evaporation onto the membranes.

2. Experiment

The investigations have been performed in an aberration-corrected (CEOS type corrector) FEI 80-300 Titan transmission electron microscope. This system was operated at an accelerating voltage of 80 kV in order to stay below the threshold for knock-on damage of graphene [15]. Sample carriers were mounted in a Fischione 2510 biasing TEM holder, and

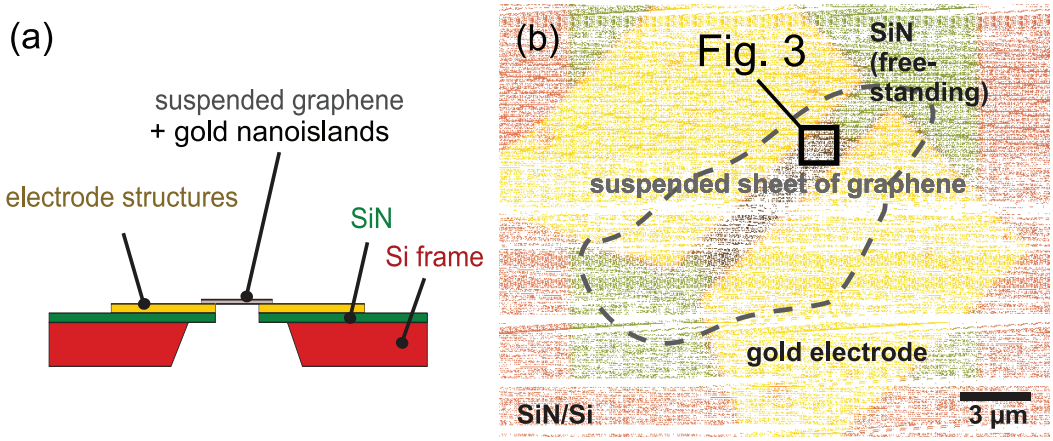

Fig. 1: (a) Cross-sectional schematic illustration of the sample carrier design. (b) Optical micrograph of the electrode support structure on which a graphene sheet is suspended. A small region is marked by a black square. In the following, we will have a closer look at this place, which corresponds to the TEM image in Fig. 3.

an electrical current was passed through the graphene sample by applying a bias voltage between the electrodes. We observed first significant transformations of gold nanoislands for an estimated current-density in the range of $2 \cdot 10^7\,\mathrm{Acm}^{-2}$ with an applied bias of about 2 V.

3. Heat Induced Phenomena

3.1 The dynamics of pre-deposited nanoislands

The initial observations under gentle heating correspond to previously described transformations and help to estimate the temperature distribution in our sample geometry. It is well known, that the diffusion of Au adatoms on the surface of gold nanoparticles is already significant at room temperature [16, 17], leading to continuous shape changes of the particles upon heating [18]. In case of our deposited gold nanoislands, we could nicely confirm the decrease of the particle surface-area-to-volume ratio, i.e. a transformation to more spherical shapes, with increasing temperature (Fig. 2a). After exceeding a certain temperature limit, the first of the almost spherically shaped particles form liquid drops and start to evaporate (Fig. 2b) [14, 19]. According to the theoretical predictions and similar experiments, the temperature related to this phase transition strongly depends on the particle size [20], and in our case was estimated to be in the range of 800 °C to 1300 °C. As the gold particles evaporate during TEM observation, a carbon shell with the shape of the original gold particle becomes visible (Fig. 2c). It appears that the carbon layer is formed on the gold particles under electron irradiation and then remains in shape even after the gold particle is removed. In previous in situ experiments with gold nanoparticles deposited on ultrathin amorphous carbon, it has been found that temperatures above 425 °C in conjunction with intense electron beam irradiation drive such a particle encapsulation [18]. Similar to our observations, these shells consist typically of

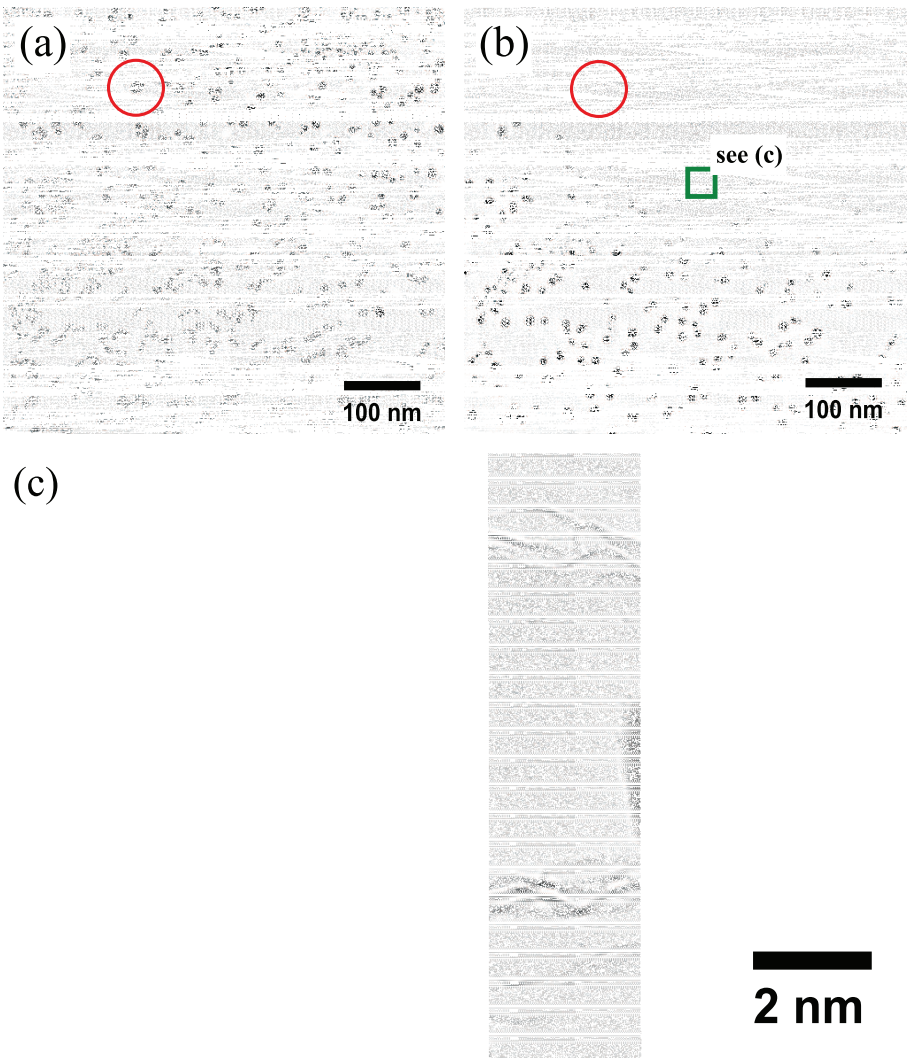

Fig. 2: (a) TEM image of gold nanoislands deposited on graphene. A temperature gradient from the lower left corner to the upper right corner corresponds to the variation of the gold particle shape. (b) The same area (the same position is indicated by an open circle) after further increasing the applied electrical current through the graphene sheet. The particles get encapsulated with carbon shells and finally evaporate. (c) A liquefied particle evaporates inside a shell of amorphous carbon (see also little square in (b)) at atomic resolution.

2–5 atomic carbon layers. Although the shells appear similar to closed graphene sheets, our atomically resolved images clearly suggest a large extent of imperfections. In particular, these atomic carbon layers don't exhibit a strict crystalline structure, but show a high degree of amorphization (Fig. 2c).

The phase transformations described above have been observed under permanent electron irradiation. Obviously this radiation is essentially accompanied with an electron beam induced demobilization and enrichment of hydrocarbons [21]. Therefore we repeated the same experiment without initial irradiation. Again we applied a current density of $2 \cdot 10^7\,\mathrm{Acm}^{-2}$, but kept wide areas of the graphene supported nanoparticles unexposed

to the e-beam for several minutes. Then, we started recording images of these regions. Two very clear differences are found in this case: First, atomically clean graphene is obtained on large areas (Fig. 3), only if heat is applied before intense electron irradiation. This confirms that, initially, we have mobile hydrocarbon deposits on our samples that

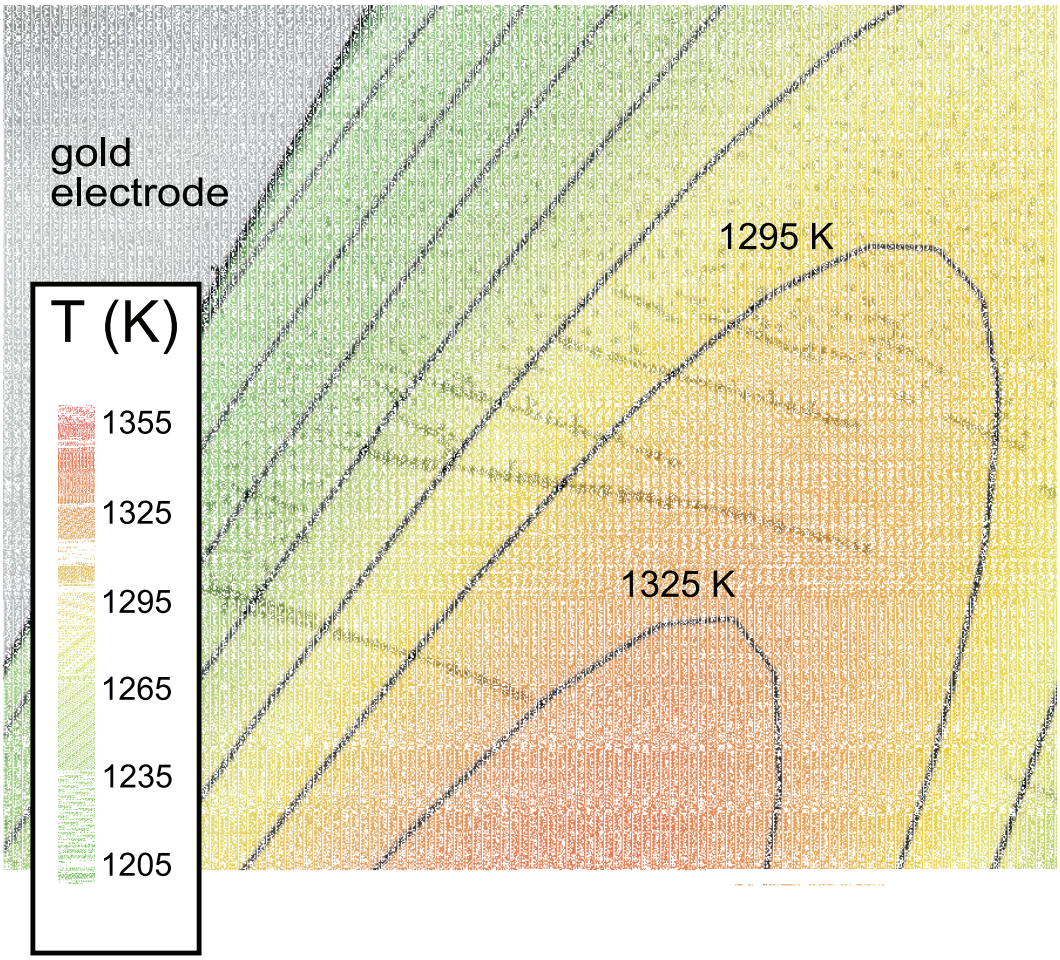

Fig. 3: TEM image of a sample area corresponding to the little empty square in Fig. 1b. In addition to the visible gold particle distribution we overlaid the corresponding temperature profile according to our FEM calculations.

can be driven off by modest heating. However, after exposure to the electron beam, the contamination is fixed and transforms under heat (as described below) but does not evaporate. Second, the gold particles do not become encapsulated and do not leave behind a carbonaceous shell. Surprisingly, instead of liquidation or evaporation, we now observe that the particles as a whole become mobile and migrate to form linear clusters at elevated temperatures.

This migration can be confirmed by molecular dynamic studies in conjunction with kinetic Monte Carlo simulations [22]. The migration or the so-called thermophoretic motion

has been already investigated for gold nanoparticles in conjunctions with carbon nanotubes [23–25], but not on a graphene substrate. We believe that the driving force of the thermophoresis-like behavior corresponds to a preference of the particles to stay in the same aggregate state. If a certain gold particle is almost reaching its melting point, then the particle simply migrates into a direction of the negative temperature gradient. This interpretation would be consistent with our observation that initially, comparatively flat nanoislands do not show this significant movement (they are still far away from their melting point), whereas the hot, spherical particles do migrate.

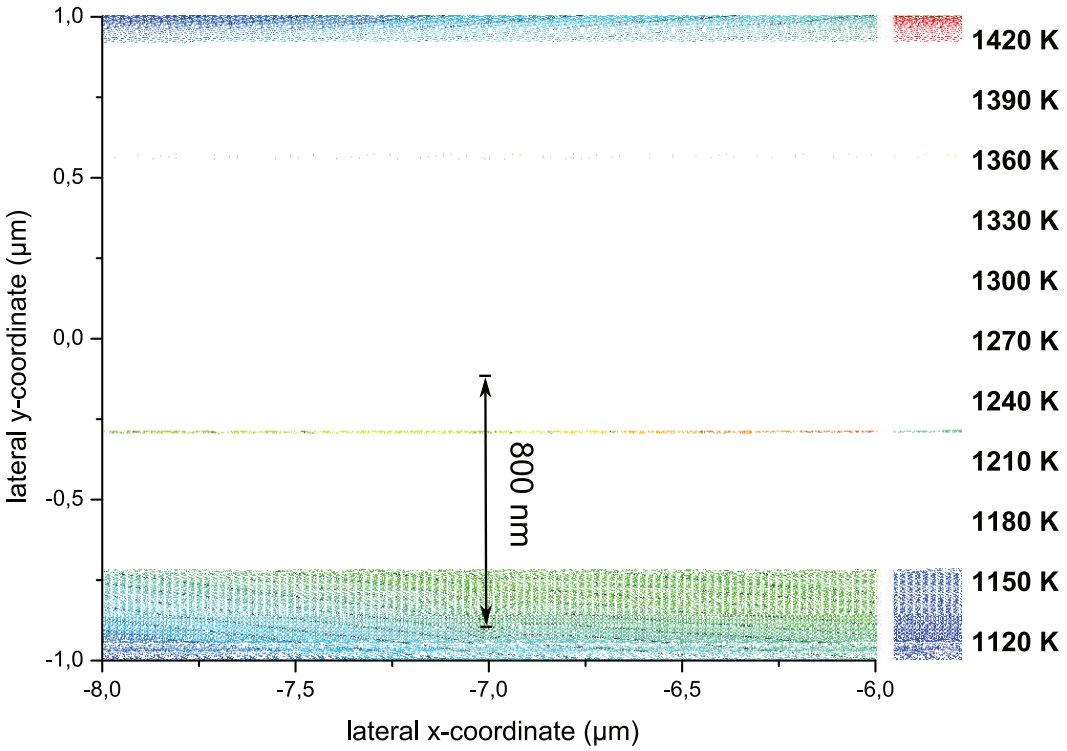

Fig. 4: FEM simulated temperature profile taking the presence of one gold particle chain into account. The gold chain perturbs the temperature profile such that gold particles which drift along the thermal gradient arrive at the end of the chain, indicating a possible mechanism for its self-organization.

Quite remarkably, the gold particles cluster into linear chains (Fig. 3). Towards a deeper understanding of this effect, we performed finite-element (FEM) simulations in order to obtain a temperature distribution for our sample geometry. In a first step, we include only the sample carrier geometry and the graphene membrane into the simulation. A resulting temperature profile is overlaid onto the image in Fig. 3. In the next step, we include a gold particle chain as a thermally conducting element into the simulation (Fig. 4). For a rough approximation we assumed a gold wire of 15 nm diameter and a length of 800 nm deposited on the graphene sheet. Furthermore, we neglected quantum size effects as well as an electrical conductance along the wire axis. For the result it was indeed important to assume the wire would rather conduct heat than electrical current perpendicular to the carbon shells (that encapsulate the gold particles). Otherwise an additional contribution of the electrical current flow through the gold wire compensates the local effect of

increased heat dissipation. Now, the obtained temperature profile indicates that the gold particle chains create a "short circuit" in the temperature profile, i.e. a nearly constant temperature along the chain and steep temperature gradients in the graphene membrane near their ends. This suggests a possible mechanism for the chain formation: Individual gold particles that migrate along the temperature gradient will most likely end up at the end of an already existing gold particle chain, thereby extending it by one element.

4. Conclusions

In summary, we presented atomically resolved in situ TEM studies of the heat-induced evolution of gold nanoislands on graphene. In case of an atomically clean graphene surface and at high temperatures, we found that the gold particles develop a surprising dynamic behavior. In particular, we investigated their migration along the negative temperature gradient that is apparently accompanied by an related self-organization effect aligning the particles into parallel straight lines.

5. Acknowledgement

Special thanks go to Jannik C. Meyer from the Electron Microscopy Group of Materials Science for his great support with respect to the microscope operation and scientific questions.

References

[1] W.H. Dobelle and M. Beer, "Chemically cleaved graphite support films for electron microscopy", *J. Cell Biol.*, vol. 39, pp. 733–735, 1968.

[2] J.C. Meyer, C.O. Girit, M.F. Crommie, and A. Zettl, "Imaging and dynamics of light atoms and molecules on graphene", *Nature*, vol. 454, pp. 319–322, 2008.

[3] J.C. Meyer, C. Kisielowski, R. Erni, M.D. Rossel, M.F. Crommie, and A. Zettl, "Direct imaging of lattice atoms and topological defects in graphene membranes", *Nano Lett.*, vol. 8, pp. 3582–3586, 2008.

[4] U. Kaiser, A. Chuvilin, J.C. Meyer, and J. Biskupek, "Microscopy at the bottom", in *Materials Science Microscopy Conference MC2009*, W. Grogger, F. Hofer, and P. P. (Eds.), vol. 3, pp. 1–6, 2009.

[5] Z. Lee, K.J. Jeon, A. Dato, R. Erni, T.J. Richardson, M. Frenklach, and V. Radmilovi, "Direct imaging of soft-hard interfaces enabled by graphene", *Nano Lett.*, vol. 9, pp. 3365–3369, 2009.

[6] P. Hartel, H. Müller, S. Uhlemann, J. Zach, U. Löbau, R. Höschen, and M. Haider, "Demonstration of CC/CS-correction in HRTEM", in *EMC 2008 14th European Microscopy Congress 1-5 September 2008, Aachen, Germany*, M. Luysberg, K. Tillmann, and T. Weirich (Eds.), pp. 27–28, Springer, Berlin and Heidelberg, 2008.

[7] A.H.C. Neto, F. Guinea, N.M.R. Peres, K.S. Novoselov, and A.K. Geim, "The electronic properties of graphene", *Rev. Mod. Phys.*, vol. 81, pp. 109–162, 2009.

[8] C. Lee, X. Wei, J.W. Kysar, and J. Hone, "Measurement of the elastic properties and intrinsic strength of monolayer graphene", *Science*, vol. 321, pp. 385–388, 2008.

[9] T.J. Booth, P. Blake, R.R. Nair, D. Jiang, E.W. Hill, U. Bangert, A. Bleloch, M. Gass, K.S. Novoselov, M.I. Katsnelson, and A.K. Geim, "Macroscopic graphene membranes and their extraordinary stiffness", *Nano Lett.*, vol. 8, pp. 2442–2446, 2008.

[10] K. Kim, W. Regan, B. Geng, B. Alemn, B.M. Kessler, F. Wang, M.F. Crommie, and A. Zettl, "High-temperature stability of suspended single-layer graphene", *phys. stat. sol. (RRL)*, vol. 4, pp. 302–304, 2010.

[11] X. Jia, M. Hofmann, V. Meunier, B.G. Sumpter, J. Campos-Delgado, J.M. Romo-Herrera, H. Son, Y.P. Hsieh, A. Reina, J. Kong, M. Terrones, and M.S. Dresselhaus, "Controlled formation of sharp zigzag and armchair edges in graphitic nanoribbons", *Science*, vol. 323, pp. 1701–1705, 2009.

[12] J.Y. Huang, F. Ding, B.I. Yakobson, P. Lu, L. Qi, and J. Li, "In situ observation of graphene sublimation and multi-layer edge reconstructions", *PNAS*, vol. 106, pp. 10103–10108, 2009.

[13] L. Qi, J.Y. Huang, J. Feng, and J. Li, "In situ observations of the nucleation and growth of atomically sharp graphene bilayer edges", *Carbon*, vol. 48, pp. 2354–2360, 2010.

[14] B. Westenfelder, J.C. Meyer, J. Biskupek, G. Algara-Siller, L.G. Lechner, J. Kusterer, U. Kaiser, C.E. Krill, E. Kohn, and F. Scholz, "Graphene-based sample supports for in situ high-resolution TEM electrical investigations", *J. Phys. D: Appl. Phys.*, vol. 44, pp. 055502-1–7, 2011.

[15] A. Zobelli, A. Gloter, C.P. Ewels, G. Seifert, and C. Colliex, "Electron knock-on cross section of carbon and boron nitride nanotubes", *Phys. Rev. B*, vol. 75, pp. 245402-1–9, 2007.

[16] J.O. Bovin, R. Wallenberg, and D.J. Smith, "Imaging of atomic clouds outside the surfaces of gold crystals by electron microscopy", *Nature*, vol. 17, pp. 47–49, 1985.

[17] S. Iijima and T. Ichihashi, "Motion of surface atoms on small gold particles revealed by HREM with real-time VTR system", *Jpn. J. Appl. Phys.*, vol. 24, pp. L125–L128, 1985.

[18] E. Sutter, P. Sutter, and Y. Zhu, "Assembly and interaction of Au/C core-shell nanostructures: in situ observation in the transmission electron microscope", *Nano Lett.*, vol. 5, pp. 2092–2096, 2005.

[19] A.S. Barnard, N.P. Young, A.I. Kirkland, M.A. van Huis, and H. Xu, "Nanogold: a quantitative phase map", *ACS Nano*, vol. 3, pp. 1431–1436, 2009.

[20] P. Buffat and J.P. Borel, "Size effect on the melting temperature of gold particles", *Phys. Rev. A*, vol. 13, pp. 2287–2298, 2000.

[21] K. Rykaczewski, W.B. White, and A.G. Fedorov, "Analysis of electron beam induced deposition (EBID) of residual hydrocarbons in electron microscopy", *J. Appl. Phys.*, vol. 101, pp. 054307-1–12, 2007.

[22] L.J. Lewis, "Diffusion of gold nanoclusters on graphite", *Phys. Rev. B*, vol. 61, pp. 16084–16090, 2000.

[23] A. Barreiro, R. Rurali, E.R. Hernández, J. Moser, T. Pichler, L. Forro, and A. Bachtold, "Subnanometer motion of cargoes driven by thermal gradients along carbon nanotubes", *Science*, vol. 320, pp. 775–778, 2008.

[24] H.A. Zambrano, J.H. Walther, and R.L. Jaffe, "Thermally driven molecular linear motors: a molecular dynamics study", *J. Chem. Phys.*, vol. 131, pp. 241104-1–3, 2009.

[25] P.A.E. Schoen, J.H. Walther, D. Poulikakos, and P. Koumoutsakos, "Phonon assisted thermophoretic motion of gold nanoparticles inside carbon nanotubes", *Appl. Phys. Lett.*, vol. 90, pp. 253116-1–3, 2007.

Photoluminescence Spectroscopy on Optically Pumped Semiconductor Disk Lasers

Frank Demaria and Alexander Hein

Photoluminescence spectra from optically pumped semiconductor disk lasers are presented. A detailled discussion of the results is given as well as a description of the measurement setup and procedure. Spectra which have been measured under different detection angles show specific features which are attributed either to the intrinsic photoluminescence of the gain region or to the distortion which arises from the optical resonances of the integral layer structure of the device. The influence of the extended resonator is investigated by applying the described technique to laser samples in configurations with and without external mirror.

1. Introduction

Photoluminescence (PL) spectra offer valuable insight to the basic physical characteristics and the principal behavior of optically pumped semiconductor disk lasers. PL arises from spontaneous emission processes which take place in the excited regions within the structure. The energy of the emitted photons is thereby determined by the difference of the energy states of the recombining carriers which is at least the band gap at their local position. Electrons and holes are generated by absorption of the incident pump radiation. Fundamental absorption processes can occur within the barriers or in the subbands of the quantum wells of the periodic gain structure [1]. From this point of view, the gain structure of an optically pumped disk laser is actually optically absorbing and amplifying at the same time. In the experiments described here, pumping is predominantly carried out within the barriers of a periodic gain structure designed for a laser emission wavelength of 920 nm. Barrier pumping is the most common way of optical pumping of semiconductor disk lasers as it is more straightforward than direct pumping of the quantum wells [2, 3]. Quantum well pumping on the other hand has the advantage of a smaller quantum defect energy given by the difference of the energy of the pump photons and the emitted laser photons [4]. Both approaches, however, require a thorough tuning of the optical resonances of the overall layer structure and the spectral absorption and amplification properties of the quantum wells to provide high efficiencies [5, 6]. Information on both is contained in the PL spectra. However, careful interpretation is necessary to designate the origin of observed spectral characteristics.

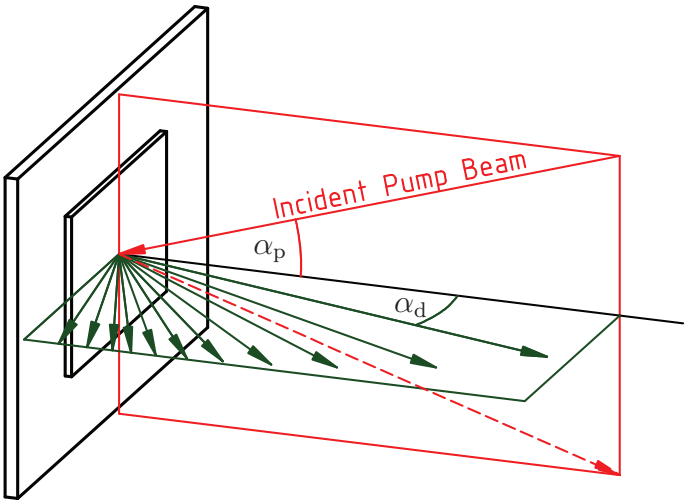

Fig. 1: Simplified arrangement of the experimental setup. Pump radiation is incident under the pump angle α_p in the vertical plane of incidence whereas the emitted PL spectrum is measured at the detection angle α_d in the horizontal plane. The thin semiconductor disk laser is mounted on a copper heat sink.

2. Experimental Setup and Design of the Disk Laser Chip

An outline of the basic geometrical arrangement of the experimental setup is given in Fig. 1. In the described experiments, optical pumping is realized at pump angles α_p between 20 ° and 30 °. At these values, the maximum absorptivity is provided for the pump wavelength, according to the layer design of the samples under investigation. The wavelength spectrum of the PL is measured at the detection angle α_d. To achieve best spatial separation between the reflected fraction of the pump beam and the emitted PL, the plane of detection is perpendicular to the plane of incidence of the pump beam. A fiber-coupled diode laser is used as a pump source. Its emission wavelength ranges between 799 and 804 nm, depending on the emitted pump power and the temperature of the cooling water. A simple arrangement of two lenses is used to focus the light from the 200 µm-core-diameter fiber to the laser sample which results in a mean pump spot diameter of approximately 0.4 mm. The pump beam possesses low spatial beam quality with a diffraction number of $M^2 \approx 55$ and therefore results in a full far-field angle of 8 ° for the given optical arrangement. This value has to be considered for the angle of convergence of the incident pump beam respectively for the divergence of its reflected fraction. It represents an inherent uncertainty of the pump angle.

Detection of the PL is realized by coupling to a fiber which is connected to an optical diffraction-grating spectrum analyzer. To do so, a lens with 14.5 mm focal length and an aperture of 8 mm is placed 130 mm away from the pumped area. That way, an angular resolution of less than 1.8 ° is established. The laser sample is soldered with indium on a gold plated copper heat sink whose temperature can be stabilized at arbitrary temperatures between −20 and +70 °C.

A detailled discussion of the layer design of sample #1 is given in [7] or our contribution to the last year's annual report [8]. Basically, sample #1 and #2 consist of a periodic gain structure [1] and a double-band Bragg reflector [9, 10]. The periodic gain structure of sample #1 is formed by a sequence of six 8 nm-thick $In_{0.08}Ga_{0.92}As$-GaAs quantum wells. The surrounding barriers of distinct quantum wells are separated by large bandgap $GaAs_{0.71}P_{0.29}$ strain compensation layers which also act as a carrier diffusion barrier.

Sample #2 contains a periodic gain structure with nine double quantum wells, consisting of 6 nm-thick $In_{0.08}Ga_{0.92}As$-GaAs quantum wells separated by a 6 nm barrier. The double-band Bragg reflector of both structures is designed to provide high reflectivity for the incident pump light and for the lasing wavelength within its two stop bands.

3. PL Spectra and Interpretation

3.1 Operation without external mirror

Typical photoluminescence spectra which have been taken from sample #1 are shown in Fig. 2. In this example, the influence of temperature and pump intensity variations can be observed. The spectra are detected at a constant angle of 20 °. Pumping is realized with a wavelength of 799 nm at a pump angle of 30 °. A distinct but low-intensity peak resulting from the pump light can be observed in the spectrum for low pump intensity and low temperature. It occurred also in the other spectra, however it is not shown there as the recorded data does not cover this wavelength.

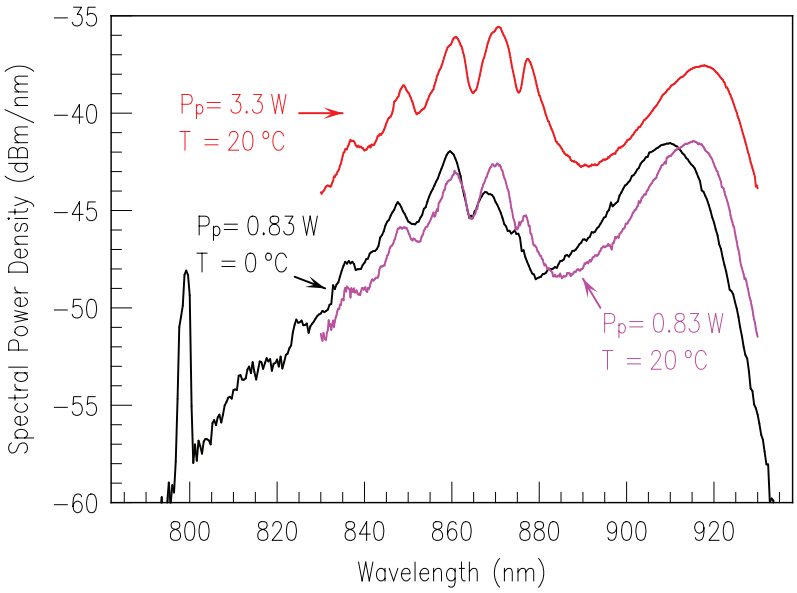

Fig. 2: PL spectra from laser sample #1 under operation without external resonator. All spectra are detected under an detection angle of $\lambda_d = 20\,°$ during operation with a pump angle of $\lambda_p = 30\,°$. The lower curves are measured at a temperature of 0 and 20 °C and refer to an optical pump power of 0.83 W which would be below threshold during laser operation with a standard external mirror. The upper curve with a heat sink temperature of 20 °C refers to an incident optical pump power of 3.3 W which would be significantly above threshold in operation with an external mirror.

Generally, all spectra can be divided into two distinct regions which represent photon energies below and above the band gap energy of the GaAs barriers. They are roughly separated by the valley around 880 nm. For the longer wavelength region, a broad smooth peak can be observed in all curves with a maximum between 910 and 920 nm. It represents the PL from the $In_{0.08}Ga_{0.92}As$ quantum wells. For the curves with weak pumping,

the maximum shifts from 909.5 nm at 0 °C to 915.5 nm at 20 °C. A wavelength shift of approximately 0.3 nm/K is usually attributed to the temperature dependent band-gap decrease.

The PL between 820 and 880 nm, has its origin in the GaAs barriers. Here, a pronounced modulation of the curves can be observed which leads to five local maxima. For a physical interpretation of the spectrum within this wavelength range it is necessary to distinguish between the broad substantial curve which represents the intrinsic PL from the gain structure and the short periodic modulation. The latter is connected to the inconstancy of reflectivity and phase which is introduced by the back sided Bragg reflector in this wavelength region. Fluctuations of reflectivity with the same origin can be observed in the measured reflectivity spectra shown in Fig. 3. Ultimately their maxima represent optical resonances within the whole structure.

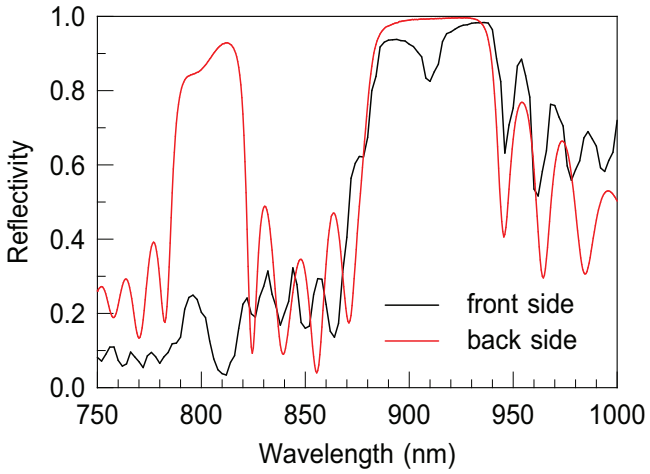

Fig. 3: Front and back side reflectivity spectra from sample #1 (same as in Fig. 2). Both are measured at a detection angle of 10 °. The back side spectrum was measured prior to metalization and mounting.

Whilst the intrinsic PL-curve shows a quite similar temperature offset above and below 880 nm, the temperature shift of the distinct resonances is significantly smaller. They arise basicly from the temperature dependent change of the optical layer thicknesses within the structure. Above 880 nm, no periodic modulation of the intrinsic curve takes place because it lies within the region of the broad stopband where a quite constant reflectivity and phase is introduced by the Bragg reflector.

The optical resonances can clearly be distinguished from the intrinsic PL curve when the angle of detection is varied. In this case, the resonance peaks move according to the cosine of the internal propagation angle. Their intensity, however, depends on the substantial PL at the particular wavelength which is independent from the detection angle. An example, which has been measured for sample #2 is given in Fig. 4. It shows an array of PL spectra for which the detection angle was varied from 0 to 90 °. The envelope of the curves roughly represents the intrinsic PL with its maximum around 873 nm for the barriers and at approximately 905 nm for the quantum wells. It is essential for this interpretation that the coupling into the fiber of the spectrometer was maximized at each detection angle with utmost care to guarantee a consistent coupling efficiency.

The observed resonance shift can be described fairly good with the direction cosine of the

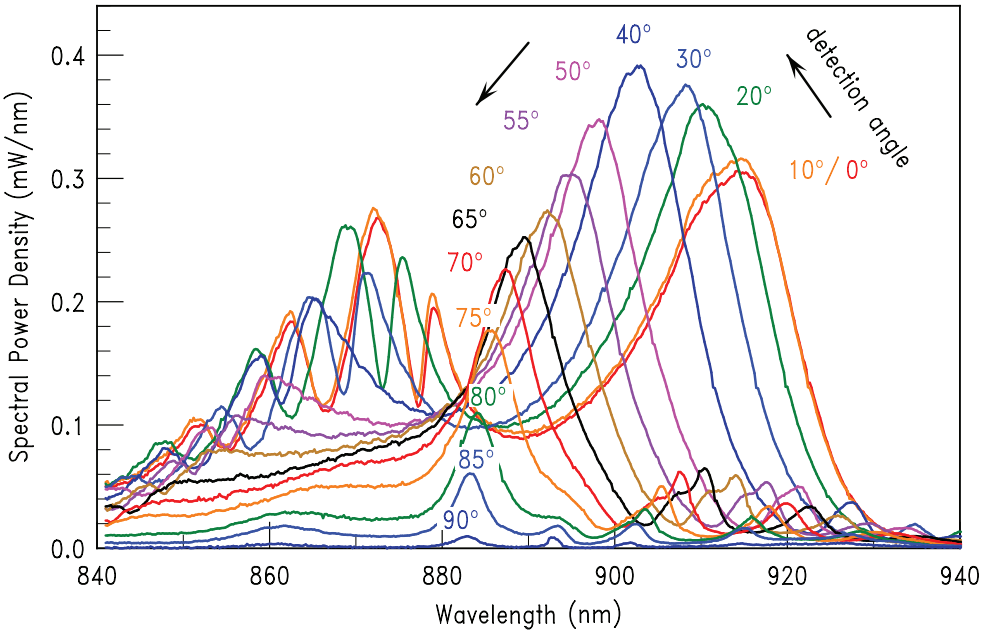

Fig. 4: PL spectra at different detection angles from sample #2. Pumping was realized with an optical pump power of 3.3 W at a heat sink temperature of 20 °C.

internally propagating optical wave

$$\lambda_{\mathrm{res}} = \lambda_0 \cos\beta, \tag{1}$$

wherein the internal propagation angle β can be deduced from the external propagation angle α_{d} by Snell's law, given by

$$\sin\beta = \frac{\sin\alpha_{\mathrm{d}}}{n_{\mathrm{eff}}}. \tag{2}$$

The influence of the layer structure is considered by the effective refractive index n_{eff}. Figure 5 shows a plot of the measured resonance wavelengths versus the detection angle, taken from Fig. 4, together with the fitted curve according to (1) and (2). From that, a

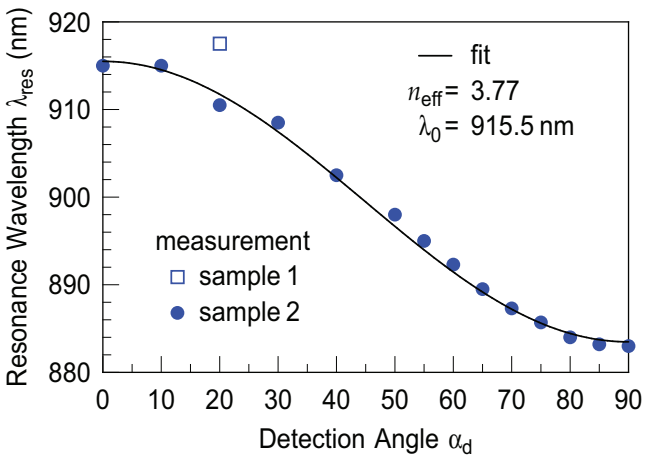

Fig. 5: The angular shift of the optical resonances from Fig. 4 (sample #2, dots) yields the effective refractive index n_{eff} and the resonance wavelength for perpendicular emission λ_0 as fit parameters from (1) and (2). The open square shows the resonance wavelength taken from Fig. 2 (sample #1) at the same temperature and pump intensity.

resonance wavelength for perpendicular emission of $\lambda_0 = 915.5\,\text{nm}$ and an effective refractive index $n_{\text{eff}} = 3.77$ can be deduced. The resonance wavelength actually determines the emission wavelength during laser operation. Obviously it is significantly shorter than the intended emission wavelength of 920 nm. The effective refractive index represents more or less an average value of the refractive index of the layer structure within the wavelength range under consideration. A quite important aspect is also at which wavelength and angle the maximum spectral PL intensity occurs. For sample #2 this is the case for 902.5 nm and 40 °, according to Fig. 4.

3.2 Laser operation with external mirror

Sample #1 reveals a comparatively good laser performance with a maximum optical output power above 4 W, which is shown in Fig. 6. The output characteristics has been recorded with external mirrors of 100 mm radius of curvature and reflectivities of 99 and 98 %. Emission wavelengths between 920 nm at threshold and 927 nm at maximum output power are observed. With sample #2 however, in the best case an optical output power of only 1 W was achieved in operation with an external mirror. Thereby, an emission wavelength between 913 nm at threshold and 916 nm at maximum optical output was observed.

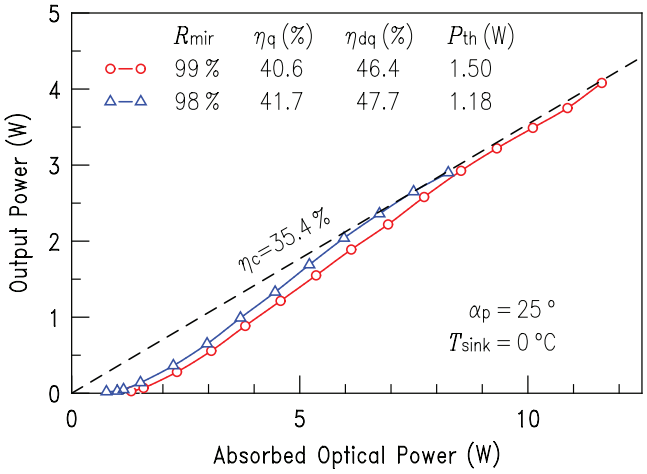

Fig. 6: Optical laser output characteristics of sample #1. A simple hemispherical resonator setup with external mirrors with 100 mm radius of curvature and reflectivities of 99 and 98 % was used. The larger threshold in operation with the mirror of higher reflectivity can be explained with a larger pump-spot diameter.

During the investigation of the PL spectra, an external mirror with 98 % and a radius of curvature of 150 mm was used. The output characteristic was not significantly changed by the different radius of the mirror.

PL spectra detected at 20 ° for various incident pump powers P_{p} are shown in Fig. 7. The heatsink temperature was stabilized at 0 °C which is the same value as for Fig. 6. All curves show a distinct peak from the pump laser which is slightly displaced from 800 nm to 801 nm with increasing pump power. Also the photoluminescence from both, the barriers and the quantum wells, can be distinguished clearly, much like in operation without external mirror from Fig. 2. Above threshold, in the curves with pump powers of 2.1 W and more, a distinct lasing peak arising from the stimulated emission of the quantum wells can be observed. It is important to note, that the laser light which establishes this peak

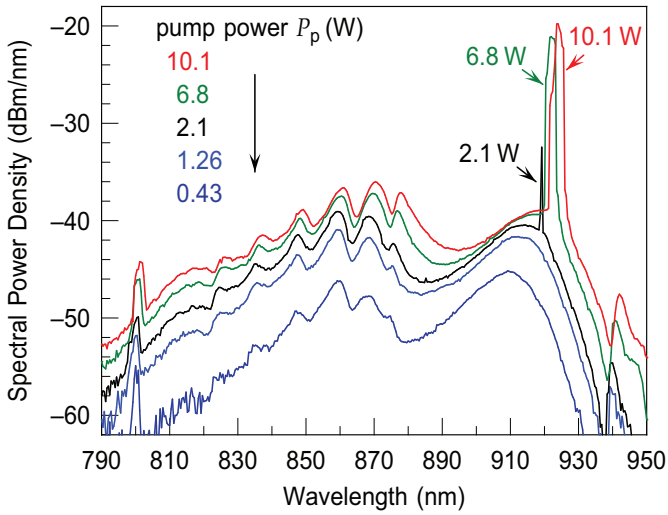

Fig. 7: PL spectra from sample #1 for various pump intensities below and above threshold in operation with an external mirror. All spectra are detected at an angle of 20 °. A mirror with a reflectivity of 98 % and a radius of curvature of 150 mm was used.

is not emitted through the external mirror. For the resonator length of approximately 100 mm, the external mirror with an aperture of 12.7 mm only covers detection angles up to 3.6 °. The difference becomes clear by comparing the 20 ° curves from Fig. 7 with the laser spectrum at an detection angle of 0 ° in Fig. 8 which was measured directly trough the outcoupling mirror. The measurement shown in Fig. 8 does not expose any spectral displacement of the laser peak for different detection angles. The reason is that much unlike the PL radiation in the rest of the spectra, the laser peaks which are detected at different angles are not related to a different direction of propagation within the laser's layer structure. The intensity of the laser peak, however, is decreasing with increasing detection angle. Both gives evidence that the detected laser light is predominantly redirected by diffraction and scattering.

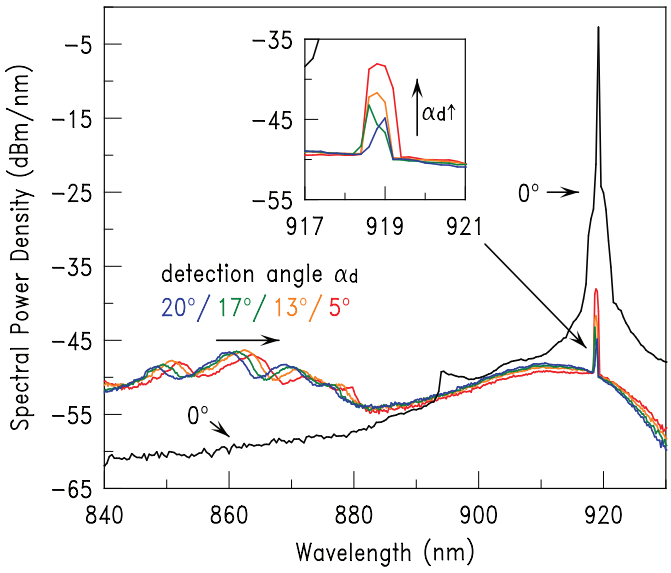

Fig. 8: PL spectra for various detection angles during laser operation with an optical pump power of 2.5 W for a heat sink temperature of 0 °C.

In Fig. 7, however, the wavelength of the laser emission is displaced for different pump intensities from 919 nm at 2.1 W to 924 nm at an incident pump power of 10.1 W. The local maxima of the resonances below 880 nm in the same measurement experience a smaller

displacement, much like in the measurement without an external resonator (Fig. 2). The displacement of the resonances is introduced mainly by the temperature dependent shift of the refractive index, whereas the shift of the lasing wavelength is related to the displacement of the spectral gain function. Remarkable is also that the intensity of the PL spectrum from the barriers (below 880 nm) increases much more than the PL intensity from the quantum wells (above 880 nm). With increasing pump intensity, the barriers become more and more populated with carriers whereas in the quantum wells, the carrier density is partially clamped. The observed increase of spontaneous emission in the barriers represents a considerable loss mechanism. A particular increase is indeed unavoidable because operation at high output powers requires a higher support of the quantum wells with carriers which is here a synonym for a higher diffusion current. This can, however, only arise from an enhanced gradient of the carrier concentration which in turn goes ahead with a higher concentration of carriers, especially in the barrier regions distant to the quantum wells.

Even though it is less pronounced, a continuous increase of the PL from the quantum wells indicates that also here, an entire clamping of the carrier density does not take place. This can particularly be explained by the reasonable assumption that the resonant gain structure is not homogeneously pumped both in the lateral and in the longitudinal direction. With increasing pump power, the non-uniform distribution of carriers over the quantum wells becomes even worse. This goes ahead with an enhanced PL, because in the regions with higher carrier density, spontaneous emission increases quadratically, due to the bimolecular recombination mechanism.

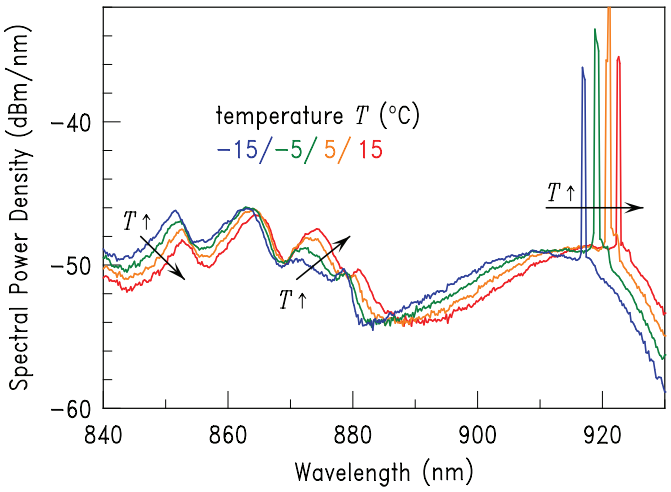

Fig. 9: PL spectra at a detection angle of $\alpha_d = 5°$ for various operation temperatures during laser operation. The optical pump power is 3.3 W for all curves.

For the sake of completeness, pure influence of a temperature change to the emitted PL and laser spectra is shown in Fig. 9. All spectra are measured at a detection angle of 5 ° with a constant optical pump power of 3.3 W. With increasing temperature, the laser peak shifts from 917.1 nm at -15 °C to 922.6 nm at 15 °C which corresponds to a spectral displacement of 0.183 nm/K. A quite similar shift can be observed for the substantial PL curves.

4. Conclusion and Outlook

We demonstrated a simple method to investigate spectral and angular resolved photoluminescence from optically pumped semiconductor disk lasers. The measurement technique can be applied for a pre-characterization of the samples prior to laser operation but also during operation of the devices in an extended resonator setup. The observed distortions of the spectra are correlated with longitudinal resonances within the layer structure of the sample. A decisive way to distinguish these resonances from the intrinsic photoluminescence is introduced by a variation of the detection angle. The resonance shift with the angle of measurement can be explained by the influence of the mean internal propagation angle. It can be calculated from Snell's law by the assumption of an effective refractive index for the layer structure. Its exact value can be evaluated from the measurement as a fit parameter.

Although measurements from two different samples have been presented, out major concern is rather to outline the principle of the measurement and to suggest an interpretation of the results, than to give a profound characterization of the devices. This would require a more extensive investigation which, of course, had to include PL spectra from sample #1 which had to be recorded over the hole angular range from 0 ° to 90 °. Anyway, the few measurements at angles of 20 ° and 5 ° which are shown in Figs. 2, 5 and 9 give evicence that the better performance of sample #1 accounts mainly for its longer resonance wavelength. It is better tuned to the gain function than the too short resonance wavelength of sample #2.

Considerable high intensities of the PL-spectra in laser operation, which can be observed in in Figs. 7 to 9 can be clearly attributed to the barriers of the structure. They reveal a serious loss mechanism which has to be considered in the quest for highly efficient devices. The presented measurement technique can be used for an elaborated examination of spectra from samples which are designed for reduced PL emission. A reduction of the PL from the barriers could be realized by means of avoiding the appearance of high carrier densities. Also a reduction of the volume of the barriers might be helpful in this context. Both can rigorously be realized by direct pumping of the quantum wells.

References

[1] S.W. Corzine, R.S. Seels, J.W. Scott, R.-H. Yan, and L.A. Coldren, "Design of Fabry-Perot surface emitting lasers with a periodic gain structure," *IEEE J. Quantum Electron.*, vol. 25, pp. 1513–1534, 1989.

[2] M. Kuznetsov, F. Hakimi, R. Sprague, and A. Mooradian, "Design and characteristics of high-power (>0.5-W cw) diode-pumped vertical-external-cavity surface-emitting semiconductor lasers with circular TEM_{00} beams," *IEEE J. Select. Topics Quantum Electron.*, vol. 5, pp. 561–573, 1999.

[3] S. Calvez, J. Hastie, A.J. Kemp, N. Laurand, and M.D. Dawson, *Thermal Management, Structure Design, and Integration Considerations for VECSELs,* in O.G.

Ohotnikov (Editor), *Semiconductor Disk Lasers*, Physics and Technology, Wiley-VCH, Weinheim, 2010.

[4] S.-S. Beyertt, U. Brauch, F. Demaria, N. Dhidah, A. Giesen, T. Kübler, S. Lorch, F. Rinaldi, and P. Unger, "Efficient gallium-arsenide disk laser," *IEEE J. Quantum Electron.*, vol. 43, pp. 869–875, 2007.

[5] J.-Y. Kim, S. Cho, J. Lee, G.B. Kim, S.-J. Lim, J. Yoo, K.-S. Kim, S.-M. Lee, J. Shim, T. Kim, and Y. Park, "A measurement of modal gain profile and its effect on the lasing performance in vertical-external-cavity surface-emitting lasers," *IEEE Photon. Technol. Lett.*, vol. 18, pp. 2496–2498, 2006.

[6] F. Demaria, S. Lorch, S. Menzel, M. Riedl, F. Rinaldi, R. Rösch, and P. Unger, "Design of highly efficient high-power optically pumped semiconductor disk lasers," *IEEE J. Select. Topics Quantum Electron.*, vol. 15, pp. 973–977, 2009.

[7] A. Hein, F. Demaria, A. Kern, S. Menzel, F. Rinaldi, R. Rösch, and P. Unger, "Efficient 460-nm second-harmonic generation with optically pumped semiconductor disk lasers," *IEEE Photon. Technol. Lett.*, vol. 23, pp. 179–181, 2011.

[8] F. Demaria and A. Hein, "Intra-cavity second-harmonic generation of blue 460 nm watt-level emission from optically pumped semiconductor disk lasers," *Annual Report 2009*, pp. 3–10. Ulm University, Institute of Optoelectronics.

[9] K.-S. Kim, J. Yoo, G. Kim, S. Lee, S. Cho, J. Kim, T. Kim, and Y. Park, "Enhancement of pumping efficiency in a vertical-external-cavity surface-emitting laser," *IEEE Photon. Technol. Lett.*, vol. 19, pp. 1925–1927, 2007.

[10] A. Hein and F. Demaria, "Bragg Mirror Design for Optically Pumped Semiconductor Disk Lasers Emitting at 920 nm," *Annual Report 2010*, pp. 121–128. Ulm University, Institute of Optoelectronics.

Bragg Mirror Design for Optically Pumped Semiconductor Disk Lasers Emitting at 920 nm

Alexander Hein and Frank Demaria

Bragg mirror designs for Optically Pumped Semiconductor Disk Lasers (OPSDLs) are presented. An optimization takes into account parameters such as reflectivity, thermal resistance, and strain. Calculations and first results are shown for devices with an emission wavelength of 920 nm. The wavelength is of particular interest since its second-harmonic yields 460 nm emission required for RGB display applications.

1. Introduction

Within the last decade, OPSDLs experienced a drastic boost. These devices cover wavelengths from the UV to the IR and are capable of delivering output powers in the watt level for most of these wavelengths [1]. Naturally, there is a demand for a high material quality and for an elaborated layer design in order to overcome degradation mechanisms and to assure extended lifetime.

2. Mirror Type and Material

OPSDLs can be regarded as an active region with an integrated mirror. Since they are low gain devices, the quality factor of the resonator has to be rather high. The integrated mirror, a Distributed Bragg Reflector (DBR), should provide a reflectivity $\geq$ 99.9 %. Taking into account the output characteristics of the OPSDLs, higher outcoupling efficiencies are always achieved for higher reflectivities of the integrated mirror [2] as depicted in Fig. 1.

Highly efficient devices [3, 4] make use of so-called Double-Band Bragg Reflectors (DBBRs), providing a high reflectivity for the pump wavelength in addition to the high reflectivity for the emission wavelength. A benefit of such mirrors is the more homogeneous pumping of the Quantum Wells (QWs) since the profile of the pump intensity is primarily governed by a standing wave distribution and only marginally by the exponential decay being the case for single-band reflector structures. A further advantage is the recycling of the pump light which is not absorbed on a single pass, thus reducing the heat contribution in the reflector. OPSDLs with emission wavelengths related to InGaAs/GaAs-QWs (900–1200 nm) typically utilize DBBRs based on the well characterized $Al_xGa_{1-x}As$ alloy with the most common composition of $Al_{0.2}Ga_{0.8}As$/AlAs. In addition to the demand for high reflectivity, designs of DBBRs also strongly depend on the chosen thermal management approach. Utilizing transparent intra-cavity heat spreaders such as diamond or

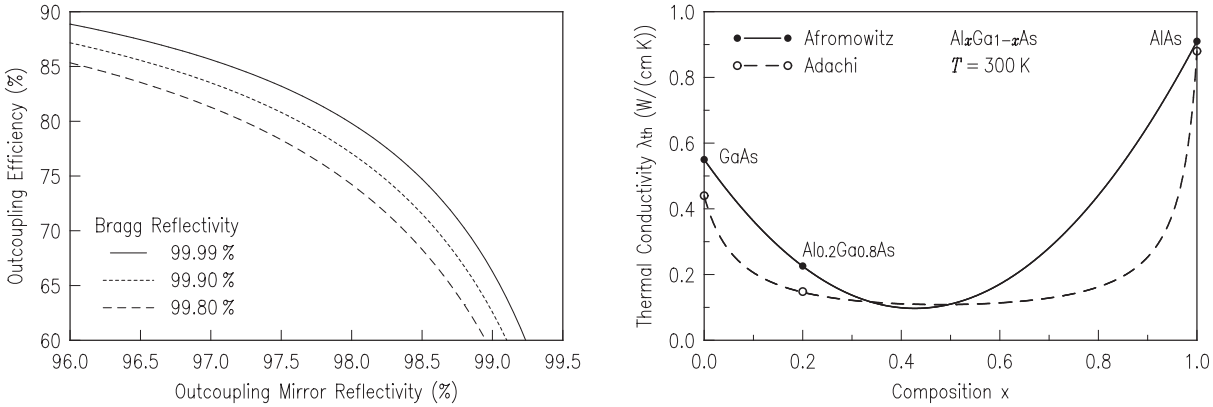

Fig. 1: Outcoupling efficiency for different Bragg mirror reflectivities (left) and thermal conductivity of the $Al_xGa_{1-x}As$ alloy (right) according to [7, 8].

silicon carbide [5], optimization of the thermal resistance of the mirror is not necessary since the largest amount of produced waste heat simply bypasses the DBBR. However, when the more cost effective thin device approach is chosen, where the laser is grown as a bottom emitter and the substrate is removed in postprocessing, the thermal resistance of the mirror should be minimized, simultaneously maintaining the high reflectivity.

3. Mirror Designs

3.1 Thermal considerations

The quantum defect for barrier pumped devices emitting at 920 nm – accounting for the typical pump wavelength of around 808 nm – is rather small compared to longer wavelength OPSDLs. However, a major challenge for the emission at 920 nm is the carrier confinement at elevated temperatures and carrier spillover at high injection levels due to the small energy difference between the InGaAs QW and GaAs barrier ($\approx$ 80 meV) [6]. The layer design of the Bragg mirror is considered with the focus on the reduction of the thermal resistance. An easy approach is to exploit the material system. As shown on the right side of Fig. 1, the AlAs layers of an $Al_{0.2}Ga_{0.8}As$/AlAs Bragg mirror have significatly higher thermal conductivity. Therefore, AlAs is used for the thicker phase matching layers needed for the dual wavelength mirrors. Figure 2 shows the calculated reflectivities of DBBRs with equal thickness, where one structure is a standard approach and the other structure incorporates the described feature. The thermal resistivity of each layer is calcultated according to

$$R_{\mathrm{th},i} = \frac{t_i}{\lambda_{\mathrm{th},i}}, \tag{1}$$

where t_i is the respective layer thickness and $\lambda_{\mathrm{th},i}$ is the temperature-dependent thermal conductivity for the $Al_xGa_{1-x}As$ alloy [8] given by

$$\lambda_{\mathrm{th}} = \frac{1}{xW_{\mathrm{GaAs}} + (1-x)W_{\mathrm{AlAs}} + x(1-x)C_{\mathrm{Ga-Al}}}, \tag{2}$$

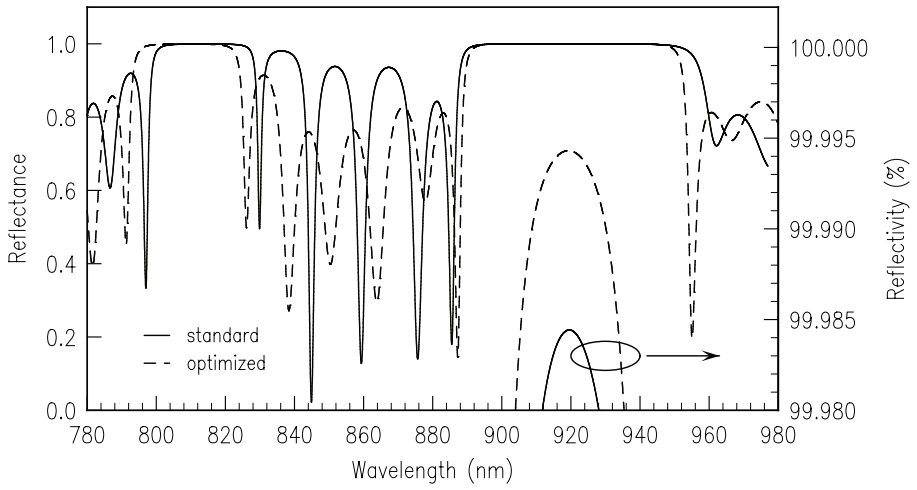

Fig. 2: Calculated reflectivity characteristics of double band Bragg reflectors for a standard and thermally optimized design.

where W_{GaAs} and W_{AlAs} are the binary thermal resistivities, and $C_{\mathrm{Ga-Al}}$ is a disorder factor. The overall thermal resistivity of the multilayer system is calculated from the series connection of the single thermal resistivities:

$$R_{\mathrm{th,tot}} = \sum_i R_{\mathrm{th},i} = \sum_i \frac{t_i}{\lambda_{\mathrm{th},i}}. \tag{3}$$

The described structures are compared in terms of their thermal resistivity according to the above equations in Fig. 3. For the structures under investigation the layer resistivities were calculated as $0.233\,\mathrm{K}\cdot\mathrm{mm}^2/\mathrm{W}$ and $0.168\,\mathrm{K}\cdot\mathrm{mm}^2/\mathrm{W}$, respectively. For typical pump spots of 300 µm diameter the thermal resistance would account to 3.29 K/W and 2.38 K/W, equivalent to an improvement of 18 %.

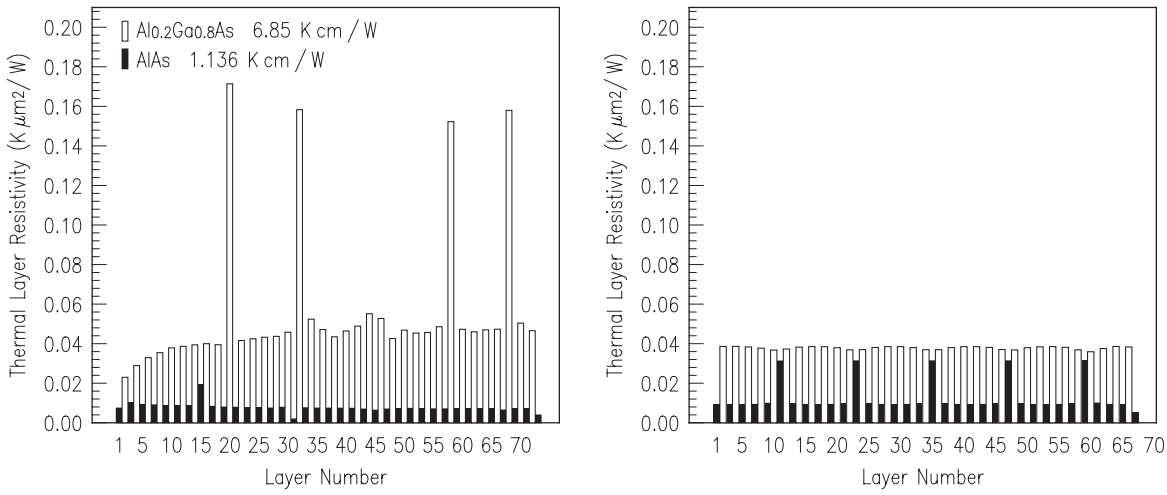

Fig. 3: Thermal layer resistivities of a standard (left) and thermally optimized structure with high AlAs content (right).

3.2 Strain considerations

A major shortcoming utilizing thick AlAs layers arises from the larger strain incorporation. Experiments revealed degradation of the thermally optimized samples, especially when values for the critical thickness in single layers were exceeded, as illustrated in Fig. 4.

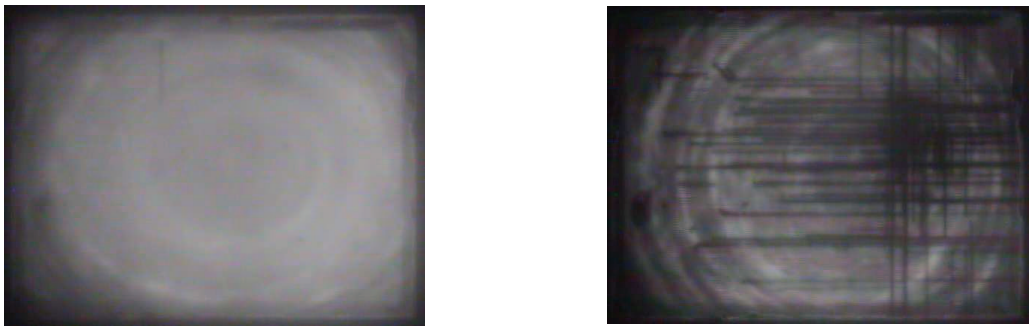

Fig. 4: Locally resolved photoluminescence images of the thermally optimized sample before (left) and after (right) laser operation. The sample was illuminated with a pump laser diode emitting at 808 nm.

A simple qualitative comparison between the structures regarding strain can be drawn weighting the energy stored in the respective structures. The stored energy of a multilayer system can be calculated according to

$$W_{\mathrm{tot}} = \sum_i W_i = \sum_i C_i t_i \epsilon_{||\,i}^2, \tag{4}$$

where $\epsilon_{||\,i}$ is the in-plaine strain given by the mismatch to the substrate and C_i represents the elastic constant of the respective materials [9]. A comparison between the standard and thermally optimized design is depicted in Fig. 5.

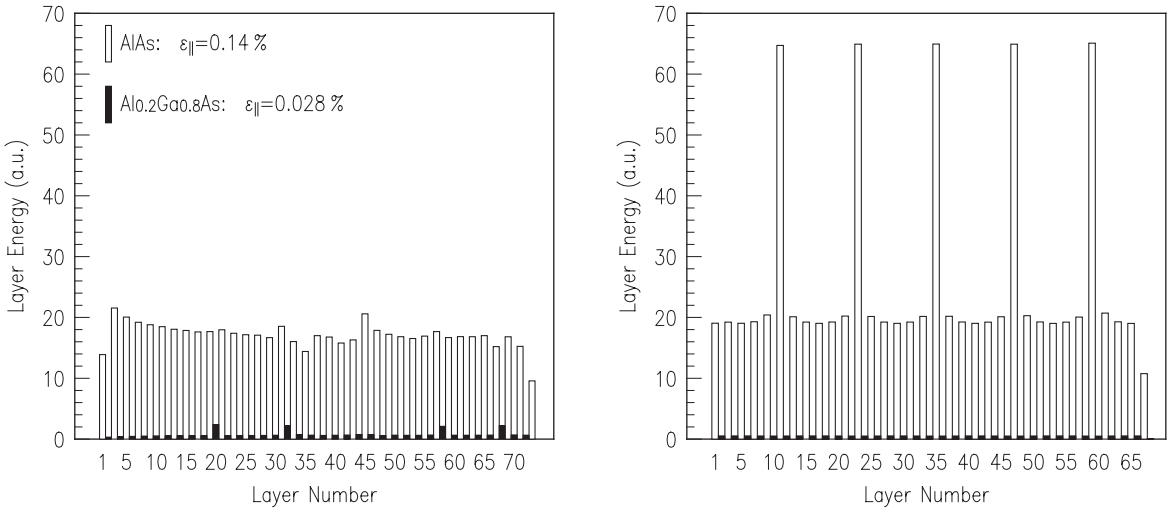

Fig. 5: Comparison of the strain incorporation by means of the respective layer energies of a standard structure (left) and one with higher AlAs content (right).

The highest strain contribution results from the thick AlAs layers. Even though the critical thickness can be exceeded without the formation of dislocations [9], the thick AlAs layers are a weak spot because the single layers already exceed the critical thickness during growth when the structure is susceptible. As described in [10] a straightforward approach would be to replace the adjacent $Al_{0.2}Ga_{0.8}As$ layers by $GaAs_{0.8}P_{0.2}$. In general, with typical layer thicknesses slightly varying around one Quarter Wave Optical Thickness (QWOT) it is not possible to simply replace $Al_{0.2}Ga_{0.8}As$ by $GaAs_{0.8}P_{0.2}$ without offending the critical thickness limitation for $GaAs_{0.8}P_{0.2}$ due to the high lattice mismatch ($\epsilon_{||}$=0.73 %). Hence, this single optical layer is in fact a two layer $Al_{0.2}Ga_{0.8}As$/GaAsP compound, where the phosphorus concentration must be set in a very precise way to match the refractive index of $Al_{0.2}Ga_{0.8}As$. This would introduce adverse conditions for the epitaxial growth. An alternative approach is a distributed compensation, where the thick AlAs layers are split by thin GaAsP intermediates. As shown in Fig. 6 the reflectivity characteristic is not impaired by this method but by proper positioning even slightly enhanced, and deviations of the phosphorus concentration are less crucial.

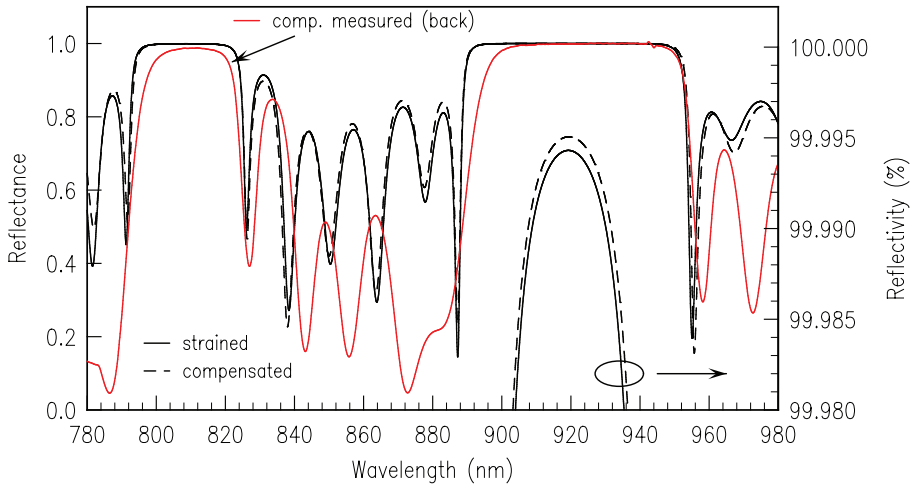

Fig. 6: Calculated reflectivities of structures without and with partial strain compensation, as well as a measured reflectivity characteristic for the compensated structure.

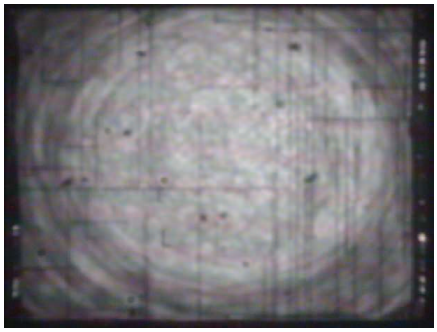

Fig. 7: Locally resolved photoluminescence image of a strain compensated structure, where dislocation defects are still clearly recognizable.

Refering to Fig. 7 a fully successful compensation utilizing the intermediate layer method was not achieved. Although degradation of the compensated structures was not observed,

the defects set a limit to the lasing perfomance. Possible options to further minimize the dislocation defects are higher phoshorus concentrations ($\geq 25\,\%$) in the compensating layers or a higher quantity of these. However, additional layers and interfaces subvert the thermal optimization, thus, a different approach is explored.

4. Hybrid Bragg Reflector

In order to reduce the limitations imposed by strain and simultaneously keeping the thermal resistance to a minimum, a hybrid mirror – combination of a double- and single-band mirror structure – with reduced AlAs content could be a promising approach. Here, a slightly lower reflectivity for the pump wavelength is traded for a thinner top DBBR structure. To maintain the high reflectivity for the emission wavelength the structure is completed with a bottom single-band mirror. The reflectivity characteristic is plotted in Fig. 8 in comparison with the designs described before.

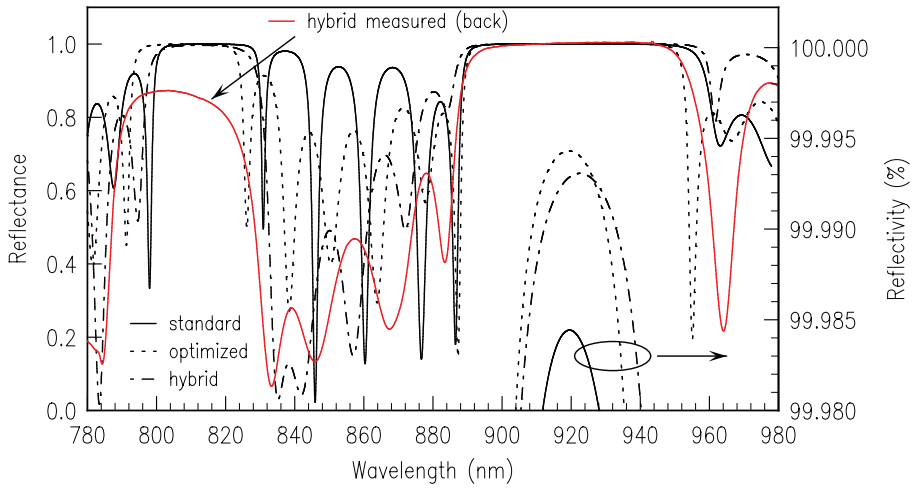

Fig. 8: Comparison of reflectivity characteristics for a hybrid structure with previously proposed designs. Measurement of the hybrid shows good agreement with the calculation except for the damped minor stop band which results from pump light absorption in the single-band mirror.

An argument in favour of such a structure is the possibility of using GaAs in the bottom reflector which due to the high absorption of the pump light normally cannot be employed in a DBBR. Further advantages are the innate better thermal conductivity compared to $Al_{0.2}Ga_{0.8}As$, a slightly reduced thickness due to a higher refractive index, and no strain contribution. It also seems advantageous to replace the high refractive index layers of $Al_{0.2}Ga_{0.8}As$ by $Al_{0.15}Ga_{0.85}As$ in the double-band part. In addition to an improvement of the thermal conductivity ($\approx 14\,\%$), a smaller lattice mismatch is noted. Taking into account the thermally induced shrinkage of the band gap of AlGaAs at the Γ-valley from the relation

$$E_\Gamma(T) = \left(1.7 - \frac{5.41 \cdot 10^{-4} \cdot T^2}{T + 204}\right) \text{ eV} \ , \tag{5}$$

the energy of $Al_{0.15}Ga_{0.85}As$ [11] is large enough to avoid absorption of pump light as long as the temperature is below 450 K. The comparison of thermal characteristics and strain evaluation are shown in Fig. 9.

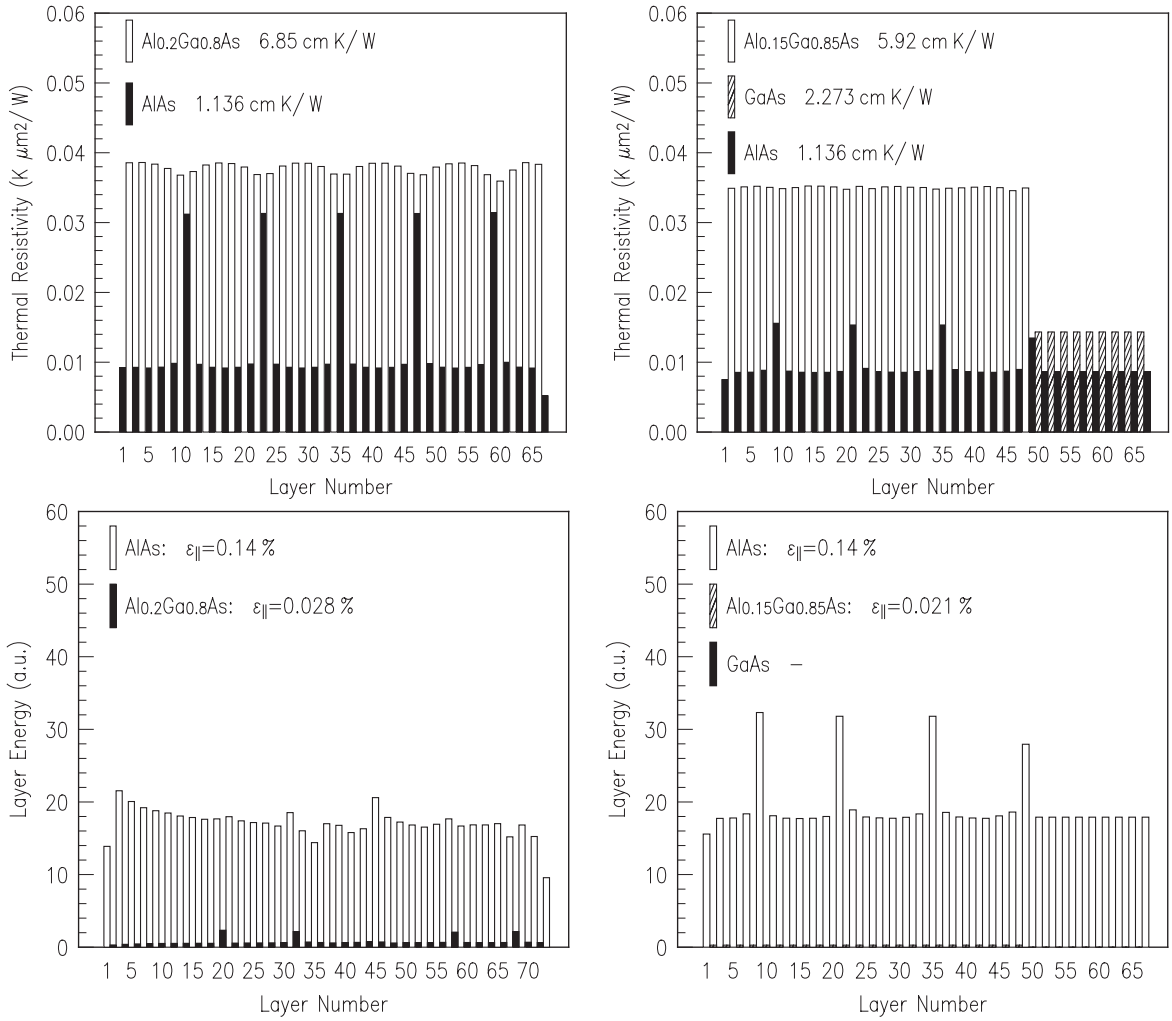

Fig. 9: Thermal resistivity and strain evaluation for the hybrid mirror (right-top and right-bottom) in a triangulation comparison. Thermal resistivity is compared to a thermally optimized structure (top left), whereas strain evaluation is refered to a standard design (bottom left).

Evaluation of the thermal resistance shows an improvement of 23 % (1.83 K/W) compared to the best thermally optimized DBBR structure. Moreover, calculation of the overall stored energy reveals a value which is only 1.3 % larger compared to the standard design.

5. Conclusion

To enhance OPSDL performance we presented new designs regarding the integrated double-band Bragg reflectors in terms of thermal optimization and structural stability. In particular, for the hybrid mirror approach there is an indication that for similar reflectivity behaviour, thermal characteristics clearly outperform standard structures as well

as structures with high AlAs contents for optimized thermal resistance. Regarding strain contribution the hybrid mirror performs equally to the strain proven standard devices and is to be employed in future OPSDL generations.

References

[1] S. Calvez, J.E. Hastie, M. Guina, O.G. Okhotnikov, and M.D. Dawson, "Semiconductor disk lasers for the generation of visible and ultraviolet radiation", *Laser and Photon. Rev.*, vol. 3, pp. 407–434, 2009.

[2] M. Kuznetsov, F. Hakimi, R. Sprague, and A. Mooradian, "Design and characteristics of high power (> 0.5-W cw) diode-pumped vertical-external-cavity surface-emitting semiconductor lasers with circular TEM_{00} beams", *IEEE J. Select. Topics Quantum Electron.*, vol. 5, pp. 561–573, 1999.

[3] F. Demaria, S. Lorch, S. Menzel, G. Riedl, F. Rinaldi, R. Rösch, and P. Unger, "Design of highly efficient high-power optically pumped semiconductor disk lasers", *IEEE J. Select. Topics Quantum Electron.*, vol. 3, pp. 973–977, 2009.

[4] A. Hein, F. Demaria, A. Kern, S. Menzel, F. Rinaldi, R. Rösch, and P. Unger, "Efficient 460-nm second-harmonic generation with optically pumped semiconductor disk lasers", *IEEE Photon. Technol. Lett.*, vol. 23, pp. 179–181, 2011.

[5] K. Kim, J. Yoo, G. Kim, S. Lee, S. Cho, J. Kim, T. Kim and Y. Park, "920-nm Vertical-external-cavity surface-emitting lasers with a slope efficiency of 58% at room temperature", *IEEE Photon. Technol. Lett.*, vol. 19, pp. 1655–1657, 2007.

[6] A.P. Ongstad, D.J. Gallant, and G.C. Dente, "Carrier lifetime saturation in InGaAs single quantum wells", *Appl. Phys. Lett.*, vol. 20, pp. 2730–2732, 1995.

[7] M.A. Afromowitz, "Thermal conductivity of $Ga_{1-x}Al_xAs$ alloys", *J. Appl. Phys.*, vol. 44, pp. 1292–1294, 1973.

[8] S. Adachi, "Lattice thermal conductivity of group-IV and III-V semiconductor alloys", *J. Appl. Phys.*, vol. 102, pp. 063502-1–063502-7, 2007.

[9] F. Rinaldi, *MBE growth and characterization of multilayer structures for vertically emitting laser devices*. Ph.D. thesis, Ulm University, Ulm, Germany, 2008.

[10] F. Rinaldi and S. Menzel, "Advanced strain compensation in MBE-grown semiconductor disk lasers", *Annual Report 2009*, pp. 11–16, Ulm University, Institute of Optoelectronics.

[11] Ioffe Physico-Technical Institute, "Electronic Archive: Physical Properties of Semiconductors", *http://www.ioffe.ru/SVA/NSM/Semicond/AlGaAs/index.html*, 2010.

Ph.D. Thesis

1. Abdel-Sattar Gadallah,
   Advancements in VCSEL Technology: Transverse Mode Control and Matrix-Addressable 2-D Arrays,
   February 2010.

2. Sarad Bahadur Thapa,
   Studies on AlN grown by MOVPE for Electronic and Optoelectronic Applications,
   July 2010.

3. Thomas Wunderer,
   Dreidimensionale Licht emittierende GaInN/GaN-Strukturen mit reduziertem piezoelektrischen Feld,
   July 2010.

4. Andrea Kroner,
   VCSEL-Based Optical Trapping Systems for Microfluidic Applications,
   November 2010.

Diploma and Master Theses

1. Ida Izadi,
   Investigations of GaInN quantum wells on nonpolar GaN,
   Master Thesis, January 2010.

2. Bo Liu,
   Processing and Characterization of Laser-Integrable PIN-Photodiodes for Bidirectional Optical Interconnection at 850 nm,
   Master Thesis, January 2010.

3. Stefan Wabra,
   Kleinsignalmodulationsverhalten von Vertikallaserdioden,
   Diploma Thesis, February 2010.

4. Simeon Renz,
   Entwurf und Herstellung von hochfrequent modulierbaren polarisationsstabilen VCSELn zur Anwendung in Atomuhren,
   Diploma Thesis, April 2010.

5. Florian Kleinert,
   Realisierung einer Matrix-Ansteuerung dicht gepackter Vertikallaserdioden zur Anwendung in optischen Fallen,
   Diploma Thesis, May 2010.

6. Mohammad Tanvir Haidar,
   Processing and Characterization of VCSEL/PIN-Photodetector Transceiver Chips for Bidirectional Multimode Fiber Transmission,
   Master Thesis, July 2010.

7. Barbara Herter,
   Ga-graded Cu(In, Ga)Se_2-layers for photovoltaics,
   Master Thesis, September 2010.

8. Stefan Jäger,
   Entwurf und Herstellung von VCSEL-Arrays zur optofluidischen Partikelfokussierung,
   Diploma Thesis, October 2010.
   Recipient of a VDI Award, Feb. 2011.

9. Andreas Strodl,
   Untersuchungen zur Integration von Halbleiterquantenpunkten in Laserbauelemente,
   Diploma Thesis, October 2010.

10. Hangrong Wu,
    Fabrication of Intentionally Doped Freestanding GaN layers by Hydride Vapor Phase Epitaxy,
    Master Thesis, November 2010.

11. Jürgen Däubler,
Wachstum und Charakterisierung von semipolarem GaN auf vorstrukturierten Saphir-Substraten,
Diploma Thesis, November 2010.

Bachelor Theses

1. Menglong Hao,
   Junction Temperature Determination of LED,
   May 2010.

2. Michael Mertens,
   In-situ Bandkantenabsorptionsspektroskopie zur Temperaturbestimmung beim MBE-Wachstum,
   October 2010.

3. Florian Schiegg,
   Untersuchungen zur Bestimmung der internen Quanteneffizienz von polaren und semipolaren InGaN-Quantentopf-Strukturen,
   October 2010.

4. Nicolas Hibst,
   Experimentelle Untersuchung der Wärmeableitung und temperaturabhängiger Lichtemission an optisch gepumpten Halbleiterscheibenlasern,
   November 2010.

Semester Projects

1. Florian Kleinert,
   Weiterentwicklung einer Simulationssoftware zur Berechnung eindimensionaler Wellenausbreitung in Mehrschichtstrukturen,
   September 2010.

2. Marian Caliebe,
   Untersuchungen von GaN- und InGaN-Schichten an überwachsenen ZnO-Nanosäulen,
   December 2010.

Talks and Conference Contributions

[1] A. Al-Samaneh, S. Renz, A. Strodl, W. Schwarz, D. Wahl, and R. Michalzik, "Polarization-stable single-mode VCSELs for Cs-based MEMS atomic clock applications", *SPIE Photonics Europe*, Conf. on *Semiconductor Lasers and Laser Dynamics IV*, Brussels, Belgium, Apr. 2010.

[2] A. Al-Samaneh, S. Renz, D. Wahl, and R. Michalzik, "Small-signal analysis and polarization stability performance of single-mode VCSELs for MEMS atomic clock applications", *Sixth Joint Symposium on Opto- and Microelectronic Devices and Circuits, SODC 2010*, Berlin, Germany, Oct. 2010.

[3] J. Däubler, S. Schwaiger, I. Tischer, R.A.R. Leute, T. Wunderer, K. Thonke, and F. Scholz, "GaN auf vorstrukturiertem Saphir: Wachstum, Charakterisierung und Lumineszenz von InGaN QWs", *25th DGKK Workshop "Epitaxie von III/V-Halbleitern"*, Aachen, Germany, Dec. 2010.

[4] M. Fikry, M. Madel, I. Tischer, K. Thonke, and F. Scholz, "Epitaxial growth of Coaxial GaN/InGaN/GaN hetero-nanotubes", *International Symposium on Growth of III-Nitrides, ISGN2010*, Montpellier, France, July 2010.

[5] M. Fikry, M. Madel, I. Tischer, Y. Men, K. Thonke, and F. Scholz, "Epitaxial Growth and Position Control of Coaxial GaN/ZnO Heterostructures and GaN/InGaN/GaN Hetero-Nanotubes", *International Workshop on Nitride Semiconductors, IWN2010*, Tampa, Florida, USA, Sept. 2010.

[6] M. Fikry, M. Madel, I. Tischer, K. Thonke, and F. Scholz, "Epitaxial GaN and InGaN around ZnO nanopillars", *5th Nanowire Growth Workshop, NWG 2010*, Rome, Italy, Nov. 2010.

[7] K. Forghani, M. Klein, F. Lipski, S. Schwaiger, J. Hertkorn, F. Scholz, B. Neuschl, K. Fujan, I. Tischer, M. Feneberg, K. Thonke, O. Klein, U. Kaiser, T. Passow, and R. Gutt, "High quality AlGaN epilayers grown directly on sapphire without GaN buffer layer", *15th International Conference on Metalorganic Vapor Phase Epitaxy, ICMOVPE-XV*, Lake Tahoe, NV, USA, May 2010.

[8] K. Forghani, M. Klein, F. Liski, S. Schwaiger, J. Hertkorn, F. Scholz, B. Neuschl, K. Fujan, I. Tischer, M. Feneberg, K. Thonke, O. Klein, U. Kaiser, T. Passow, and R. Gutt, "High quality AlGaN epilayers grown directly on sapphire without GaN buffer layer", *Palo Alto Research Center*, Palo Alto, CA, USA, June 2010.

[9] K. Forghani, O. Klein, M. Feneberg, M. Klein, B. Neuschl, F. Lipski, S. Schwaiger, M. Gharavipour, K. Thonke, U. Kaiser, and F. Scholz,"In-situ deposited SiN nanomask for crystal quality improvement in AlGaN", *International Workshop on Nitride Semiconductors, IWN2010*, Tampa, Florida, USA, Sept. 2010.

[10] A. Gadallah, A. Bergmann, and R. Michalzik, "High-power single-higher-order-mode VCSELs for optical particle manipulation", poster at *SPIE Photonics Europe*, Conf. on *Semiconductor Lasers and Laser Dynamics IV*, Brussels, Belgium, Apr. 2010.

[11] A. Gadallah and R. Michalzik, "Densely-packed 2-D matrix-addressable vertical-cavity surface-emitting laser arrays", *The 4th International Conf. on Modern Trends in Physics Research, MTPR-010*, Sharm El Sheikh, Egypt, Dec. 2010.

[12] A. Kern, D. Wahl, M.T. Haidar, B. Liu, W. Schwarz, R. Rösch, and R. Michalzik, "Monolithic integration of VCSELs and PIN photodiodes for bidirectional data communication over standard multimode fibers", *SPIE Photonics Europe*, Conf. on *Semiconductor Lasers and Laser Dynamics IV*, Brussels, Belgium, Apr. 2010.

[13] R.A.R. Leute, T. Wunderer, F. Lipski, F. Scholz, J. Biskupek, A. Chuvilin, L. Lechner, U. Kaiser, M. Brendel, A.D. Dräger, and A. Hangleiter, "GaN-based laser structure integrating three-dimensional semipolar InGaN QWs within a planar c-oriented waveguide", *E-MRS 2010 Fall Meeting*, Warsaw, Poland, Sept. 2010.

[14] R.A.R. Leute, T. Wunderer, J. Wang, S. Schwaiger, F. Lipski, K. Forghani, F. Scholz, A. Chuvilin, J. Biskupek, L. Lechner U. Kaiser, D. Dräger, M. Brendel, and A. Hangleiter "GaN-based laser structure using 3D semipolar InGaN quantum wells embedded in planar AlGaN cladding layers", *PolarCoN Summer School*, Ulm University Conference Centre Schloss Reisensburg, Günzburg, Germany, Oct. 2010.

[15] R.A.R. Leute, K. Forghani, F. Lipski, S. Schwaiger and F. Scholz, "Dreidimensionale AlGaN-Strukturen als Wellenleiter-Mantel für semipolare Laserstrukturen", *25th DGKK Workshop "Epitaxie von III/V-Halbleitern"*, Aachen, Germany, Dec. 2010.

[16] F. Lipski, H. Wu, S. Schwaiger, L. Kirste, E. Richter, and F. Scholz, "Semi-insulating GaN by Fe-Doping in Hydride Vapor Phase Epitaxy Using a Solid Source", *International Symposium on Growth of III-Nitrides, ISGN2010*, Montpellier, France, July 2010.

[17] R. Michalzik, A. Kern, M. Stach, F. Rinaldi, and D. Wahl, "True bidirectional optical interconnects over multimode fiber" (invited), *SPIE Photonics West 2010*, Conf. on *Optoelectronic Interconnects and Component Integration X*, San Francisco, CA, USA, Jan. 2010.

[18] R. Michalzik, "High-volume VCSEL applications: present and future" (invited), *Global COE PICE International Symposium – Photonics Breakthrough toward Next-generation ICT –*, Tokyo, Japan, March 2010.

[19] R. Michalzik, A. Al-Samaneh, and D. Wahl, "VCSELs for atomic clocks", *VCSEL Day 2010*, Torino, Italy, May 2010.

[20] R. Michalzik, A. Kern, M. Stach, W. Schwarz, M.T. Haidar, R. Rösch, F. Rinaldi, and D. Wahl, "VCSELs monolithically integrated with photodiodes: good for bidirectional data transmission over multimode fiber?", *European Semiconductor Laser Workshop*, Pavia, Italy, Sept. 2010.

[21] F. Scholz, T. Wunderer, M. Feneberg, K. Thonke, A. Chuvilin, U. Kaiser, S. Metzner, F. Bertram, and J. Christen, "AlGaInN heterostructures on semipolar facets of selectively grown GaN stripes for optoelectronic applications" (invited), *SPIE Photonics West*, San Francisco, CA, USA, Jan. 2010.

[22] F. Scholz, T. Wunderer, M. Feneberg, K. Thonke, A. Chuvilin, U. Kaiser, S. Metzner, F. Bertram, J. Christen, M. Brendel, D. Dräger, and A. Hangleiter, "GaInN-based LED structures on selectively grown semi-polar crystal facets" (invited), *2010 March Meeting of the American Physical Society*, Portland, OR, USA, March 2010.

[23] F. Scholz, T. Wunderer, M. Feneberg, K. Thonke, A. Chuvilin, J. Biskupek, U. Kaiser, S. Metzner, F. Bertram, J. Christen, M. Brendel, D. Dräger, and A. Hangleiter, "Patterned growth of GaN-based LED structures" (invited), *10th International Workshop on Expert Evaluation and Control of Compound Semiconductor Materials and Technologies, EXMATEC 2010*, Seeheim-Jugenheim, Germany, March 2010.

[24] F. Scholz, F. Lipski, S. Schwaiger, and T. Wunderer, "Hydride vapor phase epitaxy of thick polar and non-polar GaN layers" (invited), *The IX International Conference of Polish Crystal Growth Soc., ICPSCG-9*, Gdansk, Poland, May 2010.

[25] F. Scholz, T. Wunderer, M. Feneberg, K. Thonke, A. Chuvilin, and U. Kaiser, "Investigations about local GaInN quantum well properties grown on triangular GaN stripes", *International Workshop on Nitride Semiconductors, IWN2010*, Tampa, Florida, USA, Sept. 2010.

[26] F. Scholz, "Licht aus dem Kristall: Leuchtquellen mit höchster Effizienz" (invited), *Ulmer 3-Generationen-Uni*, Ulm University, Ulm, Germany, Nov. 2010.

[27] S. Schwaiger, I. Argut, T. Wunderer, F. Lipski, R. Rösch, and F. Scholz, "Growth of planar semipolar GaN via epitaxial lateral overgrowth on pre-patterned sapphire substrates", *DPG Frühjahrstagung*, Regensburg, Germany, March 2010.

[28] S. Schwaiger, T. Wunderer, I. Argut, F. Lipski, R. Rösch, and F. Scholz, "Planar semipolar $\{11\bar{2}2\}$ and $\{10\bar{1}1\}$ GaN on pre-patterned saphire substrates", *Neue Materialien - Halbleiter*, Otto-von-Guericke Universität Magdeburg, Magdeburg, Germany, Apr. 2010.

[29] S. Schwaiger, I. Argut, T. Wunderer, F. Lipski, R. Rösch, F. Scholz, S. Metzner, F. Bertram, and J. Christen, "Growth of planar semipolar GaN on pre-patterned sapphire substrates", *15th International Conference on Metalorganic Vapor Phase Epitaxy, ICMOVPE-XV*, Lake Tahoe, NV, USA, May 2010.

[30] S. Schwaiger, I. Argut, T. Wunderer, F. Lipski, R. Rösch, F. Scholz, S. Metzner, F. Bertram, J. Christen, K. Fujan, M. Feneberg, and K. Thonke, "Semipolar GaN on pre-patterned sapphire substrates: growth and characterization", *Palo Alto Research Center*, Palo Alto, CA, USA, June 2010.

[31] S. Schwaiger, J. Däubler, and F. Scholz, "Semipolar GaN on structured sapphire: coalescence behaviour and luminescence from InGaN quantum wells", *PolarCon Summer School*, Ulm University Conference Centre Schloss Reisensburg, Günzburg, Germany, Oct. 2010.

[32] S. Schwaiger, S. Metzner, J. Thalmair, S. Neugebauer, T. Wunderer, J. Däubler, F. Bertram, J. Zweck, J. Christen, and F. Scholz, "Koaleszenz von {11-22} orientiertem GaN auf strukturierten r-orientierten Saphir-Substraten", *25th DGKK Workshop "Epitaxie von III/V-Halbleitern"*, Aachen, Germany, Dec. 2010.

[33] D. Wahl, A. Kern, M. Stach, F. Rinaldi, R. Rösch, and R. Michalzik, "VCSELs with monolithically integrated photodiodes for single-fiber bidirectional data transmission in the Gbit/s range", *16th Int. Conf. on Molecular Beam Epitaxy, MBE 2010*, Berlin, Germany, Aug. 2010.

[34] B. Westenfelder, J.C. Meyer, J. Biskupek, G. Algara-Siller, C.E. Krill III, F. Scholz, and U. Kaiser, "In situ ultra-HRTEM electrical investigations of graphene", poster at *24th International Winterschool on: Electronic Properties of Novel Materials, IWEPNM 2010*, Kirchberg, Austria, March 2010.

[35] T. Wunderer, F. Lipski, S. Schwaiger, F. Scholz, M. Feneberg, K. Thonke, A. Chuvilin, U. Kaiser, S. Metzner, F. Bertram, J. Christen, C. Vierheilig, and U. Schwarz, "Three-dimensional GaN for semipolar light emitters" (invited), *DPG Frühjahrstagung*, Regensburg, Germany, March 2010.

[36] T. Wunderer, R.A.R. Leute, J. Wang, S. Schwaiger, F. Lipski, K. Forghani, F. Scholz, J. Biskupek, A. Chuvilin, U. Kaiser, M. Brendel, D. Dräger, and A. Hangleiter, "GaN-based laser structure with semipolar InGaN QWs realized by selective area epitaxy", *DPG Frühjahrstagung*, Regensburg, Germany, March 2010.

[37] T. Wunderer, J. Biskupek, A. Chuvilin, U. Kaiser, Y. Men, J. Wang, F. Lipski, S. Schwaiger, K. Forghani, and F. Scholz, "GaN-based laser structure using 3D semipolar InGaN qunatum wells embedded in planar AlGaN cladding layers", *15th International Conference on Metalorganic Vapor Phase Epitaxy, ICMOVPE-XV*, Lake Tahoe, NV, USA, May 2010.

[38] L. Bimboes, F. Gruet, C. Affolderbach, R. Matthey, G. Mileti, A. Al-Samaneh, D. Wahl, and R. Michalzik, "Spectral characterization of 894 nm VCSELs for MEMS atomic clocks", *Atelier à Arc-et-Senans, Les microtechniques dans le quotidien*, one-page abstract and poster. Saline Royale d'Arc-et-Senans, France, Sept. 2010.

[39] C. Borgentun, J. Bengtsson, A. Larsson, F. Demaria, A, Hein, and P. Unger, "Optically pumped high-power semiconductor disk laser with gain element engineered for wide tunability", *SPIE Photonics Europe*, Conf. on *Semiconductor Lasers and Laser Dynamics IV*, Brussels, Belgium, Apr. 2010.

[40] H. Bremers, A. Schwiegel, H. Jönen, U. Rossow, M. Brendel, A.D. Dräger, A. Hangleiter, S. Schwaiger, and F. Scholz, "Identical indium incorporation in polar

and nonpolar GaInN quantum wells: a high resolution X-ray diffraction study", *International Workshop on Nitride Semiconductors, IWN2010*, Tampa, Florida, USA, Sept. 2010.

[41] J. Christen, S. Metzner, F. Bertram, T. Wunderer, F. Lipski, S. Schwaiger, and F. Scholz, "Spatio-time-resolved cathodoluminescence spectroscopy imaging microscopic correlation of real structure and recombination kinetics in InGaN quantum wells" (invited), *SPIE Photonics West*, San Francisco, CA, USA, Jan. 2010.

[42] J. Christen, F. Bertram, S. Metzner, T. Wunderer, F. Lipski, S. Schwaiger, and F. Scholz, "Spatio-time-resolved cathodoluminescence spectroscopy imaging: microscopic recombination kinetics in semi-polar InGaN quantum wells" (invited), *M&M*, Portland, OR, USA, Aug. 2010.

[43] J. Christen, F. Bertram, S. Metzner, T. Wunderer, F. Lipski, S. Schwaiger, and F. Scholz, "Microscopic energy relaxation in semipolar InGaN quantum wells via real space transfer-directly imaged by spatio-time-resolved cathodoluminescence spectroscopy", *International Workshop on Nitride Semiconductors, IWN2010*, Tampa, Florida, USA, Sept. 2010.

[44] K.J. Fujan, M. Feneberg, B. Neuschl, I. Tischer, K. Thonke, S. Schwaiger, I. Izadi, F. Scholz, L. Lechner, J. Biskupek, and U. Kaiser, "The dominant role of pits in the emission spectra of GaInN quantum wells grown on non-polar a-plane GaN", *International Workshop on Nitride Semiconductors, IWN2010*, Tampa, Florida, USA, Sept. 2010.

[45] H. Jönen, H. Bremers, U. Rossow, A. Schwiegel, M. Brendel, A.D. Dräger, A. Hangleiter, S. Schwaiger, and F. Scholz, "Comparable indium incorporation in polar and nonpolar GaInN quantum wells for longwavelength lasers", *E-MRS Fall Meeting*, Warsaw, Poland, Sept. 2010.

[46] H. Jönen, H. Bremers, U. Rossow, L. Hoffmann, H. Schwiegel, M. Brendel, A.D. Dräger, S. Schwaiger, F. Scholz, J. Thalmaier, J. Zweck, and A. Hangleiter, "Indium-Einbau in GaInN Quantenfilmen auf polaren und nichtpolaren Oberflächen", *25th DGKK Workshop "Epitaxie von III/V-Halbleitern"*, Aachen, Germany, Dec. 2010.

[47] C. Karbaum, F. Bertram, S. Metzner, J. Christen, T. Wunderer, and F. Scholz, "Spectrally resolved cathodoluminescence microscopy of an InGaN SQW on hexagonally inverted GaN pyramids", *DPG Frühjahrstagung*, Regensburg, Germany, March 2010.

[48] M. Kunzer, R. Gutt, L. Kirste, T. Passow, K. Forghani, F. Scholz, K. Köhler, and J. Wagner, "Improved quantum efficiency of 350 nm LEDs grown on low dislocation density AlGaN buffer layers", *International Workshop on Nitride Semiconductors, IWN2010*, Tampa, Florida, USA, Sept. 2010.

[49] S. Metzner, F. Bertram, J. Christen, T. Wunderer, F. Lipski, S. Schwaiger, and F. Scholz, "Microscopic correlation of real structure and recombination kinetics in semipolar InGaN SQW using spatio-time-resolved cathodoluminescence", *DPG Frühjahrstagung*, Regensburg, Germany, March 2010.

[50] S. Metzner, F. Bertram, T. Hempel, J. Christen, T. Wunderer, F. Lipski, S. Schwaiger, and F. Scholz, "Spatio-time resolved cathodoluminescence microscopy of semipolar InGaN SQW on inverse GaN pyramids: correlation of real structure and recombination kinetics", *15th International Conference on Metalorganic Vapor Phase Epitaxy, ICMOVPE-XV*, Lake Tahoe, NV, USA, May 2010.

[51] S. Metzner, S. Neugebauer, F. Bertram, T. Hempel, J. Christen, S. Schwaiger, I. Argut, T. Wunderer, F. Lipski, R. Rösch, and F. Scholz, "Microscopic investigation of planar semipolar GaN directly grown on pre-patterned sapphire substrates by cathodoluminescence", poster at *International Workshop on Nitride Semiconductors, IWN2010*, Tampa, Florida, USA, Sept. 2010.

[52] J. Meyer, S. Kurasch, G. Algara-Siller, U. Kaiser, B. Westenfelder, F. Scholz, and C. Krill, "Towards microscopy on graphene", *Graphene Seminar Fraunhofer IPA*, Stuttgart, Germany, June 2010.

[53] S. Neugebauer, S. Metzner, F. Bertram, T. Hempel, J. Christen, S. Schwaiger, J. Däubler, and F. Scholz, "Highly spatially and spectrally resolved cathodoluminescence of planar semipolar GaN grown on pre-patterned sapphire substrate", *25th DGKK Workshop "Epitaxie von III/V-Halbleitern"*, Aachen, Germany, Dec. 2010.

Publications

[1] A. Al-Samaneh, S. Renz, D. Wahl, and R. Michalzik, "Small-signal analysis and polarization stability performance of single-mode VCSELs for MEMS atomic clock applications", in Proc. *Sixth Joint Symposium on Opto- and Microelectronic Devices and Cicuits, SODC 2010*, pp. 61–64. Berlin, Germany, Oct. 2010.

[2] A. Al-Samaneh, S. Renz, A. Strodl, W. Schwarz, D. Wahl, and R. Michalzik, "Polarization-stable single-mode VCSELs for Cs-based MEMS atomic clock applications", in *Semiconductor Lasers and Laser Dynamics IV*, K.P. Panayotov, M. Sciamanna, A.A. Valle, R. Michalzik (Eds.), Proc. SPIE 7720, pp. 772006-1–14, 2010 (Best Student Paper Award).

[3] A. Gadallah and R. Michalzik, "Densely-packed 2-D matrix-addressable vertical-cavity surface-emitting laser arrays", in Proc. *The 4th International Conf. on Modern Trends in Physics Research, MTPR-010*, p. 37. Sharm El Sheikh, Egypt, Dec. 2010.

[4] A. Gadallah, A. Bergmann, and R. Michalzik,"High-power single-higher- order-mode VCSELs for optical particle manipulation", in *Semiconductor Lasers and Laser Dynamics IV*, K.P. Panayotov, M. Sciamanna, A.A. Valle, R. Michalzik (Eds.), Proc. SPIE 7720, pp. 77201Y-1–10, 2010.

[5] A. Kern, D. Wahl, M.T. Haidar, B. Liu, W. Schwarz, R. Rösch, and R. Michalzik, "Monolithic integration of VCSELs and PIN photodiodes for bidirectional data communication over standard multimode fibers", in *Semiconductor Lasers and Laser Dynamics IV*, K.P. Panayotov, M. Sciamanna, A.A. Valle, R. Michalzik (Eds.), Proc. SPIE 7720, pp. 77200B-1–9, 2010.

[6] F. Lipski, T. Wunderer, S. Schwaiger, and F. Scholz, "Fabrication of freestanding 2"-GaN wafers by hydride vapour phase epitaxy and self-separation during cooldown", *phys. status solidi (a)*, vol. 207, pp. 1287–1291, 2010.

[7] R. Michalzik, "High-volume VCSEL applications: present and future" (invited), in Proc. *Global COE PICE International Symposium – Photonics Breakthrough toward Next-generation ICT* –, pp. 50–52. Tokyo, Japan, March 2010.

[8] R. Michalzik, A. Kern, M. Stach, F. Rinaldi, and D. Wahl, "True bidirectional optical interconnects over multimode fiber" (invited), in *Optoelectronic Interconnects and Component Integration X*, A.L. Glebov, R.T. Chen (Eds.), Proc. SPIE 7607, pp. 76070B-1–17, 2010.

[9] F. Scholz, T. Wunderer, M. Feneberg, K. Thonke, A. Chuvilin, U. Kaiser, S. Metzner, F. Bertram, and J. Christen, "GaInN-based LED structures on selectively grown semi-polar crystal facets", *phys. status solidi (a)*, vol. 207, pp. 1407–1413, 2010.

[10] S. Schwaiger, I. Argut, T. Wunderer, R. Rösch, F. Lipski, J. Biskupek, U. Kaiser, and F. Scholz, "Planar semipolar $\{10\bar{1}1\}$ GaN on $\{11\bar{2}3\}$ sapphire", *Appl. Phys. Lett.*, vol. 96, pp. 231905-1–3, 2010.

[11] S. Schwaiger, F. Lipski, T. Wunderer, and F. Scholz, "Influence of slight misorientations of r-plane sapphire substrates on the growth of nonpolar a-plane GaN layers via HVPE", *phys. status solidi (c)*, vol. 7, pp. 2069–2072, 2010.

[12] D. Wahl, A. Kern, M. Stach, F. Rinaldi, R. Rösch, and R. Michalzik, "VCSELs with monolithically integrated photodiodes for single-fiber bidirectional data transmission in the Gbit/s range", *J. Cryst. Growth*, 4 pages, in press, 2010. Online dx.doi.org/10.1016/j.jcrysgro.2010.11.103

[13] D. Wahl, A. Kern, M. Stach, F. Rinaldi, R. Rösch, and R. Michalzik, "VCSELs with monolithically integrated photodiodes for single-fiber bidirectional data transmission in the Gbit/s range", in Proc. (USB stick) *16th Int. Conf. on Molecular Beam Epitaxy, MBE 2010*, paper Tue B1.4, 2 pages. Berlin, Germany, Aug. 2010.

[14] T. Wunderer, J. Wang, F. Lipski, S. Schwaiger, A. Chuvilin, U. Kaiser, S. Metzner, F. Bertram, J. Christen, S.S. Shirokov, A.E. Yunovich, and F. Scholz, "Semipolar GaInN/GaN light-emitting diodes grown on honeycomb patterned substrates", *phys. status solidi (c)*, vol. 7, pp. 2140–2143, 2010.

[15] M. Barchuk, V. Holý, B. Miljevic, B. Krause, T. Baumbach, J. Hertkorn, and F. Scholz, "X-ray diffuse scattering from threading dislocations in epitaxial GaN layers", *J. Appl. Phys.*, vol. 108, pp. 043521-1–7, 2010.

[16] C. Borgentun, J. Bengtsson, A. Larsson, F. Demaria, A, Hein, and P. Unger, "Optimization of a broadband gain element for a widely tunable high-power semiconductor disk laser", *IEEE Photon. Technol. Lett.*, vol. 22, no. 13, pp. 978–980, 2010.

[17] C. Borgentun, J. Bengtsson, A. Larsson, F. Demaria, A. Hein, and P. Unger, "Optically pumped high-power semiconductor disk laser with gain element engineered for wide tunability", in *Semiconductor Lasers and Laser Dynamics IV*, K.P. Panayotov, M. Sciamanna, A.A. Valle, R. Michalzik (Eds.), Proc. SPIE 7720, pp. 772014-1–8, 2010.

[18] M. Feneberg, K. Thonke, T. Wunderer, F. Lipski, and F. Scholz, "Piezoelectric polarization of semipolar and polar GaInN quantum wells grown on strained GaN templates", *J. Appl. Phys.*, vol. 107, pp. 103517-1–6, 2010.

[19] K.J. Fujan, M. Feneberg, B. Neuschl, T. Meisch, I. Tischer, K. Thonke, S. Schwaiger, I. Izadi, F. Scholz, L. Lechner, J. Biskupek, and U. Kaiser, "Cathodoluminescence of GaInN quantum wells grown on nonpolar a plane GaN: intense emission from pit facets", *Appl. Phys. Lett.*, vol. 97, pp. 101904-1–3, 2010.

[20] O. Klein, J. Biskupek, U. Kaiser, K. Forghani, S.B. Thapa, and F. Scholz, "Simulation supported analysis of the effect of SiNx interlayers in AlGaN on the dislocation density reduction", *Journal of Physics: Conf. Ser.*, vol. 209, pp. 012018-1–6, 2010.

[21] D. Kück, J. Scharpf, W. Ebert, M. Fikry, F. Scholz, and E. Kohn, "Passivation of H-terminated diamond with MOCVD-aluminium nitride – a key to understand and

stabilize its surface conductivity", *phys. status solidi (a)*, vol. 207, pp. 2035–2039, 2010.

[22] A. Molitor, M. Blazek, J.M. Ostermann, R. Michalzik, P. Debernardi, and W. Elsaesser, "Investigations on the intensity noise of surface grating relief VCSELs", *IEEE J. Quantum Electron.*, vol. 46, no. 4, pp. 554–561, 2010.

[23] B. Neuschl, K.J. Fujan, M. Feneberg, I. Tischer, K. Thonke, K. Forghani, M. Klein, and F. Scholz, "Cathodoluminescence and photoluminescence study on AlGaN layers grown with SiN_x interlayers", *Appl. Phys. Lett.*, vol. 97, pp. 192108-1–3, 2010.

[24] Q.Y. Wei, Z.H. Wu, F.A. Ponce, J. Hertkorn, and F. Scholz, "Polarization effects in 2-DEG and 2-DHG AlGaN/AlN/GaN multi-heterostructures measured by electron holography", *phys. status solidi (b)*, vol. 247, pp. 1722–1724, 2010.

ulm university universität ulm

Ulm University
Institute of Optoelectronics
Albert-Einstein-Allee 45
89081 Ulm | Germany

Ulm University | Institute of Optoelectronics | Annual Report 2010